

https://dspace.org/

# Characterisation of uranium-mineral-bearing samples in the Vaal Reef of the Klerksdorp Goldfield, Witwatersrand basin

**Sebola, Tlou Piet**

**2015-01-30**
http://hdl.handle.net/10539/16820

Downloaded from a DSpace repository. https://dspace.org/




# CHARACTERISATION OF URANIUM-MINERAL-BEARING SAMPLES IN THE VAAL REEF OF THE KLERKSDORP GOLDFIELD, WITWATERSRAND BASIN

Tlou Piet Sebola

A Dissertation submitted to the Faculty of Science, University of the Witwatersrand, Johannesburg, in fulfilment of the requirements for the degree of Master Science.

23 September 2014, Johannesburg.

## DECLARATION

I declare that this dissertation is my own, unaided work. It is being submitted for the degree of Master of Science at the University of the Witwatersrand, Johannesburg. It has not been submitted before for any degree or examination at any other University.

_____

(Signature of Candidate)

_____day of_____20_____at_____

## Abstract

The Witwatersrand Basin has been mined for the last 125 years and is still one of the world's largest producers of gold and has produced over 50 000 tonnes. However, uranium has also been mined as a by-product of gold from the Witwatersrand reefs, and over 150 000 tonnes have been produced. Over the past decades, the origin of this world class gold and uranium deposit has been debated and still remains controversial. Three main hypotheses were developed, and these are the placer, modified placer and hydrothermal models. In this study, the aims are: to evaluate how many generations of uranium-bearing minerals are in the Vaal Reef samples analysed from Great Noligwa, Moab Khotsong and Kopanang mines and to determine which model among the placer, modified place and hydrothermal best supports the emplacement of the uranium-bearing minerals in the reef. The Vaal Reef occurs in the lower parts of the Strathmore Formation of the Johannesburg Subgroup in the Central Rand Group of the Klerksdorp Goldfield in the Witwatersrand Supergroup. The Vaal Reef is split into three facies, namely the C, B and A Facies; the C and A Facies are the most economic facies at the three mines. The C Facies is well developed at Kopanang mine and the A Facies is well developed at both Moab Khotsong and Great Noligwa mines. Geochemical analyses revealed that the C Facies is enriched in uranium, carbon, sulphur and aluminium; this is due to the presence of uraninite, carbonaceous matter, pyrite and sheet silicate minerals, respectively. The A Facies, however, is more enriched in gold and quartz content, although high uranium, carbon and sulphur concentrations are found, they do not exceed the C Facies concentrations.

Mineralogical investigations showed that uraninite, brannerite and uraniferous leucoxene are the uranium-bearing minerals present in the Vaal Reef samples. Uraninite is the main mineral and occurs firstly with detrital minerals such as pyrite, zircon and chromite in the quartz matrices; the second occurrence of uraninite is with the carbonaceous matter. Brannerite and uraniferous leucoxene are suggested to be formed from the breakdown of detrital uraninite grains interacting with Ti-rich minerals such as rutile. Unlike uraninite, brannerite and uraniferous leucoxene occur mainly in the C Facies matrix and occur as patchy or irregular-shaped minerals. The uraninite grains associated with the detrital minerals are mainly round in shape with sizes up to ~150 to 200 μm. This association with the detrital minerals suggests that uraninite was deposited together with the detrital minerals at the same time and that they were in hydraulic equilibrium with one another. Therefore, uraninite is also detrital in origin.

The second generation of uraninite grains in the carbonaceous matter mainly show replacement and breakdown of uraninite by the latter, in many observations, uraninite grains are penetrated by the carbonaceous matter through cracks and are further fragmented into smaller grains. The sizes of these fragmented grains vary between 5 – 80 μm and have angular shapes, suggesting that they were first rounded and later broken down and replaced by the carbonaceous matter. A four-staged paragenetic sequence of the Vaal Reef samples was developed, and more importantly the paragenesis showed that the carbonaceous matter post-dates the deposition of uraninite.

The three-dimensional microfocus X-Ray computed tomography (3D μXCT) was applied to the Vaal Reef samples and the main objectives were to visualise and analyse the uranium-bearing minerals in the Vaal Reef samples for their sizes, shapes and distribution with respect to other mineral components in the samples in 3D. The technique is currently unable to distinguish individual minerals from one another, especially when minerals have similar grey values as a result of close attenuation coefficients, mineral compositions and density. Mineral groups were identified following this similarity, include quartz and sheet silicates as one mineral group, all sulphides as another group and uranium-bearing minerals with gold as a third mineral group. The analysed uraninite with gold mineral group in the matrix, exhibited grains up to 200 μm in size which were round in shape, as observed in 2D mineralogical techniques. These observations support mineralogical observations acquired by conventional mineralogical techniques suggesting that 3D μXCT can be used to complement other mineralogical techniques in obtaining 3D information on minerals. However, 3D μXCT has limitations such as spatial resolution, partial volume effect and overlapping of mineral grey values. It is therefore, suggested that the technique not be used as an independent tool for mineral characterisation, but rather in support of the existing mineralogical techniques.

The source area of the uraninite in the Vaal Reef of the Klerksdorp Goldfield is suggested to have been the hydrothermally altered Archaean basement granite bodies of the Witwatersrand Basin hinterland, from the Hartebeesfontein Dome northwest of the goldfield in particular. High $UO_2/ThO_2$ ratios, as determined by electron microprobe analyses (EMPA), support the notion that the uraninite grains are not a product of hydrothermal fluids, and furthermore high Pb contents showing that the uraninite grains are older than the age of the Witwatersrand deposition. In conclusion, the emplacement of uranium-bearing minerals in the Vaal Reef samples analysed in this study is best explained by the modified placer model.

## Dedication

In loving memory of my late father, Manare Joseph Sebola, my thoughts are always with you and may your soul rest in peace.

**Acknowledgements**

I firstly, would like to thank MINTEK for sponsoring this study and giving me the opportunity to do my Master's Degree. I thank my supervisors Prof. Judith Kinnaird from the University of the Witwatersrand and Dr. Deshenthree Chetty from MINTEK for all their effort and time in helping and guiding me in this research journey.

The MINTEK Mineralogy division staff is especially thanked for treating me as part of their team, even though I joined the team as a student and for their contributions in enhancing my research. To the Division's Manager, Ms. Nosiphiwo Nyamane, as well as my co-supervisor, Dr. Deshenthree Chetty, thank you for all your input and assistance concerning my studies. Louis Mudalahothe, April Chili and Lucky Lesele are also thanked for the wonderful sample preparation they did for me, I thank you all.

I also would like to thank AngloGold Ashanti for allowing me access to their drilled borehole, underground sampling, accommodation, logistics and useful discussions throughout the study. Brenda Freese (Kopanang Mine Geoscience Manager), Terry Adams (Moab Khotsong Mine Geoscience Manager), Mark Watts, Lianna Hutton and the employees at the mines who opened their doors when I needed help, thank you.

To the South African Nuclear Energy Corporation (Necsa) Radiation science Tomography team (Frikkie de Beer, Robert Nshimirimana, Lunga Bam and Jakobus Hoffman); thank you for allowing me time for scanning and analysing my samples on the newly purchased Xtek HT 225 L 3D X-ray Microfocus Computed Tomography instrument.

Lastly, I would like to pass my sincere gratitude to my family, friends and everyone who has supported me throughout the research journey. To my mother (Mabjala Elizabeth Sebola), brothers and sisters, without you I would not be where I am today; my late father (Manare Joseph Sebola) my thoughts are always with you and may your soul rest in peace. My fiancé Gabisile Sharon Mothega, thank you for everything and for being there for me. Above all, I thank God the Almighty for his mercy in my life.

**CONTENTS**

DECLARATION ..... i
Abstract ..... ii
Dedication ..... iv
Acknowledgements ..... v
CONTENTS ..... vi
LIST OF FIGURES ..... ix
LIST OF TABLES ..... xxi
LIST OF ABBREVIATIONS ..... xxiii
**CHAPTER ONE** ..... 1
1.1. Introduction ..... 1
1.2. Background to the Witwatersrand Basin ..... 1
1.3. Location of Study Area ..... 2
1.4. Aims and Objectives ..... 4
**CHAPTER TWO - LITERATURE REVIEW** ..... 6
2.1. Regional Geology of the Witwatersrand Basin ..... 6
2.1.1. Stratigraphy of the Witwatersrand Supergroup ..... 7
2.1.1.1. West Rand Group ..... 7
2.1.1.2. Central Rand Group ..... 9
2.1.2. Structure of the Witwatersrand Supergroup ..... 9
2.1.3. Metamorphism in the Witwatersrand Basin ..... 11
2.2. Characteristics of Witwatersrand Ore Bodies (Reefs) ..... 11
2.2.1. Pyrite ..... 12
2.2.2. Gold ..... 13
2.2.3. Uranium-Bearing Minerals ..... 14
2.2.4. Carbonaceous Matter ..... 15
2.3. Genetic Models of the Witwatersrand Basin Mineralisation ..... 17
2.4. Source Areas for Gold and Uranium in the Witwatersrand Basin ..... 20
**CHAPTER THREE - LOCAL GEOLOGY OF THE KLERKSDORP GOLDFIELD** ..... 24
3.1. Introduction ..... 24
3.2. Stratigraphy of the Klerksdorp Goldfield ..... 25
3.3. Structure of the Klerksdorp Goldfield ..... 26
3.4. The Vaal Reef and Associated Lithologies ..... 27

3.4.1. Witkop Facies ..... 29
3.4.2. Grootdraai Facies ..... 29
3.4.3. Mizpah Package ..... 30
3.4.4. C Facies ..... 30
3.4.5. B Facies ..... 30
3.4.6. A Facies ..... 31
3.5. Lateral Distribution of the Vaal Reef ..... 33
3.5.1. 460, 430 and 440 Geozones ..... 34
3.5.2. 470 Geozone ..... 35
3.5.3. 500 Geozone ..... 36
3.5.4. 370 Geozone ..... 37
3.6. Petrology ..... 39
*3.6.1. Borehole Logging* ..... 40
3.6.1.1. Boreholes K2776, K2814 and K5303 in the 460 Geozone ..... 40
3.6.1.2. Boreholes K4111 and K4245 in the 500 geozone ..... 41
3.6.1.3. Borehole GBH 645 in the 500 geozone ..... 44
3.6.1.4. Boreholes GBH 633 and GBH 637in the 370 geozone ..... 45
3.6.1.5. Boreholes Mk179 and Mk283R in the 370 geozone ..... 47
3.7. Sampling ..... 47
3.8. Summary ..... 49
**CHAPTER FOUR - MINERALOGICAL INVESTIGATION OF THE VAAL REEF** .50
4.1. Introduction ..... 50
4.2. Methods ..... 50
4.2.1. X-Ray Diffraction (XRD) ..... 50
4.2.2. Optical Microscopy ..... 51
4.2.3. Scanning Electron Microscopy (SEM) Study ..... 51
4.2.4. Electron Microprobe Analysis (EMPA) Study ..... 51
4.3. Mineral Abundance ..... 52
4.4. Petrography ..... 53
4.4.1. C Facies ..... 53
4.4.2. A Facies ..... 59
4.5. Electron Microprobe Analysis (EMPA) ..... 66
4.6. Paragenetic Sequence ..... 70
4.7. Summary ..... 71

**CHAPTER FIVE - WHOLE-ROCK GEOCHEMISTRY** ..... 75
5.1. Introduction ..... 75
5.2. Methodology ..... 75
5.2.1. X-Ray Fluorescence (XRF) Spectrometry ..... 75
5.2.2. Inductively Coupled Plasma MS and OES ..... 76
5.2.3. Fire Assay ..... 77
5.3. Results ..... 77
5.4. Discussion ..... 82
**CHAPTER SIX - COMPUTED TOMOGRPHY** ..... 84
6.1. Introduction ..... 84
6.2. Principles of μXCT ..... 86
6.2.1. Grey values ..... 88
6.2.2. Thresholding ..... 88
6.2.3. Spatial Resolution ..... 89
6.2.4. Partial Volume Effect ..... 90
6.3. Methodology ..... 90
6.3.1. Sample Preparation ..... 90
6.3.2. Instrumentation and Sample Setup ..... 91
6.3.3. Imaging (Tomography) ..... 91
6.3.4. Image Analysis and 2D Correlation ..... 93
6.4. Results and Discussion ..... 96
6.4.1. Imaging and Visualisation of Tomograms and 2D Microscopy Images ..... 96
6.4.2. Quantitative Analysis of Uranium-bearing Minerals ..... 103
6.4.3. 3D Application (VGStudioMax) ..... 106
6.4.4. 2D Application (Image-J) ..... 108
6.5. Comparison of 2D and 3D μXCT Techniques ..... 109
6.6. Summary ..... 110
**CHAPTER SEVEN - DISCUSSION AND CONCLUSIONS** ..... 115
7.1. Discussion ..... 115
7.2. Conclusions ..... 122
**REFERENCES** ..... 124
**APPENDIX** ..... 141

## LIST OF FIGURES

**Figure 1.1:** Distribution of uranium provinces and deposits in South Africa (after Cole, 1998). The Witwatersrand Basin is the largest uranium deposit followed by the Karoo, marine phosphates, and other surficial deposits.

**Figure 1.2:** Simplified geological map of the Witwatersrand Basin showing the Archaean granitoid domes, the nine major Goldfields, major faults and palaeocurrent directions of reefs in the Central Rand Group (after Frimmel and Minter, 2002).

**Figure 2.1:** The Witwatersrand Supergroup with the West Rand and Central Rand Groups occupying the centre of the three crustal blocks of the Kaapvaal Craton constituted by older granitoids and greenstone formations (after Frimmel, 2005).

**Figure 2.2:** Simplified stratigraphic column of the Witwatersrand Supergroup, Subgroups, common Formations and lithologies (after Frimmel, 2005).

**Figure 2.3:** Illustration of the placer model with greenstone gold-rich sources areas suggested to be komatiites or metamorphosed basalts older (3.5-2.9 Ga) than the deposition of the Witwatersrand Basin. Detrital gold has been mechanically eroded from the old source areas into the basin by deltaic fluvial processes. The age of the gold in the basin is similar to the older gold sources (after Kirk *et al.*, 2003).

**Figure 2.4:** Illustration of the hydrothermal fluids (2.7-2.0 Ga) from later processes within the Witwatersrand Basin. Gold has been derived from hydrothermal sources from deep within the earth's crust and carried along faults into the basin after deposition of the conglomerates (after Kirk *et al.*, 2003).

**Figure 2.5:** Illustration of the locality of the Witwatersrand Basin with its major goldfields surrounded by older Archaean greenstone and basement granites throughout the entire basin. The location of the Witwatersrand Basin within the Kaapval Craton is shown in the insert map (after Poujol *et al*., 1999).

**Figure 3.1:** Locality map of the Witwatersrand Basin Goldfields, with the Klerksdorp Goldfield in the proximity of Klerksdorp town. The Vaal Reef occurs southwards where the AngloGold Ashanti properties are found (Rantzsch *et al.*, 2011).

**Figure 3.2:** Generalised stratigraphic column for the Witwatersrand Supergroup with the main auriferous conglomerate beds (reefs) shown, including the Klerksdorp Goldfield reefs (after Watts, 2004).

**Figure 3.3:** Geological map of major structures in the Witwatersrand Supergroup in the Klerksdorp goldfield with the younger cover removed (after Dankert and Hein, 2010).

**Figure 3.4:** Locality map of Kopanang, Great Noligwa and Moab Khotsong Mines in the Klerksdorp Goldfield (after Frimmel, 2005 and AngloGold Ashanti internal report, 2001).

**Figure 3.5:** East-west cross-section of Kopanang and Great Noligwa Mines showing lateral variations of the Vaal Reef package (C [3], B and A Facies) resting on the Witkop (1) and Grootdraai Facies (2) within the MB4 unit. The latter is overlain by the MB3 quartzite and underlain by the MB5 quartzite. The Vaal Reef package from east to west is represented by six geozones (AngloGold Ashanti internal report, 2001).

**Figure 3.6:** Layout of the Vaal Reef. a) The Vaal Reef C Facies at Kopanang Mine overlies the MB5 quartzite with a carbon seam at the base of the reef and a pyrite-rich matrix. b) The Vaal Reef A Facies at Moab Khotsong Mine showing the MB5 quartzite footwall overlain by the reef polymictic conglomerate.

**Figure 3.7:** Distribution of geozones at Kopanang, Great Noligwa and Moab Khotsong Mines (AngloGold Ashanti internal report, 2001). Kopanang Mine consists of the 460, 430, 440, 502 and 470 geozones. Great Noligwa and Moab Khotsong Mines consist largely of the 500 and 370 geozones.

**Figure 3.8:** The Vaal Reef C Facies in the 460 geozone with thin carbonaceous matter at the bottom of the reef; the reef is overlain by the B Facies and rests on the MB5 quartzite footwall. The Grootdraai conglomerate was not observed.

**Figure 3.9:** The Vaal Reef C Facies in the 430 geozone overlain by the B Facies with a carbon seam at the bottom of the reef; the Vaal reef rests on the MB5 quartzite footwall. No Grootdraai conglomerate was observed.

**Figure 3.10:** The Vaal Reef C Facies at the 440 geozone; the carbon seam is developed at the base of the reef and the quartz clasts are sub-angular ane elongated. The reef rests directly on the MB5 quartzite footwall and no Witkop conglomerate was observed.

**Figure 3.11:** The Vaal Reef A Facies at the 500 geozone at Moab Khotsong Mine. The A Facies is over 1.2 m in thickness showing internal quartzite within the reef.

**Figure 3.12:** The Vaal Reef A Facies in the 370 geozone at Moab Khotsong Mine showing the Almond Reef; the reef overlies the Mizpah quartzite.

**Figure 3.13:** Layout of the localities of thirteen drilled boreholes are shown on the map, seven from Kopanang Mine, three from Great Noligwa Mine and three from Moab Khotsong Mine. The boreholes represent different geozones across the three mines (AngloGold Ashanti internal report, 2001).

**Figure 3.14:** Photograph of borehole K2776 intersecting the MB5 quartzite and Vaal Reef C and B Facies.

**Figure 3.15:** Photograph of borehole K2814 intersecting the MB5 quartzite, C Facies, B Facies, A Facies and the Zandpan quartzite.

**Figure 3.16:** Photograph of Borehole K5303 intersecting the MB5, C Facies, B Facies, A Facies and the Zandpan quartzite.

**Figure 3.17:** Boreholes K2776, K2814 and K5303 intersecting the Vaal Reef. The C Facies is the primary economic facies hosting high grades of gold and uranium; the thickness of the C Facies is 15 cm in borehole K2776, 10 cm in borehole K2814 and 18 cm in borehole K5303.

**Figure 3.18:** Stratigraphic section of the Vaal Reef in boreholes K4111 and K4245 from Kopanang Mine representing the 500 geozone.

**Figure 3.19:** Photograph of borehole K4111 intersecting the MB5 quartzite, Bottom A Subfacies, Middle A Subfacies, Top A Subfacies and the Zandpan quartzite.

**Figure 3.20:** Photograph of borehole GBH 645 intersecting the MB5 quartzite, C Facies, Bottom A Subfacies, Middle A Subfacies, Top A Subfacies and the Zandpan quartzite.

**Figure 3.21:** Stratigraphic section of the Vaal Reef in borehole GBH 645 from Great Noligwa Mine showing the development of C and A Facies overlying each other. The borehole represents the 500 geozone.

**Figure 3.22:** Stratigraphic sections of the Vaal Reef from boreholes GBH 633 and GBH 637 representing geozone 370. The 75 cm thick Vaal Reef in both cores is represented by the A Facies which rests on the Mizpah Reef and Mizpah quartzite, the Zanpand Marker is developed in both the boreholes.

**Figure 3.23:** Stratigraphic sections of the Vaal Reef from boreholes Mk179 and MK283R representing geozone 370. The Vaal Reef A Facies is 1.5 m and 75 cm thick, respectively, and rests on the Mizpah Reef, and is overlain by the Zandpan Marker.

**Figure 4.1:** Relative mineral abundance in samples representing the Vaal Reef samples. (a) The A Facies at Moab Khotsong 370 geozone is dominated by quartz. (b) The C Facies at Kopanang 440 (1k1 and 1k3) and 460 (2k4, 2k6, 3k2 and 3k4) geozones are pyrite-rich and exhibit high sheet silicate abundances. (c) The Mizpah Reef samples are pyrite-rich and the MB5 footwall samples are quartz-rich.

**Figure 4.2:** Hand specimens from the Vaal Reef C Facies at Kopanang Mine. (a) 440 geozone with high pyrite content with sub-round quartz pebbles.

**Figure 4.3:** Photomicrographs of silicate and phyllosilicate minerals of the Vaal Reef C Facies under transmitted light microscopy. (a) Chlorite matrix surrounding quartz pebbles, with chloritoid replacing quartz, plane polarised light, and sutured quartz (ppl). (b) Chlorite replacing opaque minerals and secondary quartz (xpl). (c) Chlorite replaces pyrophyllite in the matrix (xpl), zircon grain occurs in association with opaque minerals. (d) Chloritoid replacing opaque minerals, sample dominated by opaque minerals (xpl).

**Figure 4.4:** Reflected light photomicrographs of conglomerates from the Vaal Reef C Facies at Kopanang Mine. a) Allogenic (Py I) and authigenic (Py II) pyrite with chalcopyrite (Ccp) interstitial to quartz. b) Typical Vaal Reef occurrence of uraninite (Ur) with zircon (Zrn), chromite (Chr), rutile (Rt) and pyrite. c) Brannerite (Br) in the matrix with uraninite. d) Uraninite in association with pyrite, gersdorffite (Gs) and gold (Au). e) Uraniferous leucoxene (Leu) in matrix. f) Uraninite in association with brannerite.

**Figure 4.5:** Reflected light photomicrographs of carbonaceous matter in the Vaal Reef C Facies at Kopanang Mine. a) Fragmented uraninite (Ur) grains cross-cut by carbonaceous matter. b) Uraninite enclosed in carbonaceous (C) seam. c) Uraninite in carbonaceous matter with grains fragmented. d) Authigenic pyrrhotite (Po) infilling quartz cracks; carbonaceous matter in close association with uraninite and arsenopyrite (Apy). e) Authigenic gold (Au) in chalcopyrite (Ccp) in a fractured quartz grain, surrounded by carbonaceous matter enclosing uraninite grains. f) Gold in matrix associated with arsenopyrite (APy), there are two populations of uraninites, in the matrix and also surrounded by the carbonaceous matter.

**Figure 4.6:** Backscattered electron (BSE) images from Kopanang Mine C Facies samples. a) Needle-shaped brannerite in the matrix with rutile (Rt), zircon and pyrite. b)

Allogenic or detrital nature of pyrite, zircon, chromite and uraninite. c) Uraninite grains fragmented by carbon fly speck with a second generation of carbon vein devoid of uranium mineralisation; uraninite enclosed in gersdorffite (Gs). d) Occurrence of detrital uraninite with cracks infilled by carbon; rounded pyrite and gersdorffite occur with uraninite. e) Uraninite grains that were not covered by carbonaceous matter. f) Carbonaceous seam with zircon and gold on the edges of the seam.

**Figure 4.7:** Hand specimens of the Vaal Reef A Facies from Moab Khotsong Mine 370 geozone. (a) Sample with oligomictic quartz pebbles and the carbonaceous seams enclosing pyrite gains. (b) Sample showing the carbonaceous seam cutting across the matrix; the sample is composed of a grey matrix with a few occurrences of sulphide minerals.

**Figure 4.8:** Photomicrographs of silicate and phyllosilicate minerals of the Vaal Reef C Facies under transmitted light microscopy. (a) Chloritoid replacing a quartz grain. (b) Large grain of chloritoid replacing quartz and fine-grained pyrophyllite-muscovite in the matrix. (c) Pyrophyllite laths enclosing opaque minerals in the quartz matrix. (d) Pyrophyllite laths in the quartz matrix, and chlorite replacing opaque minerals.

**Figure 4.9:** Reflected light photomicrographs of Moab Khotsong samples from the Vaal Reef A Facies. a) Fractured pyrite grain replaced by pyrrhotite, sphalerite (Sp) and galena (Gn). b) Fractured allogenic pyrite intersected by a galena vein extending into the surrounding carbonaceous matter. c) Pyrrhotite veins filling in cracked quartz grains with carbonaceous matter enclosing fine uraninite grains. d) Uraninite altered to brannerite in the matrix in association with allogenic pyrite. e) Association of carbonaceous matter with pyrite and arsenopyrite with gold in the carbonaceous matter. f) Preserved round uraninites and gold in carbonaceous matter.

**Figure 4.10:** Backscattered electron images of Moab Khotsong samples. a) Fragmented uraninite grains and pyrite in a carbonaceous groundmass. b) Elongated carbonaceous seam with fragmented uraninite grains, galena vein cross-cuts the carbonaceous seam. c) Quartz vein cross-cuts a carbonaceous seam. d) Carbonaceous seam dominated by arsenopyrite grains circled in the red ring.

**Figure 4.11:** Photomicrographs of sample sections displaying infillings and veinlets. a) Cracked detrital pyrite (Py) filled by galena (Gn) veinlets that extend into the carbonaceous matter (C) groundmass, recrystallised gold grains are observed in the carbonaceous matter. b) Pyrrhotite (Po) and galena as infillings in the fractured quartz; a quartz vein is observed crosscutting the carbonaceous matter. c) A quartz vein cuts across a series of fly specks that hosts fragmented detrital uraninite. d) A set of parallel pyrrhotite layers cross-cutting a quartz pebble; a quartz vein carrying pyrrhotite cutting through the carbonaceous matter.

**Figure 4.12:** Photomicrographs of gold in the Vaal Reef matrix and carbonaceous occurrences. a) Gold associated with detrital matrix minerals such as uraninite and Pyrite. b) Irregular and elongated-shaped gold with the matrix and carbonaceous matter. c) Gold occurring interstitial to the carbonaceous matter. d) Gold associated with uraninite and pyrrhotite (Po). e) Gold trapped in a quartz pebble. f) Thin gold grains interstitial to the carbonaceous groundmass.

**Figure 4.13:** A four stage paragenetic sequence of the Vaal Reef minerals in the Klerksdorp Goldfield. 1) Stage 1 is constituted by older detrital minerals. 2) Stage 2 is characterised by the development of mainly secondary sulphide minerals. 3) Stage 3 is the injection of the carbonaceous matter. 4) Stage 4 is development of hydrothermal quartz and sulphide minerals.

**Figure 5.1:** Plots of: (a) Whole-rock uranium vs. carbon from the A and C Facies samples. The C Facies and A Facies from the 370 geozone is generally uranium-rich. The 440 geozone representing the C Facies is carbon-rich. (b) Gold vs. Carbon; the A Facies 370 Geozone is more gold-rich than the C Facies samples. (c) Uranium vs sulphur; the C Facies is more sulphur-rich than the A Facies. (d) A Plot of gold vs. sulphur.

**Figure 5.2:** Whole-rock plots of (a) Uranium vs. $TiO_2$ where titanium is mainly enriched in the 430 geozone of the C Facies. (b) Sulphur vs.$SiO_2$, the A Facies is more quartz-rich than the C Facies. (c) FeO vs $Al_2O_3$ and the C Facies samples (440 and 460 geozones) are more aluminium-rich than the A Facies sample. (d). Gold vs. $SiO_2$ and high gold-quartz association occurs in the A Facies.

**Figure 6.1:** Illustration of Beer-Lambert Law of linear attenuation

**Figure 6.2:** Illustration of basic operation principles and components of 3D X-ray computed tomography. X-rays are produced from a tube at a point source in a form of a cone beam and pass through a rotating sample. The attenuated X-ray signals results are recorded by the detector. The data acquired are reconstructed into a 3D volume by volume reconstruction software.

**Figure 6.3:** Illustration of a 3D μXCT histogram obtained from a VGStudioMax imaging software.

**Figure 6.4:** Illustration of thresholding, where a grey value histogram has been split into several intervals. Each interval represents a mineral group equivalent to its specific grey values.

**Figure 6.5:** Illustration of similar tomograms at different resolutions (low and high resolution). At low resolution, minerals touch one another and contrast is not well defined; at high resolution individual minerals are now distinguished and contrast is well-defined.

**Figure 6.6:** Illustration of steps taken from 3D imaging until a polished section is prepared in order to compare a specific 3D slice and 2D optical microscopy and SEM results. 1) The sample was loaded in the μXCT instrument. 2) A 3D volume of the sample was acquired. 3) An axial slice of the 3D volume of the sample was viewed for mineral distribution. 4) Sample taken for preparation of a polished section, the sample was physically cut parallel to the selected axial slice then prepared as a polished section corresponding with the axial slice. 5) Sample was cut where the slice of interest was selected in step 3 after calculating the exact thickness where the sample is to be cut to expose the 3D μXCT slice. 5) Polished section produced and studied by optical microscopy and SEM for mineral identification, textural relationship, size and shape observations.

**Figure 6.7:** Example of a grey value histogram obtained from VGStudioMax 2.1 imaging software showing peaks that represent intervals of (1) air, carbonaceous matter (2) quartz and silicate minerals (3), sulphide minerals (4), uranium-bearing minerals and gold (5) derived from thresholding.

**Figure 6.8:** Photomicrograph (left) and backscattered electron (BSE) image (right) of sample 1k4 showing the distribution of uraninite in the carbonaceous matter and a gold grain (top right).

**Figure 6.9:** Comparison of 3D tomogram slice (left) and BSE image (right) of sample 1k4.

**Figure 6.10:** A tomogram slice of sample 1k4 showing the distribution of uraninite grains in the quartz-pyrite matrix and the carbonaceous matter (outlined in red).

**Figure 6.11:** A tomogram slice of sample 3k2 showing the distribution of uraninite grains in the quartz-pyrite matrix and the carbonaceous matter.

**Figure 6.12:** A tomogram slice of sample Mk367 showing the distribution of uraninite grains in the quartz-pyrite matrix and the carbonaceous matter.

**Figure 6.13:** A series of longitudinal tomograms from sample 3k2 illustrating the 3D nature and distribution of uranium minerals (white), sulphide minerals (light grey) and quartz (dark grey).

**Figure 6.14:** 3D visualisation of the distribution of uranium-bearing minerals and gold from sample 3k2. Other mineral components are transparent allowing visualisation of these minerals only.

**Figure 6.15:** Tomogram slices from sample 1k4 showing the distribution of uraninite grains in the matrix and carbonaceous matter (outlined in yellow) acquired from Image J software.

**Figure 6.16:** Illustration of 3D volume from slice 1515 to slice 1616 obtained from sample 1k4 using VGStudioMax showing only uraninite grains occurring in the matrix.

**Figure 6.17:** A plot of size vs number of grains in percentage in the matrix and the carbonaceous matter.

**Figure 6.18:** Tomogram slice of four uraninite grains (highlighted in yellow) in the carbonaceous matter (highlighted in black) touching one another and analysed as one grain.

**Figure 6.19:** A plot of roundness vs. size of uraninite grains in the matrix and the carbonaceous matter obtained from Image-J.

## LIST OF TABLES

**Table 3.1:** A summary of the 6 geozones in the Kopanang, Great Noligwa and Moab Khotsong Mines. Information on the facies responsible for mineralisation, thickness and compositional properties is presented.

**Table 4.1:** List of minerals recorded by XRD from samples under investigation. Dorminant (>75%), Major (25-50%), Intermediate (15-25%), Minor (5-15%) and Trace (0-5%).

**Table 4.2:** A list of sulphide minerals occurring in the Vaal Reef C Facies at Kopanang Mine, and their ideal chemical formulae and abundances in the samples.

**Table 4.3:** Comparison of mineral properties at Kopanang Mine C Facies and Moab Khotsong Mine A Facies.

**Table 4.4:** Electron-microprobe analyses of uraninite grains from the matrix of the Vaal Reef C Facies samples.

**Table 4.5:** Electron-microprobe analyses of uraninite grains hosted within the carbonaceous matter in the Vaal Reef C Facies samples.

**Table 5.1:** Geochemical samples collected from Kopanang, Great Noligwa and Moab Khotsong Mines Vaal Reef C and A Facies for analysis.

**Table 5.2:** Concentrations of sulphur, uranium, carbon and gold in the Vaal Reef C Facies samples from Kopanang, Great Noligwa and Moab Khotsong Mines.

**Table 5.3:** Concentrations of S, U, C and gold in the Vaal Reef A Facies samples from Kopanang, Great Noligwa and Moab Khotsong Mines.

**Table 4.4:** ICP-MS Major and trace elements results of the C Facies geozones samples (geozones 440, 430, 460, 500 and 370 are represented).

**Table 4.5:** ICP-MS Major and trace elements results of the A Facies geozones samples (geozones 370 and 500 are represented).

**Table 6.1:** General classification of computed tomography (after Ketcham and Carlson, 2001).

**Table 6.2:** Linear attenuation coefficients of minerals at different scanning energies.

**Table 6.3:** The table shows that at low energy, penetration of X-rays in thin and less dense samples is achieved and the large gap in attenuation of minerals allows best contrast to distinguish the minerals. On a contrary, at higher energies (200kV), there is low contrast between minerals.

**Table 6.4:** Comparison of 2D conventional mineralogy techniques with 3D μXCT.

## LIST OF ABBREVIATIONS

| | |
|---|---|
| 2D | Two dimensional |
| 3D μXCT | Three dimensional microfocus X-Ray computed tomography |
| Apy | Arsenopyrite |
| ASD | Analytical service division |
| Au | Gold |
| Br | Brannerite |
| C | Carbonaceous matter |
| Ccp | Chalcopyrite |
| Chr | Chromite |
| EMPA | Electron microprobe analysis |
| Gn | Galena |
| Gs | Gersdorffite |
| ICP MS | Inductively coupled plasma mass spectrometry |
| MB3 | Main Bird 3 |
| MB4 | Main Bird 4 |
| MB5 | Main Bird 5 |
| Po | Pyrrhotite |
| Ppl | Plane polarised light |
| Py I | Allogenic or detrital pyrite |
| Py II | Authigenic pyrite |
| Rt | Rutile |
| SEM | Scanning Electron Microscope |
| Sp | Sphalerite |
| Ur | Uraninite |

| | |
|---|---|
| Xpl | Crossed polarised light |
| XRD | X-Ray diffractometer |
| XRF | X-Ray Fluorescence |
| Zrn | Zircon |

# CHAPTER ONE

## 1.1. Introduction

In South Africa, uranium is hosted in different types of deposits (Cole, 1998). The first is a placer-type such as the Witwatersrand Supergroup, Dominion Group and Black Reef Formation. These are mainly quartz-pebble conglomerates (Figure 1.1). Uranium occurs in the mudrocks and sandstones of the Karoo Supergroup as coal-hosted in the Springbok Flats Coal Field of the Waterberg Group and in the Ecca Group of the Karoo uranium province in the Northern Cape Province. More placer uranium deposits occur in the Marble Hall area and as phosphatic sediments of the Dwyka Group along the coast of South Africa (Figure 1.1).

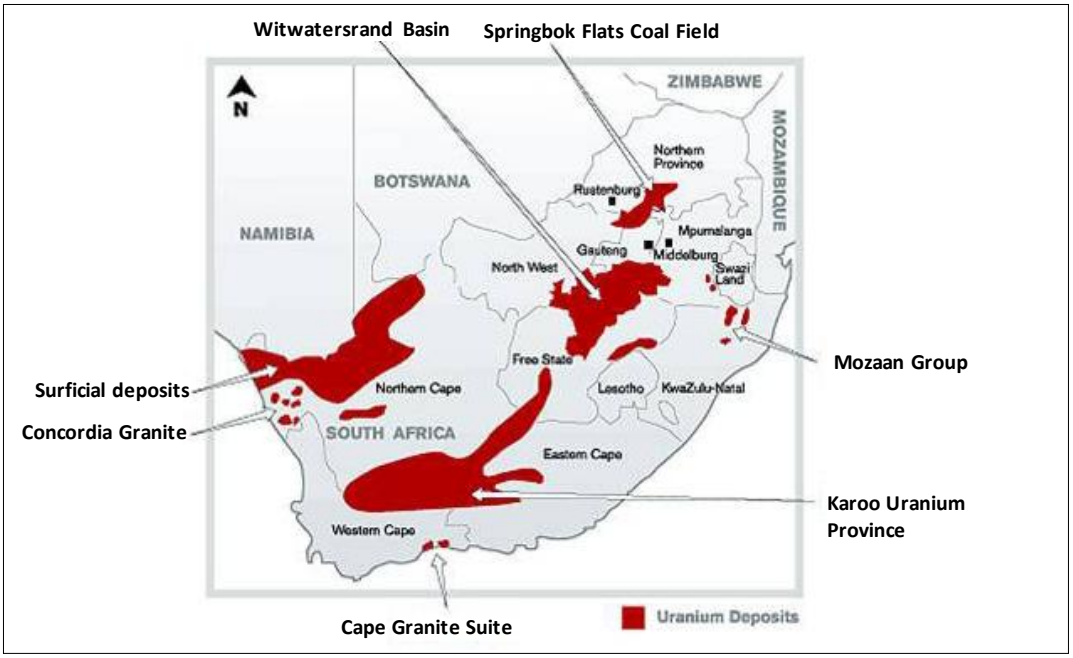



Figure 1.1: Distribution of uranium provinces and deposits in South Africa (after Cole, 1998). The Witwatersrand Basin is the largest uranium deposit followed by the Karoo, marine phosphates, and other surficial deposits.

Uranium also occurs in igneous-type bodies such as the Phalaborwa, Pilanesberg, Glenover and Sandkopsdrif igneous complexes, granite and pegmatite of the Namaqualand Metamorphic complex, the Cape Granite Suite and the Pongola granite (Figure 1.1).

## 1.2. Background to the Witwatersrand Basin

The Witwatersrand Basin is located in the Kaapvaal Craton of southern Africa. Since the discovery of gold in 1886 in the basin, it has been the world leader for gold production until 2007; currently the basin is the fourth largest gold producer in the world (Goldsheet, 2012).

The Witwatersrand Basin therefore, has produced to date more than 50, 000 tons of gold and 150, 0000 tons of uranium (as a by-product of gold mining) from the conglomerate beds (known as "reefs"), amounting to almost 35% of all the world's gold ever mined in recorded history (Frimmel and Minter, 2002; Sanders *et al*., 1994; Goldsheet, 2012). Uranium in the Witwatersrand Basin was first discovered in 1923 (Cole, 1998), and as a result of global demand during the second world war in 1944, South Africa became a potential supplier of uranium (AEC, 1984).

Although the Witwatersrand Basin has been mined for over 120 years, the origin and emplacement of gold and uranium in this basin remains controversial. There are three main hypotheses proposed for gold mineralisation in the Witwatersrand Basin. The first is a placer model, which proposes that gold is detritus derived from an older source area and has been mechanically transported into the basin and concentrated by fluvial/deltaic processes (Mellor, 1916; Pretorius, 1975; Hallbauer and Utter, 1977). The second hypothesis, of a modified placer model, shares some similarities with the placer model and suggests that detrital gold has been mobilised and re-deposited by hydrothermal or metamorphic fluids with other associated phases (Liebenberg, 1955; Robb and Meyer, 1995; Frimmel and Gartz, 1997; Minter, 1999; Kirk *et al*., 2001). The third model is the hydrothermal model, which proposes that gold was transported in solution from outside of the basin by metamorphic or hydrothermal fluids after the formation of the basin between 2.7 and 2.0 Ga (Parnell, 2001; Gray *et al*., 1998; Barnicoat *et al*., 1997; Phillips and Law, 2000; England *et al*., 2001).

In all the three models, gold occurrence in the Witwatersrand Basin is associated with uranium in the form of uraninite, brannerite and uraniferous leucoxene. Other heavy minerals such as chromite, rutile, sulphides and platinum group minerals constitute the conglomerate matrix, with pyrite being the predominant mineral in the matrix after quartz (Smits, 1984). Whereas a lot of research has focused on gold, much less attention has been given to the origin of uranium ores. This research focuses mainly on the uranium mineralisation in the Vaal Reef of the AngloGold Ashanti operations in the Klerksdorp Goldfield.

### 1.3. Location of Study Area

The Witwatersrand Basin is exploited in the Evander, East Rand, Central Rand, West Rand, Carletonville, South Deep, Western Areas, Klerksdorp and Free State Goldfields, and is subdivided into two major groups: the West Rand Group and the Central Rand Group (Figure

1.2). The latter is accountable for the anomalous production of gold and uranium, with little contribution from the West Rand Group. The discovery of gold deposits in the Witwatersrand was in 1886, hosted in quartz-pebble conglomerate known as "reefs" (Mellor, 1916; McCarthy, 2006). These gold-bearing reefs were also discovered in the Klerksdorp area (Vaal Reef), as late as the 1940s (Chapman *et al*., 1986). The study area is located 160 km south west of Johannesburg, at the AngloGold Ashanti Vaal River operations around the Orkney area of the Klerksdorp Goldfield, in the Witwatersrand Basin, North West Province of South Africa (Figure 1.2). The study was undertaken at Kopanang, Moab Khotsong and Great Noligwa Mines.

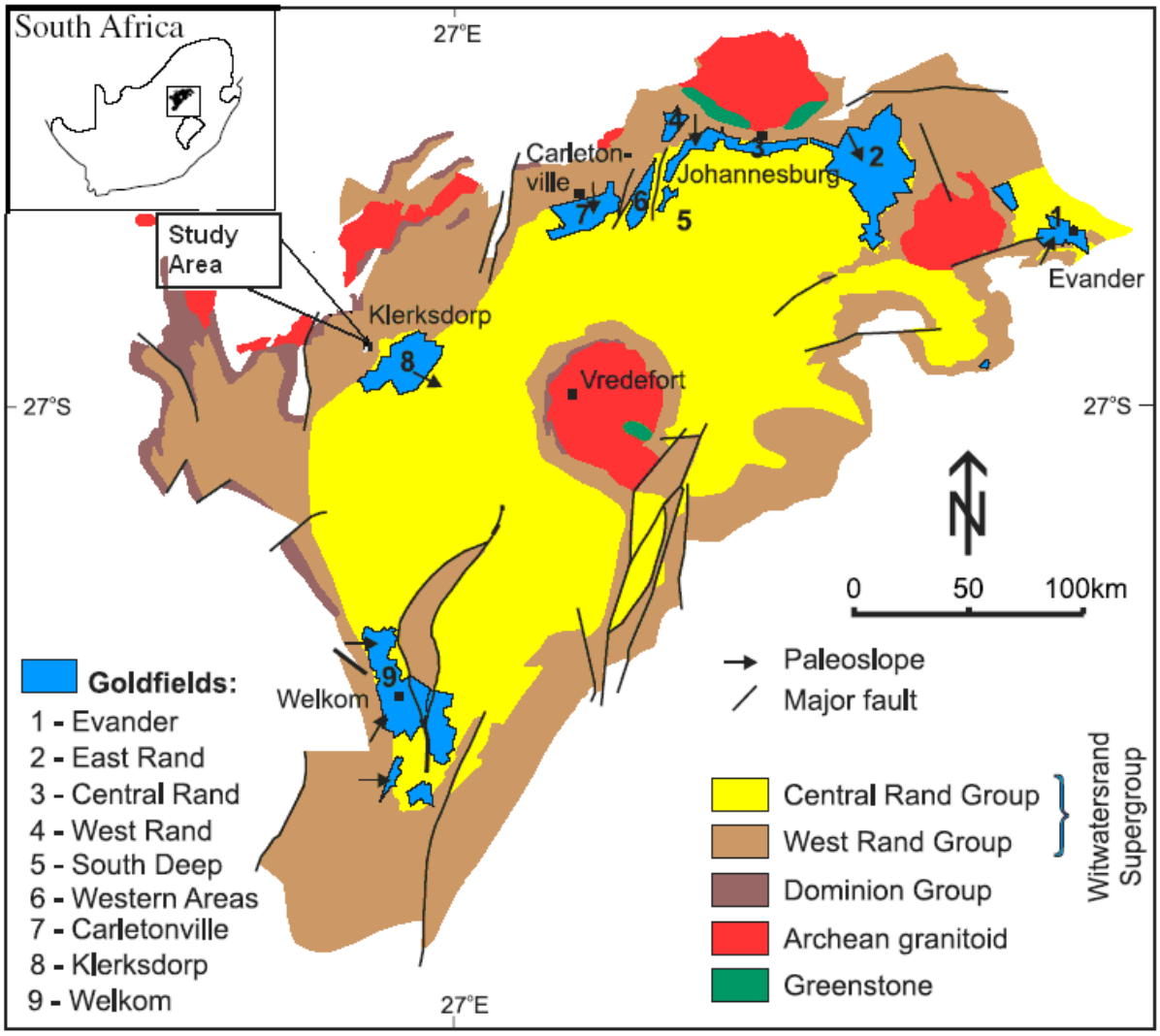



Figure 1.2: Simplified geological map of the Witwatersrand Basin showing the Archaean granitoid domes, the nine major Goldfields, major faults and palaeocurrent directions of reefs in the Central Rand Group (after Frimmel and Minter, 2002).

### 1.4. Aims and Objectives

The formation and deposition of uranium-bearing minerals in the Vaal Reef is not well understood. This research therefore, was aimed at investigating which genetic model among the placer, modified placer and hydrothermal model best supports the formation of uranium mineralisation in the Vaal Reef. Therefore, the main objective was to characterise uranium mineral-bearing samples in the Vaal Reef through the identification and quantification of these minerals in samples. This was achieved with the application of core logging and comparison of different mineralogical and geochemical techniques such as bulk geochemical analysis, electron probe microanalysis, scanning electron microscopy (SEM), optical microscopy in 2D and 3D computed tomography (3D CT).

Optical microscopy and SEM techniques allow the identification, characterisation and quantification of minerals; they also provide information on mineralogical properties such as:

- grain size,
- grain shape,
- textural relationships between minerals,
- mineral assemblage,
- alteration mineral abundance,
- paragenetic sequences can be ascertained from such studies.

The limitations to the SEM and optical microscope is that information on minerals in the sample can only be viewed in 2D and only on the surface of the polished sections and therefore, mineral information does not represent the entire sample. Three-dimensional computed tomography (3D CT) was applied to complement the SEM and optical microscopy techniques. Computed tomography yields a 3D map of the linear X-ray attenuation coefficient, which is a function of the atomic number and density of the material, and the X-ray energy used (Pullan *et al.*, 1981). Based on the compositional contrasts between different phases, various phases can be identified in a rock. Three-dimensional CT is advantageous in its non-destructive character (rock samples need not to be crushed or cut), allowing internal properties of rock samples to be analysed for quantification of mineral size, shape, distribution and orientation in 3D. The technique can produce a large number of contiguous

parallel cross-sections, which allows 3D visualisation of selected features (Mees *et al*., 2003). The high resolution X-ray source tube is able to visualise minerals with sizes down to 3 µm in three-dimensions. Uranium-bearing minerals in this study therefore, were viewed in a wide range of sizes down to µm and this contributed to understanding their shapes and helped infer their nature of deposition.

In this research a comparative study was done on the characterisation of uranium-bearing minerals of the Vaal Reef ore samples. The 2D SEM and optical microscopy studies (shapes and textural relationships) were compared with the 3D X-Ray CT study (volumes of individual mineral grains) to evaluate whether the techniques complement one another. Morphological properties such as roundness from the 2D and 3D results were studied to understand the nature of origin of the uranium-bearing minerals samples in the Witwatersrand Basin. Geochemical analyses were undertaken to evaluate the uranium with respect to other elements such as carbon, sulphur and gold for any elemental associations.

The following are some of the questions that this project has answered:

- How do the techniques of SEM and computed tomography compare (i.e. 2D and 3D) for the characterisation of uranium minerals in the Vaal Reef samples? What are their relative strengths and limitations?
- How many generations of uranium minerals are found in the Vaal Reef, which uranium minerals represent these generations and which is the dominant mineral?
- Where in the Vaal Reef is the highest uranium concentration found?
- How many types of morphologies (roundness) of uranium minerals are there in the Vaal Reef and what are their genetic implications?
- What characteristics of associated gangue can be used as indicators, if possible, for different uranium mineral types and generations, and how do these relate to different modes for uranium emplacement?
- Which model of formation among placer, modified placer and hydrothermal theories best explains the presence of the observed uranium minerals?

# CHAPTER TWO

# LITERATURE REVIEW

## 2.1. Regional Geology of the Witwatersrand Basin

The Witwatersrand Supergroup occupies a central position of the Archaean Kaapvaal Craton (Figure 2.1). It covers an area of 350 x 200 km with an average thickness of 5 to 8 km, underlain by the Dominion Group, Archaean Granitoids and Greenstone basement, and is overlain by the Ventersdorp Supergroup (Frimmel, 2005; Smieja-Krol *et al*., 2009).

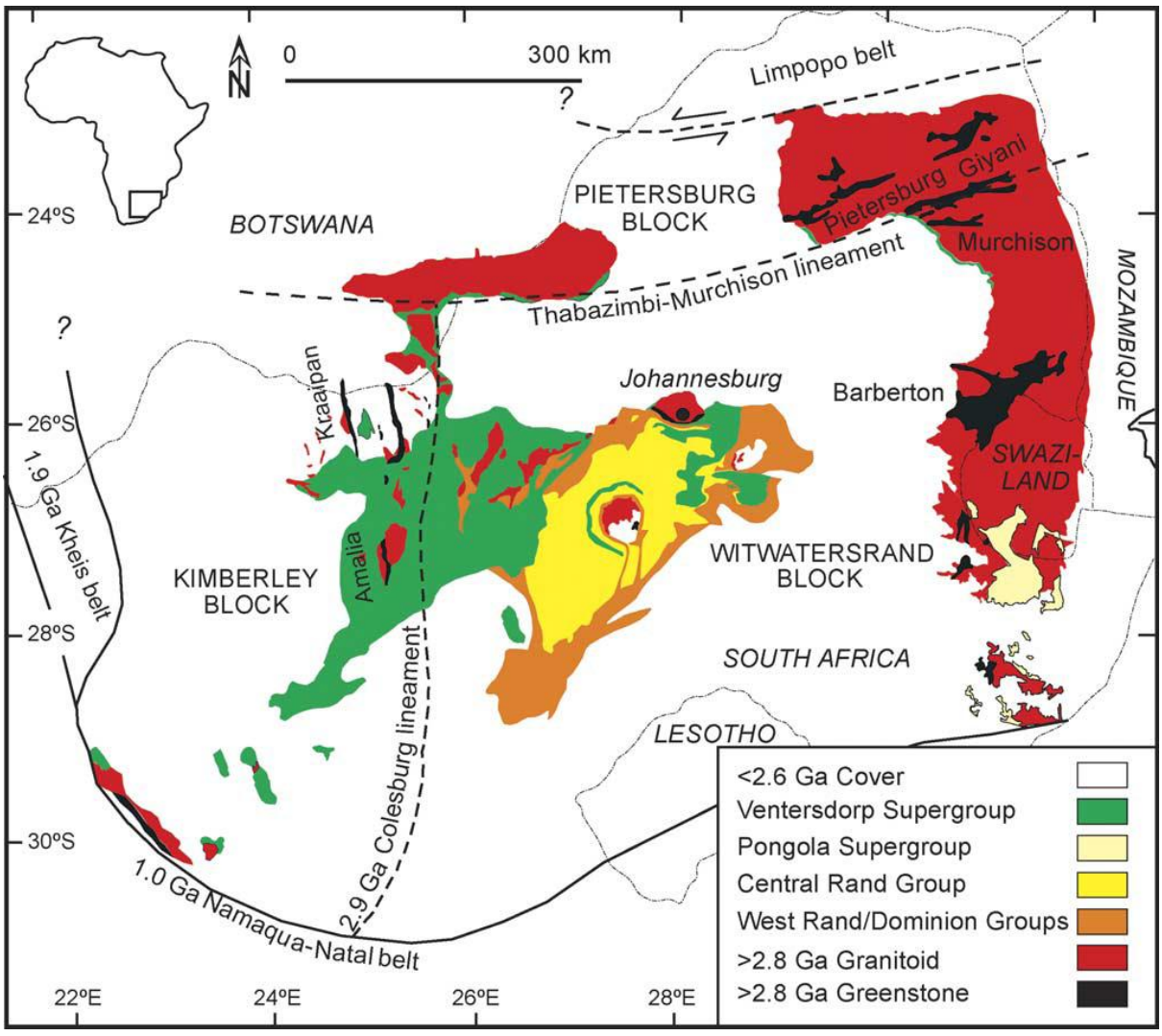



Figure 2.1: The Witwatersrand Supergroup with the West Rand and Central Rand Groups occupying the centre of the three crustal blocks of the Kaapvaal Craton constituted by older granitoids and greenstone formations (after Frimmel, 2005).

The Witwatersrand Supergroup has been dated between 2985±14 Ma (Kositcin and Krapez, 2004) from the West Rand Group detrital zircon grains by U-Pb to 2780±3 Ma in the Central Rand Group using U-Pb on xenotime grains (Kositcin, 2003). Age dating of the volcanic rocks in the underlying Dominion Group by U–Pb on zircon shows ranges of 3086±3 Ma (Robb *et al*., 1992) to 3074±6 Ma (Armstrong *et al*., 1991). The overlying Ventersdorp Supergroup zircon grains dated by U-Pb are 2714±6 Ma (Armstrong *et al*., 1991).

### 2.1.1. Stratigraphy of the Witwatersrand Supergroup

The first detailed geological mapping of the Witwatersrand Basin was produced by Mellor (1916). He subdivided the Witwatersrand into Lower and Upper divisions. The Lower Witwatersrand System comprised the Hospital Hill Series, Government Reef Series and Jeppestown Series. The Upper Witwatersrand System comprised the Kimberley-Elsburg Series and the Main-Bird Series (Mellor, 1916). The Lower Witwatersrand was predominantly constituted by shales and quartzites, and the Upper Witwatersrand mainly constituted by quartzites and conglomerates.

This classification scheme by Mellor (1916) was revised by the South African Commission of Stratigraphy and Nomenclature (SACS, 1980), the Lower Witwatersrand was changed to the West Rand Group and the Upper Witwatersrand changed to the Central Rand Group (Figure 2.2). The West Rand Group constituents retained their names as Hospital Hill, Government and Jeppestown Subgroups. The Central Rand Group constituents changed to Johannesburg and Turffontein Subgroups (Figure 2.2).

#### *2.1.1.1. West Rand Group*

The 2985±14 Ma West Rand Group (Frimmel, 2005) rests on an angular unconformity above the Dominion Group volcanic rocks, and reaches a maximum thickness of 5150 m in the Klerksdorp Goldfield and thins to the northeast (Frimmel, 2005). Where the Dominion Group is absent, the Witwatersrand overlies the 3.6 Ga to 3.2 Ga Archaean basement (Poujol *et al*., 2003) e.g. in the Central Rand Goldfield (Stanistreet *et al*., 1986). The Hospital Hill Subgroup has an upwards coarsening sequence from shale units to quartz arenite sandstone units (Frimmel, 2005). The Government Subgroup is made up of two glacial diamictite beds, which are suggested to be correlatives of the oldest known glacial deposit on earth in the Pongola Supergroup (Young *et al*., 1998). The West Rand Group therefore, consists primarily

of quartzites and shales with rare auriferous and uraniferous conglomerate reef development (McCarthy, 2006).

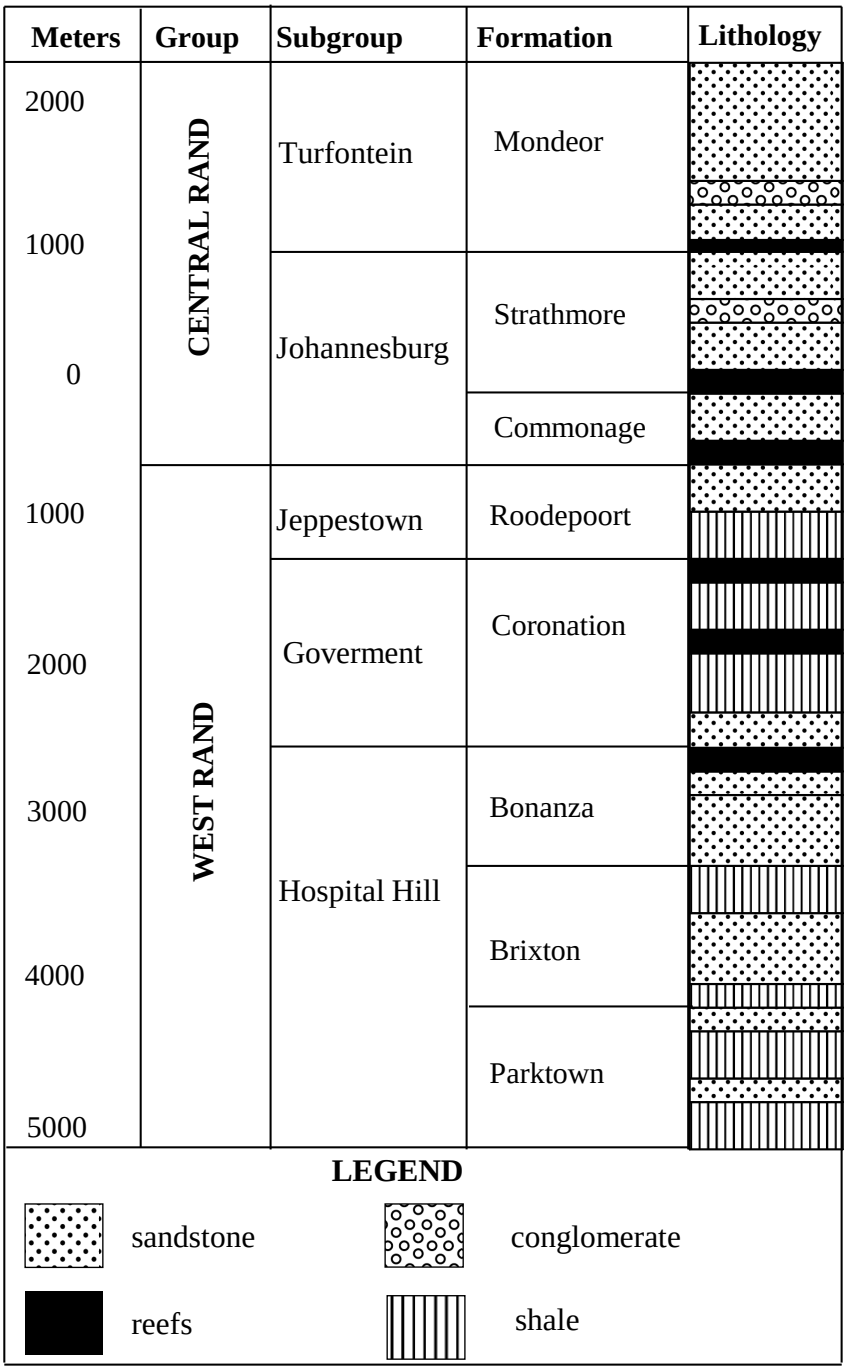



Figure 2.2: Simplified stratigraphic column of the Witwatersrand Supergroup, Subgroups, common Formations and lithologies (after Frimmel, 2005).

*2.1.1.2. Central Rand Group*

The 2780±3 Ma (Kositcin and Krapez, 2004) Central Rand Group lies unconformably above the West Rand Group reaching a maximum thickness of 2880 m near the centre of the basin, and is constituted by the Johannesburg and Turffontein Subgroups (Frimmel, 2005).

The Johannesburg Subgroup is mainly known for hosting high-grade auriferous and uranifeous reefs in the Witwatersrand Supergroup (McCarthy, 2006; Figure 2.2). These conglomerate reefs are characteristic features occurring in the sandstone beds of the Central Rand Group, with minor mud-rock components (Smieja-Krol *et al*., 2009).

### 2.1.2. Structure of the Witwatersrand Supergroup

The structure of the Witwatersrand Supergroup has been shown by many workers to be complex (Stanistreet *et al*., 1986; Myers *et al*., 1990; McCarthy *et al*., 1990; Stanistreet and McCarthy, 1991; Dankert and Hein, 2010). Coward *et al.*, 1995 showed that the Witwatersrand Basin is intracratonic and that it has undergone extension on a large detachment of faults.

The lack of application of fundamental structural geology and geometric patterns has limited structural correlation of the Witwatersrand Basin Goldfields (Dankert and Hein, 2010). In order to simplify these limitations, Dankert and Hein (2010) suggested that 3D kinematic data (meso-to macro-scale) be applied to determine the timing of tectonic events in the basin, as compared to the current 2D geomatic pattern, and that fundamentals of modern structural geology (application of descriptive, kinematic and dynamic analysis) be applied in determining the form, symmetry and geometry of structures to the Witwatersrand Basin.

In spite of these above limitations, there are similar findings from different studies on the structure of the basin. An early deformation event was syn- to post-depositional in the Central Rand Group (Kositcin and Krapez, 2004), with extension during deposition of the Ventersdorp Supergroup and deformation during the deposition of the Transvaal Supergroup (Dankert and Hein, 2010). This sequence was obtained on the basis of combining stratigraphy, chronology and qualitative-quantitative structural observations, and the following suggestions were made:

- The West Rand Group is conformably to unconformably, overlain by the Central Rand Group whose sandstones and gold-uranium-bearing conglomerates were

deposited in a retro-arc setting (Kositcin and Krapez, 2004), periodically interrupted by the development of regional-scale unconformities, block tilting and local formation of faults (McCarthy, 2006)

- The Central Rand Group was unconformably or conformably overlain by the auriferous Venterspost Conglomerate Formation (VCF; Dankert and Hein, 2010).
- The large-scale "Umzawami Deformation" dated between 2902 Ma and 2729 Ma, occurred syn- to post- deposition of the Central Rand Group (Dankert and Hein, 2010) and was characterised by the NW-NNW-trending folds in the Welkom, West Wits Line and West-Central-South-East Rand Goldfields. The deformation is further made up of N to NE-trending folds in the West Wits Line, West Rand; and NE and NNW trending folds in the Welkom, West Wits Line and the Klerksdorp Goldfields.
- Emplacement of the Klipriviersberg Group (2710 Ma) bimodal tholeiitic basalt-dacite suite lavas are related to large scale NW and NNE faulting in the West Wits Line and West-Central-South-East Rand Goldfields (Jolley *et al*., 2007).
- Deposition of the Transvaal Supergroup occurre between 2.60 to 2.22 Ga (Eriksson and Reczko, 1995; Martin *et al*., 1998; Eriksson *et al*., 2006; Walraven and Martini, 1995; Eriksson and Reczko, 1995; Frimmel and Minter, 2002).
- Deformation of the supracrustal rocks of the Witwatersrand by dominant NE, and subordinate NW-trending slip faults (all Goldfields); this was subsequent to deposition of the upper Pretoria Group (Dankert and Hein, 2010). This deformation event is suggested to be related to the Bushveld Complex (2.06 Ga) and the Vredefort structure (2.02 Ga; Kamo *et al.*, 1996; Reimold and Gibson, 2006), with the latter crosscutting the Dominion Group, Witwatersrand Basin and Ventersdorp Supergroups and lower portion of the Transvaal Supergroup. This deformation is termed the "Ukubambana Event" (Dankert and Hein, 2010).

It is believed that gold (and uranium) remobilisation in the Witwatersrand Basin, Ventersdorp and Transvaal Supergroups is associated with the regional deformation and thrust–fold formation of the Ukubambana Event synchronous with, or after deposition of, the upper Transvaal Supergroup at ca. 2.20–2.00 Ga (Dankert and Hein, 2010). Alternatively, gold mobilisation may have also taken place in some Goldfields after deposition of the Central Rand Group (ca. 2.90–2.72 Ga) and during regional deformation in the Umzawami Event in the Neo-Archaean (Dankert and Hein, 2010).

### 2.1.3. Metamorphism in the Witwatersrand Basin

The different rock types of the Witwatersrand Basin are generally overprinted by regional greenschist facies metamorphism with temperatures around 300 to 350 °C and pressures up to 3 Kbars throughout the entire basin, over a strike-length of 200 km (Phillips, 1987; Phillips and Law, 1994; Barnicoat, 1997). Pyrophyllite-chloritoid assemblages have been recorded in most of the Goldfields, and the critical assemblage of pyrophyllite-chloritoid-muscovite-chlorite-quartz-tourmaline-rutile-pyrite is found in most Goldfields. The abundant presence of chloritoid and pyrophyllite in localised units in the Witwatersrand Basin indicate that metamorphic temperatures reached $300 \pm 50^{o}$ C (Phillips, 1987).

High-grade metamorphism in the Witwatersrand Basin occurs around the Vredefort Dome, in the Evander Goldfield, and around the southern margin of the Johannesburg Dome (Schreyer and Bishoff, 1982). There is a recorded temperature increase to around 700 °C in granulites of the Johannesburg and Vredefort Domes (Phillips and Law, 1994). Greenschist metamorphism resulted from the emplacement of the Bushveld Complex around 2060 Ma and the Vredefort meteorite impact around 2025 Ma (Phillips and Law, 1994; Frimmel, 2005).

## 2.2. Characteristics of Witwatersrand Ore Bodies (Reefs)

The Witwatersrand reefs consist mainly of quartzitic conglomerates (McCarthy, 2006; Kirk *et al*., 2001). Compositionally, the conglomerate clasts are quite variable ranging from oligomictic to polymictic pebbles; e.g. quartz vein, porphyry to chert pebbles in the framework, as well as in the matrix (Frimmel, 2005; Frimmel and Minter, 2002). The pebble diameters in some of the Central Rand Group reefs in the Witwatersrand Basin generally range from 10 to 75 mm and may be as large as 150 mm in some areas, indicative of high energy rivers that were capable of moving pebbles of this size ranges (Pretorius, 1964; Grandstaff, 1980; Robb and Meyer, 1995; Catuneanu and Biddulph, 2001). The shape of the pebbles ranges from sub-angular and sub-rounded to round.

Smits (1984) defined Central Rand Group reefs matrices comprising of, in approximate order of significance: quartz, pyrite, sericite, chlorite, pyrophyllite, and chloritoid. The matrix silicates such as chlorite, chloritoid and pyrophyllite, except quartz, as observed today in the conglomerates, are all products of late diagenetic and metamorphic processes. The textural

relations between the sheet silicate minerals indicate the following order of formation: chlorite-sericite-pyrophyllite-chloritoid (Smits, 1984).

Over 70 minerals have been identified in the Witwatersrand Basin, including gold and pyrite; uraninite, brannerite, carbonaceous matter, arsenopyrite, cobaltite, galena, pyrrhotite, gersdorffite, chromite, zircon, and minerals of the platinum group (Feather and Koen, 1975; Hallbauer, 1986). The highest concentrations of allogenic minerals such as gold, uraninite, pyrite, zircon and chromite grains, and more rarely PGE-minerals and diamond, are found above unconformity surfaces, which reflect a direct relationship to the amount of erosion (Frimmel, 2005).

In those reefs that contain carbonaceous matter, such as the Carbon Leader, Basal and Vaal Reefs, the highest Au and U concentrations are located in the zones that are particularly rich in the carbonaceous matter, referred to as bitumen (Frimmel, 2005).

*2.2.1. Pyrite*

Studies have shown that pyrite is the most abundant heavy mineral in the Witwatersrand Basin (Pretorius 1975, Hallbauer 1986, Frimmel 2005, England *et al*., 2002 and Kirk *et al*., 2001) and occurs in numerous textural forms namely rounded, porous and authegenic; these different forms have implications for the genesis of the economic reefs in the basin.

The round pyrite mainly forms the main heavy mineral in the reef matrix accounting for over 40% of the matrix mass (Minter, 1976 and 1999). Round pyrite occurs in association with other heavy minerals such as rutile, chromite, zircon, uraninite and gold (Liebenberg, 1955; Ramdohr, 1958a). Specific dating by the Re-Os method on the round pyrite grains indicate that the grains are around 2.99 ± 0.11 Ga (Kirk *et al*., 2001), therefore suggesting that the round pyrite grains are older than the deposition of the Witwatersrand Basin and that they are placer in origin, hence their morphology depicting that they have been transported over long distances (Minter, 1976; Kirk *et al*., 2001). The porous pyrite are round in nature similar to the round pyrite with internal textures such as laminated aggregates and round concretion forms which are mainly broken due to mechanical transport (Frimmel, 2005).

The authigenic pyrite mainly occurs as euhedral to subhedral and generally occurs in close proximity to hydrothermal structures such as veins (Frimmel, 2005). The authigenic pyrite occurs in association with other authigenic sulphide minerals such as pyrrhotite, galena,

chalcopyrite and gersdorffite (Phillips and Law, 1994; Meyer *et al*., 1990a, b). The formation of the authigenic pyrite is suggested to be post deposition to the Witwatersrand Basin (Robb and Meyer, 1995).

*2.2.2. Gold*

Gold in the Central Rand Group accounts for over 90% of total production in the Witwatersrand Basin (Frimmel, 2005) and occurs mainly in the fine-grained matrix in conglomerate reefs associated with quartz, sericite, chloritoid, pyrophyllite and pyrite. Occasionally, microveinlets of gold are found in cracks of quartz pebbles. The most common type of gold observed is in an authigenic form and is rarely found as allogenic grains (Liebenberg, 1955; Frimmel, 2005).

Allogenic gold grains are generally rounded and oval in shape, and tend to occur as single grains loosely cemented by matrix material. These features show that these gold particles were initially rounded pellets. Perfectly preserved rounded and oval grains of gold are sometimes present in fine-grained phyllosilicates occupying small cavities in, or along edges of secondary quartz fragments (Liebenberg, 1955). Some of the detrital gold grains typically display flattened and edge-overturned (or peaned) morphologies (Robb and Meyer, 1995) with rounded, spheroidal, disc-like and toroidal forms.

Authigenic gold is characterised by the replacement of the matrix minerals, mainly pyrite and quartz fragments. The authigenic gold tends to replace pyrite in irregular patches, as minute gold stringers in pyrite and cracks in the pyrite occupied by gold (Liebenberg, 1955). Gold is suggested to be associated with a late stage of the paragenetic sequence, texturally associated with phyllosilicates, within the carbonaceous matter and as inclusions within euhedral authigenic pyrite (Ramdohr, 1958a; Gartz and Frimmel, 1999; Barnicoat *et al*., 1997; Jolley *et al*., 2004).

Both detrital and authigenic gold can occur together on a micro-scale, i.e., within millimetres in the same thin section (Minter *et al*., 1993). This provides strong evidence for a polyphase gold formation history, with the rounded particles derived by mechanical (fluvial) transport and secondary gold by precipitation from a hydrothermal fluid. From observation of photomicrographs (Frimmel, 2005), the sizes of these detrital and authigenic gold particles range from 60 µm 3 mm.

*2.2.3. Uranium-Bearing Minerals*

Major uranium minerals in the Witwatersrand Basin are uraninite, brannerite (a secondary uranium mineral) and uraniferous leucoxene (titanium oxide of earthy habit) (Frimmel, 2005). The primary uranium mineral in the Witwatersrand is uraninite. Brannerite and uraniferous leucoxene are considered to be products of partial mobilisation of the detrital rounded uraninite (England *et al*., 2001). Coffinite is present in other reefs, although in very low proportions as compared with uraninite and brannerite e.g. in the Vaal Reef, (Lottering *et al*., 2008).

According to Smits (1984), uranium minerals (mainly uraninite) were introduced into the Witwatersrand sediments as detrital grains, and hydraulic sorting processes were responsible for the selective concentration of the minerals. When the sedimentary trap was favourable for the growth of primitive carbonaceous matter, uranium minerals were trapped (detrital grains), and broken down into fragments. Owing to the continuous multiplication of the micro-organisms, the uraninite fragments gradually disintegrated to increasingly smaller sizes. Several textural features of the intergrowth of carbon with uraninite and with phyllosilicates strongly suggest that the multiplication of the carbonaceous matter was responsible for the fragmentation of the uraninite grains but that chemical interaction was negligible.

Uraninite grains are mainly concentrated as clusters at the base of conglomerate (reef) beds along with gold and other heavy minerals such as pyrite, chromite, zircon, rutile, etc. (Liebenberg, 1955; Schidlowski, 1981). Uraninite grain size distribution ranges from 30 to 350 μm, with an average of size 70 μm (Robb and Meyer, 1995). Detrital uraninite occurs mostly as rounded (muffin-shaped) to oval in shape.

Uraninite grains are characterised by galena inclusions which are responsible for the breaking down of the grains *in situ* by high burial pressure (Liebenberg, 1955), and the inclusions mainly occur as round microscopic (<1 μm) specks and veinlets. The galena inclusions occur as irregular patches always occupying uraninite cracks, gold is occasionally observered as inclusions in the uraninite as well (Liebenberg, 1955; Schidlowski, 1981).

Brannerite occurs in a secondary form (as a result of uranium interaction with titanium-oxide-rich minerals), as veinlets and irregular patches in the matrix replacing uraninite and occupying cracks in primary and secondary quartz (Smit, 1984). These cracks in quartz are

sometimes infilled by authigenic sulphides (pyrite, pyrrhotite, pentlandite, etc.); brannerite is also occasionally associated with carbon (Liebenberg, 1955). Minute inclusions of galena are also common in brannerite, but not as numerous as in uraninite (Liebenberg, 1955). As a secondary mineral, brannerite is suggested to have formed "in-situ" by the so-called "Pronto reaction" i.e. $UO_2 + 2\text{-}3TiO_2 \rightarrow UTi_{2\text{-}3}\ O_{6\text{-}3}$ in which uranium migrates to Ti phase or titanium to uranium titanites (Ramdohr, 1957). According to Ramdohr (1958b) the "Pronto reaction" takes place under hydrothermal conditions at minimum temperatures of about $250^{o}C$.

*2.2.4. Carbonaceous Matter*

Uranium minerals and gold mineralisation in the Witwatersrand Basin reefs are commonly associated with carbonaceous matter in a form of bitumen and kerogen (Nagy, 1993). At first the carbonaceous matter used to be referred to as thucholite as suggested to be composed of thorium, uranium and hydrocarbons (Liebenberg, 1955; Hallbauer and van Warmelo, 1974). Mossman *et al*. (2008) defined kerogen as remains of former living organisms (organic carbon) specifically a solid polymer-like organic substance which has remained *in situ* since deposition. Bitumen is a macromolecular organic compound that was once mobile as a viscous fluid but which has since solidified (Spangenberg and Frimmel, 2001; Mossman *et al*., 2008).

Carbonaceous matter is distributed through the quartz-pebble conglomerates in different forms, as stratiform seams, spherical, glassy and brittle globules (Spangenberg and Frimmel, 2001); the spherical form is generally known as flyspecks. The seams occur mainly at the base and rarely at the top of the reefs, and they are normally a few millimetres thick and at times up to several centimetres in thickness. These seams mainly carry with them, grains of uraninite and gold; the uraninite grains show evidence of partial replacement and fragmentation by the carbonaceous seams. Carbon seams mainly exhibit a fibrous or 'columnar' texture which is always developed perpendicular to seam margins (Hallbauer and van Warmelo, 1974; Pretorius, 1975; Hallbauer, 1986; Smieja-Krol *et al*., 2009).

The spherical or nodular flyspecks bitumen are typically less than 1 mm in diameter and usually occur surrounding uraninite grains as if they coat the grains, they also penetrate through cracks of uraninite grains; the flyspecks, unlike the carbon seams, are disseminated throughout the reefs matrices (Smieja-Krol *et al*., 2009).

There is a strong affinity between gold, uranium and the carbonaceous matter. Gold occurs interstitial to the carbonaceous matter and is suggested to have been remobilised by the latter (Schidlowski, 1981). Reefs such as the Carbon Leader, Basal and Vaal Reefs have the highest Au and U in the carbonaceous matter, in a form of seams in particular (Frimmel, 2005). Nagy (1993) estimated that about 40% of all mined Witwatersrand gold was hosted by such bitumen seams. The carbonaceous matter, on a microscale in the reefs, occurs as microfractures in the uraninite and quartz typically containing some gold. Smits (1984) found that in some of the Witwatersrand Basin reefs, the detrital uraninite and gold are altered by the carbonaceous matter, and within these zones of high gold and uraninite association with the carbonaceous matter, the gold and uranium grades exceeds those in the ordinary reefs where the carbonaceous matter is absent. This led to the suggestion that these carbon seams trapped uranium and gold grains and therefore, prevented them from being transported further (Pretorius, 1975).

Different authors have suggested possible sources of the Witwatersrand hydrocarbons ranging from (i) Late Archean algal–bacterial kerogens derived from extensive microbial mats, which once colonised the Witwatersrand clastic sediment (Liebenberg, 1955; Hallbauer and van Warmelo, 1974; Schidlowski, 1981). (ii) Kerogens disseminated in the shale units within the Witwatersrand Supergroup (e.g., Robb *et al*., 1997; Gray *et al*., 1998); to (iii) an external source, such as the shale units in the Wolkberg Group or the 2.6–2.5 Ga carbonaceous shallow marine carbonates in the lower Transvaal Supergroup (Robb *et al*., 1997).

Spangenberg and Frimmel (2001) showed that all forms of the carbonaceous matter are regarded as solid pyrobitumen derived from indigenous algal-bacterial lipids; this was determined based on bulk and molecular isotopic compositions of the carbonaceous matter and that the bacteria was developed under anoxic environments. Spangenberg and Frimmel (2001) further showed that the source of the hydrocarbon was not from outside the Witwatersrand, but internal as shown by Barnicoat *et al.,* (1997); however, the difficulty currently is determining the distance of the hydrocarbon mobilisation.

## 2.3. Genetic Models of the Witwatersrand Basin Mineralisation

In spite of the extensive research that has been carried out in the Witwatersrand Basin, the source of mineralisation is still debated. There are three major models, the placer and hydrothermal models that are suggested to be responsible for the deposition of gold and associated uranium in the basin.

The placer model proposes that gold is detrital, derived from an older source area (>2.9 Ga) such as greenstones and granitoids, and was mechanically transported into the basin and concentrated by fluvial processes (Mellor, 1916; Pretorius, 1975; Hallbauer and Utter, 1977: Figure 2.3). Direct dating on gold grains using Re-Os dating yielded an age of 3016±110 Ma and 3033±21 Ma when combined with rounded pyrite from the same hand-sample (Kirk *et al*., 2003). Gold grains display rounded-flattened and edge-overturned (or peaned) morphologies that are characteristic of its malleability acquired during transportation, as it was hammered by pebbles, whereas some flaky gold particles may be rolled into more compact particles (Minter, 1976; Hallbauer and Utter, 1977). Uranium-bearing minerals, which are often concentrated at the base of conglomerates reef matrices, have rounded shaped grains within organic matter and this is regarded as clear evidence for the allogenic nature of the mineral (Schidlowski, 1981).

Direct dating of uraninite grains from the Dominion Reef yielded a U–Pb age of 3050±50 Ma (Rundle and Snelling, 1977). This age overlaps with that of the Dominion Group sedimentation but is distinctly older than the Witwatersrand sedimentary rocks (Frimmel, 2005).

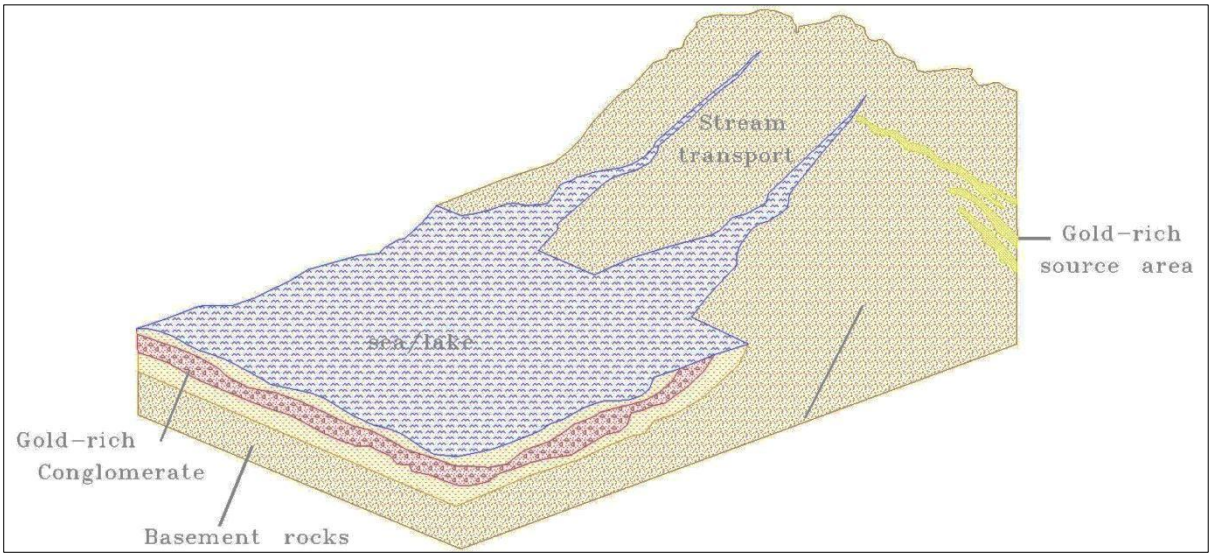



Figure 2.3: Illustration of the placer model with greenstone gold-rich sources areas suggested to be komatiites or metamorphosed basalts older (3.5-2.9 Ga) than the deposition of the Witwatersrand Basin. Detrital gold has been mechanically eroded from the old source areas into the basin (sea or lake) by deltaic fluvial processes. The age of the gold in the basin is similar to the older gold sources (after Kirk *et al.*, 2003).

Studies suggest that when detrital uraninite was deposited in the Archaean environment, atmospheric conditions were less oxic than current atmospheric conditions (England *et al*., 2001). It is considered that the pre-2.35 Ga atmosphere was essentially oxygen free ($PO_2$< 10 to 1 bars) and comprised mainly of $CO_2$ ($PCO_2$< 1 bar) and $N_2$, with minor $H_2S$ ($PH_2S$ = 10 to 7.5 bars) and $H_2$; rainfall and surface runoff under these conditions was acidic (pH < 4), giving rise to pronounced chemical weathering in the continental domain (Krupp *et al*., 1994). During sediment deposition under these conditions, river waters were within the pyrite stability field, but outside the stable region for Fe-Ti oxides, alluvial gold would retain its high silver content, and uraninite solubility would also be very low in the extremely anoxic surface environment (Krupp *et al*., 1994).

Chemical analysis of the uraninite grains by Robb and Meyer (1995) revealed highly variable U/Th ratios and this led to a suggestion that uraninite originated from either a granitic or pegmatitic source rock and could not have formed within the basin by low temperature hydrothermal fluids as Th contents are too high. This led to a suggestion that the possible source rock for primary uraninite in the basin might be a 3.1 Ga peraluminous S-type granite (uranium-specific with high U/Th ratios). Another viable source rock for uraninite in the basin with high U/Th ratio but low Th contents might be the 3.174 Ga greisenised granite around Hartebeestfontein (Robb and Meyer, 1995).

The modified placer model shares some similarities with the placer model. The modified placer model suggests that detrital gold has been mobilised and re-precipitated by hydrothermal or metamorphic fluids with other associated phases (Robb and Meyer, 1995; Frimmel and Gartz, 1997; Minter, 1999; Kirk *et al*., 2001; Kirk *et al*., 2003). This model is supported by gold grains displaying authigenic textures, probably as a result of post-burial dissolution and reprecipitation. Many workers have suggested that dissolution and reprecitation took place virtually *in situ (*Liebenberg, 1955; Ramdohr, 1955; Schidlowski, 1970; Frimmel *et al*., 1993; Meyer *et al*., 1994b). Remobilised gold is preferentially associated with paragenetically-late phases such as authigenic sulphides, carbonaceous matter and secondary chlorite, but also commonly occurs as fracture-fillings in, and as overgrowths on, allogenic pyrite which only rarely contains primary gold inclusions (Meyer *et al*., 1990a, b). Textural evidence has shown that fluid-related gold (secondary gold) remobilisation and reprecipitation has partially replaced compact pyrite (Robb and Meyer, 1995). When traced over a kilometer scale, the mean gold composition for the same reef in different mines can vary drastically, confirming that these placer deposits have been subjected to metamorphism and hydrothermal modification (Barnicoat *et al*., 1997).

The hydrothermal model proposes that gold (and associated uranium) was transported in solution from outside of the basin by metamorphic or hydrothermal fluids after the formation of the basin between 2.7 and 2.0 Ga (Parnell, 2001; Gray *et al*., 1998; Barnicoat *et al*., 1997; Phillips and Law, 2000), as shown in Figure 2.4.

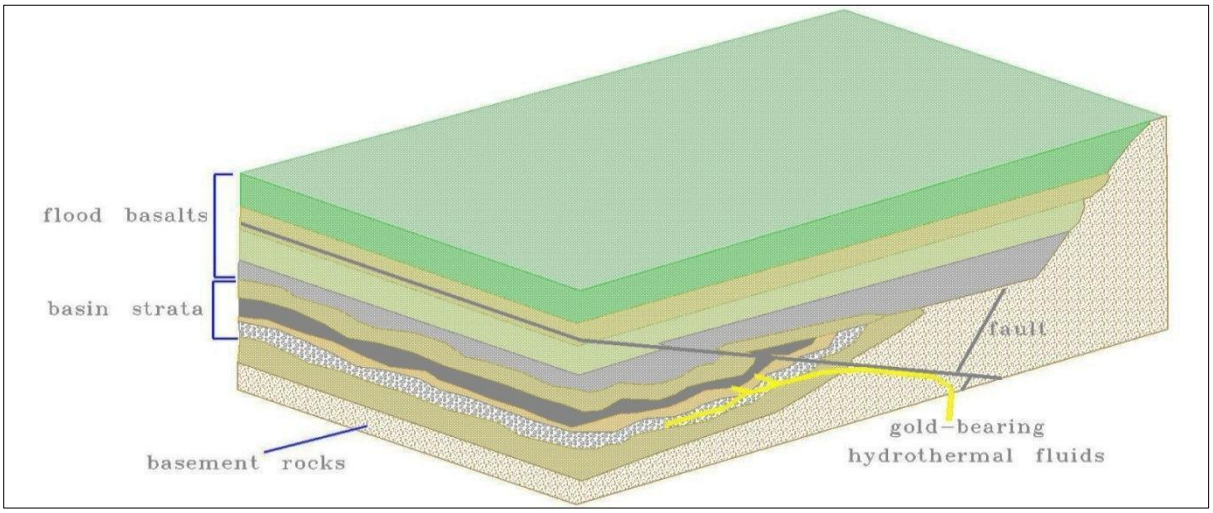



Figure 2.4: Illustration of the hydrothermal fluids (2.7-2.0 Ga) from later processes within the Witwatersrand Basin. Gold has been derived from hydrothermal sources from deep within the earth's crust and carried along faults into the basin after deposition of the conglomerates (after Kirk *et al.*, 2003).

The Veredefort meteorite impact around 2025 Ma shows more evidence of gold remobilisation in the reefs (Robb and Meyer, 1995; Frimmel, 2005). In order to support the hydrothermal model, a four-stage paragenetic interpretation was developed (Barnicoat *et al*., 1997):

Stage 1. Diagenesis, involving quartz overgrowths, illite formation (now muscovite), chlorite and pyrite.

Stage 2. Development of pyrophyllite-rich material as a result of high-temperature (above 300$^{o}$C at pressures between 2.5 to 3.45 Kbar) deformation of muscovite.

Stage 3. Mineralisation by hydrothermal carriers containing uranium, hydrocarbons, quartz, kaolinite, pyrite, pyrrhotite, gersdorffite, arsenopyrite, galena and gold, filling sub-horizontal fractures.

Stage 4. Post-mineralisation events include localised fracturing, veining, further shearing and pressure solutions.

The metamorphic replacement for gold genesis implicates metamorphic fluids in the transport of gold into the Witwatersrand Basin during metamorphism; it is suggested that the temperature during peak metamorphism, and high pyrite content was adequate to remobilise gold from the Archaean basement (Phillips, 1987) during the emplacement of the Bushveld Igneous Complex around 2060 Ma and the Vredefort meteorite impact around 2025 Ma (Robb and Meyer, 1995; Frimmel, 2005). Gold was carried by a bisulphide complex and was easily destabilised by reaction with Fe and/or C. A close analogy was made with the gold-forming processes in major greenstone gold deposits, also of Archaean age (Phillips and Law, 1994).

From the above stages, it is suggested that uraninite precipitated from the hydrothermal fluid as a result of reduction by either pre-existing minerals or hydrocarbons. This continuous process lead to the alteration of the hydrocarbons by uraninite to pyrobitumen, and further reduction of hydrothermal fluid by the hydrocarbon resulted in gold precipitation (Barnicoat *et al*., 1997).

### 2.4. Source Areas for Gold and Uranium in the Witwatersrand Basin

Similar to the style of mineralisation, the source for gold and uranium in the Witwatersrand Basin has long been debated. Recently, it was shown that the possible sources that were fertile in both uranium and gold are from the north and west of the Witwatersrand Basin as a

results of sedimentary structures on the Witwatersrand sediments (Robb and Meyer, 1995), and therefore, ruling out the possibility of the Barberton greenstone being a source for uranium and gold (Robb and Meyer, 1995; Kirk *et al.*, 2003; Frimmel; 2005). The main reasons for the Barberton greenstone belt not to being a viable uranium source to the Witwatersrand Basin is that it does not contain primary uraninite grains and have U/Th <0.5 (Robb and Meyer, 1995). To date, the possible suggested uranium sources are the Archaean basement granitoids from the Witwatersrand Basin hinterland (Robb *et al.*, 1989). It is suggested that these granite bodies were weathered and eroded due to tectonism that rejuvenated and deposited uranium into the upper Central Group of the Witwatersrand Basin (Robb and Meyer, 1985).

The Archaean granitoids bodies from the Witwatersrand Basin hinterland are characterised mainly by surface outcrops and buried granite basement (Figure 2.5). The Witwatersrand Basin is surrounded by granites of the Johannesburg, Devon, Westerdam, Hartebeesfontein, Ottosdal-Coligny and Schweizer-Reneke domes (Robb and Meyer, 1985). The Johannesburg Dome in the north of the Central Rand Goldfield, has been shown by U-Pb zircon age dating to be 3170±34 Ma, is the best exposed granite body due to its elevation, and has been found to contain a wide variety of granites and some remnants of the greenstone rocks (Anhaeusser, 1973). The rest of the granite domes are not well exposed and have not been mapped in as much detail as the Johannesburg Dome (Robb and Meyer, 1985).

The Witwatersrand hinterland granitoid bodies are generally hydrothermally altered granites (HAGS), as observed in the majority of the fresh sub-surface granite borehole cores by Robb and Meyer (1985). These granites contain significantly high uranium contents (Robb *et al.*, 1989). The HAGS are generally characterised by a wide diversity of alteration and replacements such as chlorite, sericitization of feldspars, carbonate and fluorite veins with secondary pyrite (Robb and Meyer, 1985). The most common accessory minerals in these HAGS are zircon, monazite, leucoxene, uraninite, pyrite, chalcopyrite, arsenopyrite, magnetite and carbon nodules (Robb and Meyer, 1985). Prior to the deposition of the Dominion and Witwatersrand Basins, the HAGS were eroded to form palaeoregoliths (Gay and Grandstaff, 1980). These palaeoregoliths are quartz-sericitic and characterised by leucoxene and sulphides; the leucoxene is uranium-rich and is suggested to represent the brannerite found in the Witwatersrand Reefs (Robb and Meyer, 1985).

In the Klerksdorp Goldfields area, the closest granite dome is the Hartebeesfontein Archaean basement in the northwest of the region (Figure 2.5); uraninite is abundant as an accessory phase in the Hartebeesfontein Archaean basement (Robb *et al*., 1989). This suggests that uranium-bearing minerals in the Vaal Reef of the Klerksdorp Goldfield might have been derived from the Hartebeesfontein dome. Gold analyses in the Vaal Reef of the Witwatersrand Basin were dated by the Os-Re method and revealed ages around 3.01 Ga, which are older than the deposition of the basin, suggesting that the gold is detrital (Kirk *et al*., 2003). The Os-Re method was applied due to elevated amounts of osmium in the gold grains.

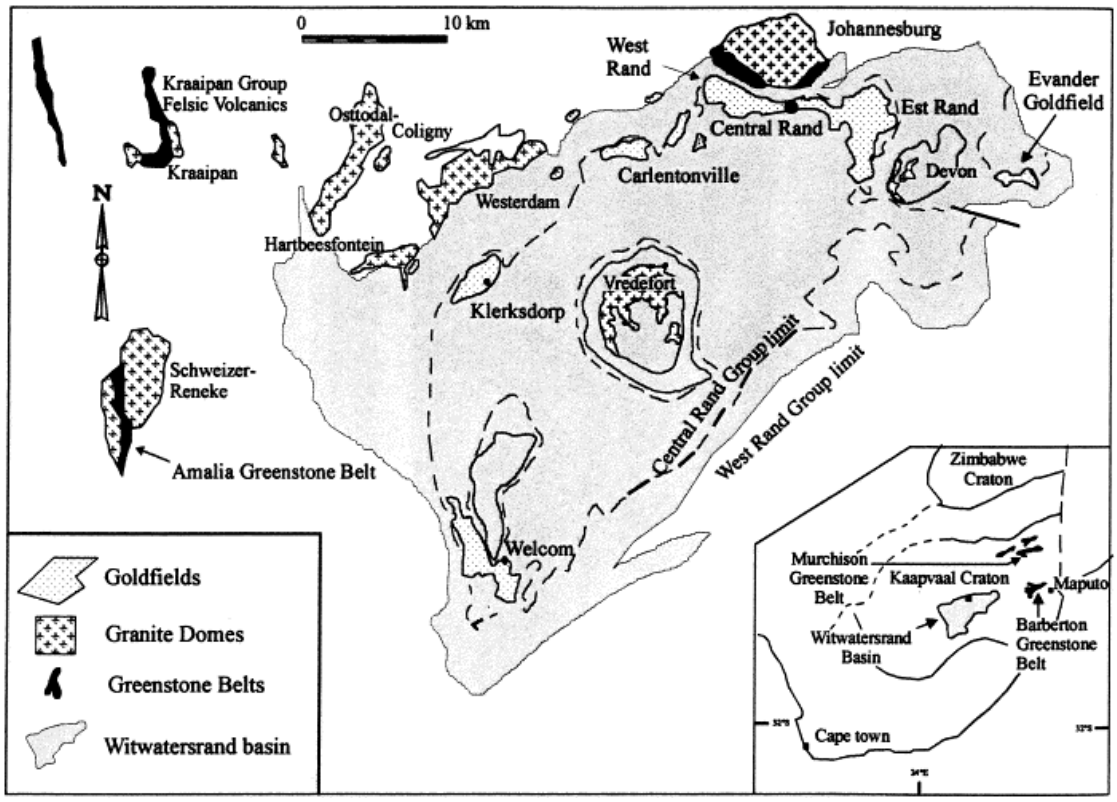



Figure 2.5: Illustration of the locality of the Witwatersrand Basin with its major goldfields surrounded by older Archaean greenstone and basement granites throughout the entire basin. The location of the Witwatersrand Basin within the Kaapval Craton is shown in the insert map (after Poujol *et al*., 1999).

The osmium contents in the Witwatersrand sediments match those of the komatiites or metamorphosed basalts and the latter contain gold with high osmium concentrations (Kirk *et al*., 2003). There are two greenstone areas suggested as being responsible for sources of the komatiites (Figure 2.6), and they are the Murchison granite-greenstone belt from the north of the Witwatersrand and the Kraaipan granite-greenstone occurring west of the Witwatersrand

and both these areas are suggested by the river drainage pattern to be the sources of the Witwatersrand sediments (Kirk *et al.*, 2003; Frimmel, 2005).

## CHAPTER THREE

## LOCAL GEOLOGY OF THE KLERKSDORP GOLDFIELD

### 3.1. Introduction

The Klerksdorp Goldfield is located 160 km southwest of Johannesburg, and lies on the western rim of the Witwatersrand Basin (Antrobus, 1986). The Klerksdorp Goldfield has been an area of active mining since the discovery of gold and uranium on the Western Reefs Mine and the Vaal Reef in the 1940s and 1950s (Chapman *et al*., 1986; Figure 3.1).

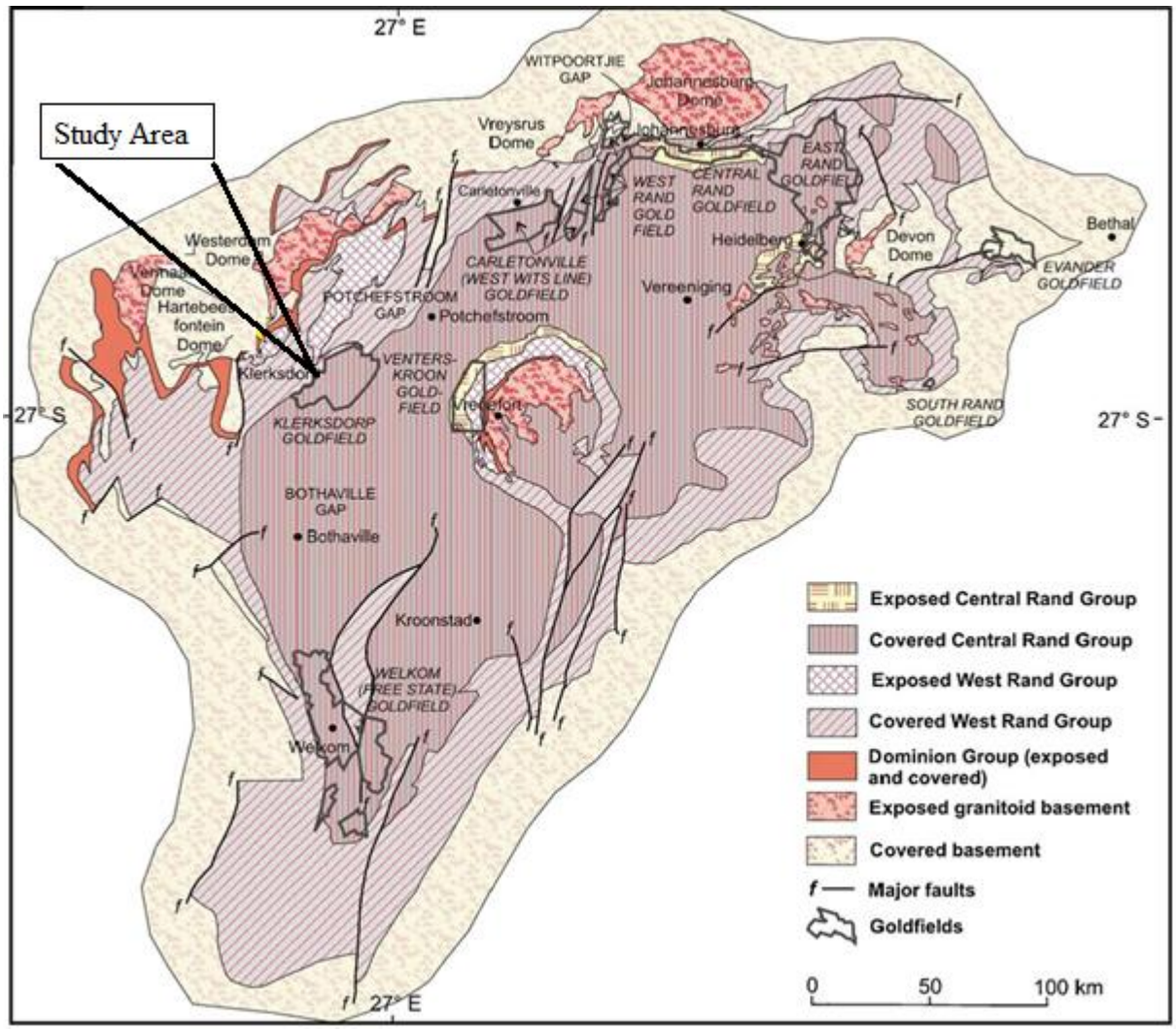



Figure 3.1: Locality map of the Witwatersrand Basin Goldfields, with the Klerksdorp Goldfield in the proximity of Klerksdorp town. The Vaal Reef occurs southwards where the AngloGold Ashanti properties are found (Rantzsch *et al.*, 2011).

### 3.2. Stratigraphy of the Klerksdorp Goldfield

The Klerksdorp Goldfield occurs in the upper Johannesburg Subgroup (Figure 3.2) of the Central Rand Group (Frimmel, 2005). The geology of the Klerksdorp area is complicated by erosional truncation of lower formations and by overstepping by younger formations (McCarthy, 2006).

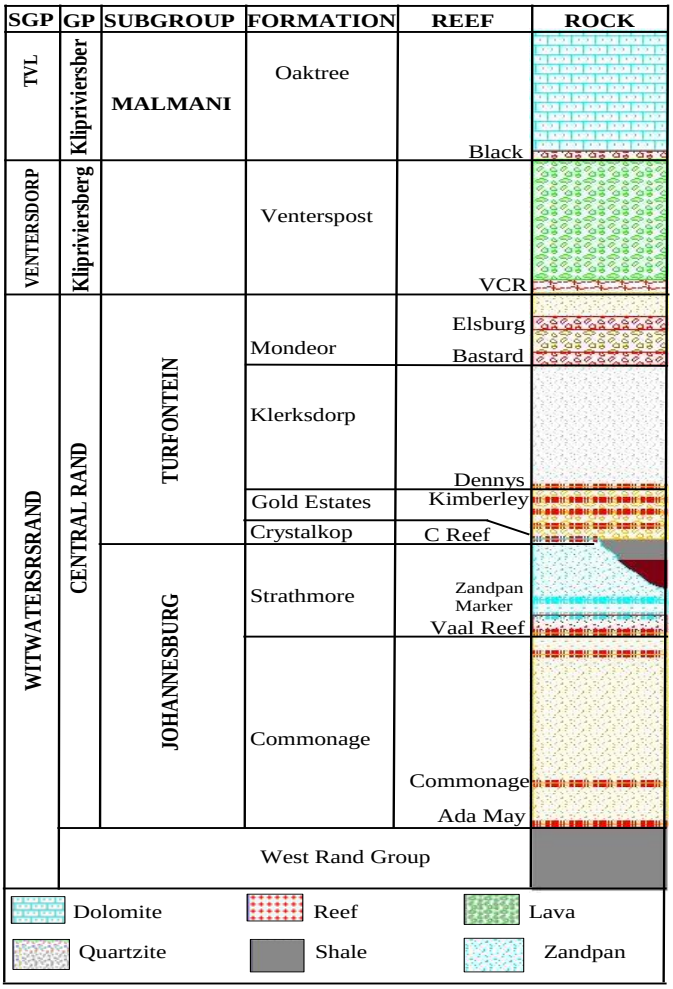



Figure 3.2: Generalised stratigraphic column for the Witwatersrand Supergroup with the main auriferous conglomerate beds (reefs) shown, including the Klerksdorp Goldfield reefs (after Watts, 2004).

Several economic reefs are found in the Klerksdorp Goldfield stratigraphy (McCarthy, 2006). The base of the Johannesburg Subgroup is marked by the Ada May Reef, which is overlain by grits and quartzites of the Blyvooruitzicht Formation (McCarthy, 2006). The Commonage Reef is found at the base of the Main Formation, overlain by quartzites of the Randfontein Formation, the Livingstone Reef marks the base of the Luipaarsdvlei Formation, the base of the Krugersdorp Formation, is made of the Vaal Reef, and the Booysens Formation marks the

top of the Johannesburg Subgroup (McCarthy, 2006). The Crystalkop Reef occurs at the base of the Robinson Formation (Catuneanu and Biddulph, 2001).

### 3.3. Structure of the Klerksdorp Goldfield

The structure of the Klerksdorp Goldfield has been regarded as the most complex of all the goldfields (McCarthy, 2006). The general orientation of meta-sedimentary sequences of the Witwatersrand Supergroup in the goldfield is NE-trending and SE-dipping (Figure 3.3).

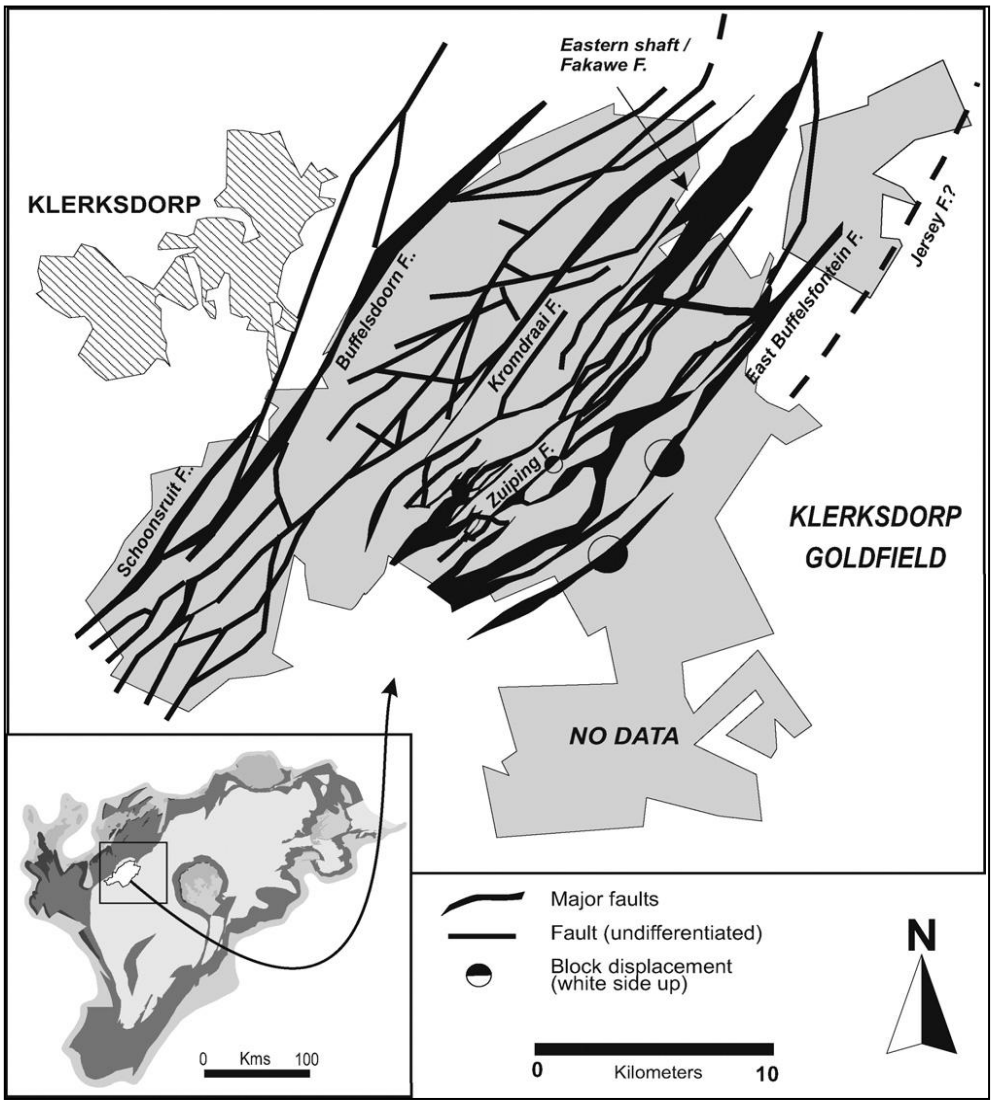



Figure 3.3: Geological map of major structures in the Witwatersrand Supergroup in the Klerksdorp goldfield with the younger cover removed (after Dankert and Hein, 2010).

The goldfield is crosscut by a series of NE-striking faults including the Schoonspruit, Buffelsdoorn, Kroomdraai, Fakawe, Zuiping, East Buffelsfontein and Jersey faults, and a

complex array of mafic dykes that formed a feeder system to the flood basalts of the Klipriviersberg Group (Dankert and Hein, 2010).

### 3.4. The Vaal Reef and Associated Lithologies

A detailed review on the Vaal Reef geology was undertaken in order to gain an understanding of the geology and stratigraphy of the Vaal Reef at the Kopanang, Great Noligwa and Moab Khotsong Mines (Figure 3.4). Drilled borehole cores from underground workings were logged from each of the three mines. The combination of literature and information obtained from the drilled cores contributed in understanding the distribution of the Vaal Reef on these three mines and this guided sample collection from the mineralised sections of the boreholes.

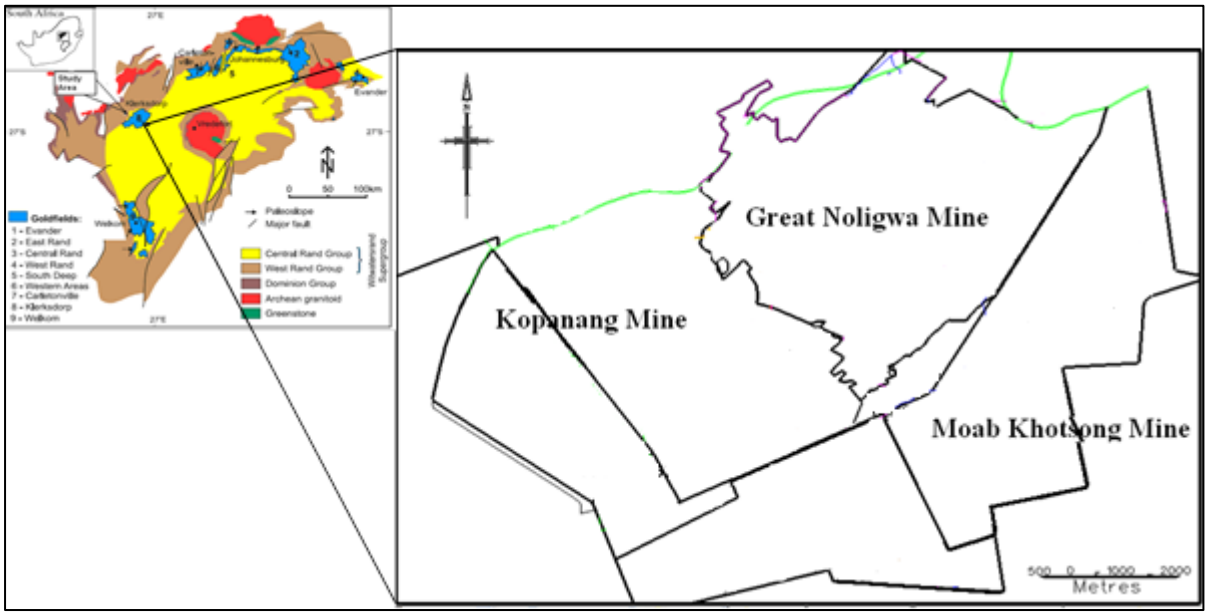



Figure 3.4: Locality map of Kopanang, Great Noligwa and Moab Khotsong Mines in the Klerksdorp Goldfield (after Frimmel, 2005 and AngloGold Ashanti internal report, 2001).

The Vaal Reef is situated in the Central Rand Group and occurs within the Johannesburg Sub-Group in the lower parts of the Strathmore Formation in the Klerksdorp Goldfields (as shown in Figure 3.2). According to Catuneanu and Biddulph (2001), the Vaal Reef is vertically and laterally variable from the western part of Kopanang Mine to the Great Noligwa Mine and the eastern boundary of Moab Khotsong Mine. The Vaal Reef is constituted by a quartz-pebble, oligomictic conglomerate, containing a high grade of gold and uranium (Antrobus *et al*., 1986), and was deposited at approximately 2870 Ma (Frimmel, 2005).

The Vaal Reef rests occasionally on the Witkop and Grootdraai Facies which mainly forms the base of the Main Bird 4 (MB4) unit in the west at Kopanang Mine and the Mizpah Reef and Mizpah Quartzite in the Great Noligwa and Moab Khotsong Mines. Where the Witkop and Grootdraai Facies are absent the Vaal Reef C Facies or A Facies mark the base of the MB4 unit. The MB4 unit is underlain by the Main Bird 5 (MB5) quartzite footwall and overlain by the Main Bird 3 (MB3) quartzite hangingwall in all the mines studied (Figure 3.5). The MB4 unit is made up of the Witkop and Grootdraai Facies, C Facies, B Facies, A Facies (the A Facies is subdivided into Bottom, Middle and Top Sub-facies), Streakies quartzite (Clean and Dirty Streakies), the Zandpan Quartzite and Zandpan Marker (Figure 3.5).

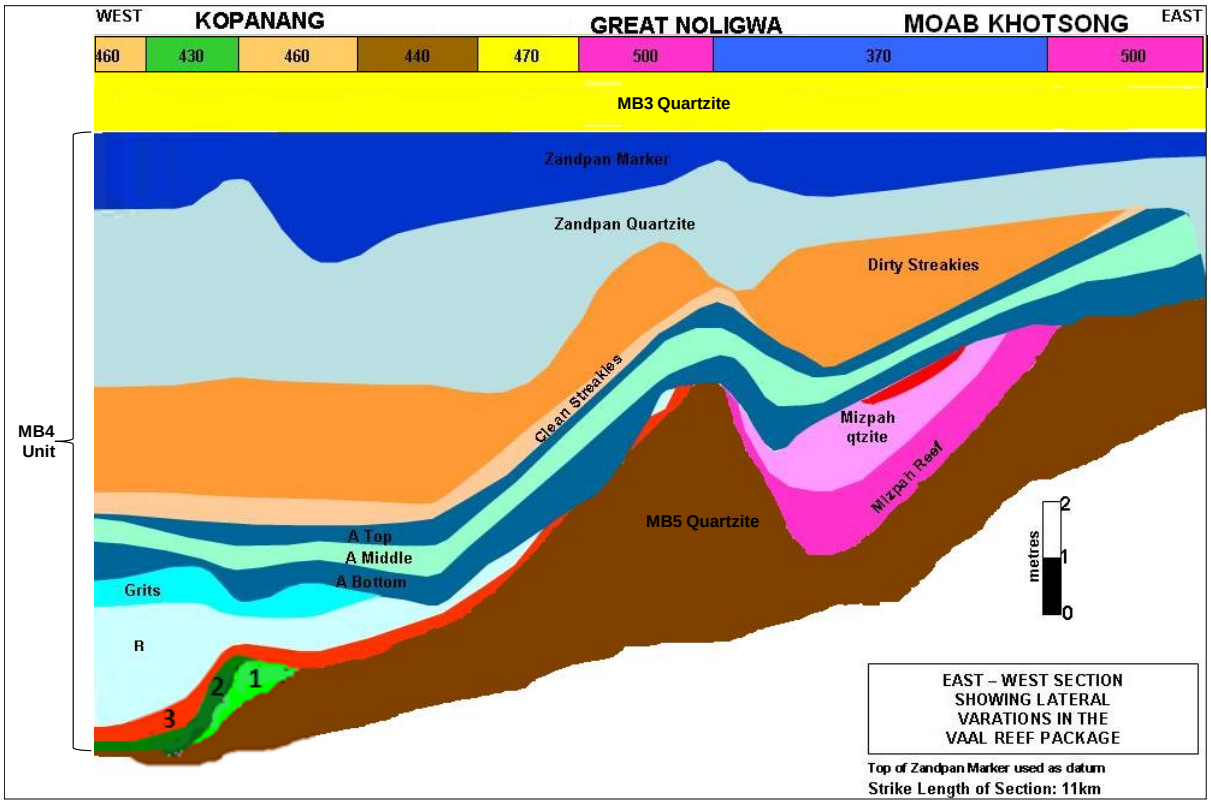



Figure 3.5: East-west cross-section of Kopanang and Great Noligwa Mines showing lateral variations of the Vaal Reef package (C [3], B and A Facies) resting on the Witkop (1) and Grootdraai Facies (2) within the MB4 unit. The latter is overlain by the MB3 quartzite and underlain by the MB5 quartzite. The Vaal Reef package from east to west is represented by six geozones (AngloGold Ashanti internal report, 2001).

The Vaal Reef varies in lateral continuity from west to east (from Kopanang, Great Noligwa and Moab Khotsong Mines) and is disturbed mainly in the C Facies which is poorly developed in the Great Noligwa and Moab Khotsong Mines; however, all the A Subfacies are well-developed throughout the three mines (Figure 3.5). The C Facies is the main economic

and most exploitable facies at Kopanang Mine and the A Facies is the main economic facies at both Great Noligwa and Moab Khotsong Mines.

Figure 3.6 shows images of the Vaal Reef with the C Facies (Figure 3.6A) at Kopanang Mine and the A Facies (Figure 3.6B) at Moab Khotsong Mine. The C Facies is mainly constituted of a carbonaceous matter at the base of the reef and the A Facies has rare carbonaceous matter development.

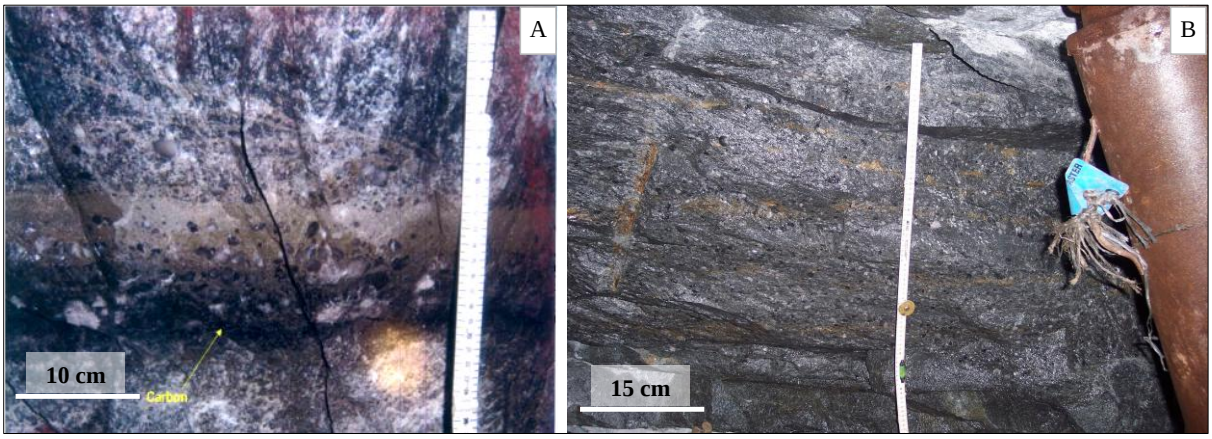



Figure 3.6: Layout of the Vaal Reef. a) The Vaal Reef C Facies at Kopanang Mine overlies the MB5 quartzite with a carbon seam at the base of the reef and a pyrite-rich matrix. b) The Vaal Reef A Facies at Moab Khotsong Mine showing the MB5 quartzite footwall overlain by the reef polymictic conglomerate.

Based on Figure 3.5, the MB4 unit across all the three mines is made up of the following lithologies:

### *3.4.1. Witkop Facies*

The Witkop Facies forms the base of the MB4 unit, and is generally 1 m thick and up to 7 m wide overlying the MB5 quartzite footwall unit (Figure 3.5). It is a highly channelized unit ranging from a medium to small pebble (10 mm) conglomerate to a siliceous quartzite. The clast assemblage mainly consists of vein quartz pebbles (95-100%), with rare chert (0-5%), quartzite (0-2%) and porphyry (0-3%), with a light grey, medium- to coarse-grained matrix.

### *3.4.2. Grootdraai Facies*

The Grootdraai Facies is about 35 cm thick and in some areas in the Kopanang Mine, the facies cuts into the MB5 unit footwall (Figure 3.5). The unit consists of sub-rounded to rounded (15-35 mm) conglomerate lag with a light grey-coloured, medium- to coarse-grained, sub-siliceous matrix. The facies has a low pyrite content.

### *3.4.3. Mizpah Package*

The Mizpah Reef and Mizpah Quartzite are well developed at the Great Noligwa and Moab Khotsong Mines in the eastern part of the AngloGold Ashanti mining property (Figure 3.5). The Mizpah Reef conglomerate is well sorted with self-supported clasts (8-16 mm in diameter). The clasts are sub-angular to sub-rounded and consist of smoky and milky quartz, sub-angular black chert and sub-rounded grey porphyry clasts. The matrix consists of light grey to yellow grey colour, reflecting pyrite at some places reaching 50 % in abundance. The Mizpah Reef conglomerate shows a fining upward sequence (Catuneanu and Biddulph, 2001).

The Mizpah Quartzite is made of moderately mature to immature yellowish grey or brown quartzite ranging from 1 to 6 m in thickness. At some places, the Mizpah Quartzite has scattered angular to sub-angular grits. Where the Mizpah Quartzite is not present, the A Facies rests on the Mizpah Reef conglomerate and it can become difficult to separate the two rock types.

### *3.4.4. C Facies*

The C Facies unit is relatively thin, ranging between 2 and 36 cm, and rests on the Grootdraai and lower Witkop Facies conglomerates at Kopanang and on the Mizpah Reef and Mizpah quartzite when occurring at the western boundary of Great Noligwa Mine. The C Facies conglomerate is generally made of the following clasts: rounded (15 mm) white and smoky vein quartz (85 to 95%), sub-angular to sub-rounded black chert (12%) and sub-angular to sub-rounded grey porphyry (0.2%; Minter, 1972).

The matrix size is about 350 μm and dark grey in colour due to chloritic alteration, and is very pyritic. A carbonaceous layer is widespread at the base of the unit, and in places only a carbon contact may be present, with no occurrence of the conglomerate reef. Carbon thickness can be up to 5 cm, although typically the seam is only a millimetre or two thick (AngloGold Ashanti internal report, 2001).

### *3.4.5. B Facies*

The B Facies is a clean, pale grey, trough cross-bedded quartzite that is about 1.5 m thick and overlies the C Facies (Figure 3.5). This unit is characterised by 3 cycles of quartzite. The first cycle is the lower dark grey to purple quartzite, with little internal structures. The second

cycle is a light greyish-white quartzite with cross bedding and grits of black chert. There is a "B" grit unit found in the B Facies quartzite of up to 10 cm thickness with a poorly developed oligomictic (white quartz pebble) conglomeratic band. Black chert specks are usually present in the quartzite, and in areas these grains can become very prominent. A poorly developed grit band may be developed at the base of the B Facies, but is often difficult to identify. Where the B Facies is thicker (the western side of Kopanang) the upper part of this facies may contain more grits, as well as pyrite stringers. Where the base of the A Facies is not well developed it may be very difficult distinguishing the B Facies quartzites from the A Facies quartzites, especially where the Upper gritty B is present. The B Facies thins gradually towards the east, where it can be as thin as 8 cm (AngloGold Ashanti internal report, 2001).

### *3.4.6. A Facies*

The A Facies is the most well-preserved part of the Vaal Reef throughout the three mines and forms the economic reef at Great Noligwa and Moab Khotsong Mines, as the development of the C Facies is very poor in these areas (Figure 3.5). The A Facies at these mines is generally underlain by the Mizpah quartzite and the Mizpah Reef.

The A Facies (Kopanang, Great Noligwa and Moab Khotsong) is sub-divided as follows:

- The Bottom A sub-facies is usually the gold-bearing unit and is more economic compared to the Middle and Top sub-facies. The conglomerate has small pebbles at the base of this sub-facies, together with seams of carbon that are associated with high grade areas. The top of this bottom sub-facies has a clean pale grey quartzite matrix, and in high grade areas the quartzite is altered to dark grey (AngloGold Ashanti internal report, 2001). The second high grade host occurs just at the top of the Bottom A sub-facies, where the conglomerate is characterised by elongated almond-shaped pebbles, hence called the "Almond Reef". The pebbles can be as large as 25 mm in size and the rounded shape of these pebbles makes it easy to distinguish from the C Facies pebbles. Carbonaceous matter is not well developed but occurs in nodular form.

- The Middle A sub-facies is characterised by a clean cross-bedded orthoquartzite with layers of pyrite stringers sometimes present. The quartzites can be pebbly, these

pebbles may cluster and form matrix-supported conglomerates (AngloGold Ashanti internal report, 2001).

- The Top A sub-facies is generally identical throughout the Kopanang, Moab Khotsong and Great Noligwa Mines and is referred to as "ubiquitous A".

### *3.4.7. Streaky Quartzite*

The Streaky Quartzites overlie the Vaal Reef and can be up to two metres thick (Figure 3.5). Two sub-units can often be identified, a lower cleaner zone, and an upper more argillaceous zone. The lower sub-unit, the Clean Streakies, is typically less than 60 cm thick. Where these quartzites overlie the Top A, they may partially rework the A, and small scattered clasts may therefore be present within the lower 10 cm. A distinctive feature of the Streaky Quartzite is that pyrite stringers are extremely rare, and if found it is unlikely that more than one or two stringers will be found in a borehole. The lower sub-unit is slightly green and the upper sub-unit, the Dirty Streakies is commonly developed, although locally it may be removed by the overlying Zandpan Quartzite (AngloGold Ashanti internal report, 2001).

### *3.4.8. Zandpan*

The Zandpan is a 30 to 100 cm thick package constituted of the Zandpan Marker and Quartzite (Figure 3.5), and is split into three units, an upper and lower conglomerate separated by an internal quartzite. The Zandpan Marker is overlain by the Main Bird (MB3). The Zandpan is distinguishable from the A Reef because of its porphyritic lava clast content. The upper conglomerate is typically more pyritic and polymictic than the lower conglomerate, towards Moab Khotsong and Great Noligwa Mines. Clast size in the west can exceed 40 mm, but is generally smaller in the east. The conglomerates are not as well developed in the east. The internal quartzite is a gritty, usually argillaceous quartzite, often containing scattered clasts, and sometimes containing narrow pebble lag conglomerates. Where the Zandpan marker is thin and the internal quartzite is very conglomeratic it may be difficult to separate the three components. In other parts, the quartzite might be mistaken for the Streaky Quartzite if the basal conglomerate is not well developed, and the quartzite can still rework the streakies and some top parts of the A Reef (AngloGold Ashanti internal report, 2001).

### 3.5. Lateral Distribution of the Vaal Reef

From west to east of the mining area, the Vaal Reef is split into geological zones called ‘geozones’. Division of the Vaal Reef into these geozones was based on changes in mineralisation, sedimentological properties and alteration with respect to lateral distribution of the Vaal Reef. From west (Kopanang Mine) to east (Great Noligwa and Moab Khotsong Mines), six geozones were recorded and these are numbered 460, 430, 440, 470, 500 and 370 (Figures 3.5 and 3.7). Information on the seventh geozone (502) was not provided for this study from the mining company.

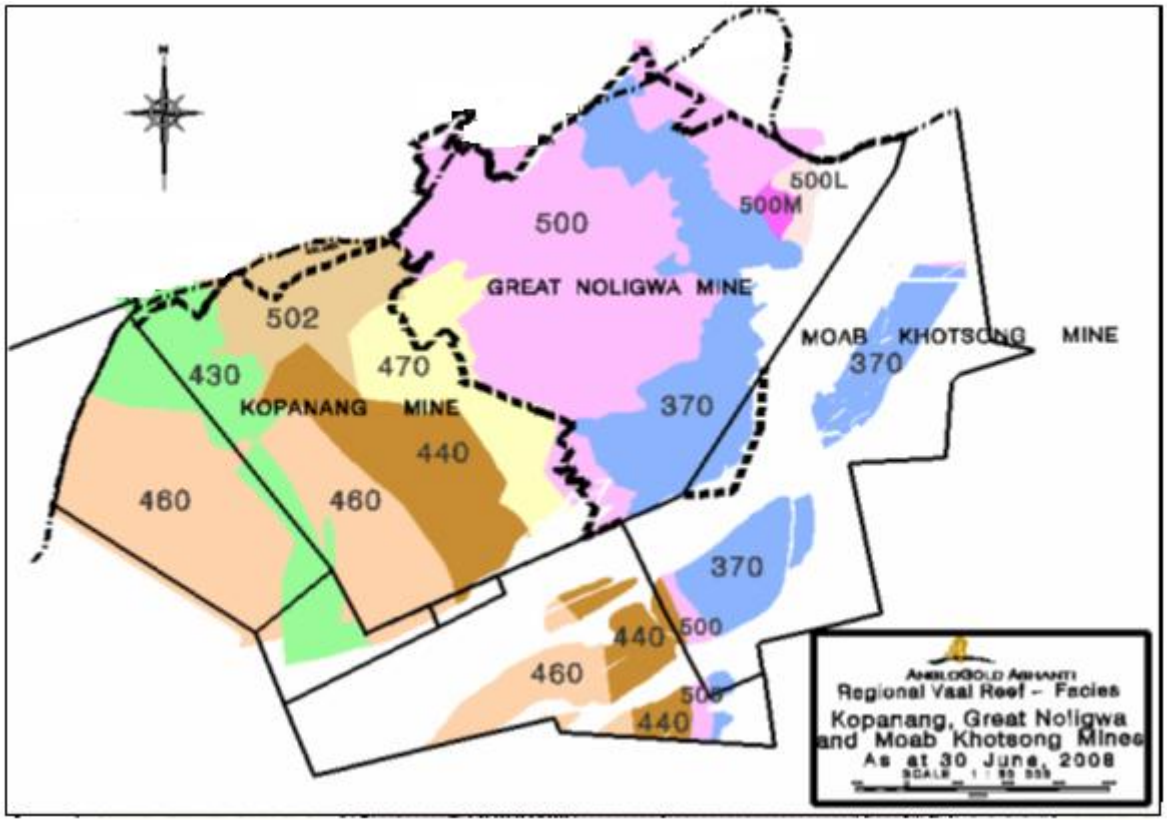



Figure 3.7: Distribution of geozones at Kopanang, Great Noligwa and Moab Khotsong Mines (AngloGold Ashanti internal report, 2001). Kopanang Mine consists of the 460, 430, 440, 502 and 470 geozones. Great Noligwa and Moab Khotsong Mines consist largely of the 500 and 370 geozones.

The Vaal Reef (Figure 3.5) in the geozones is poorly developed in the C Facies and B Facies. The latter varies in thickness (in the 460, 430, 440, 470 and 500 geozones) and is not developed in the 370 geozone and 500 geozone east of Great Noligwa Mine; the C Facies is poorly developed in the 470, 500 and 370 geozones, and overlies the Mizpah quartzite and Mizpah Reef in the 370 geozone. The A Facies is generally consistent in occurrence in all the geozones, with the Bottom, Middle and Top Sub-facies well-developed.

*3.5.1. 460, 430 and 440 Geozones*

The 460, 430 and 440 geozones occur at Kopanang Mine (Figure 3.7), and have common properties such as intense chloritic alteration within the reef. The 460 geozone occurs in the west of Kopanang Mine (Figures 3.5 and 3.7). It is characterised by the presence of A, B and C Facies. The C Facies is the dominant economic horizon and is relatively thin (~10 cm) and usually rests on the immediate MB5 quartzite footwall. The 460 geozone has a thick carbon seam, but gold-barren (Figure 3.8). The B facies thins towards the east. The Grootdraai Facies conglomerate underlies the C Facies in the 460 and 430 geozones.

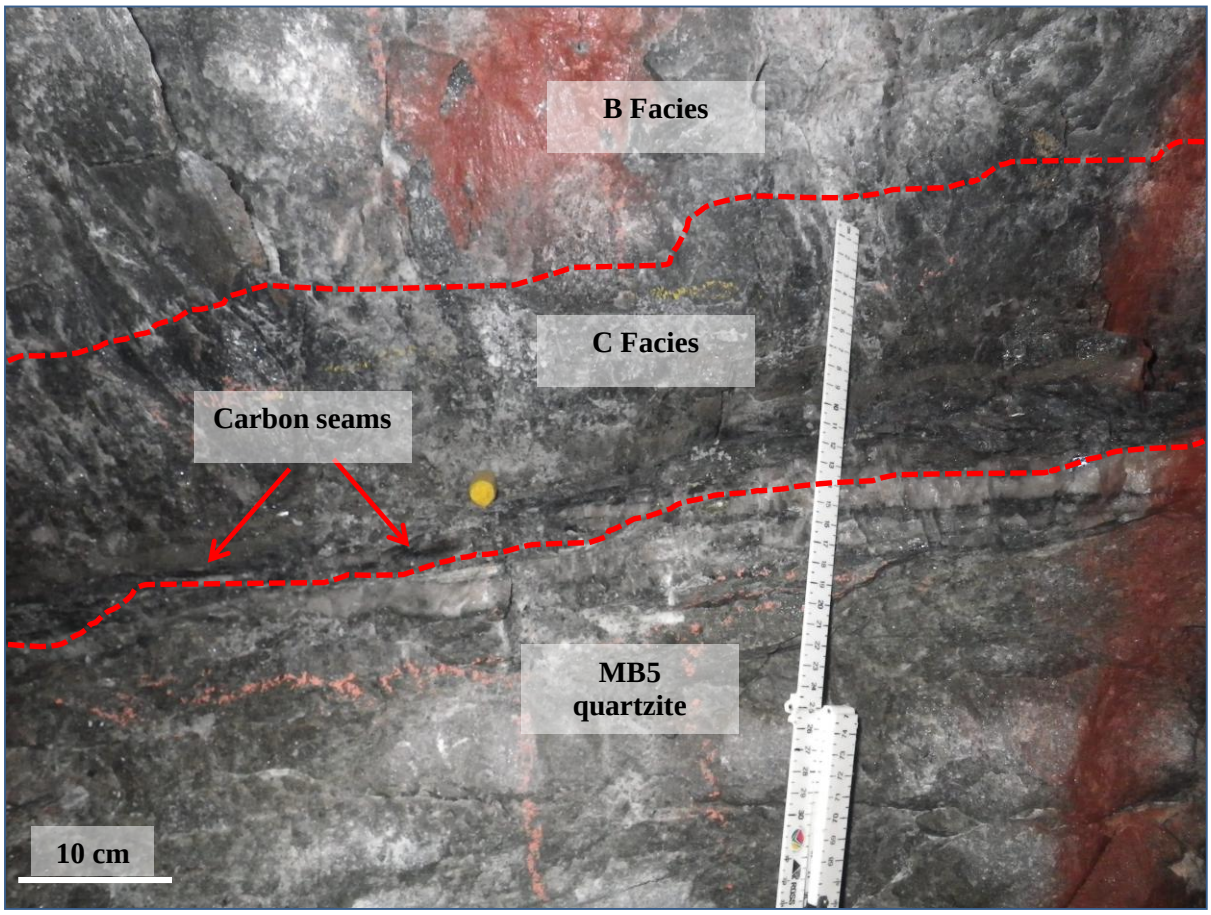



Figure 3.8: The Vaal Reef C Facies in the 460 geozone with thin carbonaceous matter at the bottom of the reef; the reef is overlain by the B Facies and rests on the MB5 quartzite footwall. The Grootdraai conglomerate was not observed.

The 430 geozone occurs in the west, surrounded by the 460 geozone (Figures 3.5 and 3.7). Mineralisation of the 430 geozone resembles that of the 460 geozone, and has a carbon seam at the base of the C Facies (Figure 3.9); however, the B Facies quartzite in this geozone varies in thickness, increasing from east with a maximum thickness in the west.

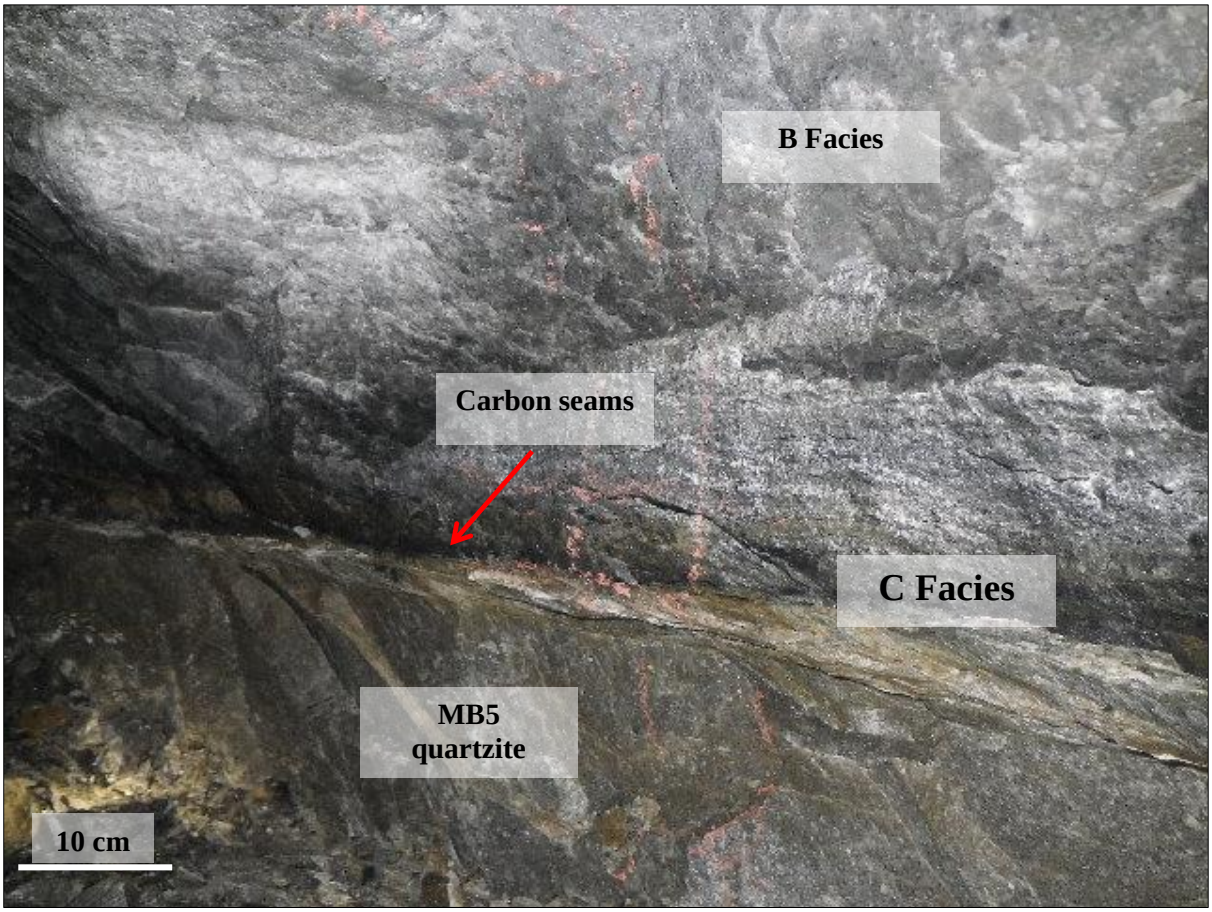



Figure 3.9: The Vaal Reef C Facies in the 430 geozone overlain by the B Facies with a carbon seam at the bottom of the reef; the Vaal reef rests on the MB5 quartzite footwall. No Grootdraai conglomerate was observed.

The 440 geozone occurs towards the east of Kopanang Mine (Figures 3.5 and 3.7). The Vaal Reef in the 440 geozone is characterised by an oligomictic conglomerate (Figure 3.10), and flyspeck carbon is present and carries good mineralisation. The geozone is underlain by the Witkop Facies conglomerate, and has a poorly-developed A Bottom Facies.

*3.5.2. 470 Geozone*

The 470 geozone is a low grade geozone that occurs near the boundary separating Kopanang from Great Noligwa Mines; the geozone differs from the 460, 430, and 440 geozones in that it has an irregularly developed C Facies and the geozone rests directly on the MB5 unit quartzite so that the Witkop and Grootdraai Facies conglomerates are missing (Figure 3.5). The A Facies is economically important in this part and the A Facies becomes more conglomeratic to the east (Great Noligwa Mine) and quartzitic to the west.

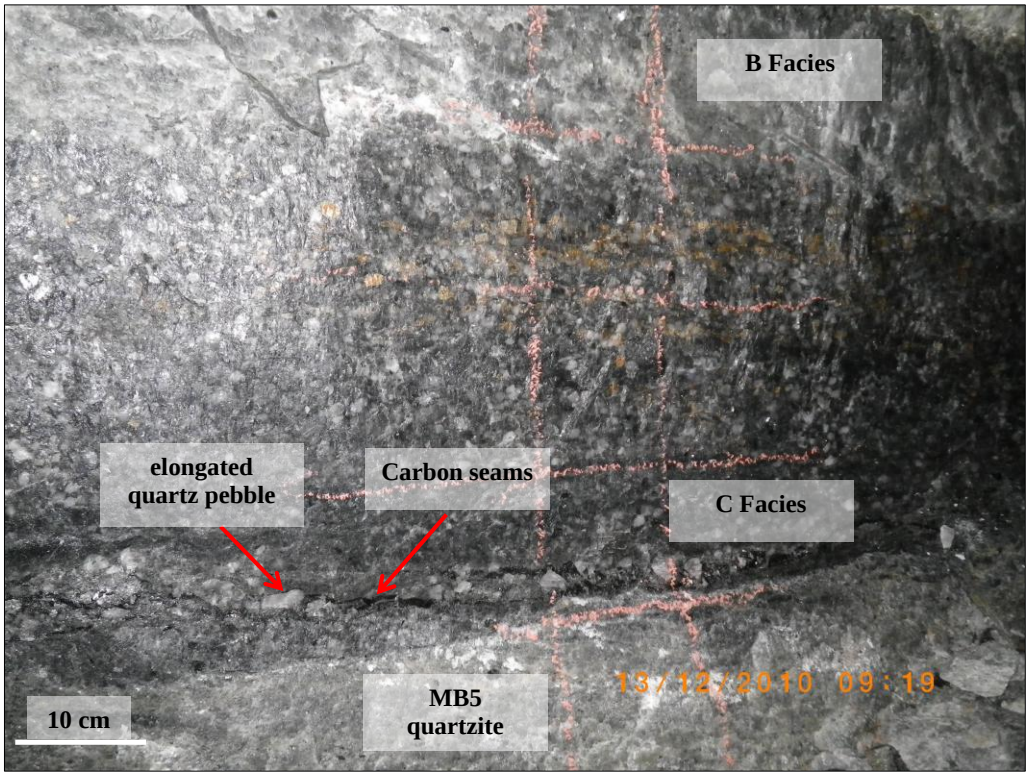



Figure 3.10: The Vaal Reef C Facies at the 440 geozone; the carbon seam is developed at the base of the reef and the quartz clasts are sub-angular and elongated. The reef rests directly on the MB5 quartzite footwall and no Witkop conglomerate was observed.

The clasts in the A Facies are usually small and well rounded compared with the C Facies and composed of milky quartz pebbles, and the pyrite can be both clustered and disseminated in the matrix or partially replace the pebbles. The conglomerate has a clean overlying matrix-supported orthoquartzite.

*3.5.3. 500 Geozone*

The A Facies is the economic gold-bearing facies in the 500 geozone, but some parts of the C and B Facies are still evident (Figure 3.5). The A Facies is generally over 1.2 m in thickness and is present in both the western and eastern parts of Great Noligwa (Figure 3.11) as well as in the Moab Khotsong Mine extension. The A Facies is characterised by a more matrix-supported polymictic conglomerate and light grey matrix with more than 60% internal quartzite. The Almond Reef, which occurs in the upper part of the A Bottom Sub-facies, is not developed in the 500 geozone and carbon development is sporadic. The pyrite is clustered and changes to disseminated at the 500-370 geozone boundary. The overlying Zandpan Quartzite cuts down through some of the upper parts of the 500 geozone reworking the reef.




Figure 3.11: The Vaal Reef A Facies at the 500 geozone at Moab Khotsong Mine. The A Facies is over 1.2 m in thickness showing internal quartzite within the reef.

### *3.5.4. 370 Geozone*

The 370 geozone is represented by the well-developed and well-mineralised A Facies. In some areas where the C facies is present (Figure 3.5), mineralisation is enhanced. The 370 geozone is a thin and high grade zone at Great Noligwa and Moab Khotsong, and is regarded to be thinner than the rest of the geozones with the high grade zone less than 80 cm thick (Figure 3.12). The Almond Reef, which occurs in the A Bottom Sub-facies, is the primary mineralised horizon, and is characterised by an extensive, well-mineralised carbon seam.




Figure 3.12: The Vaal Reef A Facies in the 370 geozone at Moab Khotsong Mine showing the Almond Reef; the reef overlies the Mizpah quartzite.

In contrast to the 500 geozone, the 370 geozone is underlain by Mizpah Reef and quartzite (Figure 3.5). Chloritic alteration is dominant throughout the rest of the 370 geozone, characterised by a dark colour. The pyrite is disseminated in the matrix as compared to the 500 geozone. Eastwards of Great Noligwa Mine, the Zandpan Quartzite has reworked the A Facies. Table 3.1 presents a summary of the Vaal Reef geozones and their properties across the three mines.

Table 3.1: A summary of the six main geozones in the Kopanang, Great Noligwa (GN) and Moab Khotsong (MK) Mines.

| **Geozone** | **Economic facies** | **Underlying FW to C and A Facies** | **Thickness** | **Location (Mines)** | **Composition** |
|---|---|---|---|---|---|
| **430** | C | Grootdraai | ~15 cm | Kopanang | Carbon flyspecks, carries good gold and uranium mineralisation. Chloritic alteration. Angular elongated clasts. |
| **440** | C | Witkop | ~10 cm | Kopanang | |
| **460** | C | Grootdraai | ~10 cm | Kopanang | Carbon seam thick, but barren. Minor chloritic alteration. Angular elongated clasts. |

| Continuation of Table 3.1 | | | | | |
|---|---|---|---|---|---|
| **470** | C | MB5 | ~10 cm | Kopanang and GN boundary | No carbon. Chloritic alteration. Well-rounded clasts (10 mm). |
| **500** | A | MB5 | ~120 cm | GN and MK | Carbon seam disturbed. |
| **370** | A | Mizpah package | ~80 cm | GN and MK | Carbon seam with good gold and uranium mineralisation. |

### 3.6. Petrology

The main aim of undertaking core logging was to study the occurrence, thickness and lithological characteristics of the Vaal Reef with its associated rock types i.e. footwall quartzite (MB5) and the rest of the overlying MB4 package, and, more importantly, to verify the geozone properties in the three mines identified through detailed core logging of underground drilled boreholes. Thirteen boreholes were provided by AngloGold Ashanti for this study and are shown in Figure 3.13.

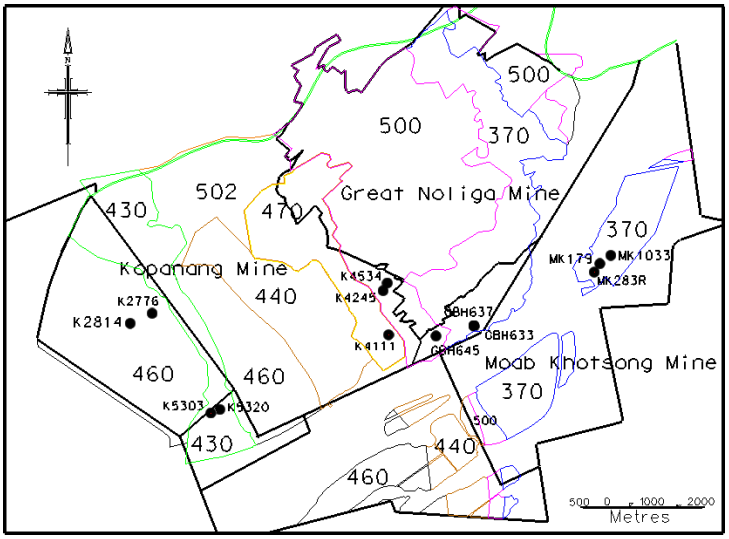



Figure 3.13: Layout of the localities of thirteen drilled boreholes are shown on the map, seven from Kopanang Mine, three from Great Noligwa Mine and three from Moab Khotsong Mine. The boreholes represent different geozones across the three mines (AngloGold Ashanti internal report, 2001).

The boreholes from Kopanang Mine are K2776, K2814, K4111, K4245, K4534, K5303 and K5320; boreholes from Great Noligwa Mine are GBH633, GBH637 and GBH645; boreholes

from Moab Khotsong Mine are MK1033, MK179 and MK283R. These boreholes were collected from regions of different geozones; only 10 boreholes were investigated from the three mines as the remaining three were not complete. Furthermore, underground samples from the three mines (Kopanang, Great Noligwa and Moab Khotsong) at different panels representing both the C and the A Facies were provided.

### *3.6.1. Borehole Logging*

#### *3.6.1.1. Boreholes K2776, K2814 and K5303 in the 460 Geozone*

The 460 geozone is represented by boreholes K2776 (Figure 3.14), K2814 (Figure 3.15) and K5303 (Figure 3.16). The boreholes are constituted by the C Facies, which is the main carrier of good uranium and gold grades, the B and A Facies and the Zandpan quartzite. The Vaal Reef rests directly over the MB5 footwall and is overlain by the MB3 hangingwall; the complete sets of these boreholes are illustrated in Figure 3.17.

In borehole K2776, Figures 3.14 and 3.17, the C Facies is 15 cm thick and the rest of the MB4 unit is about 3 to 4 m in thickness, and overlain by the MB3 quartzite. Scintillometer readings (0.5 μSv/hr) where recorded in the flyspeck carbon, indicating high radioactive levels.

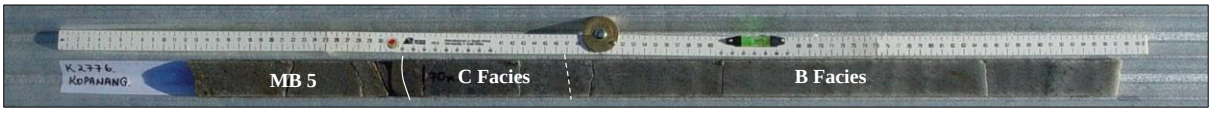



Figure 3.14: Photograph of borehole K2776 intersecting the MB5 quartzite and Vaal Reef C and B Facies.

In borehole 2814, the C Facies is only 10 cm thick (Figures 3.15 and 3.17) and constitutes a 3mm carbonaceous seam with higher scintillometer scans reaching 3.5 μSv/hr suggesting high uranium-bearing minerals abundances. The C Facies is overlain by the B and A Facies and Zandpan quartzite making up the MB4 unit.

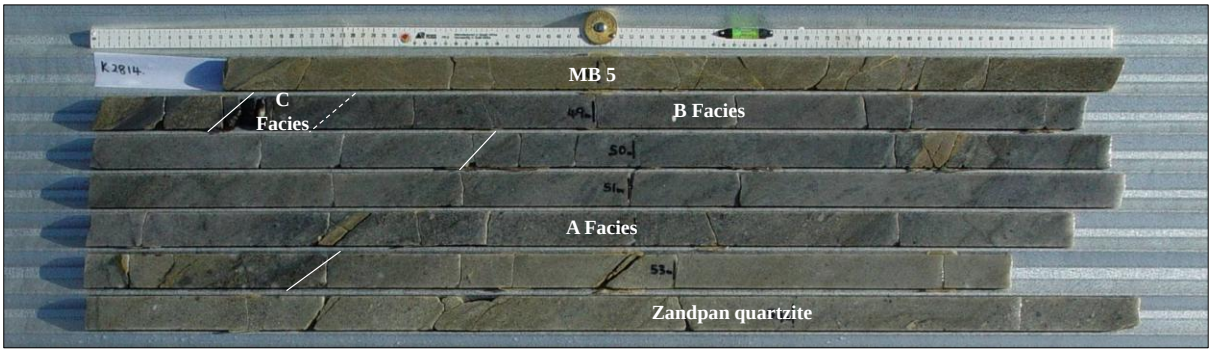



Figure 3.15: Photograph of borehole K2814 intersecting the MB5 quartzite, C Facies, B Facies, A Facies and the Zandpan quartzite.

Borehole K5303 intersected the footwall quartzite from the MB5 unit; MB4 unit consisting of the Vaal Reef (C, B and A Facies), Zandpan and MB3 quartzite (Figures 3.16 and 3.17). The C Facies is 18 cm thick and is composed of an oligomictic conglomerate, with 10-15 mm sub-rounded quartz pebbles; the facies is in gradational contact with the B Facies. Radioactivity levels of 2.60 μSv/hr associated with pyrite were recorded in the C Facies also indicating high levels of uranium content in the facies, there was no carbonaceous matter observed in this borehole.

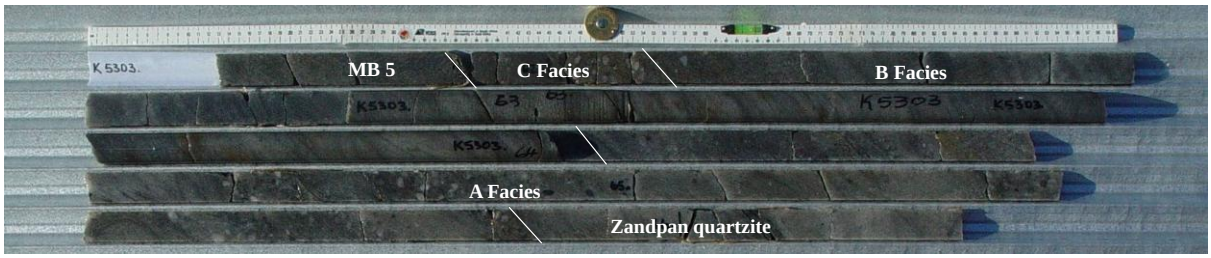



Figure 3.16: Photograph of Borehole K5303 intersecting the MB5, C Facies, B Facies, A Facies and the Zandpan quartzite.

*3.6.1.2. Boreholes K4111 and K4245 in the 500 geozone*

The 500 geozone is represented by boreholes K4111 and K4245 (Figure 3.18). The boreholes contain the A Facies, which is the main carrier of good uranium and gold grades. In the two boreholes, the C Facies is absent and the MB4 unit is only comprised of the A Facies and the Zandpan package. The MB5 quartzites form the immediate footwall, and the MB3 quartzites form the hangingwall.

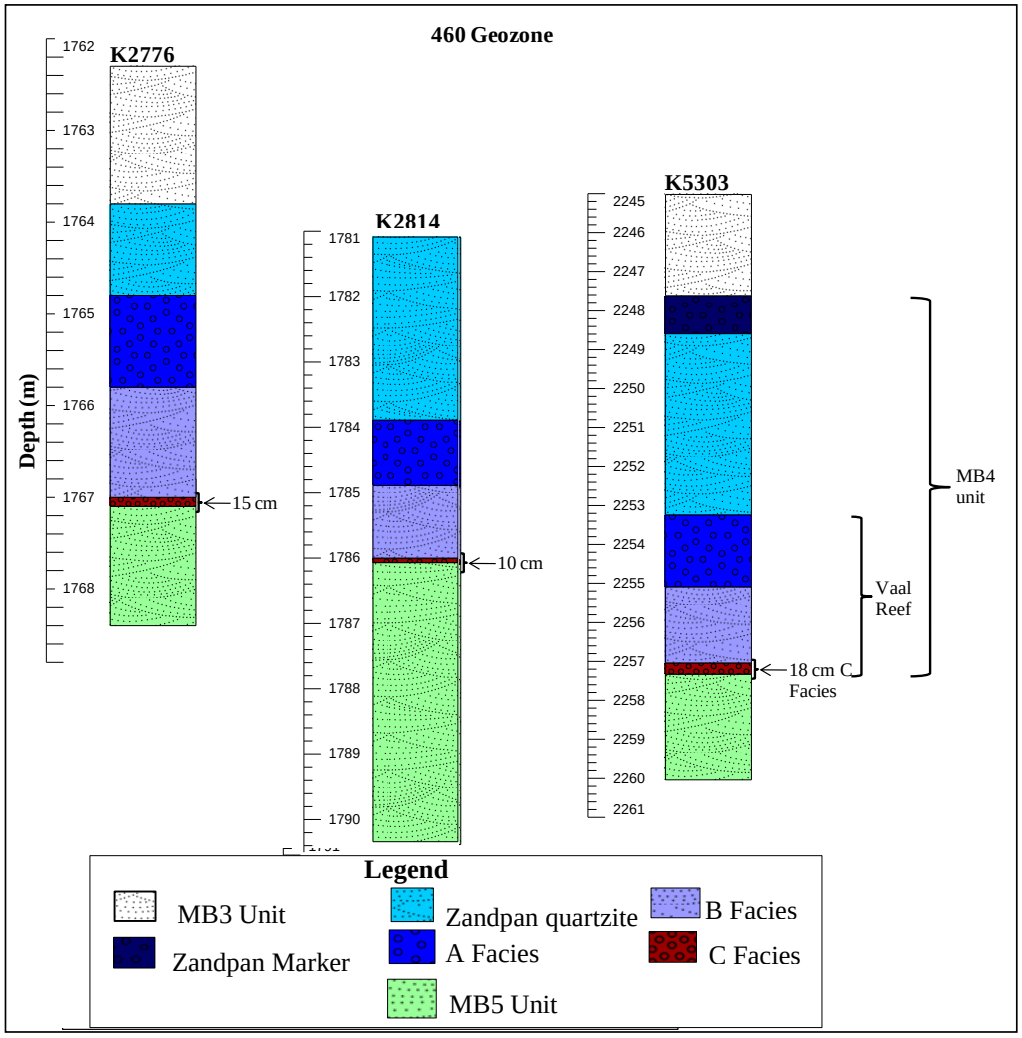



Figure 3.17: Boreholes K2776, K2814 and K5303 intersecting the Vaal Reef. The C Facies is the primary economic facies hosting high grades of gold and uranium; the thickness of the C Facies is 15 cm in borehole K2776, 10 cm in borehole K2814 and 18 cm in borehole K5303.

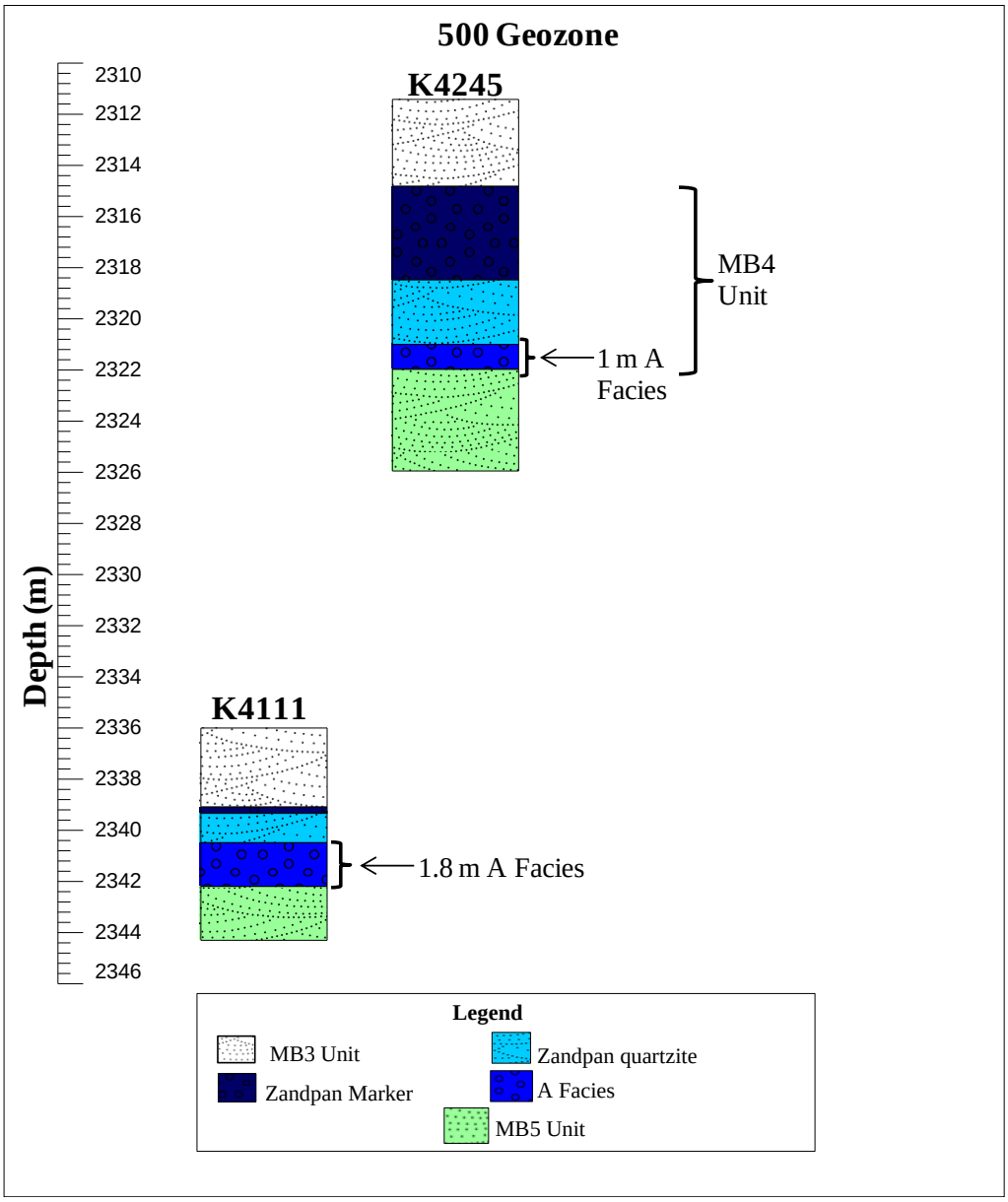



Figure 3.18: Stratigraphic section of the Vaal Reef in boreholes K4111 and K4245 from Kopanang Mine representing the 500 geozone.

In borehole K4111 (Figures 3.18 and 3.19), the A Facies is 1.8 m thick and is split into three sub-facies, Bottom, Middle and Top Sub-facies. The Bottom Sub-facies comprises a grey conglomerate composed of quartz clasts and pyrite with angular pebbles. This Sub-facies is fairly well-mineralised, although with a very low scintillometer reading (<0.5 μSv/hr). The middle Subfacies is mainly composed of a light grey quartzite with some pyrite stringers. The overlying Top Sub-facies is darker with more rounded pebbles and minor chert as compared to the Bottom Sub-facies.

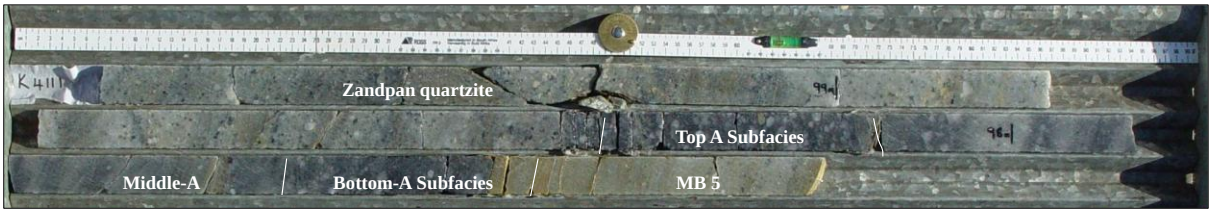



Figure 3.19: Photograph of borehole K4111 intersecting the MB5 quartzite, Bottom A Subfacies, Middle A Subfacies, Top A Subfacies and the Zandpan quartzite.

In borehole K4245, the A Facies is 1m in thickness and also has the three A Subfacies (Figure 3.18); similar to K4111, the Bottom Sub-facies is well mineralised.

*3.6.1.3. Borehole GBH 645 in the 500 geozone*

Borehole GBH 645 comes from the 500 geozone which marks the boundary between Kopanang Mine and Great Noligwa Mine (Figure 3.13), and is represented by the C and A Facies, no B Facies was observed in core (Figures 3.20 and 3.21).

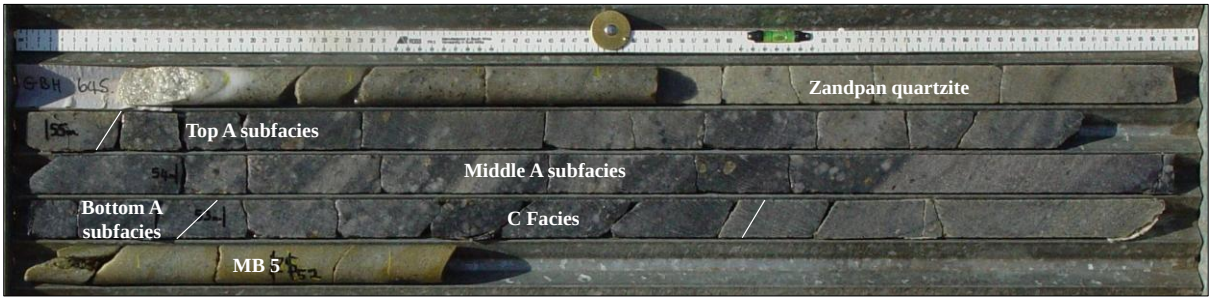



Figure 3.20: Photograph of borehole GBH 645 intersecting the MB5 quartzite, C Facies, Bottom A Subfacies, Middle A Subfacies, Top A Subfacies and the Zandpan quartzite.

The C Facies is 40 cm thick, and composed of quartz and minor chert pebbles. There are occurrences of authigenic pyrite crystals in the matrix. Carbon flyspecks were associated with high radioactivity (1.5 µSv/hr) at the base of the C Facies. The Vaal Reef C Facies is in contact with the Vaal A Reef Bottom Sub-facies. The entire A Facies in this borehole is 1.8 m in thickness (Figure 3.21). The Middle A Sub-facies is composed of rounded quartz and angular chert pebbles, euhedral pyrite crystals larger than 10 mm replacing the quartz and chert pebbles at some places. The Middle A Sub-facies is in contact with the Top A Sub-facies, and the conglomerate is well rounded with disseminated pyrite.

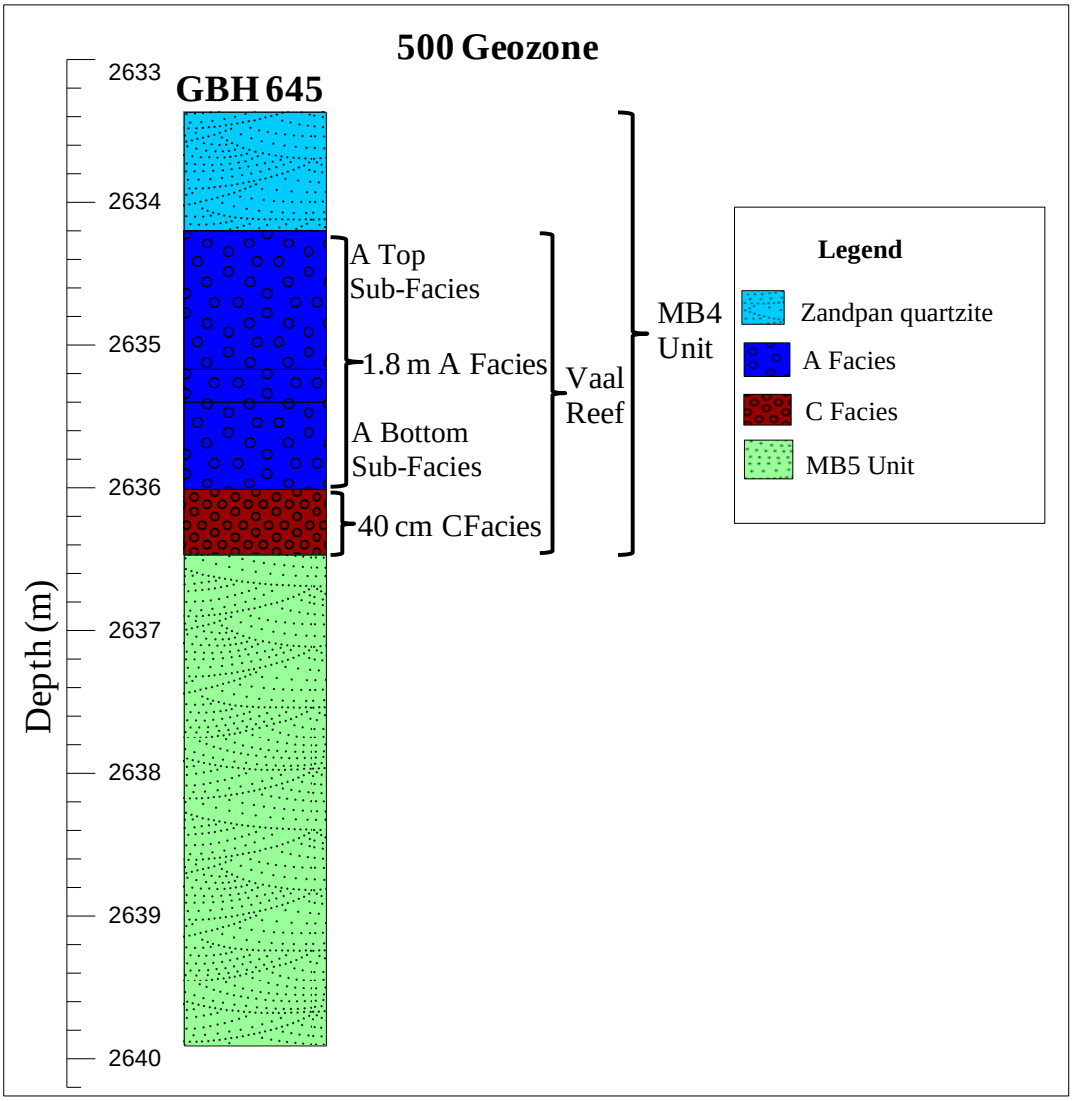



Figure 3.21: Stratigraphic section of the Vaal Reef in borehole GBH 645 from Great Noligwa Mine showing the development of C and A Facies overlying each other. The borehole represents the 500 geozone.

*3.6.1.4. Boreholes GBH 633 and GBH 637in the 370 geozone*

Boreholes GBH 633 and GBH 637 (Figure 3.22) represent the 370 geozone. These boreholes are characterised by the footwall quartzite of the MB5 unit which is overlain by the MB4 unit's Mizpah Reef, Vaal Reef A Facies and the Zandpan quartzite.

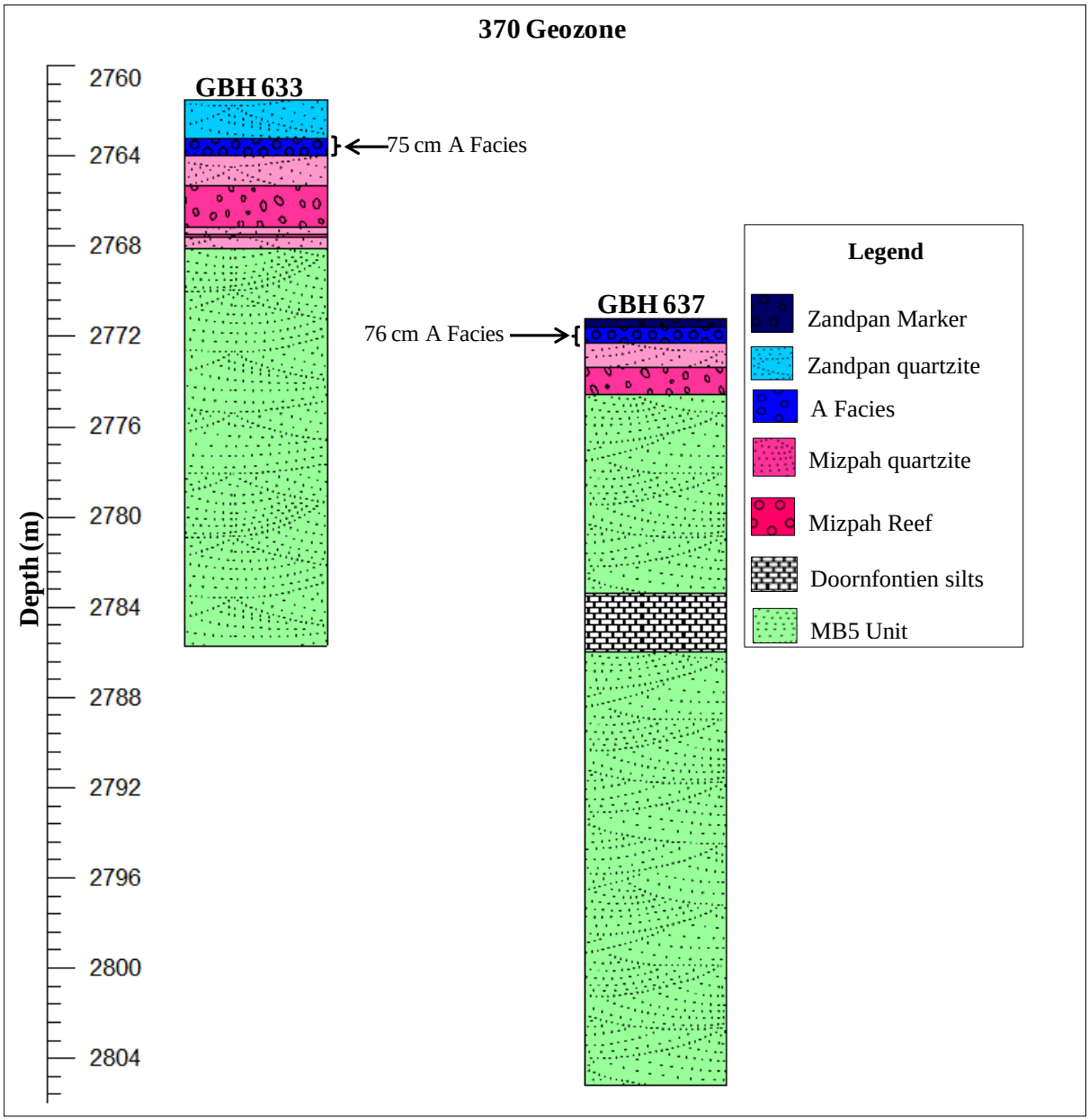



Figure 3.22: Stratigraphic sections of the Vaal Reef from boreholes GBH 633 and GBH 637 representing geozone 370. The 75 cm thick Vaal Reef in both cores is represented by the A Facies which rests on the Mizpah Reef and Mizpah quartzite, the Zandpan Marker is developed in both the boreholes.

In borehole GBH 633, the A Facies is the main economic horizon and is subdivided into the Top and Bottom Sub-facies with a total thickness of 75 cm. The A Facies rests on the interlayered Mizpah quartzite and Mizpah Reef, and is overlain by the Zandpan quartzite (Figure 3.22). The Vaal Reef A Bottom Sub-facies is the economic horizon and displays a 35 cm thick oligomictic conglomerate with sub-rounded quartz clast sizes between 10 and 15 mm. The A Bottom Sub-facies also has a high pyrite content throughout with radioactivity levels of 0.60 µSv/hr.

The Mizpah Reef and Mizpah quartzite package are 3.5 m in thickness. The Mizpah Reef is greyish-brown in colour, with a conglomerate framework of sub-rounded quartz and angular chert clasts, with an average grain size of 10 to 15 mm. The brown-yellow colour is due to high pyrite content in the matrix. The Mizpah Reef has three cycles of fining upward sequences into the Mizpah quartzite in borehole GBH 633, resulting in an interbedding of the Mizpah Reef and the Mizpah quartzite. The Mizpah quartzite is darker in colour than the Mizpah Reef and also has occurrences of pyrite stringers.

In borehole GBH637, the Mizpah quartzite is in contact with the A Facies. The A Facies is 76 cm thick, with a grey oligomictic conglomerate, made of 10 mm sized pebbles and the matrix dominated by pyrite. Radioactivity levels around 0.50 μSv/hr in the A Facies were recorded.

#### *3.6.1.5. Boreholes Mk179 and Mk283R in the 370 geozone*

Similar to the GBH633 and GBH637 boreholes from Great Noligwa Mine, boreholes MK179 and MK283R represent the 370 geozone at Moab Khotsong Mine (Figure 3.23). The Vaal Reef A Facies in these boreholes rests directly on the Mizpah Reef, with no development of the Mizpah quartzite. In borehole MK179, the A Facies is 1.5 m in thickness and shows rounded quartz clasts with disseminated pyrite. The MK179 A Facies is overlain by the Zandpan quartite and Zandpan Marker.

Borehole MK283R intersects the MB5, Mizpah Reef, Vaal Reef A Facies, Zandpan quartzite and Zandpan Marker. The A Facies is 71 cm in thickness and is composed of mainly rounded quartz clasts and minor chert.

## 3.7. Sampling

The importance of core sampling was to select representative samples from all the boreholes across Great Noligwa, Kopanang and Moab Khotsong Mines for further petrographic, XRD, SEM and tomography studies. Samples were selected from all the geozones (460, 430, 440, 500 and 370) and more importantly these were samples containing carbon seams or specks, high radioactivity, alteration zones, well pyritised and typical Vaal Reef conglomerates. Samples that were selected were believed to contain uranium minerals and therefore, mineral abundances, textural association, grain size, shape, morphology, alteration, paragenetic sequences and chemistry of these uranium minerals and surrounding minerals were studied.

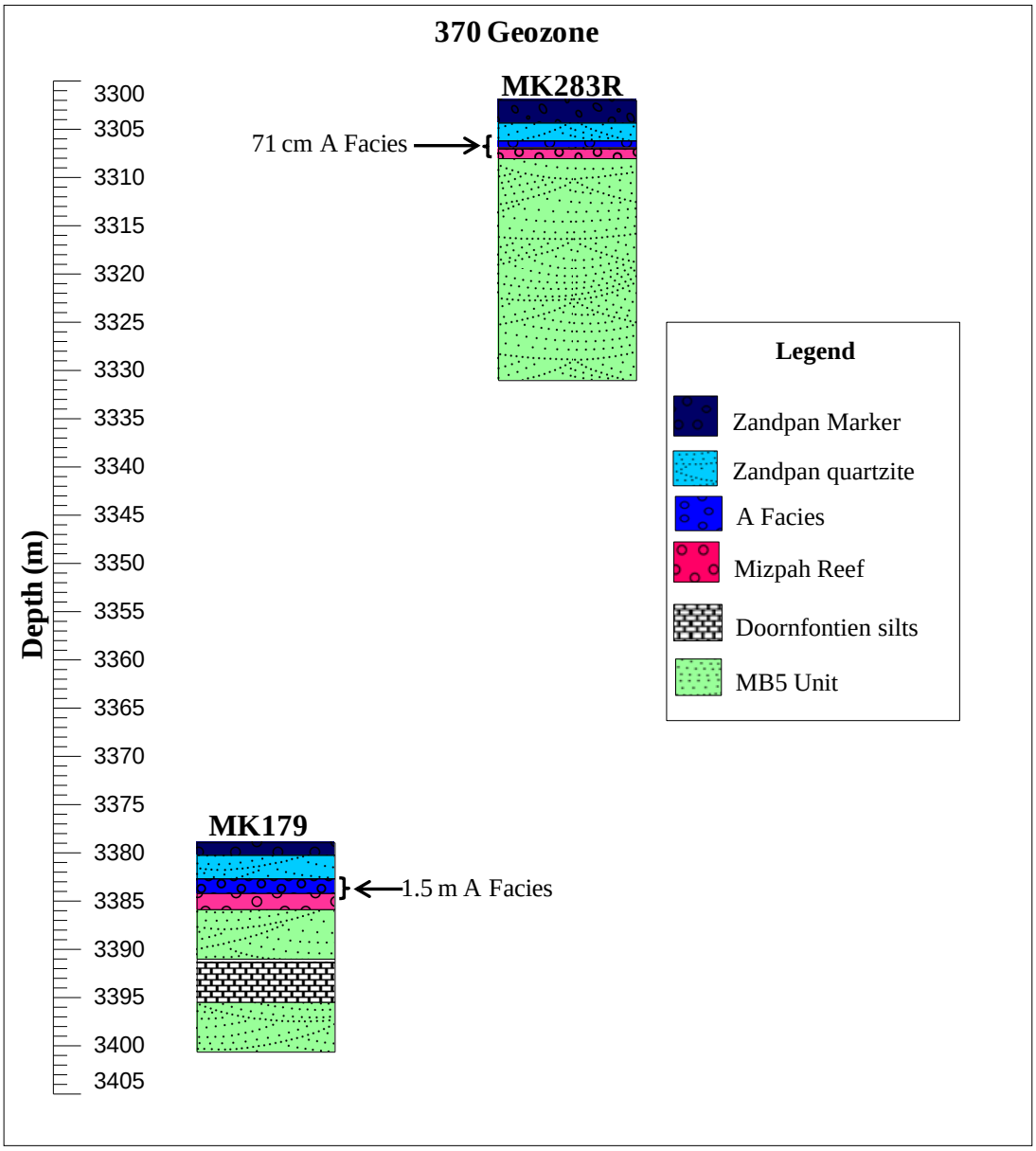



Figure 3.23: Stratigraphic sections of the Vaal Reef from boreholes MK179 and MK283R representing geozone 370. The Vaal Reef A Facies is 1.5 m and 75 cm thick, respectively, and rests on the Mizpah Reef, and is overlain by the Zandpan Marker.

Thirty nine (38) samples were collected from all the boreholes and underground workings representing the Vaal Reef C and A Facies, samples from the Mizpah Reef and footwall quartzite MB5 unit were also collected (Appendices 11 to 15 ). The underground samples were located in exposures of reef facies types, that, based on visual observation (routine underground geological mapping) and assay data (conducted for grade control purposes), are considered as typical (i.e. representative) of the Vaal Reef.

### 3.8. Summary

The Vaal Reef occurs across the Kopanang, Great Noligwa and Moab Khotsong Mines and is represented by three Facies (A, B and C; AngloGold Ashanti internal report, 2001). The C Facies is the main uranium and gold carrier at Kopanang Mine, and the A Facies the main gold and uranium carrier at Great Noligwa and Moab Khotsong Mines. However, the C Facies is sporadically developed at Great Noligwa and Moab Khotsong Mines and carries little mineralisation as compared with the C Facies at Kopanang Mine.

Core logging results showed that:

- Three boreholes (K2776, K2814 and K5303) represent the 460 geozone at Kopanang Mine. The C Facies is about 10 to 18 cm in thickness, and the carbonaceous matter occurs in seams and flyspeck enhancing uranium mineralisation, this was verified by the high radioactivity anomalies from the scintillometer readings.
- The C Facies also occurs in the 500 geozone in borehole GBH 645, the facies is 40 cm thick and has carbon flyspecks associated with high uranium mineralisation. Two boreholes at Kopanang Mine (K4111 and K4245) represent the 500 geozone as well; however, the C Facies in these boreholes (K4111 and K4245) is absent. The A Facies is the main uranium carrier and has thicknesses between 1 to 1.8 m.
- Four boreholes, two from Great Noligwa (GBH 633 and 637) and another two from Moab Khotsong (MK179 and 283R) represent the 370 geozone. The Mizpah Reef and Mizpah quartzite are common in these boreholes and underlies the A Facies. The A Facies ranges from 70 cm to 1.5 m in thickness and is well mineralised in uranium.

Samples were selected from the geozones in the boreholes and underground workings for petrographic and geochemical investigations. The criteria for selecting samples from all the underground drilled borehole cores were based on radioactivity as measured by the scintillometer, presence of carbon seam or fly specks, alteration, sulphide presence within the conglomerate matrix in both the C and A Facies. These properties are further explained in Chapter 4.

# CHAPTER FOUR

# MINERALOGICAL INVESTIGATION OF THE VAAL REEF

## 4.1. Introduction

The main aims of this chapter are to evaluate whether there are any mineralogical similarities between the economic C and A Facies of the Vaal Reef; document mineral assemblages; types of uranium-bearing minerals and their association with other minerals and developing a paragenetic sequence for the Vaal Reef samples. A total of 38 samples (Appendices 11 to 15) were selected from drilled cores, underground mine workings and footwall (from drilled cores) of the Vaal Reef C and A Facies, and were studied using different mineralogical techniques. The majority of the samples were collected for petrography investigations from the C Facies of the 440 and 460 geozones of the Kopanang Mine and the A Facies of the 370 geozone of the Moab Khotsong Mine.

## 4.2. Methods

Mineralogical techniques employed were: X-ray diffraction (XRD), optical microscopy and scanning electron microscopy (SEM). The XRD technique was used to identify minerals present in the Vaal Reef samples. Optical microscopy and SEM methods were also applied for mineral identification, but mainly to study sizes, shapes and textural relationships of minerals.

Thin and polished section samples were prepared using standard preparation techniques in the Mineralogy Division at Mintek, based in Randburg, South Africa.

### *4.2.1. X-Ray Diffraction (XRD)*

X-ray diffraction is a powerful tool for characterising structures of crystalline materials. In particular, the powder diffraction method allows semi-quantification of different minerals present in a rock sample (Mintek internal Report, 2012). X-rays are generated by accelerating electrons onto an anode. The X-ray beam is filtered to maximise monochromatic radiation, and is directed towards the sample through a slit configuration. The interaction of the incident rays with the sample produces constructive interference (and a diffracted ray) when conditions satisfy Bragg's Law ($n\lambda=2d \sin \theta$); the diffracted rays are then analysed to determine which minerals are present (Mintek Internal Report, 2012).

To obtain the bulk mineralogical composition the samples were pulverised and analysed in a Siemens D500 X-ray diffractometer. The diffractometer was operated under the following conditions: Cu Kα radiation, accerated voltage of 40 kV, current of 30 mA, a 2θ scan range of 5-80$^{o}$, a step size of 0.02$^{o}$ 2θ, and counting time of 3 s per step. Only crystalline phases that are present in amounts sufficient to diffract (usually 3-4 mass %), are detectable.

*4.2.2. Optical Microscopy*

Vaal Reef samples were studied in hand specimen on a macro-scale and thin section and polished section petrography was undertaken on a micro-scale using an Olympus BX 51 petrographic microscope. Grain sizes, shapes, textures and associations of minerals were obtained using this technique.

*4.2.3. Scanning Electron Microscopy (SEM) Study*

Samples were examined on a Zeiss EVO® MA15 SEM equipped with a Bruker Energy Dispersive X-ray Spectrometer (EDS) and Quantax software (Mintek internal Report, 2012). The SEM was operated at an acceleration voltage of 20 kV, working distance of 12 mm and stage tilt angle of 0.0$^{o}$. The SEM analysis is based on a bright phase search which locates U-bearing minerals based on their higher backscattered electron intensity compared with gangue minerals. Backscattered electron (BSE) images of polished surfaces provide atomic number contrast, which enables the recognition of different mineral phases. This fact therefore, makes BSE well suited for petrographic studies. Each located and identified U-bearing mineral was recorded, its size measured and the associated minerals recorded. Backscattered electron images were taken to illustrate the mineral textures, U-bearing mineral occurrences and associations.

*4.2.4. Electron Microprobe Analysis (EMPA) Study*

Electron microprobe analysis was performed with a Cameca SX50 microprobe equipped with Wavelength Dispersive Spectrometers (WDS). The system was calibrated with oxide reference standards. Analysis was done at an accelerating voltage of 20kV with a beam current of 30nA. The beam diameter was 10 µm. A counting time of 20 seconds on peak and 5 seconds on each of two background positions was employed. Matrix correction was automatically done by the PAP procedure in the SAMX Analysis software. Detection limits (in weight %) are as follows: $SiO_2$ 0.03, CaO 0.03, $TiO_2$ 0.03, FeO 0.05, PbO 0.18, $ThO_2$ 0.10, $UO_2$ 0.16.

### 4.3. Mineral Abundance

Semi-quantitative XRD was firstly applied to the samples to investigate common minerals present in both the C and A Facies of the Vaal Reef samples; however, minerals constituting less than 3 to 4% in the samples were not detected due to the limitation of the technique. Identified minerals and their relative abundances are presented in Table 4.1.

Table 4.1: List of minerals recorded by XRD from samples under investigation. Dominant (>75%), Major (25-50%), Intermediate (15-25%), Minor (5-15%) and Trace (0-5%).

| **Compound Name** | **Formula** | **Mineral Abundance** |
|---|---|---|
| Quartz | $SiO_2$ | Major |
| Pyrite | $FeS_2$ | Minor |
| Galena | PbS | Trace |
| Uraninite | $UO_2$ | Trace |
| Chlorite | $Mg_5Al_2Si_3O_{10}(OH)_8$ | Minor |
| Pyrophyllite | $Al(Si_2O_5)(OH)$ | Trace-minor |
| Muscovite | $KAl_2(AlSi_3O_{10})(OH)_2$ | Trace |
| Chloritoid | $FeAl_2OSiO_4(OH)_2$ | Trace-minor |

Samples analysed for XRD are representative of the C and A Facies. Thirty grams of material was analysed from every sample.

X-Ray diffraction (XRD) results show highest quartz content in the A Facies samples of Moab Khotsong's 370 geozone (Figure 4.1a). Pyrite content is the highest in the C Facies of the 440 and 460 geozones (Figure 4.1b), the C Facies is also dominated by a high frequency of trace minerals, mainly sheet silicates. Footwall samples from the Mizpah Reef (MK179 and GBH633) show a higher pyrite content than the MB5 quartzites (GBH637 and K2814) which are dominated by a high quartz content (Figure 4.1c). Further details of all these samples are presented in Appendix 16 to Appendix 27.

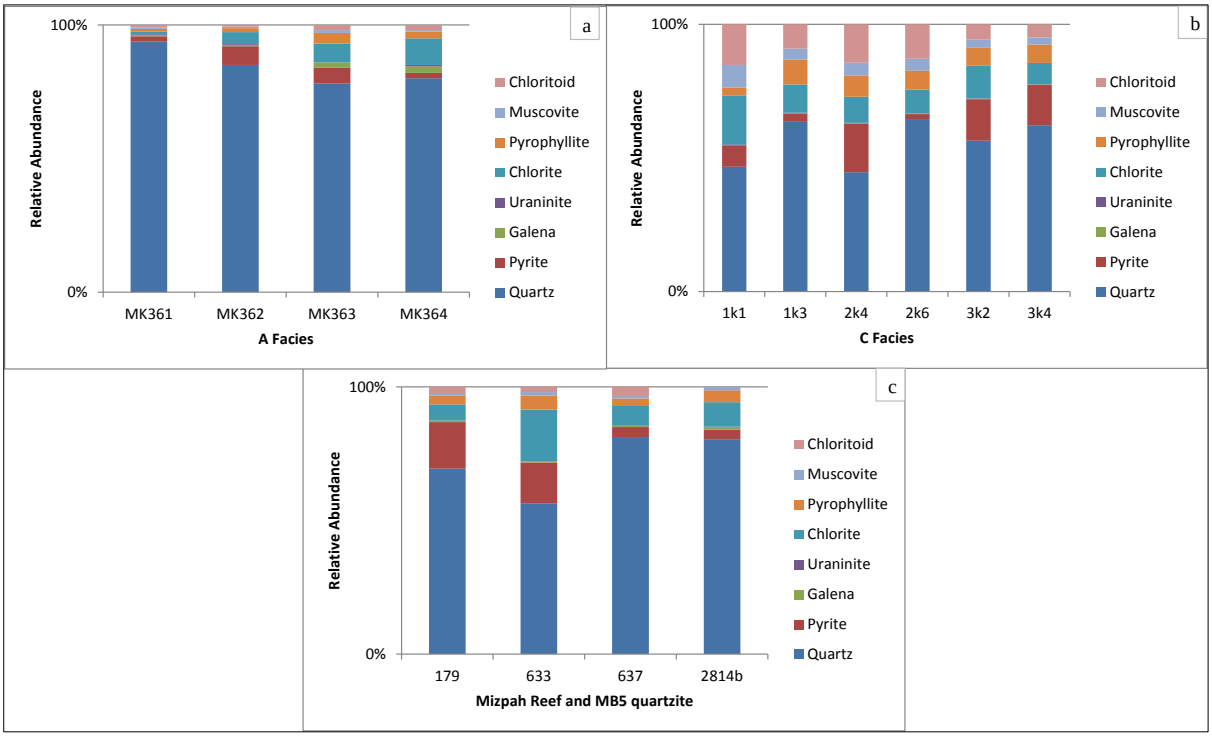



Figure 4.1: Relative mineral abundance in samples representing the Vaal Reef samples. (a) The A Facies at Moab Khotsong 370 geozone is dominated by quartz. (b) The C Facies at Kopanang 440 (1k1 and 1k3) and 460 (2k4, 2k6, 3k2 and 3k4) geozones are pyrite-rich and exhibit high sheet silicate abundances. (c) The Mizpah Reef samples are pyrite-rich and the MB5 footwall samples are quartz-rich.

## 4.4. Petrography

### *4.4.1. C Facies*

Nineteen samples of the uranium and gold-bearing carbonaceous C Facies were studied, 18 from Kopanang Mine and one from Great Noligwa Mine. The majority of the samples in this section were collected from Kopanang Mine underground workings. Details of the relative mineral abundances are presented in Table 4.1. Hand specimens show a clast-supported quartz pebble conglomerate comprised of clasts of white and smoky vein quartz (85 to 95%) and subangular chert pebbles 10 to 20 mm in size in a light-grey quartzose matrix. Sulphide minerals, pyrite in particular, comprise the second dominant matrix minerals following quartz (Figure 4.2).




Figure 4.2: Hand specimens from the Vaal Reef C Facies at Kopanang Mine collected from the 440 geozone with high pyrite content with sub-round quartz pebbles.

In thin section, sub-rounded to sub-angular quartz clasts dominate. These commonly show sutured margins (Figure 4.3a) composite grains (Figure 4.3b) and strain extinction with chloritoid replacing quartz (Figure 4.3b). The matrix comprises a range of minerals in order of abundance quartz, opaque minerals and sheet silicates as shown in Table 4.1. Chlorite, chloritoid and pyrophyllite are the common sheet silicate minerals replacing quartz in Figures 4.3a and c; however, these minerals also replace zircon (Figure 4.3c) and opaque minerals (Figures 4.3b and d). Chlorite ranges in size from 100 microns to >1 mm and is commonly associated with secondary quartz, chloritoid (<250 microns to 1.5 mm) and laths of pyrophyllite (50 microns to 1 mm) and may partially replace matrix pyrite while chlorite typically replaces both chloritoid and pyrophyllite. Minor muscovite is present with pyrophyllite and chloritoid.

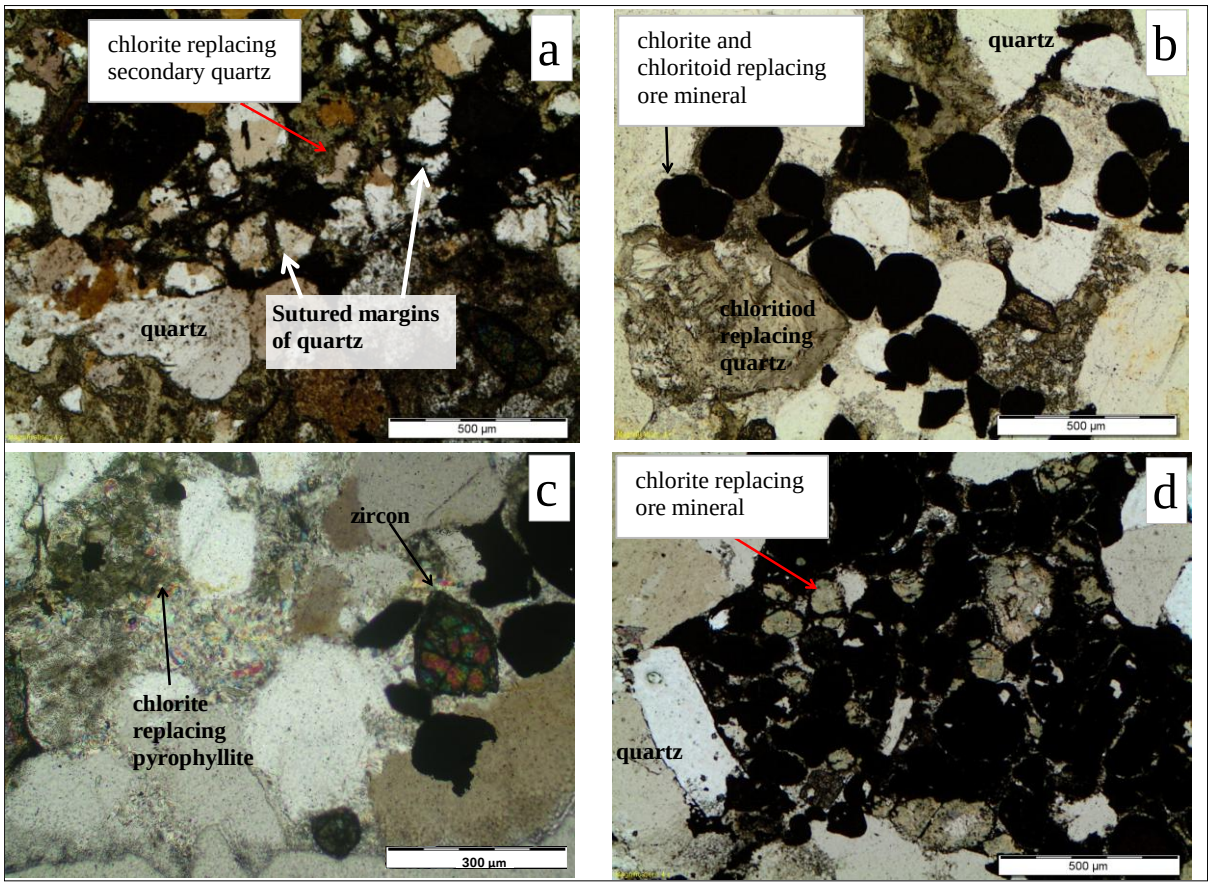



Figure 4.3: Photomicrographs of silicate and phyllosilicate minerals of the Vaal Reef C Facies under transmitted light microscopy. (a) Chlorite matrix surrounding quartz pebbles, with chloritoid replacing quartz, and sutured quartz (plane polarised light, ppl). (b) Chlorite replacing opaque minerals and secondary quartz (crossed polarised light, xpl). (c) Chlorite replaces pyrophyllite in the matrix (xpl), zircon grain occurs in association with opaque minerals. (d) Chloritoid replacing opaque minerals, sample dominated by opaque minerals (xpl).

The sulphide minerals comprise 10 to 30% occurring in the Vaal Reef C Facies at Kopanang Mine, with pyrite being predominant (Table 4.2). Pyrite occurs in two forms. The dominant allogenic sub-rounded pyrite ranges in size from 80 µm to 500 µm and varies in abundance from 5 to 30%, and authigenic pyrite is euhedral (Figure 4.4a) with size ranges from 90 to 250 microns in size. Allogenic pyrite generally occurs in clusters with detrital sub-rounded chromite, rutile and zircon (Figures 4.4b and c) and commonly exhibits cracked rims and fractures; gold occurs in association with these detrital minerals also showing round shapes (Figure 4.4d). Other authigenic sulphide minerals such as chalcopyrite (Figure 4.4.a) and gersdorffite occur in the samples (Figure 4.4d).

Table 4.2: A list of sulphide minerals occurring in the Vaal Reef C Facies at Kopanang Mine, their ideal chemical formulae and abundances in the samples.

| Name of sulphide mineral | Chemical formula | Abundance |
|---|---|---|
| pyrite | $FeS_2$ | Predominant (55-60%) |
| chalcopyrite | $CuFeS_2$ | Accessory (<5%) |
| pyrrhotite | $Fe_{1-x}S$ | Minor (<10%) |
| arsenopyrite | FeAsS | Trace (<5%) |
| gersdorffite | NiAsS | Accessory (<1%) |
| galena | PbS | Minor (<10%) |
| sphalerite | ZnS | Accessory (<1%) |

Uraninite is the dominant uranium-bearing phase although forming less than 10% of the mineral assemblage, followed by trace amounts of brannerite and uraniferous leucoxene. Uraninite occurs in two occurrences, in the matrix and in the carbonaceous matter. In the matrix it occurs as oval to sub-rounded grains with sizes up to 150 microns (Figure 4.4) associated with detrital zircon, chromite and allogenic sub-rounded pyrite grains (Figure 4.4b). Galena blebs occur on uraninite margins or infilling cracks in the mineral. Brannerite and uraniferous leucoxene occur as replacements along uraninite rims and edges (Figures 4.4e and f).

Carbonaceous matter occurs in two forms: seams and nodules or fly specks. The seams and fly specks generally break down uraninite grains along weak boundaries to form micro-veins or nodules (Figure 4.5a). The seams show a fibrous or columnar habit perpendicular to internal bedding planes (Figures 4.5b, c and d); sometimes the seams themselves result from a stacking of carbon nodules. Within the seams uraninite is common as highly fragmented grains (Figure 4.5e) sometimes replaced by the carbonaceous matter (Figure 4.5f). Other minerals such as pyrite, arsenopyrite, pyrrhotite, gold and chalcopyrite (Figures 4.5d, e and f) are also found in the vicinity of carbon columns.

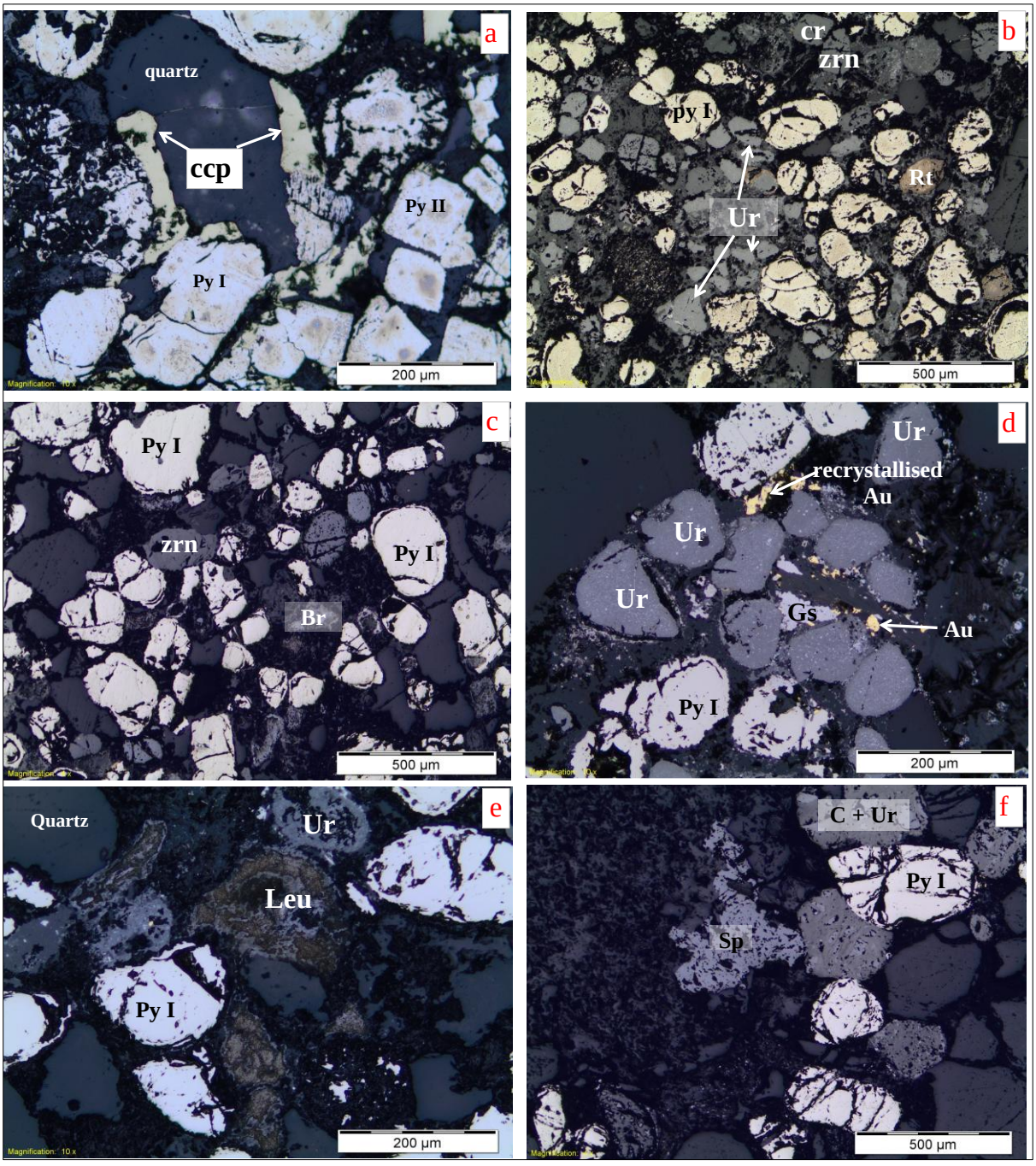



Figure 4.4: Reflected light photomicrographs of conglomerates from the Vaal Reef C Facies at Kopanang Mine. a) Allogenic (Py I) and authigenic (Py II) pyrite with chalcopyrite (Ccp) interstitial to quartz. b) Typical Vaal Reef occurrence of uraninite (Ur) with zircon (Zrn), chromite (Chr), rutile (Rt) and pyrite. c) Brannerite (Br) in the matrix with uraninite. d) Uraninite in association with pyrite, gersdorffite (Gs) and gold (Au). e) Uraniferous leucoxene (Leu) in matrix. f) Uraninite in association with brannerite.

Gold occurs both in the matrix and in carbonaceous matter. In the matrix (Figure 4.4d, e and f) gold is mainly associated with oval-shaped uraninite and allogenic pyrite grains. In Figure 4.4f minute grains of gold occur in the altered uraninite grains and surrounded by brannerite.

Subhedral to anhedral gold grains occur about 100 microns away from the carbonaceous matter, and also occur along the boundaries of the carbonaceous matter (Figure 4.5e), in association with chalcopyrite (Figure 4.5e) arsenopyrite and allogenic pyrite (Figure 4.5f).

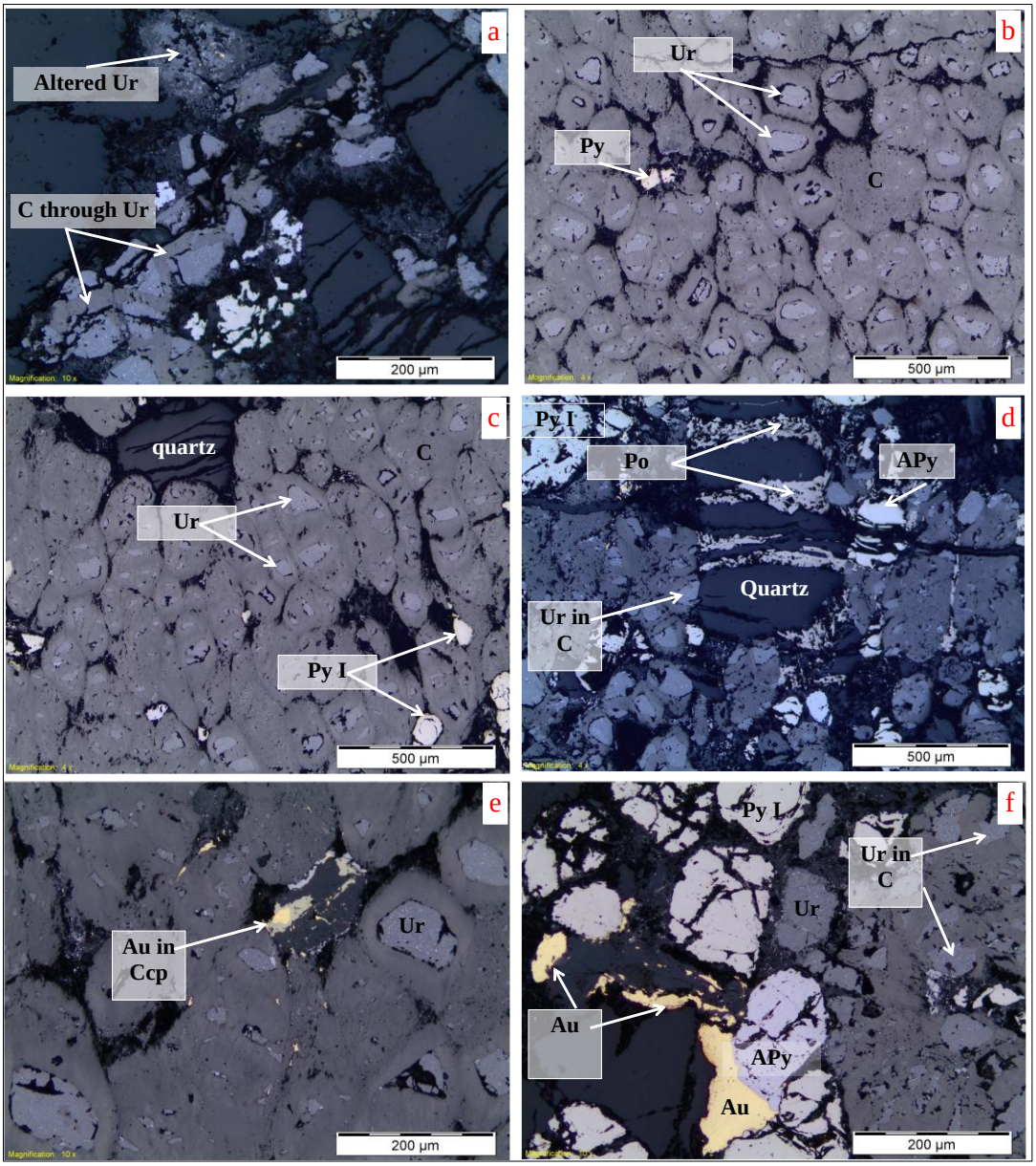



Figure 4.5: Reflected light photomicrographs of carbonaceous matter in the Vaal Reef C Facies at Kopanang Mine. a) Fragmented uraninite (Ur) grains cross-cut by carbonaceous matter. b) Uraninite enclosed in carbonaceous (C) seam. c) Uraninite in carbonaceous matter with grains fragmented. d) Authigenic pyrrhotite (Po) infilling quartz cracks; carbonaceous matter in close association with uraninite and arsenopyrite (Apy). e) Authigenic gold (Au) in chalcopyrite (Ccp) in a fractured quartz grain, surrounded by carbonaceous matter enclosing uraninite grains. f) Gold in matrix associated with arsenopyrite (APy), there are two populations of uraninites, in the matrix and also surrounded by the carbonaceous matter.

Backscattered electron images from the SEM shows that the majority of the uraninite grains in the matrix are sub-rounded in shape, associated with detrital pyrite, rutile, gersdorffite,

chromite and zircon, showing signatures of a detrital origin (Figures 4.6a, b, c and d). Other detrital minerals such as zircon and pyrite (Figure 4.6) were identified occurring in association with the carbonaceous matter.

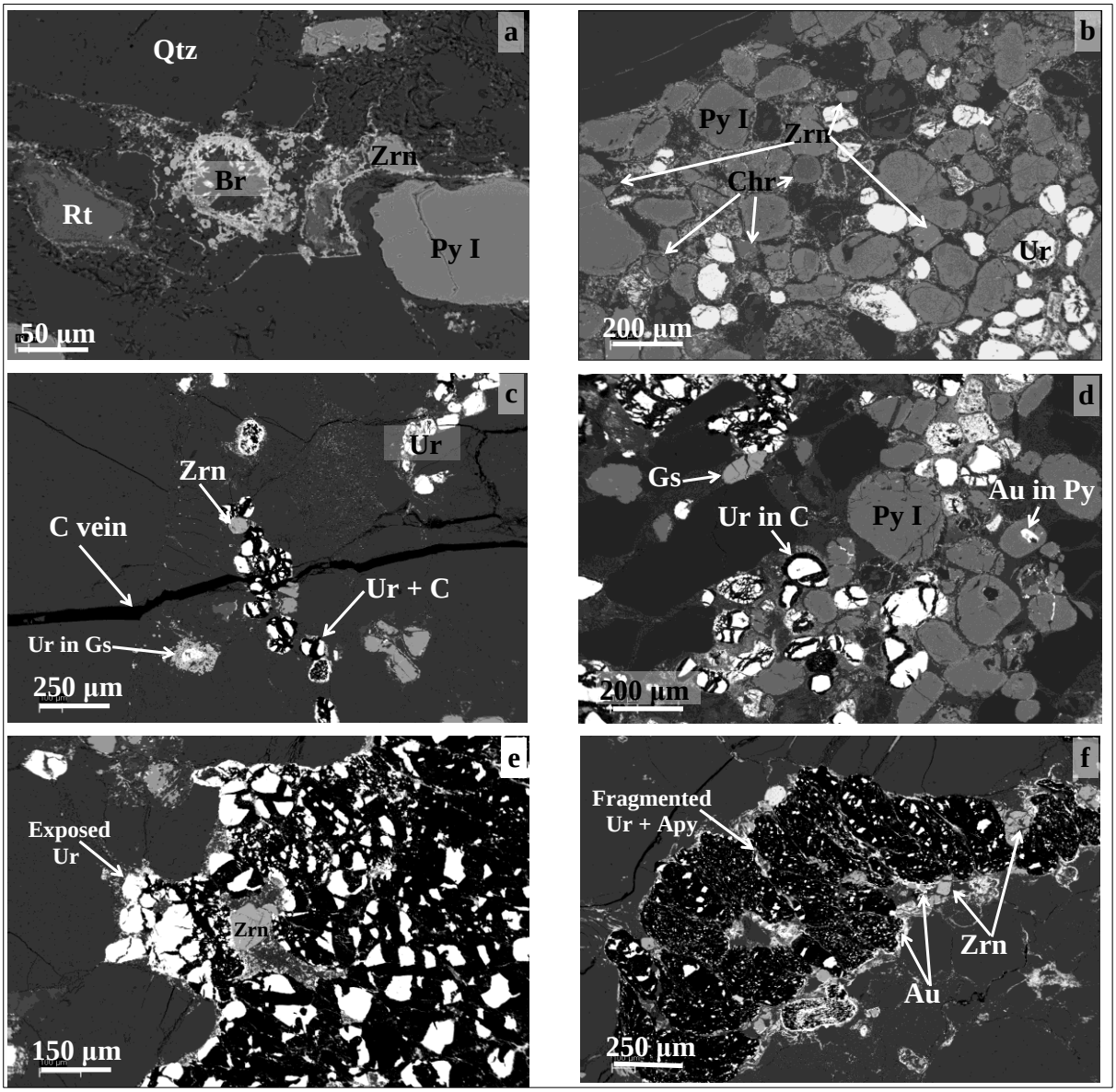



Figure 4.6: Backscattered electron (BSE) images from Kopanang Mine C Facies samples. a) Needle-shaped brannerite (Br) in the matrix with rutile (Rt), zircon (Zrn) and pyrite (PyI). b) Allogenic or detrital nature of pyrite, zircon, chromite (Chr) and uraninite (Ur). c) Uraninite grains fragmented by carbon (C) fly speck with a second generation of carbon vein devoid of uranium mineralisation; uraninite enclosed in gersdorffite (Gs). d) Occurrence of detrital uraninite with cracks infilled by carbon; rounded pyrite and gersdorffite occur with uraninite. e) Uraninite grains that were not covered by carbonaceous matter. f) Carbonaceous seam fragmenting uraninite and arsenopyrite (Apy), with zircon and gold on the edges of the seam.

*4.4.2. A Facies*

Twenty two samples of the gold-bearing Vaal Reef A Facies were studied, 14 from Moab Khotsong and 8 from Kopanang. The A Facies petrography in this section was mainly

undertaken on Moab Khotsong underground samples since they are more gold and uranium mineralised than the A Facies samples from Kopanang Mine.

Hand specimens show a matrix supported oligomictic sub-angular to sub-rounded (10 to 20 mm) quartz-pebble conglomerate (Figure 4.7). The pebbles are white and smoky quartz vein (45 to 50%) in a grey matrix (up to 30%). Pyrite (<5%) is disseminated throughout the matrix. Carbonaceous material (10 to 15%) occurs as seams 2 to 4 cm thick at the top of the facies.

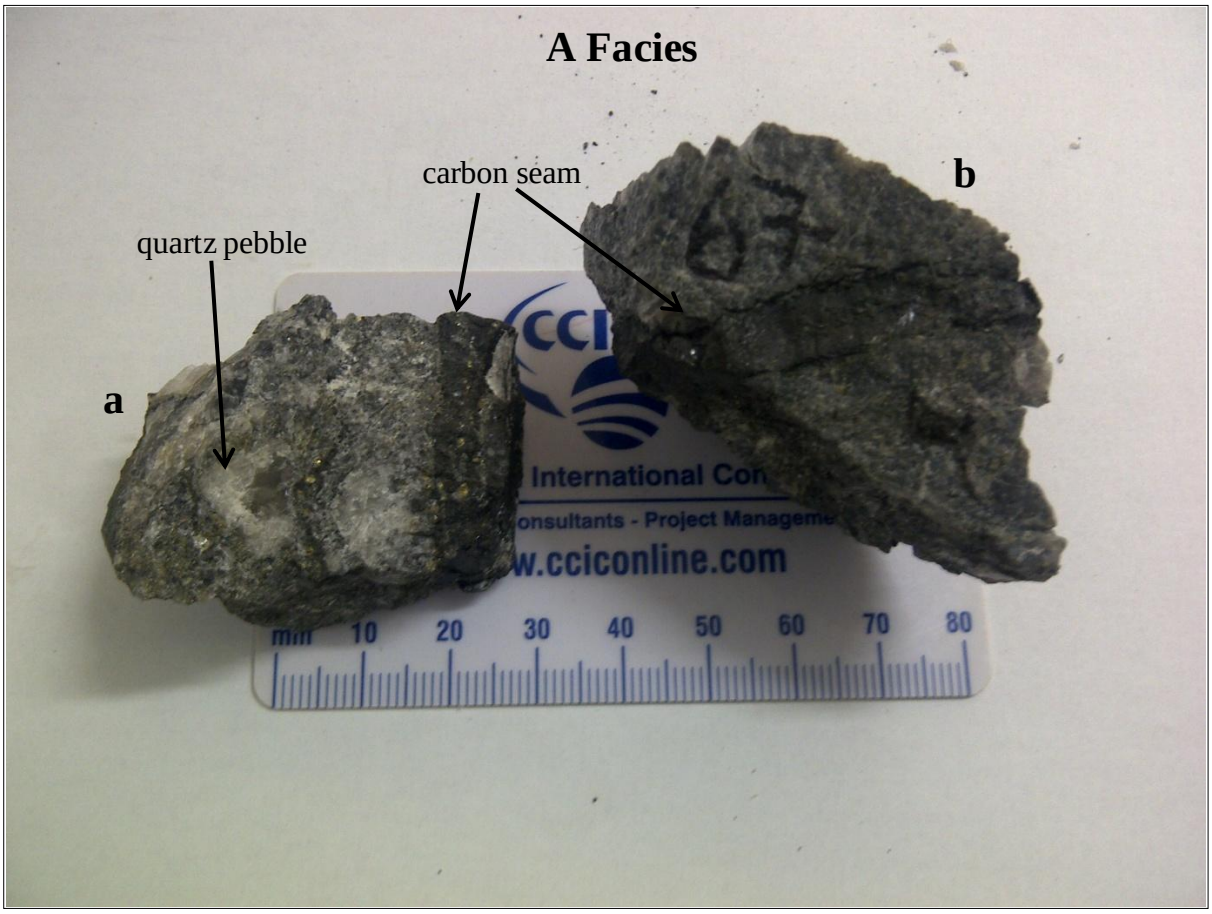



Figure 4.7: Hand specimens of the top of the Vaal Reef A Facies from Moab Khotsong Mine 370 geozone. (a) Sample with oligomictic quartz pebbles and the carbonaceous seams enclosing pyrite gains. (b) Sample showing the carbonaceous seam cutting across the matrix; the sample is composed of a grey matrix with a few occurrences of sulphide minerals.

In thin section, the A Facies has similar mineralogy to the C Facies (Figure 4.8). The samples are constituted primarily by quartz and sheet silicate minerals and less frequent occurrence of the opaque minerals. Chloritoid mainly replaces quartz grains along the quartz boundaries (Figures 4.8a and b); pyrophyllite and muscovite occur as well replacing the matrix quartz and some parts of the chloritoid (Figure 4.8b). Elongated pyrophyllite laths are well

developed in the A Facies matrices, some of the pyrophyllite is associated with opaque minerals (Figures 4.8 c and d); chlorite mainly replaces the opaque minerals (Figure 4.8d).

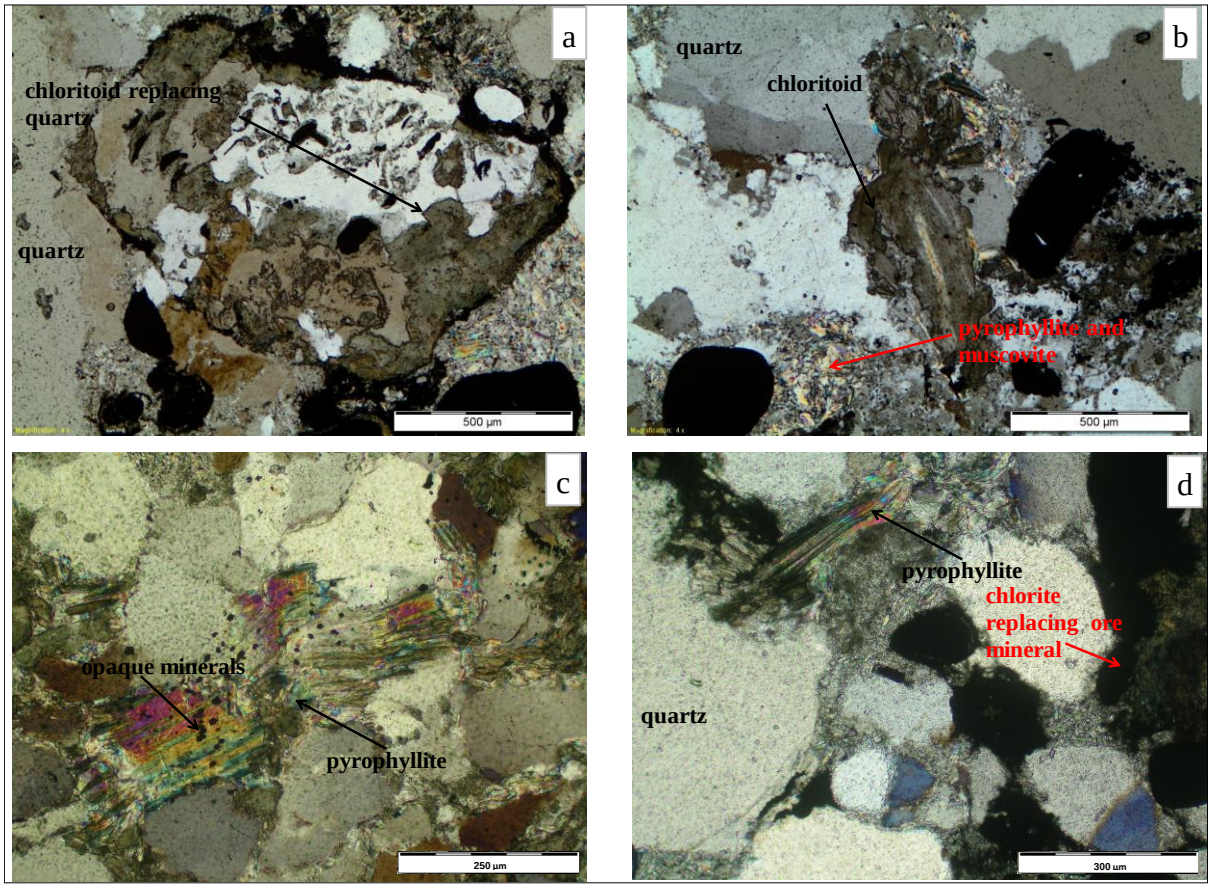



Figure 4.8: Photomicrographs of silicate and phyllosilicate minerals of the Vaal Reef C Facies, all images were taken under crossed polarised light (Xpl). (a) Chloritoid replacing a quartz grain. (b) Large grain of chloritoid replacing quartz and fine-grained pyrophyllite-muscovite in the matrix. (c) Pyrophyllite laths enclosing opaque minerals in the quartz matrix. (d) Pyrophyllite laths in the quartz matrix, and chlorite replacing opaque minerals.

In polished section, pyrite is the main (70%) sulphide mineral followed by galena (5%), pyrrhotite (5%), sphalerite (5%) and arsenopyrite (5%). Pyrite is allogenic sub-rounded and highly fractured with sizes from 100 microns up to 1 mm displayed. The pyrite cracks are mainly filled and replaced by galena, sphalerite, pyrrhotite veinlets and gold (Figures 4.9a, b and c). Arsenopyrite occurs in allogenic form and ranges in sizes from 80 to 120 microns.

Uraninite in the A Facies is mainly hosted within the carbonaceous matter.

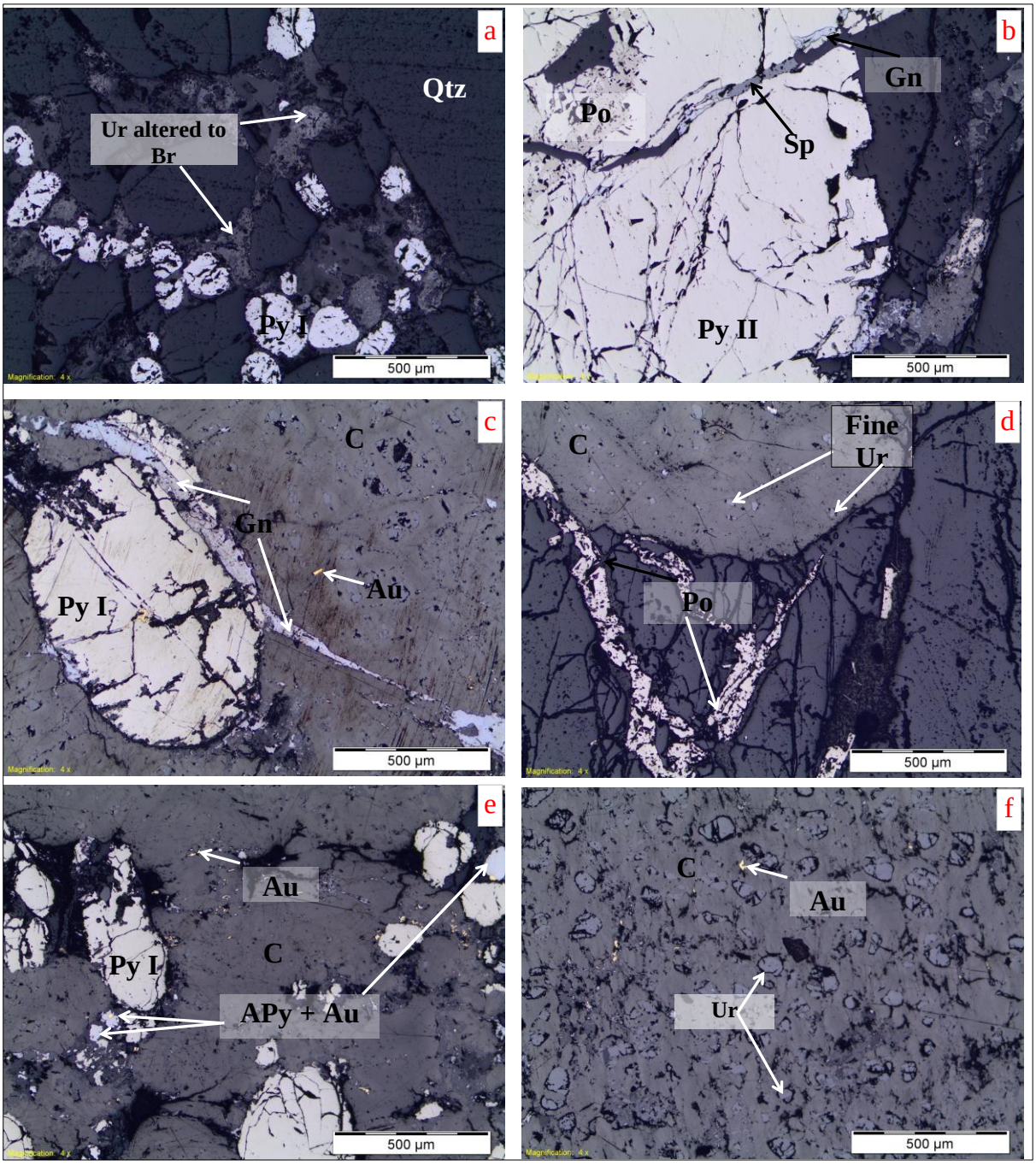



Figure 4.9: Reflected light photomicrographs of Moab Khotsong samples from the Vaal Reef A Facies. a) Fractured pyrite (Py II) grain replaced by pyrrhotite (Po), sphalerite (Sp) and galena (Gn). b) Fractured allogenic pyrite intersected by a galena vein extending into the surrounding carbonaceous matter; gold (Au) is enclosed in the carbonaceous matter. c) Pyrrhotite (po) veins filling in cracked quartz grains with carbonaceous matter enclosing fine uraninite grains. d) Uraninite altered to brannerite in the matrix in association with allogenic pyrite. e) Association of carbonaceous matter with pyrite and arsenopyrite (Apy) with gold in the carbonaceous matter. f) Preserved round uraninites and irregular-shaped gold grains in carbonaceous matter.

Uraninite occurring in the matrix is altered to brannerite (Figure 4.9d). The carbonaceous matter in the A Facies occurs as seams. Within the seams uraninite is highly fragmented (up

to 80-100 microns in size) and replaced by the carbonaceous matter (Figures 4.9b, c, e and f). The carbonaceous matter also encloses pyrite, galena and arsenopyrite (Figures 4.9b and e). Gold occurs in cracks of allogenic pyrite (Figure 4.9b), in association with arsenopyrite (Figure 4.9e) and within the carbonaceous matter (Figures 4.9c and f); the average sizes of the gold grains is around 40 to 50 microns and the majority of these gold grains seem to be recrystallised along and interstitial to the the columnar orientation of the carbonaceous matter.

Scanning electron microscopy (SEM) results of the A Facies samples of Moab Khotsong show intense fragmentation has taken place in all the minerals, including quartz, sulphides and uraninites (Figures 4.10a, b and c). The carbonaceous seams in the A Facies are extensively elongated and uraninite grains are finely broken down throughout the carbonaceous groundmass.

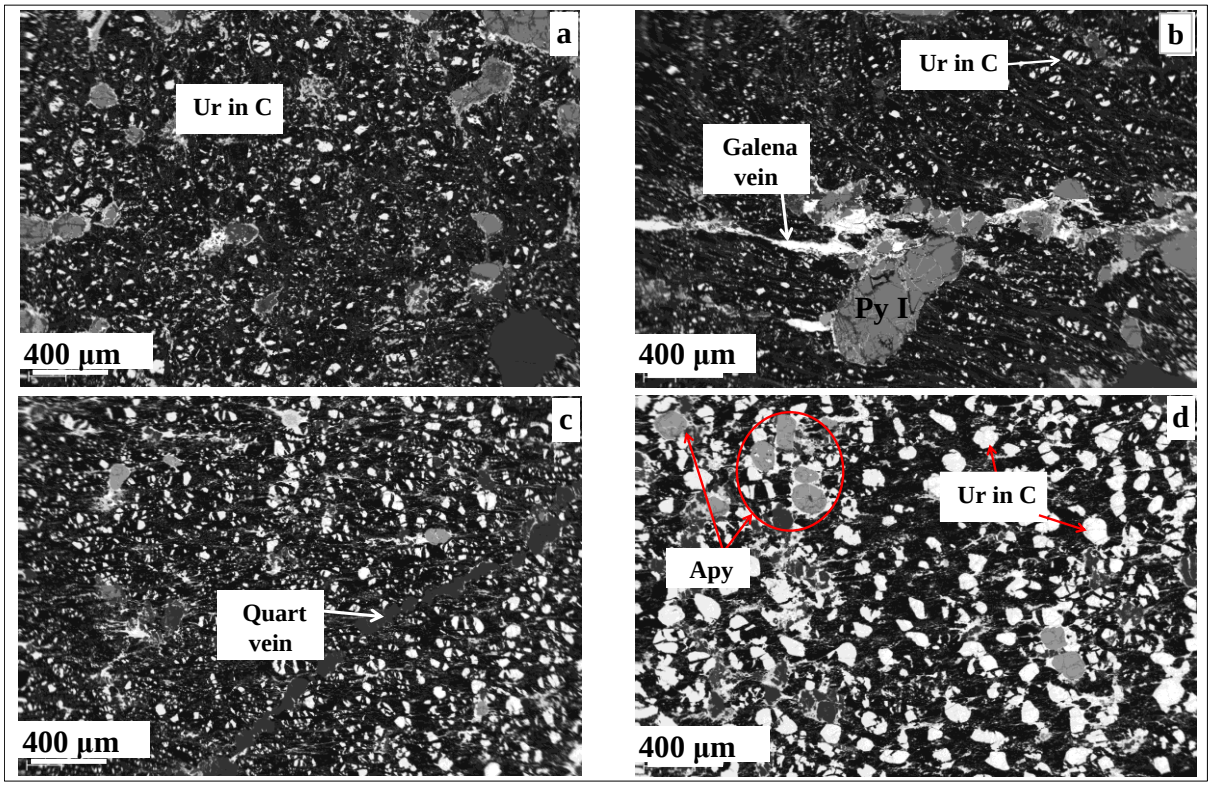



Figure 4.10: Backscattered electron images of Moab Khotsong samples. a) Fragmented uraninite grains and pyrite in a carbonaceous groundmass. b) Elongated carbonaceous seam with fragmented uraninite grains, galena vein cross-cuts the carbonaceous seam. c) Quartz vein cross-cuts a carbonaceous seam. d) Carbonaceous seam dominated by uraninite with minor arsenopyrite grains circled in the red ring.

Cross-cut veins of quartz and galena are common in carbonaceous seams and occur in a few samples (Figures 4.10b and c).

Similar to the C Facies samples, there is a presence of detrital sulphide minerals in the vicinity of the carbonaceous seams in the Moab Khotsong samples as well, arsenopyrite in particular (Figure 4.10d), is a common sulphide.

Infilling of cracks in the matrix detrital minerals and the carbonaceous matter by secondary mineral veinlets is common in most of the samples (Figure 4.11). Galena mainly fills cracked detrital pyrite and also extends into the carbonaceous matter (Figure 4.11a). Pyrrhotite is commonly observed as infillings in the matrix quartz and the quartz pebbles (Figures 4.11b and d).

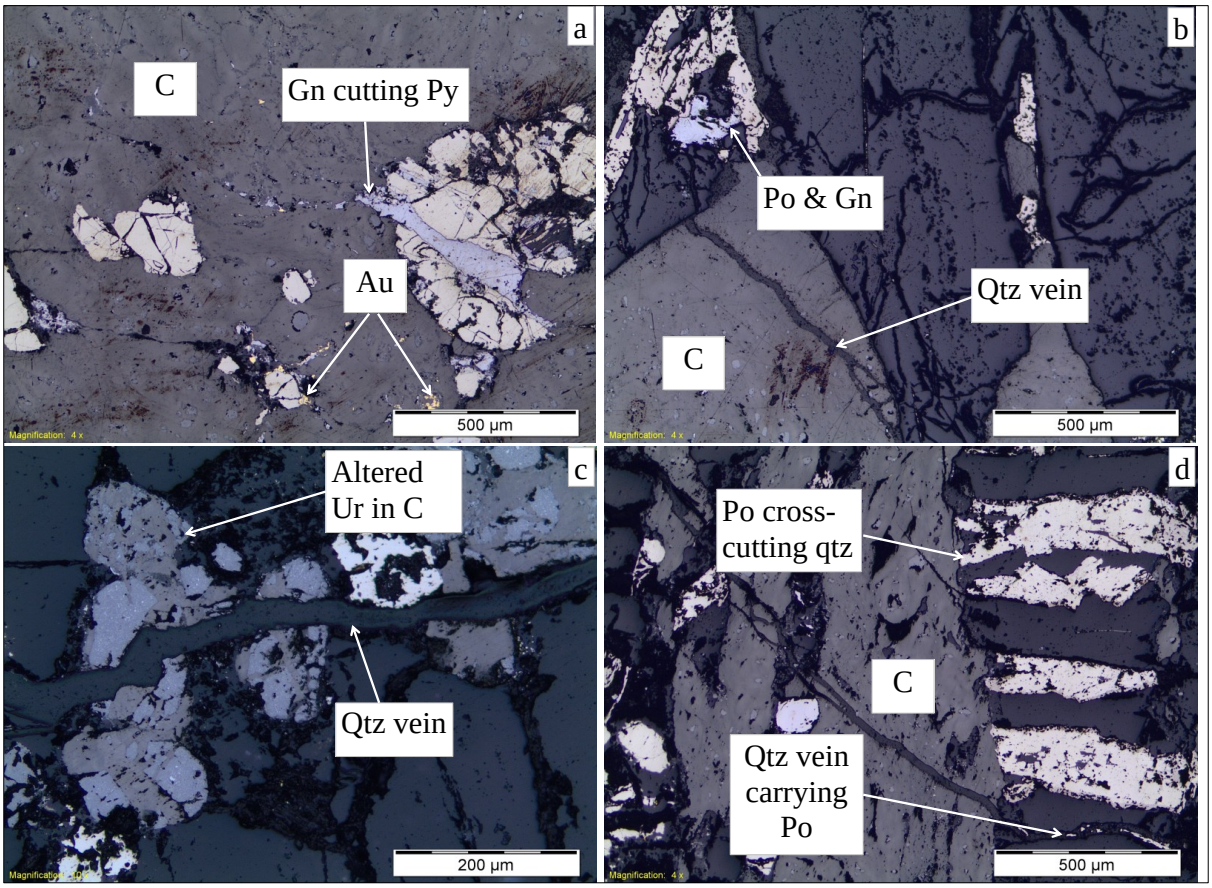



Figure 4.11: Photomicrographs of sample sections displaying infillings and veinlets. a) Cracked detrital pyrite (Py) filled by galena (Gn) veinlets that extend into the carbonaceous matter (C) groundmass, recrystallised gold grains are observed in the carbonaceous matter. b) Pyrrhotite (Po) and galena as infillings in the fractured quartz; a quartz vein is observed crosscutting the carbonaceous matter. c) A quartz vein cuts across a series of fly specks that hosts fragmented detrital uraninite. d) A set of parallel pyrrhotite layers cross-cutting a quartz pebble; a quartz vein carrying pyrrhotite cuts through the carbonaceous matter.

Quartz veinlets also cut across the carbonaceous matter and uraninite (Figures 4.11b and c); furthermore, the quartz veinlets also occur in association with pyrrhotite cutting through an entire phase of the quartz pebble and the carbonaceous matter (Figure 4.11d).

Additional photomicrographs on gold grains are presented in Figure 4.12.

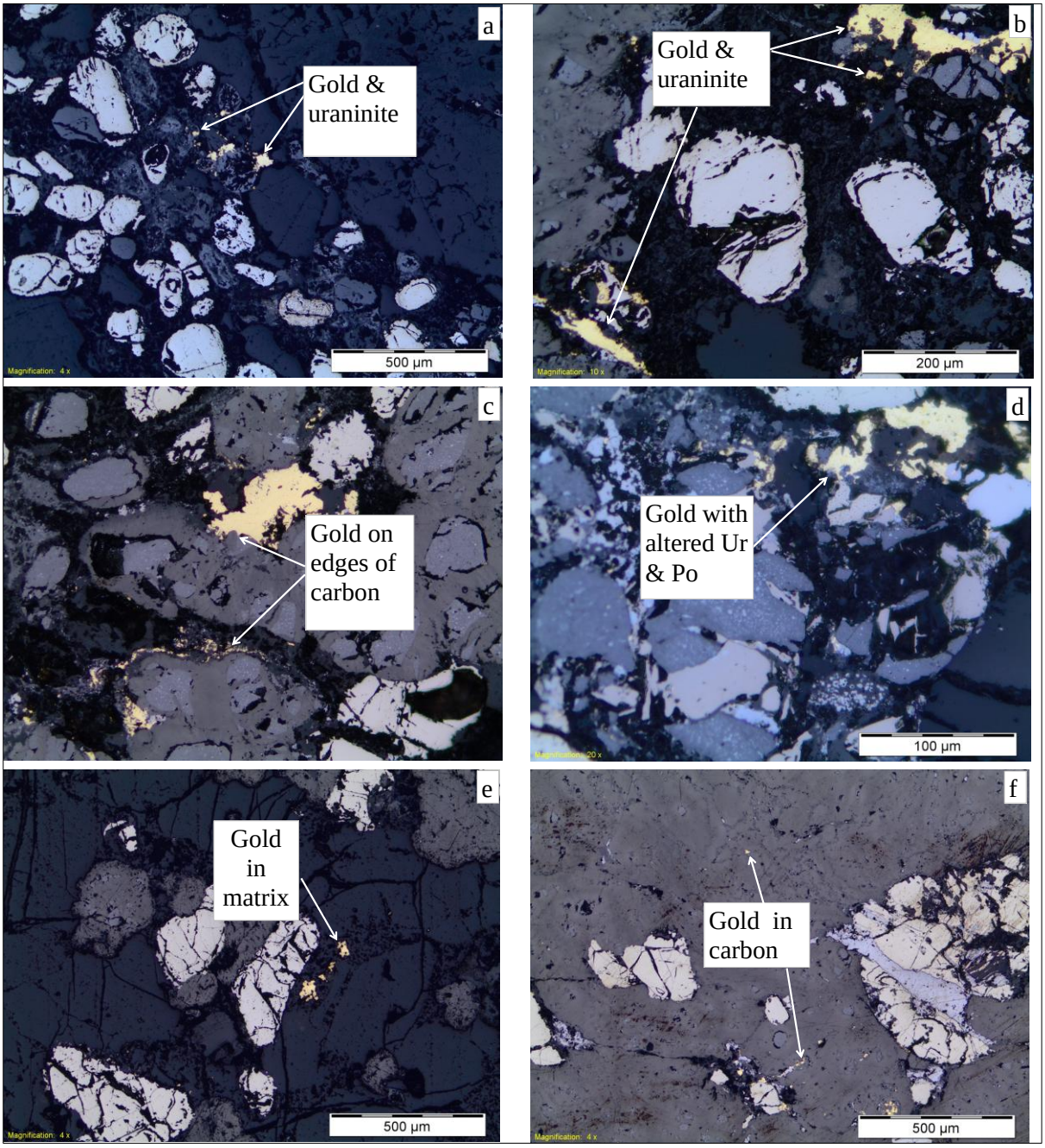



Figure 4.12: Photomicrographs of gold grains in the Vaal Reef matrix and carbonaceous occurrences. a) Gold associated with detrital matrix minerals such as uraninite and Pyrite. b) Irregular and elongated-shaped gold with the matrix and carbonaceous matter. c) Gold occurring interstitial to the carbonaceous matter. d) Gold associated with uraninite and pyrrhotite (Po). e) Gold trapped in a quartz pebble. f) Thin gold grains interstitial to the carbonaceous groundmass.

The samples showed that gold occurs in a detrital form associated with uraninite, pyrite and quartz (Figure 4.12a and e) and as secondary or recrystallised gold interstitial to the carbonaceous matter columnar edges (Figures 4.12b, c and f) and associated with secondary sulphide minerals such as pyrrhotite (Figure 4.12d).

A summary of grain size and shape distributions was made based on results from both reflected light and SEM studies for both facies. The information was grouped into two different mines with respect to the C and A Facies represented in these mines. The information is presented in Tables 4.3 for Kopanang (C Facies) and Moab Khotsong mines (A Facies), respectively.

The C Facies at Kopanang Mine is dominated by allogenic minerals; the sizes of the minerals in the C Facies are generally larger than minerals in the A Facies and the shapes of these allogenic minerals are mainly rounded (Table 4.3). Samples from the A Facies at Moab Khotsong Mine are constituted by secondary minerals which display replacement of the primary minerals by metamorphic and/or hydrothermal activity, mainly sulphide minerals; most of these minerals occur infilling primary rounded minerals that are cracked (Table 4.3).

### 4.5. Electron Microprobe Analysis (EMPA)

Electron-microprobe analyses (EMPA) were conducted on the Vaal Reef C and A Facies uraninite in order to investigate any variations in chemistry of these grains between uraninite grains in the matrix and in the carbonaceous matter. The C Facies is generally dominated by allogenic uraninite in the quartz-pyrite matrix and the A Facies uraninite grains are generally enclosed by the carbonaceous matter; therefore, uraninite grains from the matrix, where collected from the C Facies and uraninite grains hosted in the carbonaceous matter, are from the A Facies. Results revealed minor differences in the composition of the uraninite grains in both the C and A Facies.

Four samples from the C Facies at Kopanang Mine were analysed. In sample 1K4, seven grains of detrital uraninite were selected and showed an average of 65.1 % uranium content (Table 4.4). The second sample (1K5), showed an average of 67.8 % uranium content from

14 grains analysed. The third sample (2k3) was 67.9 % uranium content from 27 grains and the last sample 3k2 with 69.2 % uranium content from the 14 grains analysed.

Table 4.3: Comparison of mineral properties at Kopanang Mine C Facies and Moab Khotsong Mine A Facies

| **Mineral** | **Mode of occurrence/shape** | | **Grains size distribution** | |
|---|---|---|---|---|
| | ***C Facies*** | ***A Facies*** | ***C Facies*** | ***A Facies*** |
| **Uraninite** | Sub-rounded to oval | Sub-rounded and fragmented | 40-150 μm | 20-100 μm |
| **Brannerite** | Patchy, irregular | Patchy, irregular | 30-120 μm | 30-120 μm |
| **Uraniferous leucoxene** | Sub-rounded | Not encountered | 80-240 μm | Absent |
| **Gold** | Round to anhedral | Anhedral | 20-90 μm | 20-50 μm |
| **Pyrite** | Round and cubic (secondary) | Round and cubic (secondary) | 100-500 μm | 100 μm – 1.5 mm |
| **Pyrrhotite** | Anhedral (secondary) | Anhedral and veins (secondary) | 80-300 μm | 80 μm |
| **Arsenopyrite** | Rounded | Rounded | 100-150 μm | 50-150 μm |
| **Chalcopyrite** | Anhedral (secondary) | Not encountered | 40-80 μm | Absent |
| **Galena** | Not encountered | Anhedral and veins (secondary) | Absent | 100-150 μm |
| **sphalerite** | Anhedral (secondary) | Anhedral and veins | 150-350 μm | 20-50 μm |
| **Chromite** | Rounded | Not encountered | 100-150 μm | Absent |
| **Zircon** | Rounded | Not encountered | 100-200 μm | Absent |
| **Rutile** | Rounded | Not encountered | 200 μm | Absent |
| **Carbonaceous matter** | Nodular and minor seams (secondary) | Nodular and seams (secondary) | 200 μm – 3 mm | 200 μm >3 mm |

The A Facies samples from Moab Khotsong Mine representing uraninite grains within the carbonaceous matter have slightly higher uranium contents than the uraninite grains in the matrix of the C Facies (Table 4.5). Three samples were analysed from the A Facies; from

sample MK361, 10 grains show average uranium content of 71 %. Sample MK363 has a uranium content of 73.9 % from 17 analyses and MK365 with eight analyses with average of 68.3 %.

Tables 4.4 and 4.5 further show that the Th content in both the C and A Facies uraninite grains are similar, and also the $UO_2/ThO_2$ ratios are similar. The C Facies is characterised by relatively high PbO contents in the uraninite (ranging from 18.2 % to 25.7 %). However, PbO content in the A Facies uraninite is low as compared to the C Facies uraninite grains (range from 11.5 % to 14 %). The average of the PbO content in the A Facies uraninite is lower than that of the C Facies PbO content by approximately 6.1 %. The A Facies uraninite is also high in FeO, $TiO_2$, CaO and $SiO_2$ contents as compared to the C Facies.

Table 4.4: Electron-microprobe analyses of uraninite grains from the matrix of the Vaal Reef C Facies samples

| Source | Sample | Number of analyses (n) | $UO_2$ % | $ThO_2$ % | PbO % | FeO % | $TiO_2$ % | CaO % | $SiO_2$ % | Total % | $UO_2/ThO_2$ |
|---|---|---|---|---|---|---|---|---|---|---|---|
| C Facies | 1k4 | 7 | 65.1 | 3.5 | 25.7 | 0.3 | 0.2 | 0.7 | 0.6 | 96.1 | 18.4 |
| | 1k5 | 14 | 67.8 | 4.2 | 21.5 | 0.2 | 0.2 | 0.8 | 0.7 | 95.4 | 16.2 |
| | 2k3 | 27 | 67.9 | 4.8 | 18.2 | 0.2 | 1.0 | 1.1 | 1.7 | 94.9 | 14.1 |
| | 3k2 | 14 | 69.2 | 3.9 | 20.1 | 0.3 | 0.1 | 1.4 | 0.9 | 96.0 | 17.7 |

Table 4.5: Electron-microprobe analyses of uraninite grains hosted within the carbonaceous matter in the Vaal Reef A Facies samples

| Source | Sample | Number of analyses (n) | $UO_2$ % | $ThO_2$ % | PbO % | FeO % | $TiO_2$ % | CaO % | $SiO_2$ % | Total % | $UO_2/ThO_2$ |
|---|---|---|---|---|---|---|---|---|---|---|---|
| A Facies | MK361 | 10 | 71.0 | 4.8 | 13.6 | 0.3 | 1.0 | 1.4 | 2.1 | 95.4 | 14.9 |
| | MK363 | 17 | 73.9 | 2.6 | 14.0 | 0.4 | 0.4 | 1.1 | 0.6 | 94.1 | 28.0 |
| | MK365 | 8 | 68.3 | 4.9 | 11.5 | 0.3 | 0.3 | 1.6 | 4.6 | 94.8 | 13.8 |

### 4.6. Paragenetic Sequence

Optical microscopy, SEM and electron-microprobe studies have contributed significantly to the identification and understandying the mineralogy and chemistry of the Vaal Reef samples, more particularly the uranium-bearing minerals. Therefore, a paragenetic sequence of the Vaal Reef at the mines (Kopanang and Moab Khotsong) was developed (Figure 4.13). Four stages of developments were defined in the paragenetic sequence of the samples and are explained in detail.

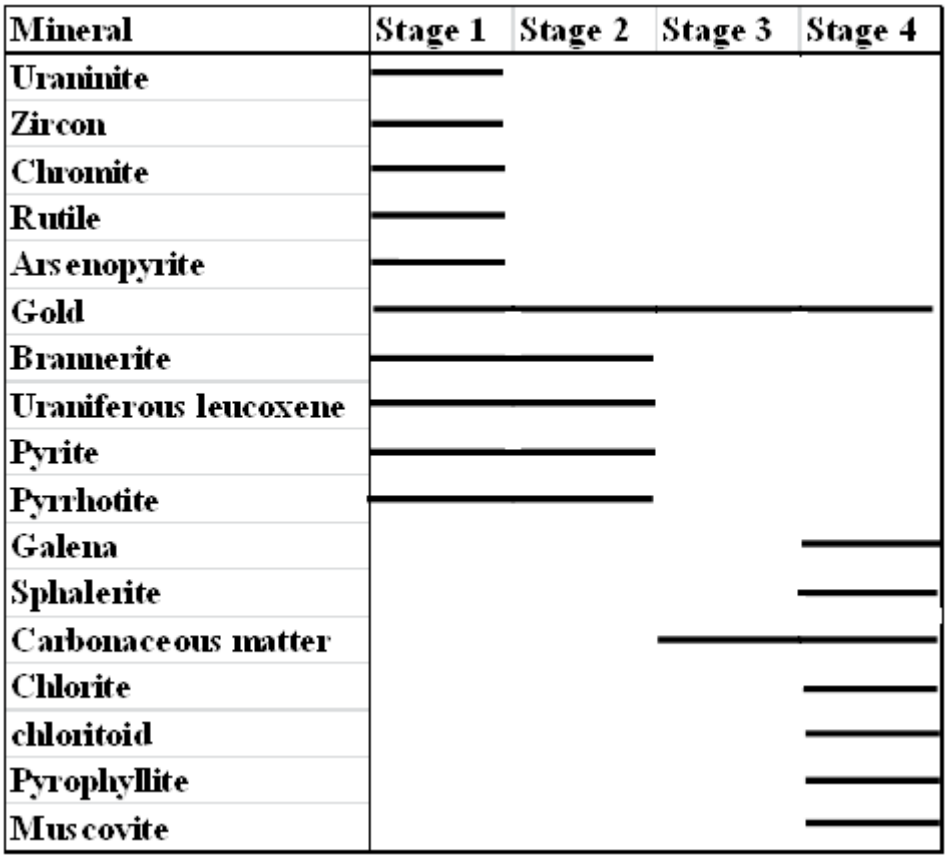



Figure 4.13: A four stage paragenetic sequence of the Vaal Reef minerals in the Klerksdorp Goldfield. 1) Stage 1 is constituted by older detrital minerals. 2) Stage 2 is characterised by the development of mainly secondary sulphide minerals. 3) Stage 3 is the injection of the carbonaceous matter. 4) Stage 4 is development of hydrothermal quartz and sulphide minerals.

The paragenetic sequence of the Vaal Reef is suggested to be grouped into four phases:

- Stage 1: Deposition of allogenic minerals, primary pyrite, arsenopyrite, zircon, chromite, rutile, uraninite and gold (Figure 4.4). Gold is an exception in this association as is does not always occur with the above mentioned minerals, but the rounded nature of gold is evidence of detrital origin (Figure 4.4).

- Stage 2: Secondary formation of pyrite (Figure 4.4a), chalcopyrite, gersdorffite, brannerite and leucoxene (Figures 4.9 and 4.10). Pyrite is the most common authigenic mineral. A great abundance of these authigenic minerals is in the A Facies at Moab Khotsong Mine, where the samples have high degrees of fracturing.
- Stage 3: The third stage in the paragenetic sequence of the Vaal Reef is the development of the carbonaceous matter in both the C and A Facies. The carbonaceous matter occurs as seams and as nodular bodies or "fly specks". The carbon seams are columnar or fibrous in texture and developed perpendicular to the quartz cracks as shown in the petrography studies (Figure 4.5f). The carbon seams are mainly associated with uraninite grains (Figure 4.5e). The majority of the uraninites in the carbonaceous seams are fragmented (Figure 4.10). Uraninite grains are also found within the fly specks as well (Figure 4.5d); this was well observed using the SEM.
- Stage 4: A late quartz-sulphide association post-dates all the phases in the Vaal Reef. This has been observed in both the A and C Facies samples. This is well supported by the regional peak metamorphism that was responsible for the development of phyllosilicate mineral assemblages in the majority of the samples studied. Therefore, the pyrophyllite, chlorite, chloritoid and muscovite phases in the samples have contributed in understanding peak metamorphism of the Witwatersrand Basin. Pyrrhotite generally occurs as veins, filling in fractures of quartz pebbles (Figure 4.5d and Figure 4.11d); pyrrhotite is also carried by the quartz veins (Figure 4.11). Galena and sphalerite (Figure 4.9a and b) occur in the form of veins cross-cutting pyrite and also cross-cuts carbonaceous matter as well (Figure 4.9a and c). There is also evidence of recrystallisation of gold in this stage and the gold mainly occurs interstitial to the carbonaceous matter **(**Figures 4.5e and 4.12c and e).

### 4.7. Summary

Quartz is the dominant mineral in the Vaal Reef samples. The common secondary silicate minerals in the samples as shown by XRD and microscopy following quartz in abundance are sheet silicate minerals (chlorite, chloritoid, pyrophyllite and muscovite). The A Facies is quartz-rich, but low in sheet silicate minerals. On the contrary, sheet silicate minerals are more frequently encountered in the C Facies compared with the A Facies.

Petrographic observations show that the main detrital minerals are suggested to be pyrite, chromite, zircon, rutile, uraninite and gold. These minerals are generally sub-round to round in shape and occur in clusters in the quartz-pebble conglomerate matrices. The detrital minerals, other than the quartz pebbles, display grain sizes ranging from as small as 80 μm to 1.5 mm (mainly the pyrite grains). Gold is smaller in size and only observed in a few cases with detrital minerals.

Pyrite occurs in the reef but not in the carbonaceous matter at the base of the reef, it is the main matrix and sulphide mineral, and occurs in two forms in the majority of the samples from the C and A Facies, these are the round (detrital) and secondary (authigenic) grains (Figure 4.4). Detrital pyrites have large grains sizes (up to 1-2 mm in size), and display cracking; the mineral occurs in cluster with the rest of the detrital minerals.

Other sulphide minerals such as chalcopyrite, pyrrhotite, galena, sphalerite, gersdorffite and arsenopyrite are present in accessory amounts in the Vaal Reef samples (Figures 4.4, 4.5, 4.9 and 4.10). Most of the sulphide minerals occur in close association with one another i.e. galena, sphalerite and pyrrhotite (Figure 4.9). Pyrite is the most common authigenic sulphide mineral followed by pyrrhotite. The latter is found in many occurrences as veins filling in fractures of quartz (Figure 4.5). A great abundance of these authigenic minerals occur at Moab Khotsong Mine in the A Facies, where the samples show high degrees of fracturing (Figures 4.9 and 4.10), e.g. galena occurs in a form of veins cross-cutting the detrital pyrite and the carbonaceous matter as well. Other secondary sulphides occurring alongside galena are pyrrhotite and sphalerite (Figure 4.9a). The paragenitic sequences of the Vaal Reef mineralogy has revealed that these minerals (chalcopyrite, pyrrhotite, galena, sphalerite, gersdorffite and arsenopyrite) were formed and deposited at different times.

Uraninite is the main uranium-bearing mineral phase in both the C and A Facies samples of the Vaal Reef. Brannerite and uraniferous leucoxene are the secondary uranium-bearing mineral phases and are suggested to be formed from the breakdown of detrital uraninite grains interacting with Ti-rich minerals such as detrital rutile. Brannerite occurs in both the C and A Facies samples; uraniferous leucoxene has only been observed in the C Facies samples.

Uraninite grains in both the C and A Facies of the Vaal Reef have sizes ranging from 20 to 200 μm (Figure 4.4), and are generally oval to sub-round in shape, and are also angular when enclosed by the carbonaceous matter (Figures 4.5 and 4.9), due to the fragmentation and by growth of the latter. The SEM results further showed that the carbonaceous matter mainly replaces the detrital uraninite grains along their weak cracked zones (Figure 4.6). Primary detrital minerals such as zircon and chromite are found in association with round pyrite, suggesting that these minerals were deposited at the same time as uraninite prior to the breakdown by the carbonaceous matter. This has been observed in areas where uraninite grains occur both in the matrix, and secondly enclosed within the carbonaceous matter (Figures 4.6e and f).

Electron-microprobe analyses in this study show that uraninites have average Th contents of 4.1 % in both the C and A Facies; another major observation is that the C Facies matrices uraninite grains are more Pb-rich than the A Facies carbonaceous matter-hosted uraninite grains (Tables 4.4 and 4.5).

Gold is found in the matrix in association with detrital pyrite and quartz in a few instaces (Figure 4.4d). The shapes of gold in these locations resemble detrital minerals in the C Facies, and therefore, this suggests that some gold grains in the reef are detrital in origin. Anhedral gold grains up to 150 μm occur in the quartz-pyrite matrix just less than 200 μm away from the carbonaceous matter in the C Facies (Figure 4.5f). Gold is also observed occurring interstitial to the carbonaceous matter (Figures 4.5e, 4.12c and e). The interstitial gold is suggested to be secondary in formation, mainly, as a result of recrystallisation due to the carbonaceous matter; the gold is observed recrystallising along the columnar edges of the carbonaceous matter.

The A Facies gold is mainly associated with sulphide minerals. This has been observed in the photomicrographs, but this is not obvious in the C Facies samples, where the C Facies gold grains can occur in the matrix with little association with the sulphide minerals. The gold grains in the A Facies are generally small in size (around 50 μm) and have been remobilised by the carbonaceous matter (Figures 4.9 e and f).

Two forms of carbonaceous matter are found in the samples and these are the carbon seams and as nodular bodies or “fly specks”. These two forms are generally associated with detrital

uraninite. The majority of the uraninites in the carbonaceous seams are fragmented (Figure 4.10) and broken down into small irregularly shaped uraninites by the carbonaceous matter.

In a single sample in the C Facies, detrital uraninite is observed in the matrix as well as encapsulated by the carbonaceous matter (Figure 4.6d). Fly specks surround and break down grains of uraninite (Figure 4.6d). In some cases, fragmention and penetration of uraninite by carbon precipitating along cracks in uraninite grains is very common and causing the detrital uraninite grains to break up into smaller, more angular fragments. This is a clear indication that the carbonaceous matter post-dates uraninite.

This study suggests that it seems impossible that uraninite grains and carbonaceous matter were deposited syngenetically by metamorphic or hydrothermal fluids. Clear evidence in the physical cracking of the uraninite grains by cross-cutting veins of the carbonaceous matter indicate it post-dates uraninites in the Vaal Reef. Gold on the other hand has shown detrital nature in other samples and on the contrary, there are also recrystallised gold grains associated with secondary sulphides and in the carbon, occurring interstitial to the carbon fibre growth structures.

The occurrence of the carbonaceous seams in some samples from the A Facies, show a great dominance and does not only enclose uraninite, but encloses the majority of the heavy detrital minerals such as pyrite, zircon, chromite, etc; this is also observed in the C Facies, but in less frequent occurrences as compared to the A Facies. Therefore, the C Facies 440 and 460 geozone samples from the Kopanang Mine are mainly characterised by detrital uraninite occurring in the matrix; on the other hand, the Moab Khotsong A Facies 370 geozone samples are characterised by uraninite entirely enclosed in the carbonaceous matter.

# CHAPTER FIVE

# WHOLE-ROCK GEOCHEMISTRY

## 5.1. Introduction

Whole-rock geochemistry was undertaken in order to establish compositional relationships between uranium, gold, carbon and sulphur content in the C and A Facies of the Vaal Reef samples. This also assisted in validating the petrography results in Chapter 4 that revealed different associations of uraninite with pyrite, uraninite with the carbonaceous matter, uraninite with gold, gold with sulphide minerals and gold with the carbonaceous matter. The main aim was to evaluate the distribution of these elements in the different geozone samples (Table 5.1). Samples studied in this chapter are mainly from the underground workings at Kopanang (C Facies, 10 samples) and Moab Khotsong (A Facies, 11 samples); samples were collected from the C and A Facies boreholes as well.

Table 5.1: Number of samples collected for geochemical analysis from Kopanang, Great Noligwa and Moab Khotsong Mines; Vaal Reef C and A Facies.

| Facies | Geozone 440 | Geozone 460 | Geozone 500 | Geozone 370 | Total sample number |
|---|---|---|---|---|---|
| **A** | - | - | 2 | 9 | 11 |
| **C** | 2 | 6 | 1 | 1 | 10 |

## 5.2. Methodology

All the analyses were performed at MINTEK Analytical Service Division (ASD) laboratories (an ISO 17025 accredited laboratory) in Randburg, Johannesburg, South Africa, except for the uranium analysis which was conducted at Perfomance Laboratories. Details of methodologies are as follows:

### *5.2.1. X-Ray Fluorescence (XRF) Spectrometry*

The Spectro X LAB 2000 XRF was employed for elemental analyses in this study. Samples were analysed using energy dispersive XRF (EDX). The technique is non-destructive. The results were semi-quantitative, hence indicative of element concentration levels that allowed

for more relevant techniques to be used (ICP-MS, fire assay, total sulphur and carbon combustion and uranium analyses) to obtain accurate results. The samples were analysed under helium gas. Light element analyses (Al to Ca) limits of detection are in the range 25 – 50 ppm and 1 – 5 ppm for heavy elements.

The uranium analyses were conducted by Performance Laboratories, who determined the uranium content by XRF.

*5.2.2. LECO method*

The sulphur and carbon analyses were done using a combustion ("LECO") method. For both elements, the sample is placed in a ceramic crucible, along with an accelerator. The crucible is moved into the instrument furnace, where the sample is heated and the sulphur (and carbon) released. This is carried in a stream of high-purity oxygen, where it is converted to $SO_2$ (and $CO_2$). It is carried to an infrared detector, where the $SO_2$ (and $CO_2$) is detected quantitatively. LECO CS200 and an Eltra CS2000 analysers were used for this work.

*5.2.3. Inductively Coupled Plasma MS and OES*

A portion of the sample was weighed into a crucible and mixed with sodium peroxide and sodium bicarbonate flux and then fused and the resulting product leached in acid and made up to a flask volume mark with water.

The sample was then analysed on the ICP-OES instrument (Varian Vista Pro) supplied by Agilent technologies (previously known as Varian) against standards of know elemental concentrations. The samples were prepared along with reference samples, which are samples with certified elemental concentrations as a quality control measure of the process. The results obtained from the instrument were reported in percentage and ppm units. Major oxide elements (MgO, PbO, $Al_2O_3$, $SiO_2$, CaO, $TiO_2$, $V_2O_5$, $Cr_2O_3$, MnO, FeO and ZnO) and trace elements (Co, Ni and Cu) were analysed.

*5.2.3. Fire Assay*

Fire assay is a pyro-technique where the Platinum Group Metals and gold (PGM's & Au) are separated from other elements. Low temperature cupellation was employed for gold analysis in the samples and the procedure is described below.

The button was placed onto the hollow of a preheated cupel for 1 hour at 1000$^{o}$C. The intention of cupeling the sample is to separate lead from the gold where they would be positioned on the hollow of the cupel as a lead and gold prill. Lead is taken by the cupel and some of it oxidized.

For 3E elements, the prills were dissolved on a hotplate using aqua regia.

- The solution of gold and aqua regia was transferred into a volumetric flask.
- An internal scandium standard was added and the solution made up to the volume mark with de-ionized water.
- It was analysed on an ICP-OES for gold.

**5.3. Results**

Samples from the three mines were analysed for total sulphur, uranium and gold. Results from the C Facies samples are shown in Table 5.2 and results from the A Facies are shown in Table 5.3.

Table 5.2: Concentrations of sulphur, uranium, carbon and gold in the Vaal Reef C Facies samples from Kopanang, Great Noligwa and Moab Khotsong Mines.

| **Sample Name** | **Sample Facies** | **Geozone** | **S** ppm | **U** ppm | **C** ppm | **Au** g/t |
|---|---|---|---|---|---|---|
| 1k1* | C | 440 | 2780 | 2531 | 1330 | 401 |
| 1k3* | C | 440 | 1350 | 2091 | 670 | 305 |
| 2k4* | C | 460 | 14310 | 1170 | 160 | 251 |
| 2k6* | C | 460 | 130 | 764 | 70 | 67.1 |
| 3k2* | C | 460 | 10340 | 2537 | 210 | 23.7 |
| 3k4* | C | 460 | 7190 | 257 | 40 | 2.93 |
| K2776 | C | 460 | 7240 | 679 | 6 | 4.08 |
| GBH645 | C | 500 | 1050 | 2762 | 500 | 14.8 |
| K2814 | C | 460 | 4300 | 7720 | 5400 | 240 |
| MK1033 | C | 370 | 5690 | 3711 | 100 | 95.2 |

*samples 1k1 to 3k4 are hand specimens collected from underground panels.

Table 5.3: Concentrations of S, U, C and gold in the Vaal Reef A Facies samples from Kopanang, Great Noligwa and Moab Khotsong Mines.

| **Sample Name** | **Sample Facies** | **Geozone** | **S** ppm | **U** ppm | **C** ppm | **Au** g/t |
|---|---|---|---|---|---|---|
| Mk361* | A | 370 | 1600 | 260 | 250 | 343 |
| Mk362* | A | 370 | 2490 | 2916 | - | 39.2 |
| Mk363* | A | 370 | 5260 | 3976 | 170 | 1950 |
| Mk364* | A | 370 | 5390 | 4365 | 52 | 353 |
| Mk365* | A | 370 | 2890 | 10 | 4730 | 727 |
| Mk366* | A | 370 | 5400 | 2332 | 38 | 2560 |
| Mk367* | A | 370 | 3650 | 1633 | 0 | 1350 |
| GBH637 | A | 370 | 730 | 1223 | 170 | 25.8 |
| GBH645 | A | 500 | 130 | 1914 | 220 | 2.62 |
| K4111 | A | 500 | 1770 | 420 | 40 | 3.62 |
| MK283R | A | 370 | 2140 | 2990 | 6 | 89.4 |

*samples Mk361 to Mk367 are hand specimens collected from underground panels

Major and trace elements results obtained from ICP-OES and ICP-MS, respectively, representing the C and A Facies samples of the Vaal Reef in all the three mines are shown in Tables 5.4 and 5.5, respectively.

Table 5.4: ICP-OES and ICP-MS Major and trace elements results of the C Facies geozones samples (geozones 440, 430, 460, 500 and 370 are represented).

| Geozone | Co ppm | Ni ppm | Cu ppm | MgO Wt% | PbO Wt% | $Al_2O_3$ Wt% | $SiO_2$ Wt% | CaO Wt% | $TiO_2$ Wt% | $V_2O_5$ Wt% | $Cr_2O_3$ Wt% | MnO Wt% | FeO Wt% | ZnO Wt% |
|---|---|---|---|---|---|---|---|---|---|---|---|---|---|---|
| 440 – 1k1 | 12 | 0 | 18 | 0.177 | 0.514 | 6.7 | 82.2 | <0.07 | 0.438 | <0.09 | 0.084 | <0.06 | 6.03 | <0.06 |
| 440 – 1k3 | 16 | 0 | 9.7 | 0.099 | 0.353 | 8.4 | 81.5 | <0.07 | 0.348 | <0.09 | 0.077 | <0.06 | 3.16 | <0.06 |
| 430 – 2k4 | 40 | 0 | 27 | 0.348 | 1.71 | 6.83 | 54 | <0.07 | 1.23 | <0.09 | 0.273 | <0.06 | 27.5 | 0.074 |
| 430 – 2k6 | 0 | 0 | 6.9 | <0.08 | 0.092 | 9.6 | 78 | 0.117 | 0.136 | <0.09 | <0.07 | <0.06 | 1.08 | <0.06 |
| 430 – 3k3 | 10 | 0 | 14 | 0.144 | 0.198 | 5.65 | 60.3 | <0.07 | 0.897 | <0.09 | 0.176 | <0.06 | 19.3 | <0.06 |
| 430 – 3k4 | 7 | 0 | 13 | 0.217 | 0.05 | 4.62 | 68.1 | 0.089 | 0.668 | <0.09 | 0.162 | <0.06 | 13.9 | <0.06 |
| 460 – K2776 | 10 | 0 | 8.5 | 0.243 | 0.078 | 4.21 | 68.5 | 0.076 | 0.479 | <0.09 | 0.145 | <0.06 | 14.58 | <0.06 |
| 500–GBH645 | 4 | 0 | 4.7 | 0.429 | 0.122 | 1.78 | 77.6 | <0.07 | 0.08 | <0.09 | <0.07 | <0.06 | 6 | <0.06 |
| 460-K2814 | 30 | 0 | 15 | 0.409 | 0.902 | 5.02 | 62.4 | 0.091 | 0.408 | <0.09 | 0.102 | <0.06 | 8.82 | <0.06 |
| 370-MK1033 | 15 | 0 | 15 | 0.241 | 0.257 | 2.27 | 72.5 | <0.07 | 0.103 | <0.09 | <0.07 | <0.06 | 12.82 | <0.06 |
| 370-MK283R | 45 | 0 | 34 | 0.363 | 0.376 | 1.45 | 63.6 | <0.07 | 0.08 | <0.09 | <0.07 | <0.06 | 7.44 | <0.06 |

Table 5.5: ICP-EOS and ICP-MS Major and trace elements results of the A Facies geozones samples (geozones 370 and 500 are represented).

| Geozone | Co ppm | Ni ppm | Cu ppm | MgO Wt% | PbO Wt% | $Al_2O_3$ Wt% | $SiO_2$ Wt% | CaO Wt% | $TiO_2$ Wt% | $V_2O_5$ Wt% | $Cr_2O_3$ Wt% | MnO Wt% | FeO Wt% | ZnO Wt% |
|---|---|---|---|---|---|---|---|---|---|---|---|---|---|---|
| 370-MK361 | 43 | 0 | 14 | 0.411 | 1.64 | 2.07 | 85.8 | <0.07 | 0.204 | <0.09 | 0.077 | <0.06 | 7.8 | 0.531 |
| 370-MK362 | 70 | 0 | 11 | <0.08 | 0.173 | 3.47 | 65.4 | <0.07 | 0.186 | <0.09 | <0.07 | <0.06 | 5.67 | <0.06 |
| 370-MK363 | 17 | 0 | 14 | <0.08 | 0.334 | 3.32 | 82.4 | <0.07 | 0.142 | <0.09 | <0.07 | <0.06 | 10.82 | <0.06 |
| 370-MK364 | 26 | 0 | 15 | 0.196 | 0.94 | 1.34 | 81.4 | <0.07 | 0.146 | <0.09 | <0.07 | <0.06 | 12.1 | 0.193 |
| 370-MK365 | 15 | 0 | 10 | 0.092 | 0.916 | 2.45 | 81.9 | <0.07 | 0.139 | <0.09 | <0.07 | <0.06 | 6.36 | 0.066 |
| 370-MK366 | 29 | 0 | 11 | 0.117 | 0.79 | 1.9 | 68.5 | <0.07 | 0.128 | <0.09 | 0.073 | <0.06 | 11.08 | <0.06 |
| 370-MK367 | 87 | 77 | 25 | <0.08 | 5.69 | 0.665 | 9.21 | 0.133 | 0.26 | <0.09 | <0.07 | <0.06 | 5.14 | <0.06 |
| 370-GBH637 | 2 | 0 | 4.9 | 0.153 | 0.064 | 2.83 | 84.7 | <0.07 | 0.08 | <0.09 | <0.07 | <0.06 | 2.34 | <0.06 |
| 500-GBH645 | 0 | 0 | 24 | 0.238 | 0.065 | 1.45 | 84 | <0.07 | 0.08 | <0.09 | <0.07 | <0.06 | 2.74 | <0.06 |
| 500-K4111 | 13 | 0 | 12 | 0.319 | 0.05 | 2.07 | 81.7 | <0.07 | 0.202 | <0.09 | <0.07 | <0.06 | 7.55 | <0.06 |

In general, both the A and C Facies samples are enriched in uranium, gold, carbon and sulphur content (Figure 5.1). The C Facies samples show a slightly higher carbon and sulphur content (Figure 5.1a) than the A Facies samples. Uranium distribution in the C and A Facies is slightly similar with the C Facies 460 geozone being more uranium-rich than the rest of the samples (Figures 5.1a and c). The 370 geozone samples from the A Facies show a good correlation between sulphur and gold (Figure 5.1d). There is a weak correlation between gold and carbon in both the A and C Facies geozone samples (Figure 5.1b).

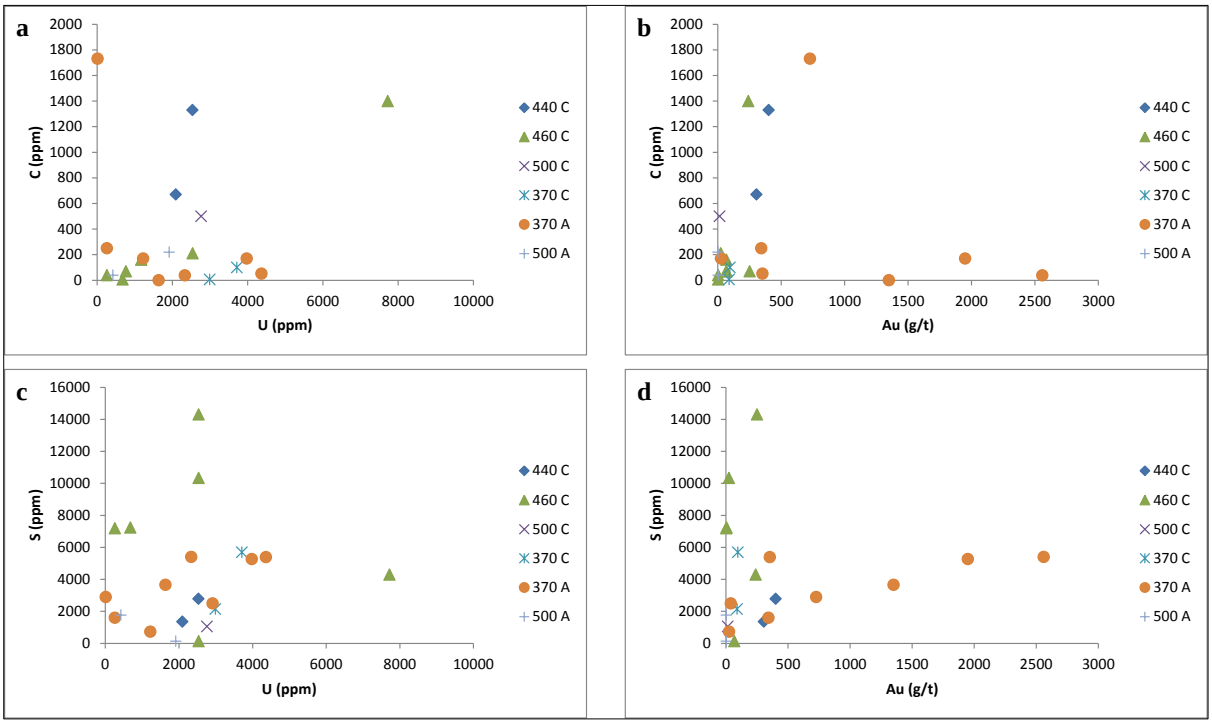



Figure 5.1: Plots of: (a) Whole-rock uranium vs. carbon from the A and C Facies samples. The C Facies and A Facies from the 370 geozone is generally uranium-rich. The 440 geozone representing the C Facies is carbon-rich. (b) Gold vs. Carbon; the A Facies 370 Geozone is more gold-rich than the C Facies samples. (c) Uranium vs sulphur; the C Facies is more sulphur-rich than the A Facies. (d) A plot of gold vs. sulphur.

Major elements that occur in the Vaal Reef C and A Facies are mainly $SiO_2$, FeO, $Al_2O_3$ and minor to trace $TiO_2$ (Figure 5.2). The C Facies is more $TiO_2$-rich in the 460 and 440 geozones (Figure 5.2a) than the A Facies; the A Facies is more $SiO_2$-rich than the C Facies (Figure 5.2b). FeO vs. $Al_2O_3$ plot (Figure 5.2c) shows that the C Facies geozones (440 and 460) have high contents of both aluminium and iron compared with the A Facies. There is a good correlation between $SiO_2$ and gold in the A Facies (Figure 5.2d), which is not the case in the C Facies samples.

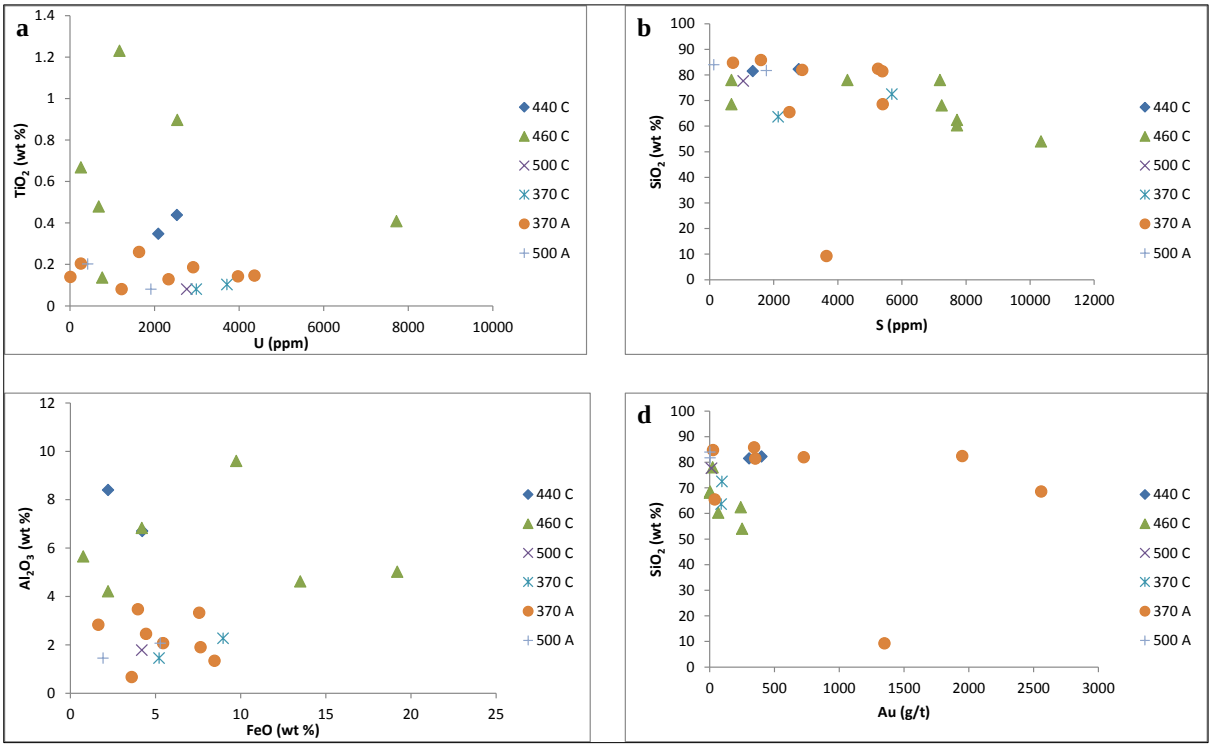



Figure 5.2: Whole-rock plots of (a) Uranium vs. $TiO_2$ where titanium is mainly enriched in the 430 geozone of the C Facies. (b) Sulphur vs.$SiO_2$, the A Facies is more quartz-rich than the C Facies. (c) FeO vs $Al_2O_3$ and the C Facies samples (440 and 460 geozones) are more aluminium-rich than the A Facies sample. (d). Gold vs. $SiO_2$ and high gold-quartz association occurs in the A Facies.

## 5.4. Summary

Geochemical analyses were discussed in this chapter to evaluate the association among uranium, carbon, sulphur, gold, iron, aluminium, titanium and silica in the Vaal Reef C and A Facies samples. Results revealed that uranium distribution is similar in the C and A Facies samples from Kopanang, Great Noligwa and Moab Khotsong samples; uranium is extremely high in one sample from the C Facies 460 geozone. The high uranium concentrations in the C Facies are supported by the increased abundance of uranium-bearing minerals, detrital uraninite in particular, however uraninite is also present in the A Facies, but mainly within the carbonaceous matter. The C Facies is also $TiO_2$-rich as compared with the A Facies and this is suggested to be as a result of the presence of detrital rutile, which has further broken down together with uraninite to form secondary uranium-bearing minerals such as brannerite and uraniferous leucoxene. The C Facies further has a high aluminium content that represents the increased abundance of sheet silicate minerals as supported by XRD results in Chapter 4.

The high sulphur content in the C Facies is associated with sulphide minerals, mainly pyrite and pyrrhotite; pyrite is the main sulphide matrix mineral in the C Facies samples and mainly occurs in an allogenic form and, in a few occurrences as secondary. Pyrrhotite is generally secondary in all its occurrences.

Carbon distribution in the C and A Facies samples is similar in the C Facies samples; the results do not show a good correlation between carbon and uranium in the A Facies as seen mineralogically in Chapter 4, where uraninite is entirely hosted by the carbonaceous matter. Gold is highest specifically in the A Facies 370 geozone samples, but low in the C Facies samples. There is no good correlatable relationship between gold and carbon in the A Facies samples; this supports the petrography observations where the carbonaceous matter in the A Facies hosts the majority of the gold. There is also a strong association of sulphur and gold in the A Facies 370 geozone, which is suggested to result from the presence of high pyrite content associated with gold. The A Facies is more $SiO_2$-rich than the C Facies, and this was also shown in the XRD results.

# CHAPTER SIX

# COMPUTED TOMOGRPHY

## 6.1. Introduction

In this chapter, 3D Microfocus X-Ray Computed Tomography (μXCT) has been applied to evaluate whether the technique is able to complement the 2D mineralogical results obtained from optical microscopy and scanning electron microscopy (SEM) in Chapter 4. Two - dimensional mineralogical techniques have been useful in understanding the mineralogy of the Vaal Reef samples; the techniques gave information on which minerals occur in the Vaal Reef samples, their textural relationships, sizes as well as shape of minerals. It is very important to note that mineral information was acquired from the surface of polished and thin sections, hence giving only 2D information on the samples.

Three-dimensional μXCT as an analytical technique was applied to three samples from three different geozones (440, 460 and 370 geozones) for this study; only three geozones were analysed due to the limited beam time that was offered for scanning, as the machine had recently been acquired and was in high demand for use by other science disciplines as well. The main aim was to conduct a full virtual volumetric analysis of the uranium-bearing minerals from the Vaal Reef samples. This could be achieved because the technique is able to analyse for internal structures, size, shape and volume distribution of the mineral components within the rock sample in a single scan (Kasteel *et al*., 2000; Perret et al., 2000; Ketcham and Carlson, 2001; Gualda and Rivers, 2006). Computed tomography as a 3D virtual technique, has the following advantages: it has a non-destructive character (rock samples need no crushing or polishing); it allows internal properties of rock samples to be analysed in a 3D orientation and it also allows segmentation of specific features of interest (Mees *et al*., 2003).

Computed tomography (CT), as applied in this study, is explained as the process where a large number of 2D X-ray transmission radiographs, taken at regular angular intervals over a $360^{o}$ rotation of the sample, are reconstructed into 2D sequential slices of images which when stacked, allow visualisation of a virtual volume of the total sample in 3D (Ketcham and Carlson, 2001 and Mees *et al*., 2003). Computed tomography yields a 3D map of the X-ray linear attenuation coefficients of components in the sample (Pullan *et al*., 1981), which is a function of the atomic number and density of these components at a specific X-ray energy.

Based on the X-ray attenuation contrasts between different mineral phases, minerals, or groups of minerals, can be identified in a rock.

X-ray CT was first applied in the medical science industry by Hounsfield (1973) and the technique was later introduced in the geosciences by Conroy and Vannier (1984) in paleontology, and by Fransham and Jelen (1987) in petroleum engineering. It is only relatively recently (in the last decade or so) that the technique has been utilised for mineralogical investigations (Kalukin *et al*., 2000; Van Geet et al., 2000; Van Geet and Swennen, 2001; Van Geet *et al*., 2001; Thompson *et al*., 2006; Remeysen and Swennen, 2007; Long *et al*., 2009). To date, X-ray CT has been applied to a wide range of ore bodies and rock types ranging from magmatic deposits of the Bushveld and Stillwater Complexes (Godel *et al*., 2006), to porphyroblasts in metamorphic rocks (Kretz, 1966, 1969, 1993). The technique has also been applied in visualisation of sedimentary rocks such as sandstones by studying the morphology of sand grains (Nshimirimana *et al*., 2011). A few of these authors have also compared 3D and 2D mineralogical analytical techniques (Godel 2006, 2010; Elliot and Heck, 2007).

Ketcham and Carlson (2001) classified X-ray CT scanners into four categories, based on the spatial resolution obtained in samples, and the size of objects they are most suitable for scanning (Table 6.1).

Table 6.1: General classification of computed tomography (after Ketcham and Carlson, 2001).

| **Type** | **Scale of observation** | **Scale of resolution** |
|---|---|---|
| Conventional | m | mm |
| High-resolution | dm | 100 µm |
| Ultra-high resolution | cm | 10 µm |
| Microfocus tomography | mm | µm |

It is important to take into consideration the concepts of 3D µXCT that have been employed in this chapter which are explained below.

### 6.2. Principles of µXCT

The method of 3D µXCT involves the passing of a cone beam of X-ray radiation of a given energy through a rotating sample and the collection of data from the existing cone beam to produce a 3D image. High resolution (micron scale) evaluation of the sample becomes possible due to the fact that the X-rays originate (are being generated) from a 1 to 3 micron scale area, defined as a point source of radiation. The principle is based on the Beer-Lambert Law (de Beer *et al., 2004)*, where the measured intensity $I$ of the transmitted beam through a material with thickness $x$ is related to the incident intensity $I_0$ according to the inverse exponential power law referred to as (Fig. 6.1):

$$I=I_0e^{-\mu x} \qquad \text{Eq. 5.1}$$

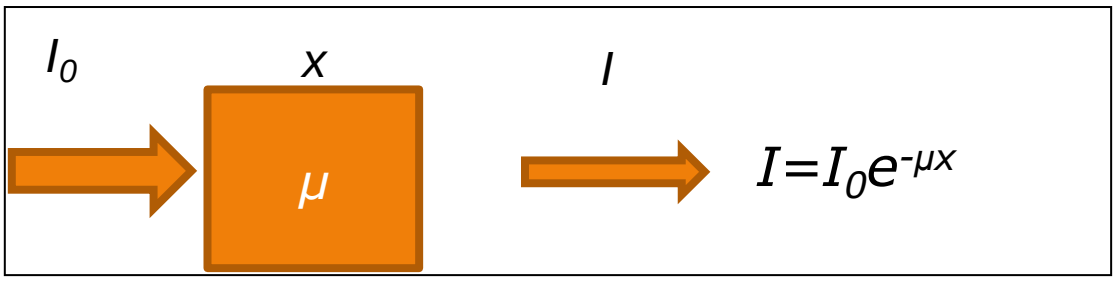



Figure 6.1: Illustration of Beer-Lambert Law of linear attenuation (de Beer *et al., 2004).*

Where:

$I$ = the intensity of photons transmitted across some distance x (Photons / $cm^2$)

$I_0$= the initial intensity of photons (Photons / $cm^2$)

$e$ = a proportionality constant for scattering or absorption

$\mu$ = the linear attenuation coefficient ($cm^{-1}$)

$x$ = Thickness of the sample *(cm)*

For geological samples, mineral components are distinguished from one another by their unique attenuation coefficients. The attenuation coefficient describes how much the intensity of a beam of radiation is reduced through scattering or absorption as it passes through a specific material; in this context the radiation is in the form of X-rays, and the manner it is attenuated is being expressed using the symbol µ, and measured in $cm^{-1}$ (Pullan et al., 1981). The attenuation coefficient (µ) is a function of the macroscopic cross section and density of the material which is X-ray energy dependant.

The important step in the above process is the acquisition of 2D digital radiographs at every 0.96$^{o}$ as the X-ray cone beam passes through the rotating sample; therefore, 375 projections are produced on the sample for a full rotation of 360$^{o}$ (Figure 6.2; Nshimirimana *et al.*, 2011). This is referred to as cone beam tomography. The 375 2D projections are then reconstructed into a 3D volume by reconstruction software (Nshimirimana *et al.*, 2011). This 3D volume is called a tomogram. Visualisation and analysis is possible; the tomogram can be viewed as 2D slices or segmented to reveal mineral components. The tomogram can be viewed in orthogonal 2D planes in an x-y-z co-ordinate system i.e. axial, sagittal and frontal planes (Fig. 6.2; Mees *et al.*, 2003).

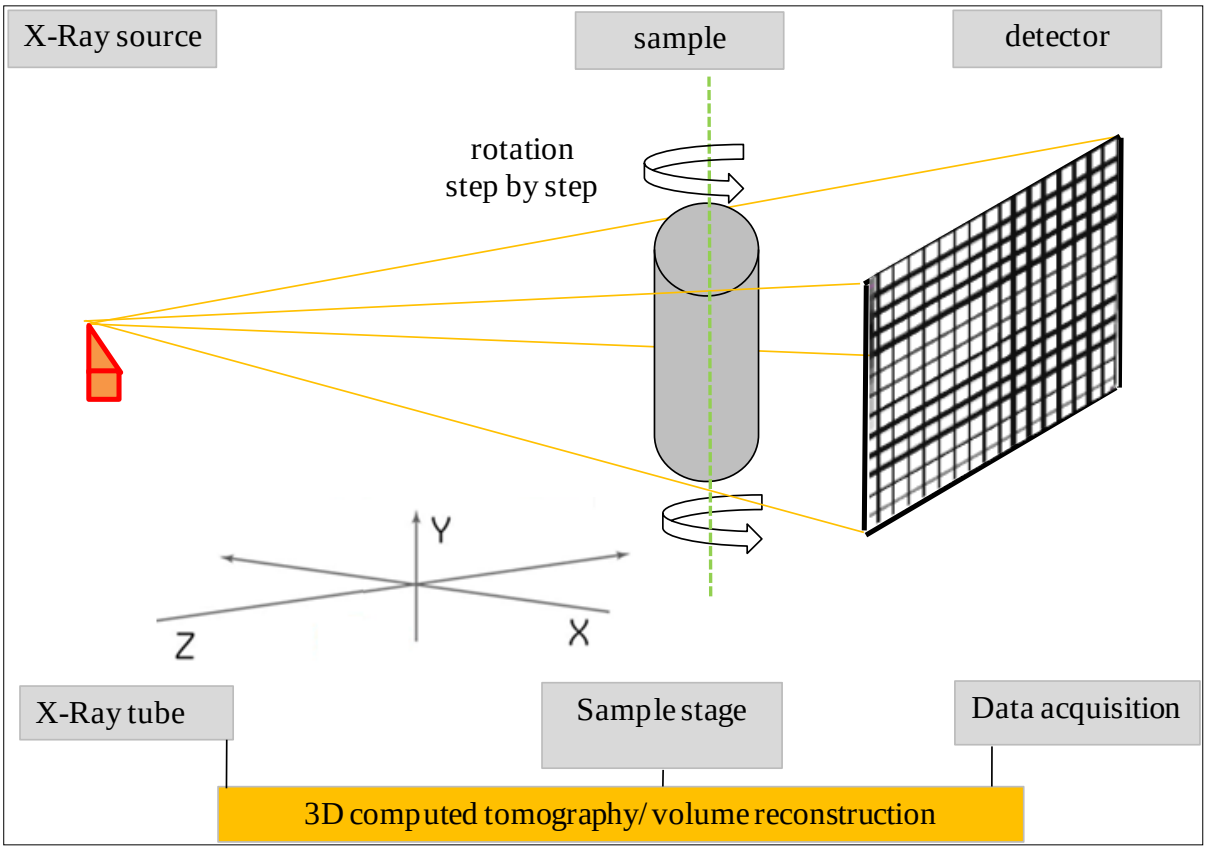



Figure 6.2: Illustration of basic operation principles and components of 3D X-ray computed tomography. X-rays are produced from a tube at a point source in a form of a cone beam and pass through a rotating sample. The attenuated X-ray signal results are recorded by the detector. The data acquired are reconstructed into a 3D volume by volume reconstruction software (Nshimirimana *et al.*, 2011).

Practical operation of 3D µXCT involves the understanding and use of the following aspects:

### *6.2.1. Grey values*

Grey values are assigned to images in which the value of each voxel (vo=volume and xel=element or a 3D pixel), is a single unit of a volume element referring to intensity. Images represented by grey values are composed of shades of grey, varying from black at the weakest intensity to white at the strongest (Figure 6.3; Stephen, 2006). The grey value is inversely related to the attenuation coefficient of mineral components in a sample; low attenuating minerals display high grey values as a result of the low intensity and appear brighter; whereas high attenuating minerals will have low grey values and appear darker in the image. Grey values, (65536 of these in a 16bit image) are plotted against the number of voxels displaying such values, to form histograms of the total sample with peaks representing a specific type of mineral or mineral group.

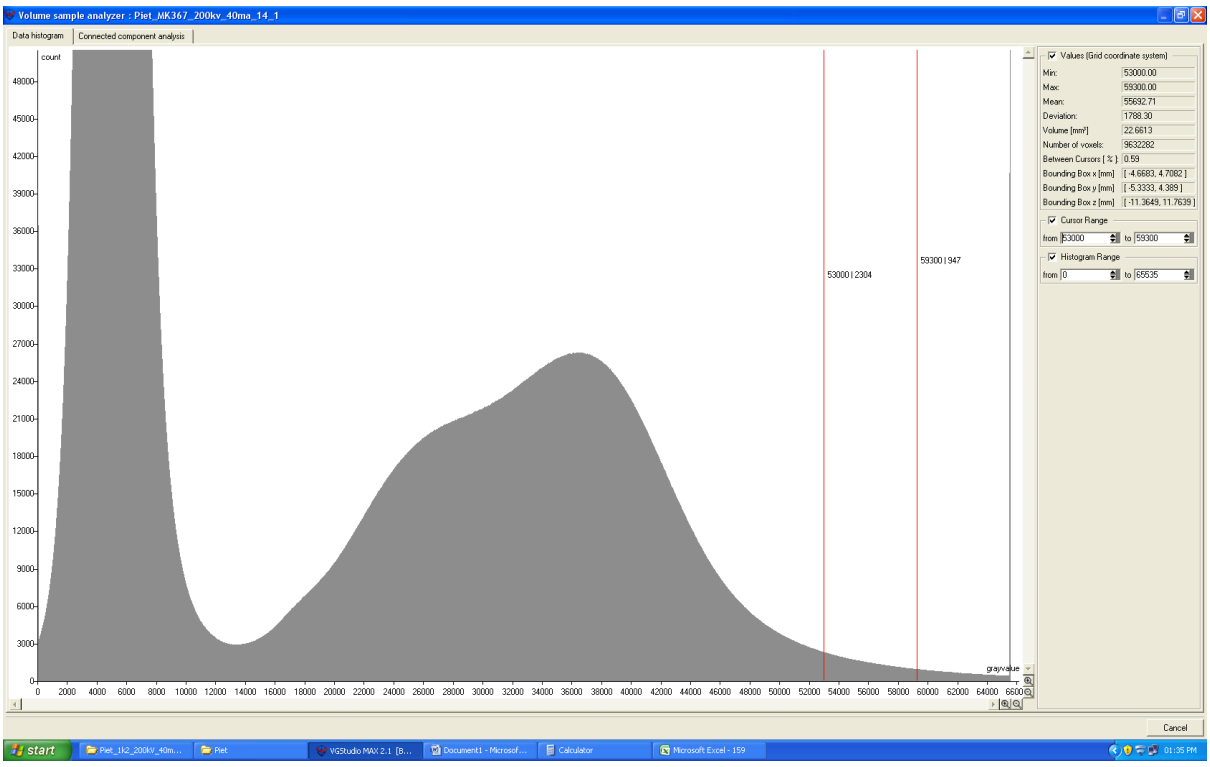



Figure 6.3: Illustration of a 3D XCT histogram obtained from a VGStudioMax imaging software.

### *6.2.2. Thresholding*

The distribution of grey values into distinct peaks in the histograms make it theoretically possible to distinguish mineral components from one another, also allowing the separation of a single mineral component from the rest of the minerals in a sample with the assistance of

the grey value range of that particular mineral of interest (Figure 6.4). This phenomenon is known as thresholding or segmentation (Long et al., 2009).

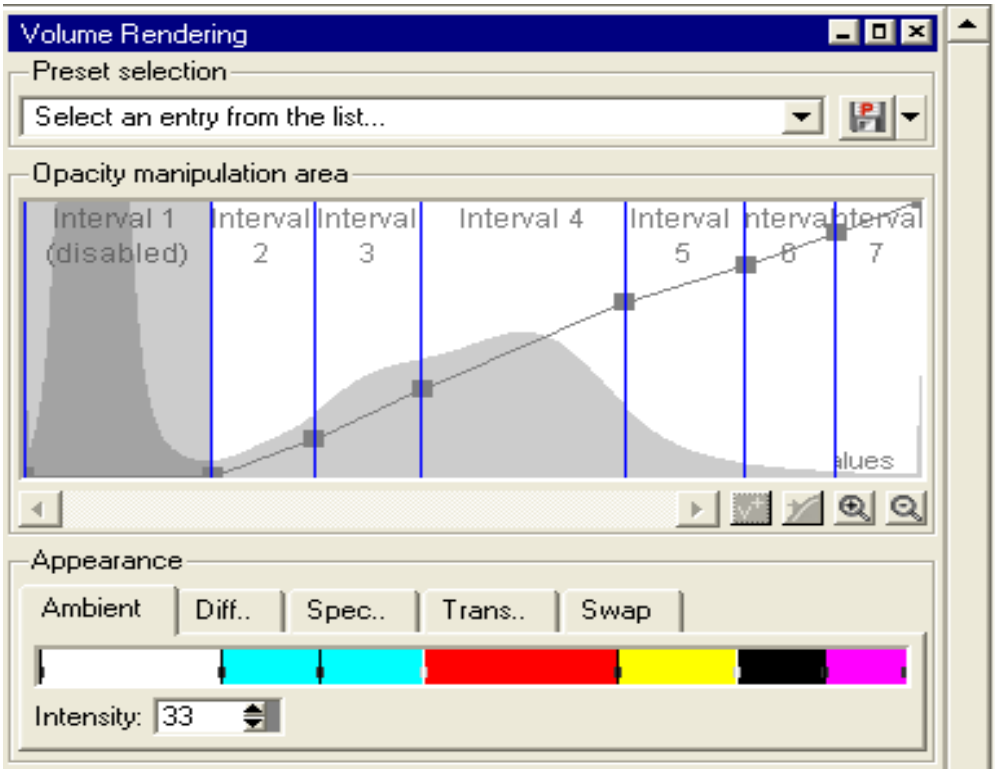



Figure 6.4: Illustration of thresholding, where a grey value histogram has been split into several intervals. Each interval represents a mineral group equivalent to its specific grey values.

### *6.2.3. Spatial Resolution*

Spatial resolution refers to the size of the smallest object that can be resolved in an image and is limited by the voxel size, i.e. the smallest resolvable object cannot be smaller than the pixel size; in this case it refers to mineral grains (Figure 6.5).

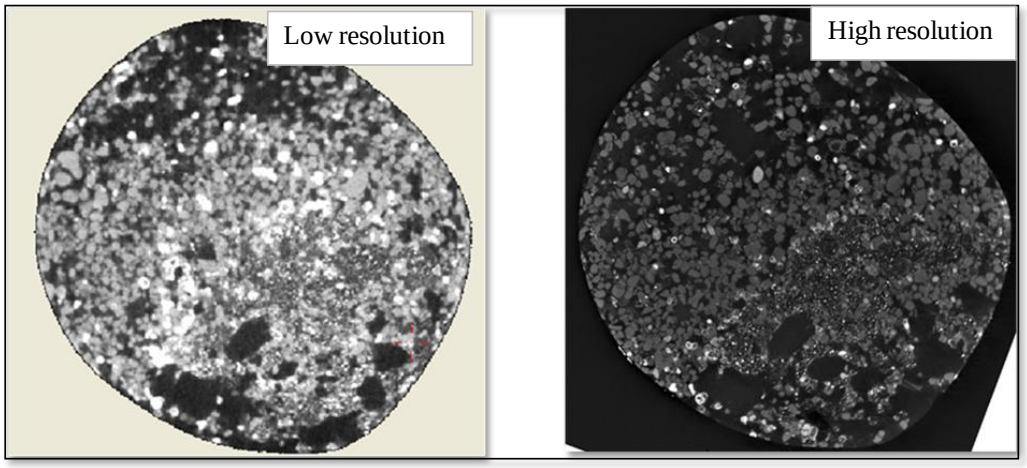



Figure 6.5: Illustration of tomograms of the same sample at different resolutions (low and high resolution). At low resolution, minerals touch one another and contrast is not well defined; at high resolution individual minerals are now distinguished and contrast is well-defined.

### *6.2.4. Partial Volume Effect*

Each voxel in a CT image represents the attenuation properties of a specific mineral component volume; if that volume is comprised of a number of different objects then the resulting grey value represents some average of their properties, if an object is smaller than the volume, its density will be averaged with the information in the remainder of the volume. This is termed the partial volume effect (Ketcham and Carlson, 2001). Furthermore, because of the inherent resolution limitations of X-ray CT, all material boundaries are blurred to some extent, and thus the material in any one voxel can affect grey values of surrounding voxels (Ketcham and Carlson, 2001).

## 6.3. Methodology

### *6.3.1. Sample Preparation*

Three samples (1K4 of Kopanang Mine C Facies 440 geozone, 3K2 of Kopanang Mine C Facies 460 geozone and MK367 of Moab Khotsong Mine A Facies 370 geozone) were selected and investigated using 3D μXCT. Sample 1k4 represents the Vaal Reef C Facies in the 440 Geozone, sample 3k2 represents the Vaal Reef C Facies in the 460 geozone and sample MK367 represents the Vaal Reef A Facies in the 370 geozone. The samples were cut into ~10 mm thick and 25 mm long cylindrical shapes. The cutting was only to ensure that the sample could be positioned to fit the field of view (FOV) of the beam, to have enough penetration of X-rays through the sample at an appropriate X-ray energy level and to achieve optimum spatial resolution; the most effective shape for 3D μXCT scans is cylindrical

(Ketcham and Carlson, 2001). The samples were selected on the basis of high uranium and gold grades, but also the carbonaceous matter that is known to host uraninite grains. After 3D μXCT scanning, the samples were physically cut at appropriate positions, so as to intersect the uraninite and gold grains acquired as visualised in the 3D tomograms. The appropriate surfaces were polished and analysed by conventional 2D mineralogical techniques (optical microscopy and SEM) at Mintek.

*6.3.2. Instrumentation and Sample Setup*

Each sample was scanned by the 3D μXCT instrument hosted at Necsa, Pelindaba, South Africa. The facility is an XTek XT H 225 L system equipped with the following:

- SOURCE
    - 225 kV X-ray energy source
    - Micro-focus source with 3μm focal spot size
    - X-ray targets: Mo, W, Cu, Ag
- DETECTOR
    - 2048 x 2048 pixel array flat panel (PERKIN ELMER)
- SOFTWARE (IMAGING)
    - Reconstruction to virtual 3D image
    - VGStudioMax 2.1 and Image-J for visualisation and analysis

The size of a sample is an important factor contributing to resolution during the acquisition of μXCT images; the smaller the size of a sample, the higher the resolution and contrast that is possible on individual mineral components. A second important factor is the size limitation of the scanner; this is determined by the ratio of the distance between the source and the detector over the distance between the source and the sample. A third factor is the focal spot size of the X-ray point source; the size of the focal spot needs to be larger than the mineral sizes in order to visualise the minerals (Long *et al*., 2009). In this study, cylindrical shapes of 10 x 25 mm were prepared to give a good representation of the mineral distribution.

*6.3.3. Imaging (Tomography)*

Imaging was undertaken on all 3 samples, and the first important step was to calculate attenuation coefficients (μ) of the different mineral components in the samples (Table 6.2) at different scanning energies (kV). The main objective for these simulations was to determine

whether 3D μXCT is able to distinguish these minerals from one another and also to visualise the uranium minerals-carbonaceous matter association, since distinction, is related to the differences in the attenuation of minerals. Different X-ray energies (100, 120, 160, 200 and 220 kV) were used on a Tungsten (W) target material to compare resolution and contrast between minerals.

Table 6.2: Linear attenuation coefficients of minerals at different scanning energies. The blue columns represent the two energies (120 and 200 kV) that showed best contrast in distinguishing the common mineral phases in the samples.

| Ideal Mineral formula | Density ($g/cm^3$) | 100 kV $\mu(cm^{-1})$ | 120 kV $\mu(cm^{-1})$ | 160 kV $\mu(cm^{-1})$ | 200 kV $\mu(cm^{-1})$ | 220 kV $\mu(cm^{-1})$ |
|---|---|---|---|---|---|---|
| C | 2.26 | 0.402 | 0.398 | 0.409 | 0.435 | 0.454 |
| $SiO_2$ | 2.65 | 0.746 | 0.682 | 0.6 | 0.543 | 0.526 |
| $FeS_2$ | 4.8 | 4.6 | 3.76 | 2.9 | 2.23 | 2.17 |
| $UO_2$ | 11 | 83 | 69.5 | 54.6 | 43.7 | 40.6 |
| Au | 19 | 107 | 88 | 70.2 | 56.7 | 52.5 |
| % Difference between C & $SiO_2$ (relation to $SiO_2$) | | 46 | 41 | 32 | 19 | 13 |
| % Difference between $UO_2$ & Au (relation to Au) | | 22.4 | 21 | 22.2 | 22.9 | 22.5 |

The penetration of X-rays is influenced by the density and the thickness of the sample. For a thicker sample with dense a matrix, penetration is achieved by high energy (e.g. around 200kV), however, if the sample is relatively thin (~10 mm) and composed of a less dense matrix such as quartz, low energy (120kV) is suitable. Table 6.2 also shows that at low energies (e.g. 120kV) there is a large gap in attenuation coefficients of minerals and therefore this resulted in higher contrast than evident when using higher energies (200kV). The choice in energy influences contrast in minerals and X-ray penetration in a sample (Table 6.3). In this study the best scanning parameters were achieved at 120 kV due to the thinness of the sample and the low density of the silicate matrices that allowed easy penetration, and also that low energy (120kV) gives high contrast in minerals such as quartz and the carbonaceous matter, implying that the uraninite-carbon association will be visualised at 120kV (Tables 6.2 and 6.3). Additionally, the size of the sample was suitable to be placed closer to the X-ray

tube source and was within the FOV, which also contributed to magnifying the sample in order to better visualise the minerals.

Table 6.3: Penetration, sample density and attenuation differences at two energies (120kV and 200kV, respectively).

| | Low energy (120kV) | High energy (200kV) |
|---|---|---|
| Penetration and density of material | • Thin sample (~10 mm)<br>• Low density matrix | • Thicker samples (~5cm)<br>• High density matrix |
| Attenuation differences | High contrast (best in distinguishing minerals) | Low contrast in distinguishing minerals |

*6.3.4. Image Analysis and 2D Correlation*

Petrographic studies in the previous chapters showed that the Vaal Reef mineralogy comprises mainly the following minerals, in general decreasing order of abundance: quartz, pyrite, phyllosilicates, carbonaceous matter, uranium-bearing minerals and gold. The following accessory minerals are also present: rutile, zircon and chromite.

VGStudioMax 2.1 imaging software was used mainly for μXCT 3D visualisation (Figure 6.6), analyses and acquisition of mineral information from samples. Information obtained from the grey value histograms generated by the software was useful in matching mineral components in a sample with peaks on the histogram and these peaks were separated from each other by classifying them as intervals (Figure 6.7) using the thresholding procedure. These intervals have been assigned to minerals with which they correspond, with the aid of optical microscopy and attenuation coefficient data. Thresholding was done based on these overlaps to determine if the data on samples were reproducible and consistent in all the samples, to identify which intervals in grey values are expected for which mineral components, the extent to which these grey values overlap for different mineral components and also to define uncertainties in volume percentages of the uranium-bearing minerals in the samples.

For all three samples (1k4, 3k2 and Mk367), slices of interest were noted and their corresponding physical surfaces were studied using 2D mineralogical techniques i.e. optical microscopy and SEM. The 2D techniques were used for validation of mineral identification and other properties such as size, shape and textural distribution acquired in 3D. The procedure is illustrated in Figure 6.3 following the above procedure, an important stage was the matching of the selected 3D axial μXCT slice with the polished section obtained on cutting the sample to make the polished section.

In order to know the exact 3D slice position that needed to be prepared for thin section cutting, the spatial resolution (voxel size) of the 3D volume and the slice number (top to bottom of sample) are important. The calculations involved are explained below:

- Spatial resolution obtained is 0.06 μm, equivalent to 0.006 mm, this is also the thickness of each slice.
- Slice number 806 (from top part of sample to bottom) was chosen as the slice of interest.
- Length of sample (25 mm) was considered.

To locate the physical surface of slice number 806 from the top, where the sample was to be cut, the slice number was multiplied with the spatial resolution of the sample (806 x 0.006 mm = 4.8 mm). The sample was cut from top to ~4.5 mm, followed by grinding and polishing until the 4.8 mm mark representing the slice number 806 was reached, representing the desired surface, which was then studied using optical microscopy and SEM. The main reason for cutting the sample at 4.5 mm from top was due to the thickness of the diamond cutting saw which was relatively thick, therefore the aim was to avoid cutting at 4.8 mm as this was going to cut out the slice number 806, as the slice of interest; grinding from 4.5 to 4.8 was the best solution.

The main objective of using 2D techniques was to validate the 3D μXCT results as the latter is only capable of visualisation of features. Optical microscopy was used primarily for mineral identification and SEM was used for determination of the chemical composition of minerals by using energy dispersive spectrometry (EDS) analysis. This also allowed analysis

of small-sized minerals as small as 20 to 5 μm, particularly the uranium-bearing minerals enclosed by the carbonaceous material.

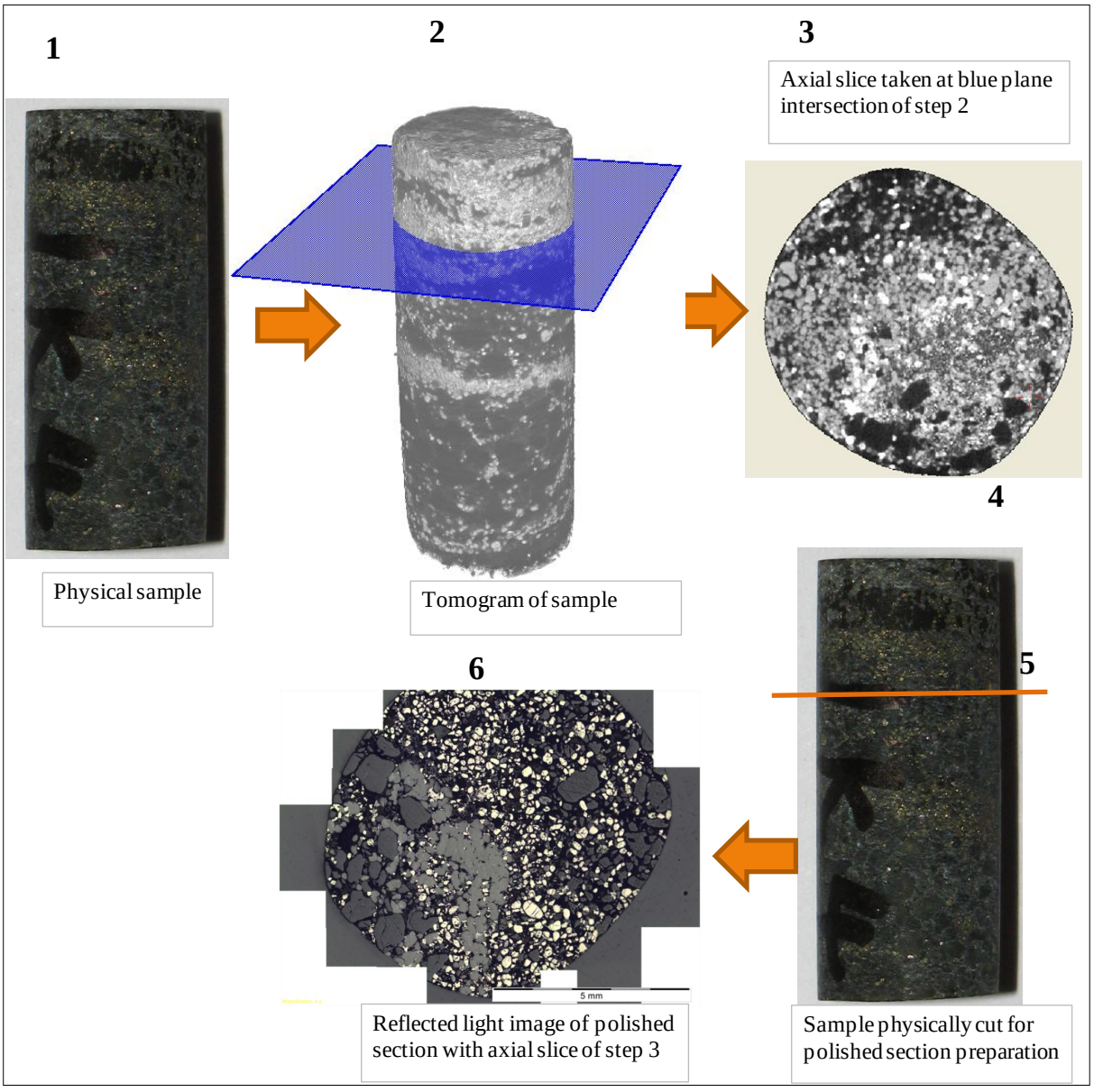



Figure 6.6: Illustration of steps taken from 3D imaging until a polished section is prepared in order to compare a specific 3D slice and 2D optical microscopy and SEM results. 1) The sample was loaded in the μCT instrument. 2) A 3D volume of the sample was acquired. 3) An axial slice of the 3D volume of the sample was viewed for mineral distribution. 4) Sample taken for preparation of a polished section, the sample was physically cut parallel to the selected axial slice then prepared as a polished section corresponding with the axial slice. 5) Sample was cut where the slice of interest was selected in step 3 after calculating the exact thickness where the sample is to be cut to expose the 3D μCT slice. 5) Polished section produced and studied by optical microscopy and SEM for mineral identification, textural relationships, size and shape observations.

## 6.4. Results and Discussion

*6.4.1. Imaging and Visualisation of Tomograms and 2D Microscopy Images*

As discussed, the increase in grey values on a histogram is directly related to the linear attenuation coefficients of minerals; peaks in the histogram can be grouped into intervals. The grey level intervals assigned to different minerals are as follows:

Interval 1: Air surrounding the sample acquired as the sample is scanned (0 to 50)

Interval 2: Carbonaceous matter 50 to 100

Interval 3: quartz and phyllosilicates (100 to 150)

Interval 4: sulphide minerals (pyrite, pyrrhotite, arsenopyrite, chalcopyrite, etc.) (150 to 350)

Interval 5: uranium minerals (1800) and gold (~3200) were identified

No distinct peaks were noted for these last two minerals, owing to their very low concentrations in the samples.

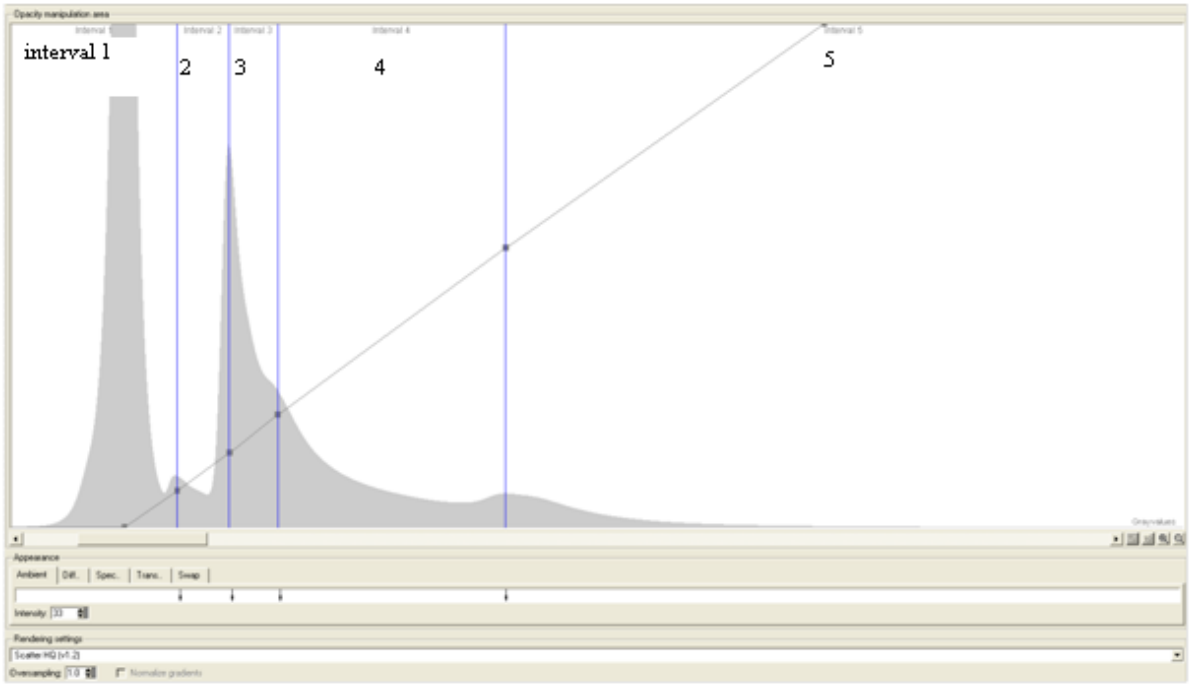



Figure 6.7: Example of a grey value histogram obtained from VGStudioMax 2.1 imaging software showing peaks that represent intervals of (1) air, carbonaceous matter (2) quartz and silicate minerals (3), sulphide minerals (4), uranium-bearing minerals and gold (5) derived from thresholding.

Even with intervals being made from thresholding, there is overlapping of mineral grey values. This is suggested to be as a result of variability in chemical composition of these minerals i.e. phyllosilicates (muscovite, chlorite, chloritoid and pyrophyllite), sulphides (pyrite, chalcopyrite, arsenopyrite, pyrrhotite and galena) and the uranium-bearing minerals (uraninite, brannerite and uraniferous leucoxene); this variation was confirmed by the electron microprobe analyses (EMPA) in Chapter 4, section 4.5. One peak, therefore, will necessarily represent the entire phyllosilicate mineral suite as a result of their similarities in linear attenuation coefficients, the same applies to the sulphides and uranium-bearing minerals respectively. The end result of this wide composition of minerals is that their peaks overlap on the histogram.

The phenomenon described above is applicable to most of the mineral components and this made it difficult to confidently distinguish specific grey values of minerals that corresponded with the peaks on the histograms. Thus, broad intervals were selected to only distinguish mineral groups.

It is important to note that in all these samples, scanning by 3D µXCT took about 45 minutes; the entire process of loading the sample into the instrument and scanning it and reconstructing the volume, therefore, can take up to an hour. Such analytical speed therefore, makes 3D µXCT relatively faster in data acquisition compared with the 2D conventional mineralogical techniques which takes up to approximately 3 hours to perfom the full cycle of preparing a sample surface for observation.

Whereas thresholding could not entirely separate individual minerals from each other based on grey values, optical and EDS differentiation of these minerals is possible, and this ability was used to help with identifying minerals in the intervals chosen from the grey value histograms.

Optical microscopy and SEM showed the following minerals in the polished section (1k4) in their order of abundance: quartz, pyrite, carbonaceous matter, uraninite, rutile, uraniferous leucoxene and brannerite, some of which are illustrated in Figure 6.8 from the SEM. Results showed that the majority of the uranium mineralisation is found enclosed in the carbonaceous matter; with only a few occurrences found in association with the allogenic quartz and pyrite in the matrix. The main minerals of interest were gold and uranium-bearing minerals. One

grain of gold was identified in the section in both the optical and the SEM images (Figure 6.8) and this was verified by the SEM EDS analysis.

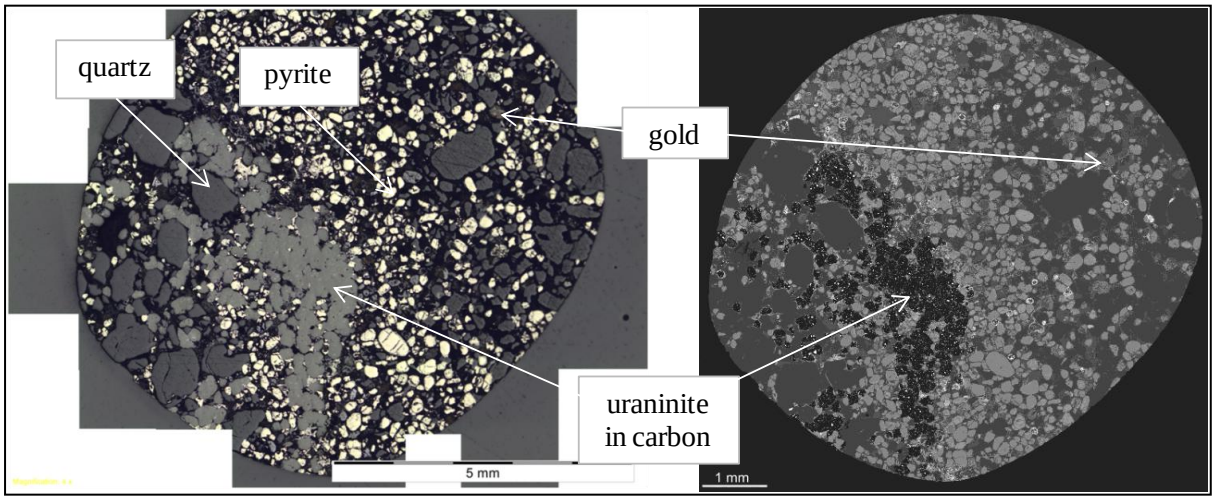



Figure 6.8: Photomicrograph (left) and backscattered electron (BSE) image (right) of sample 1k4 showing the distribution of uraninite in the carbonaceous matter and a gold grain (top right).

The 2D BSE image was compared with the 3D tomogram slice to evaluate whether μXCT is able to visualize gold and uranium-bearing minerals and also to assess the reliability of information from the 3D μXCT. The majority of the common features such as texture, grain size, grain shapes and mineral associations recorded from the BSE image were easily recorded by the 3D μXCT as well (Figure 6.8). The allogenic shapes of both the main constituent minerals quartz and pyrite were readily observed, together with the small-sized minerals such as uraninite. The actual carbon-uraninite association, however, could not be confidently defined as a result of the very low attenuation of the carbonaceous matter, which is close to the attenuation coefficienct of the air surrounding the sample, and also the small size of the uraninite grains due to the limited spatial resolution of 6 μm.

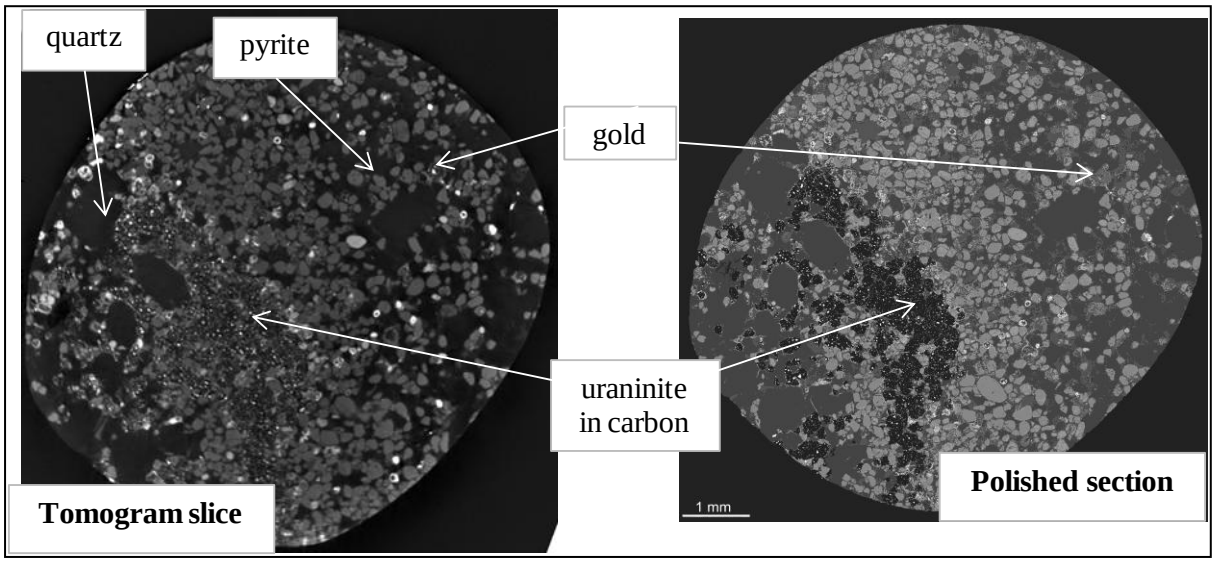



Figure 6.9: Comparison of 3D tomogram slice (left) and BSE image (right) of sample 1k4.

For all three samples (1k4, 3k2 and MK 367), full axial tomograms were investigated for size differences between the uraninite grains in the quartz-pyrite matrix and the uraninite grain in the carbonaceous matter. A tomogram slice from sample 1k4 shows that the uraninite grains in the matrix are generally large in size (up to 200 µm) and sub-round to round in shape (Figure 6.10). These large round uraninite grains are distributed throughout the matrix in the sample and are mainly surrounded by round or detrital pyrite grains.

In the same slice of sample 1k4, uraninite grains are also observed enclosed in the carbonaceous matter. The size of the uraninite grains in this carbonaceous occurrence is relatively small as compared to the earlier uraninite grains in the quartz-pyrite matrix occurrence, and show sizes of up to 80 – 90 µm. The shapes of these small-sized grains are mainly angular to sub-round as a result of being broken apart by carbon growth, hence the small sizes and angular shapes. It is important to note that the carbonaceous matter in the tomogram images is rather difficult to visualize as it has a very low attenuation coefficient close to that of the background (0.398 $cm^{-1}$).

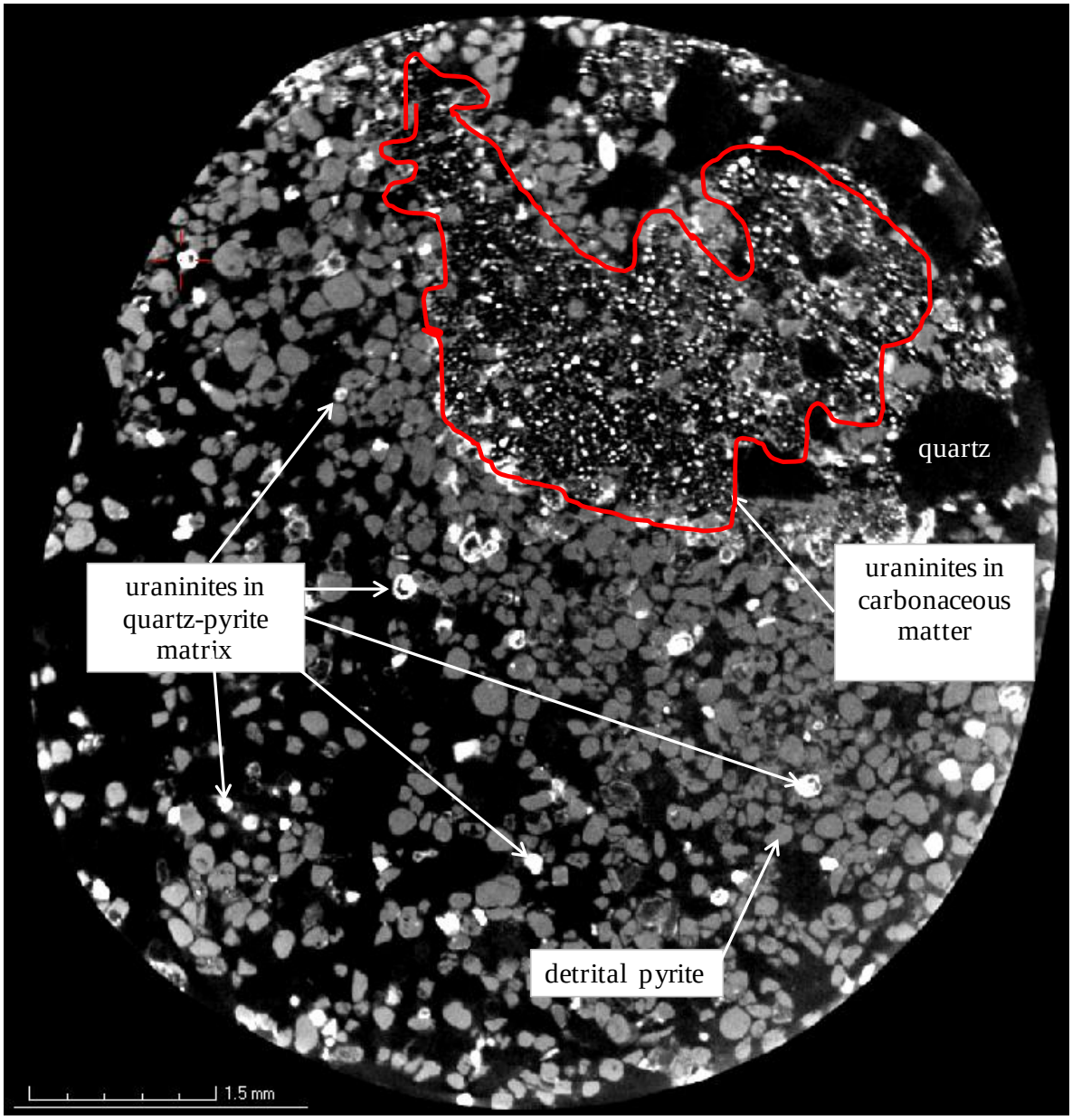



Figure 6.10: A tomogram slice of sample 1k4 showing the distribution of uraninite grains in the quartz-pyrite matrix and the carbonaceous matter (outlined in red).

A similar distribution and occurrence of uraninite grains in the quartz-pyrite and carbonaceous matter was also found in sample 3k2 (Figure 6.11). The size distribution of uraninite grains in the quartz-pyrite matrix is mainly also around 200 µm as well. The shape of these minerals also ranges from sub-round to well-rounded. The uraninite grains enclosed in the carbonaceous matter have grain sizes of up to around 80 µm as well, and their shapes are mainly angular to sub-round.

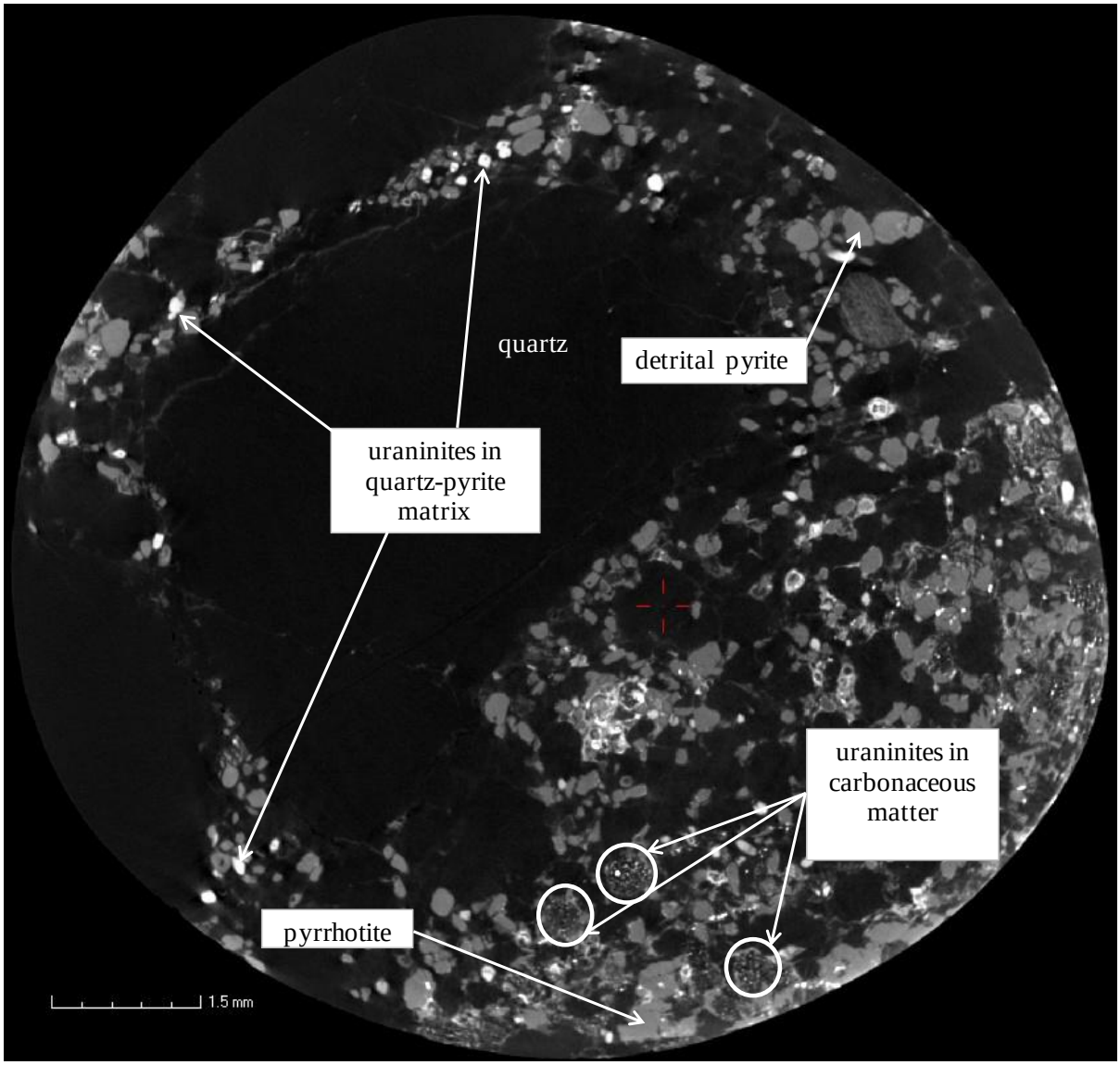



Figure 6.11: A tomogram slice of sample 3k2 showing the distribution of uraninite grains in the quartz-pyrite matrix and the carbonaceous matter (fly-speck carbon).

In sample Mk 367, there is a high abundance of both the carbonaceous matter and uraninite grains (Figure 6.12). The carbonaceous matter is developed throughout the sample and is observed breaking down and replacing the majority of the uraninite grains. The uraninite grains that are not affected by the carbonaceous matter replacement and breakdown generally show a more oval to round shape with sizes around 200 µm. The round and large grains of uraninite occur close to the detrital quartz and pyrite. The rest of the small-sized uraninite grains in the sample show intensive fragmention by the carbonaceous matter.

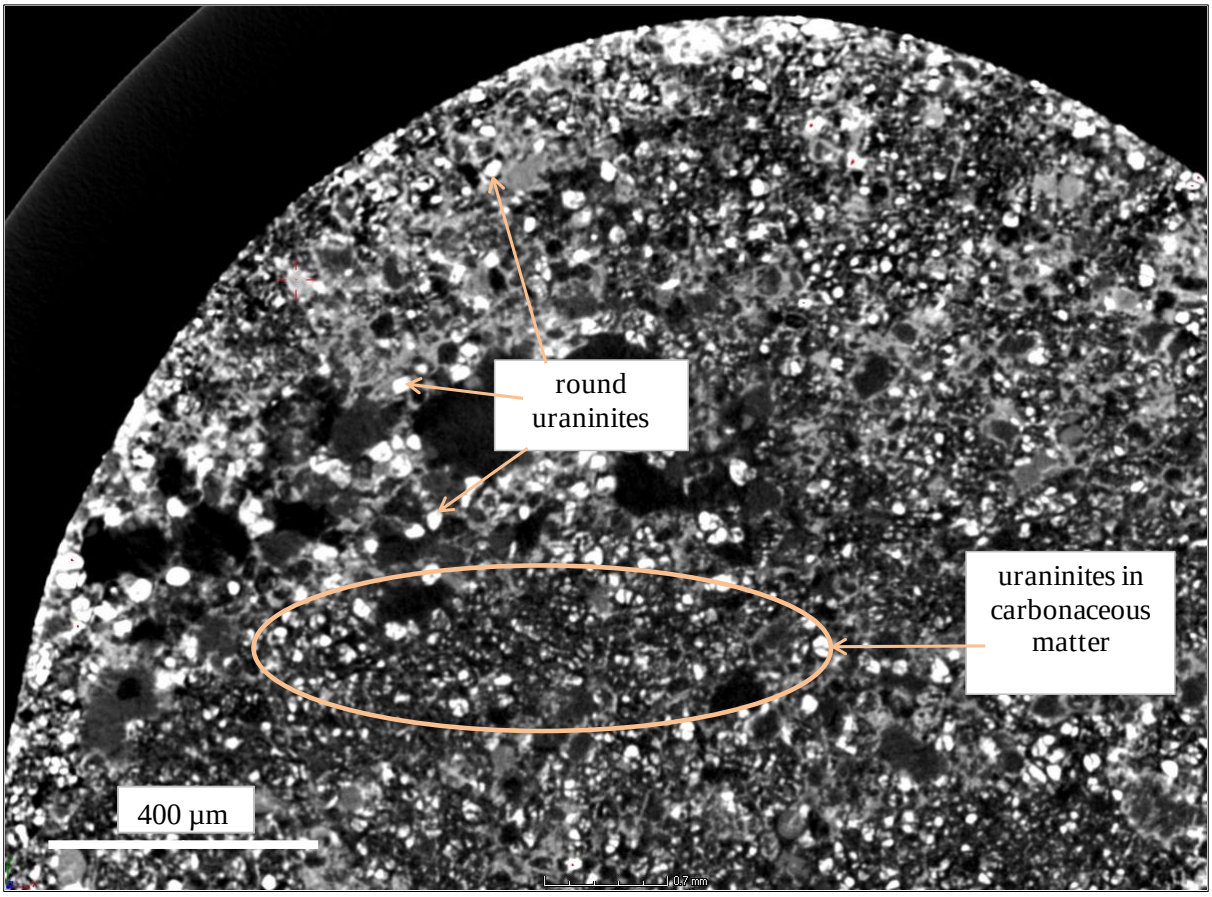



Figure 6.12: A tomogram slice of sample Mk367 showing the distribution of uraninite grains in the quartz-pyrite matrix and the carbonaceous matter.

A full 3D µXCT scan of sample 3k2 was done and a cross-section visual analysis was undertaken using VGStudioMax 2.1 software (Figure 6.13). The results from the virtual cross-sections (sagittal projections) showed an entire distribution of mineral components in the sample. From the cross-sections the following were noted:

- Uranium minerals (mainly uraninite) occur in a quartz-pyrite matrix and are enclosed in carbonaceous matter in two shapes, round and angular fragmented respectively.
- Uraninites in the quartz-pyrite matrix showed larger grain sizes that were more rounded than the ones occurring in carbonaceous matter (which were fragmented).
- Secondary sulphide minerals (pyrrhotite) infilling cracks in the quartz grains.

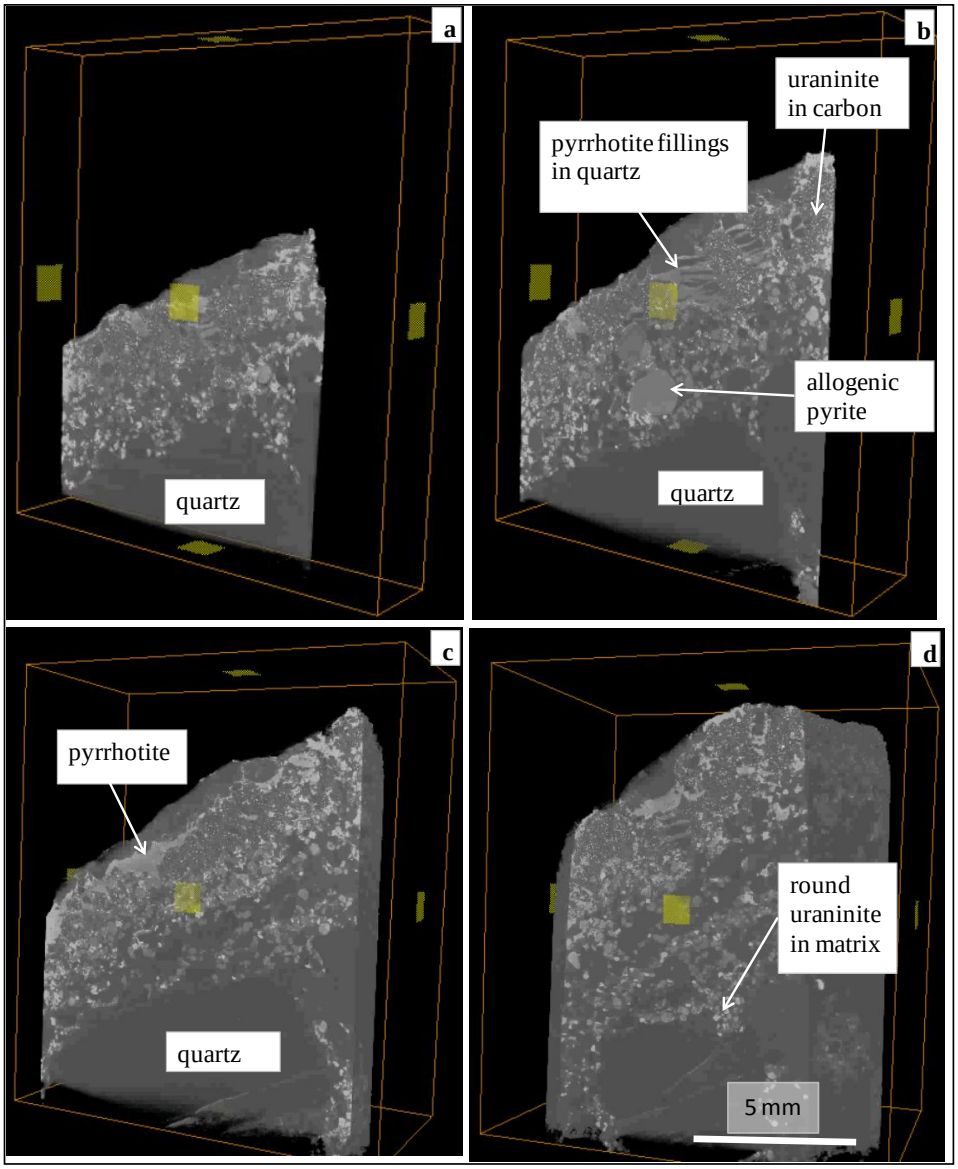



Figure 6.13: A series of longitudinal tomograms from sample 3k2 illustrating the 3D nature and distribution of uranium minerals (white), sulphide minerals (light grey) and quartz (dark grey).

Following the points mentioned above, it is clear that 3D μXCT also can be used to assess and develop the paragenetic sequence of the Vaal Reef samples. The technique contributed in assessing mineral associations and relationships from a series of slices through a 3D volume in a short time (an hour) for data acquisition. Analysis of this data is the only part of the analytical procedure that may take hours depending on the level of investigation.

### *6.4.2. Quantitative Analysis of Uranium-bearing Minerals*

The mineral identity validation of 3D data by 2D information made it possible to investigate shape parameters and proportions of gold and uranium minerals; these two minerals were

grouped together as they have high grey values, more importantly, gold has higher grey values, but very small grain sizes therefore, it is difficult to distinguish from the uranium-bearing minerals. VGStudioMax and Image-J imaging software were used for this study. Using the histogram data of Figure 6.7 from VGStudio Max imaging software, it was possible to extract the grey values interval for the minerals of interest and work on these selected minerals as discrete components. Figure 6.13 shows quartz, pyrite, pyrrhotite and uranium bearing-minerals. The uranium bearing-minerals (and gold) in the volume were isolated and extracted and are presented in Figure 6.14; the rest of the minerals are transparent in this image.

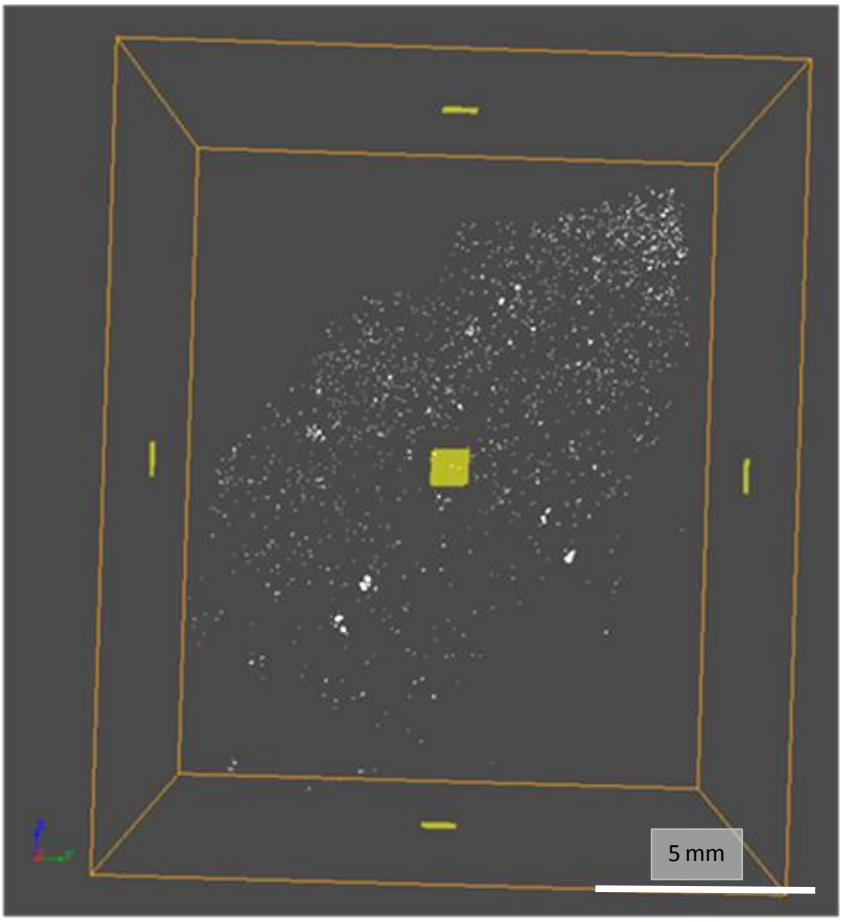



Figure 6.14: 3D visualisation of the distribution of uranium-bearing minerals and gold (both minerals are seen as one component) from sample 3k2. Other mineral components are transparent allowing visualisation of these minerals only.

All the information on the particular mineral of interest was acquired from the defect detection analysis and volume sample analyser in VGStudioMax; the imaging software was useful in providing information on the selected mineral of interest, in this case uranium-bearing minerals, classed as uraninite.

Once visualised, (Figure 6.14) these mineral grains were characterised for sizes, shapes distribution and volume of the uranium-bearing minerals (e.g. Figure 6.15). In sample 3k2, the volume sample analyser showed that the uranium minerals constitute ~0.34% of the total volume of the sample.

VGStudioMax was used first to extract the uranium-bearing minerals by thresholding, and visualising the uranium minerals as a single mineral component; to achieve this, 100 slices (slice numbers 1516 to 1616 in sample 1k4) were selected for analysis as they showed occurrences of uraninite grains in both the matrix and enclosed within the carbonaceous matter. Following the extraction of the uranium minerals component, Image-J was used to separate the uraninite grains in the matrix from the uraninite grains enclosed by the carbonaceous matter on each of the 100 slices (Figure 6.15).

Sizes in the form of equivalent circle and equivalent sphere diameters (ECD and ESD, respectively) of the individual uraninite grains were calculated from the area of each individual grain from the results obtained using the following formula:

$$ECD = 2*(\text{“Area”}/\pi)^{-0.5} \quad \text{(for 2D)} \quad \text{Eq. 6.3}$$

$$ECD = ((6*\text{Volume})/\pi)^{-0.3} \quad \text{(for 3D)} \quad \text{Eq. 6.4}$$

Both software results are presented, it being borne in mind that Image-J operates on the basis of 2D information from individual slices, whereas VGStudioMax works directly from the 3D volume.

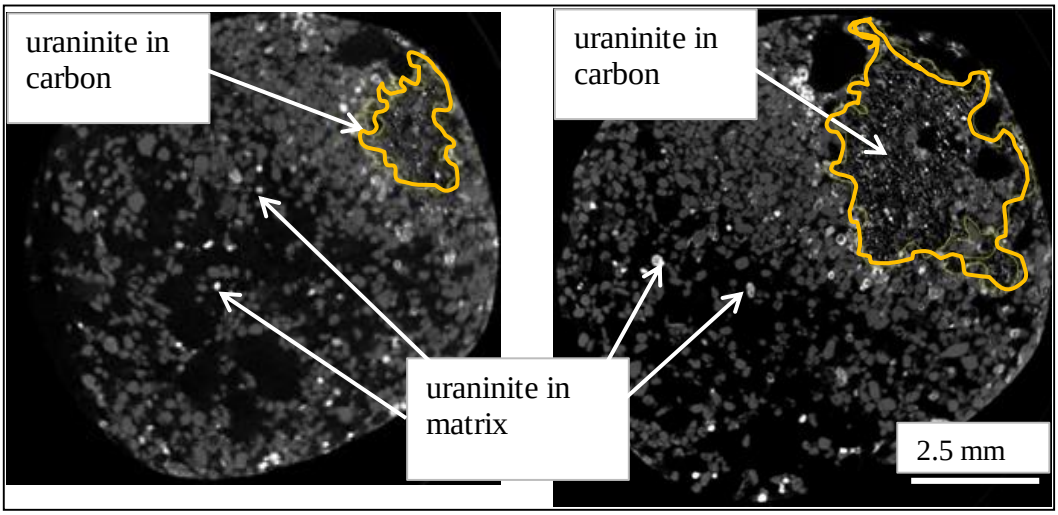



Figure 6.15: Tomogram slices from sample 1k4 showing the distribution of uraninite grains in the matrix and carbonaceous matter (outlined in yellow) acquired from Image J software.

*6.4.3. 3D Application (VGStudioMax)*

VGStudioMax was useful in comparing the uranium group of minerals in the quartz-pyrite matrix with the ones enclosed by the carbonaceous matter, and evaluating their differences in grain size distribution and shape parameters. This allowed visualisation of the uranium group of minerals distribution in the matrix as a 3D volume only (Figure 6.16). From the figure, different shapes of uraninites, mainly sub-round to round are noted to be common in the sample; the grey block in the image represents the uranium group of minerals in the carbonaceous matter data that has been removed or extracted in this analysis, so that only the matrix hosted uranium and gold cluster would remain and be analysed separately. The carbonaceous matter-uranium group of minerals cluster will be explained in the next 2D application sub-section.

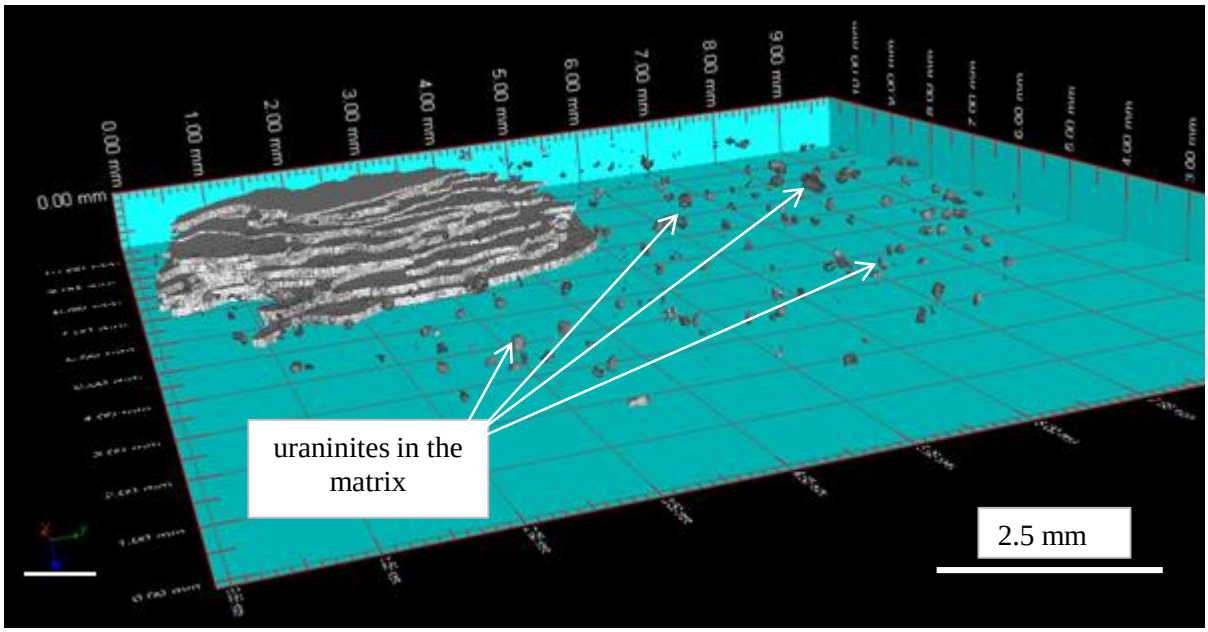



Figure 6.16: Illustration of 3D volume from slice 1515 to slice 1616 obtained from sample 1k4 using VGStudioMax showing only uranium group of minerals occurring in the matrix.

The 3D shape analysis was attempted by calculating sphericity of the individual grains and the results show that this ranges from 0.2 – 0.9. However, 3D statistical results on the sizes of the individual grains show less variation in size of uraninite grains in the matrix and carbonaceous matter (Figure 6.17), therefore, confirming two distinct populations. About 889 grains in the uranium group of minerals in the carbonaceous populations were analysed for grain ESD. Results show that over 70 % grains have grain sizes around 60 – 90 µm, 20 % of

the grains with ESD between 90 – 120 µm. About 5 % of the grains show sizes between 120 – 150 µm, and 1 % of the grains just over 180 µm.

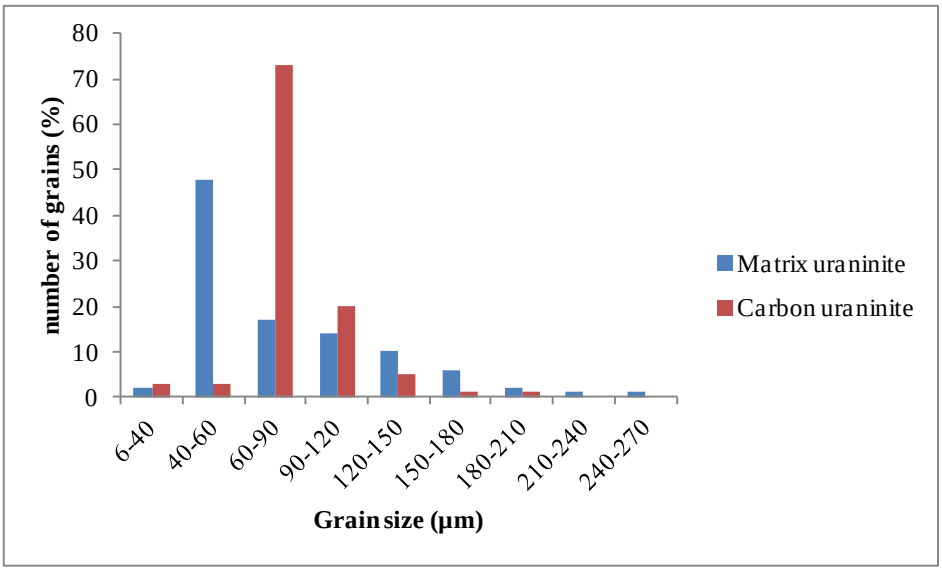



Figure 6.17: A plot of size vs number of grains in percentage in the matrix and the carbonaceous matter.

The larger uraninite grains (>200 µm) are less in number as compared to the smaller-sized grains (~40 µm). The data show that around 70 % by number of the uraninite grains in the carbonaceous matter have sizes between 60 – 90 µm.

The larger grain sizes of the uranium group of minerals in the carbonaceous matter has been noted as being in direct contrast to petrographic observation, but the discrepancy is explained as follows: VGStudioMax software at this point is unable to separate these minerals so that they can be separated from one another; rather, they occur attached as one grain. This affects the accuracy in the calculation of actual grain sizes of individual uranium group of minerals. The main reason behind this is the resolution of the 3D µXCT; the technique gave resolution down to 6 µm in the samples, therefore implying that minerals below and around 6 µm in size could not be visualised and also that mineral grains spaced within 6 µm from each other will therefore, be grouped as one mineral grain. Minerals that touch one another cannot be separated and as a result the software groups all these minerals as a single mineral component. An example is shown where four grains of uranium group of minerals are grouped as a single grain (Figure 6.18).

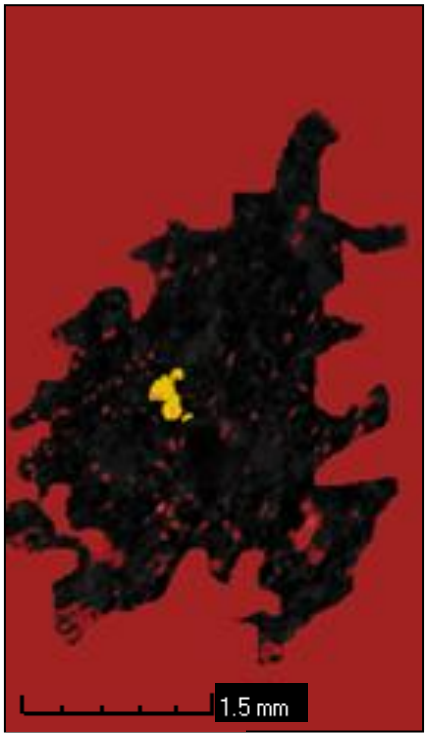



Figure 6.18: Tomogram slice of four gold and uranium group of minerals grains (highlighted in yellow) in the carbonaceous matter (highlighted in black) touching one another and analysed as one grain.

*6.4.4. 2D Application (Image-J)*

Image-J results were useful in giving 2D grain shapes of the uranium group of minerals in both the matrix and the carbonaceous matter (Figure 6.19). The software could not provide accurate grain sizes of the actual grains, not only because of resolution effects, but also because it adds up each slice therefore multiplying single mineral grains that extend across a series of slices and therefore, overestimating the number of grains in the stack of the 100 slices. An attempt was made to analyse roundness of the uranium group of minerals grains in both the matrix and the carbonaceous matter using the 2D Image-J software (Figure 6.19). The results show that, overall, the uranium group of minerals grains have an average roundness of 0.67 ranging from 0.2 – 1. Therefore, following the definition of 2D roundness, this means that the uranium group of minerals grains in the sample are sub-rounded to rounded as their average roundness is close to 1. No difference is calculated in roundness between the matrix and the carbonaceous matter uranium group of minerals grains. It is suggested that this is because of poor resolution that causes most grains to appear round rather than angular, owing to the partial volume effect (section 6.1). The 2D nature of the

Image-J analysis therefore, makes it unsuitable for determining grain size distribution and shape criteria in a quantitative manner.

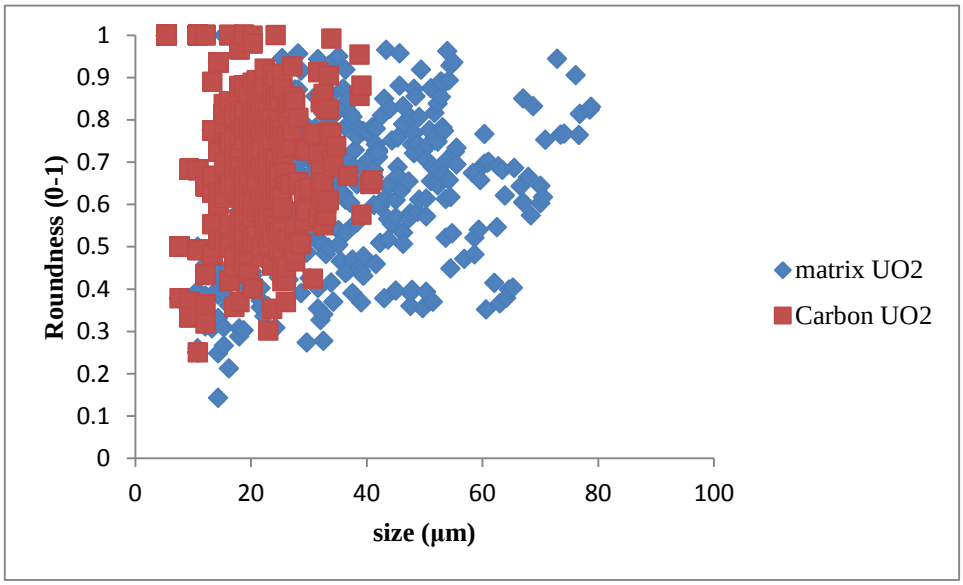



Figure 6.19: A plot of roundness vs. size of uranium group of minerals grains in the matrix and the carbonaceous matter obtained fro Image-J.

### 6.5. Comparison of 2D and 3D µXCT Techniques

Table 6.4 lists some important deductions made when comparing 2D conventional mineralogical techniques and 3D µXCT.

The table basically shows that the key difference of the two approaches is that reconstruction gives an entire volume, whereas SEM and optical microscopy image stitching is of one surface only. 3D µXCT information can be, therefore, used to increase confidence for visualisation, assisting in the identification and distribution of minerals. However, in this case, gold and uranium-bearing minerals were grouped together as uranium group of minerals.

Table 6.4: Comparison of 2D conventional mineralogy techniques with 3D μXCT.

| **2D Mineralogical Techniques** | **3D Computed Tomography** |
|---|---|
| Sample preparation requires polished section preparation, relatively time consuming up to 2-3 days. | No sample preparation involved other than cutting a desirable small piece of rock for analysis (<1 hour). |
| The sample is impregnated by resin, and polished so that sample integrity is lost. | Non-destructive method, sample integrity maintained. |
| Gives 2D information on surface only. | Gives 3D information of total volume of sample, including internal components. |
| Image acquisition of entire section surface can be time-consuming to obtain resolution from SEM through stitching of individual fields of view. | About 1 hour scan at high resolution with up to 2000 projections, providing resolution down to 6 μm (including reconstruction), but cannot separate minerals smaller than 6 μm or minerals that are touching one another. |

## 6.6. Summary

The main objective of utilising 3D μXCT was to evaluate the capabilities of the technique vs. conventional techniques in order to visualise and analyse the uranium-bearing minerals in the Vaal Reef samples for their sizes, shapes and distribution with respect to other mineral components in the samples in 3D. The use of this technique has contributed significantly in understanding the mineralogy of the Vaal Reef, specifically the uranium-bearing minerals, as it has complemented information obtained from the 2D conventional mineralogical techniques (optical microscopy and SEM) in Chapter 4.

3D μXCT was able to visualise and distinguish mineral components (i.e. the carbonaceous matter, quartz + phyllosilicates, sulphides, uranium-bearing minerals + gold) based on their linear attenuation coefficients at the energy level of 120 kV. VGStudioMax and Image-J imaging software were utilised for the visualisation and analysis of the 3D data. The imaging software provided sizes, shapes, distribution, and volumes in 3D of the different mineral gropings and components in the samples. VGStudioMax was useful in classifying mineral components in terms of grey value intervals on the histogram based on their attenuation coefficients. Thresholding aided with the visualisation of uranium group of minerals and these minerals were analysed as a single component in 3D; sizes, shapes, distribution, area and the volumes they constituted in the samples were determined by the defect detection and volume sample analyser in VGStudioMax.

Thresholding was useful in distinguishing mineral group components such as quartz + phyllosilicates from the sulphide minerals. This was made possible by the differing attenuation coefficients (Eq. 6.1) of the two mineral components, with gold having an attenuation coefficient of 88 $cm^{-1}$ and uraninite one of 69.5 $cm^{-1}$ respectively at 120 kV scanning energy (Table 6.2). These results were also supported by the high grey values of gold at 3200 and low grey values of uranium-bearing minerals at 1800 (Figure 6.7). An attempt to distinguish gold from uranium-bearing minerals by the 3D μXCT was made, and show high probabilities of separating the two minerals from each other; the 120 kV scanning energy was applied for all the samples as it provided better visualisation and distinction of different mineral components from one another, compared with data obtained at 200kV. This was verified by 2D optical and SEM identification in all the samples (Figures 6.8 and 6.9). The 3D μXCT technique is therefore able to distinguish gold from the uranium-bearing minerals, the main challenge in this study is the small grain sizes of gold that record similar attenuation coeffiencies with uranium-bearing minerals. If the gold partcles had similar grains sizes such as the uraninite (~150 μm), it would be easier to distinguish the two minerals from each other.

Visualisation of the total volume of the mineral components in a sample with their mineralogical associations (Figures 6.10, 6.11, 6.12 and 6.13) allowed an attempt to develop a paragenetic sequence in 3D. The 3D μXCT contributed in understanding the paragenesis of the Vaal Reef sample that was undertaken in Chapter 4, which showed four stages in the paragenetic sequence of the Vaal Reef samples. The results showed that detrital minerals such as quartz + phyllosilicates, sulphides and uranium group of minerals are easily visualised, and that they occur in association with secondary authigenic sulphide minerals, as well as being observed in cross-cutting fracture infill in detrital quartz. The uranium group of minerals are smaller than the rest of the allogenic minerals, and this is suggested to have resulted from remobilisation and fragmentation by the carbonaceous matter. Similar to observations in Chapter 4 by SEM studies, it was found in 3D μXCT that the carbonaceous matter shows an association with the uranium group of minerals. The carbonaceous matter was also observed in 3D fragmenting the uranium group of minerals; this supports the suggestion that the carbonaceous matter post-dates the detrital uraninites and the authigenic sulphides.

The VGStudioMax software was able to provide a 3D visualisation of the uranium group of minerals grains in the matrix as well as the uranium group of minerals grains in the carbonaceous matter separately (Figures 6.10, 6.11, 6.12 and 6.15, respectively). The uranium group of minerals grains in the matrix range from sub-angular to rounded in shape (Figure 6.16) and have sphericity of up to 0.9. The uranium group of minerals in the carbonaceous matter do not show much difference in both the grain sizes and shapes from the ones in the matrix. It was expected that the uranium group of minerals grains in the matrix would exhibit round and larger grains (about 200 μm) than the grains in the carbonaceous matter, but a few grains around the 180 μm sizes were also recorded in the carbonaceous matter as well. This was mainly due to the natural attachment of grains in the carbonaceous matter as these grains occur close to one another and the 3D μXCT was not able to resolve these minerals individually at 6 μm spatial resolution. As a result of this some of these attachments end up being classed together as one mineral component. An example of the attachment of grains is in Figure 6.18, where four grains of uranium group of minerals in the matrix are visualised as a single grain. This therefore, affects negatively, the grain size and shape calculation of these grains using the technique.

Image-J software provided 2D information on mineral properties such as roundness. The results showed that the shapes (roundness) of the majority of the uranium group of minerals grains range from 0.4 – 1 (Figure 6.19), suggesting that the uranium group of minerals grains could be detrital in origin; this was also supported by petrographic observations. The carbonaceous matter has been responsible for the fragmentation and break down of detrital uraninite; hence the sizes of the uraninites in the carbonaceous matter were small due to fragmentation. Although the shapes of the uranium group of minerals grains in both the matrix and carbonaceous matter differed, the majority of the shapes of uranium group of minerals grains were close to a roundness of 1 in both the occurrences; this could mean that they resemble round shapes, but they do not, particularly the grains hosted by the carbonaceous matter as they are fragmented and have angular shapes. This is best explained as partial volume effect, more especially when the minerals were smaller than the 3-5 micron resolution.

The following are the limitations that were noted with the use of 3D μXCT in the study:

- The technique, as employed, is unable to separate individual sulphide and uranium-bearing minerals from each other (pyrite, pyrrhotite and chalcopyrite; and brannerite, uraniferous leucoxene and uraninite).
- 3D μXCT could not be used as a single tool to identify mineral components; mineral identification was first done using optical microscopy and SEM before 3D μXCT could be used. These techniques were used for mineral identification and the electron microprobe was used for chemistry of the minerals. Therefore, 3D μXCT cannot be used alone as a single tool for mineralogical studies, but can be used as a 3D visualisation tool to complement 2D techniques for mineralogical characterisation. Previous studies also show that discrimination of minerals is not properly done with confidence (Long et al., 2009, Ketcham and Carlson, 2001).
- The partial volume effect was noted in most of the small-sized uraninite and gold associations in the matrices and in the carbonaceous matter; visualisation of uranium-bearing minerals and gold clusters at some portions of the samples was restricted owing to the averaged grey values of both minerals being similar and, therefore, making the distinction of these minerals rather difficult. Consequently, actual size determination of minerals (uranium-bearing minerals + gold) could not be determined using the 3D μXCT technique, especially for minerals with sizes lower than the detection limit of the focal point.
- Overlapping of grey values makes it difficult to know which grey values represent an individual mineral component. This uncertainty in defining the start and end of a mineral peak on the histogram makes it difficult to define the grey value intervals that are used in thresholding and differentiating minerals for determining the volume percentage of an individual mineral component in a total volume of the sample.

Three-dimensional μXCT results on the other hand showed positive outcomes in terms of visualisation of Vaal Reef samples. The most advantageous aspects of the technique are that:

- It is a non-destructive method, therefore, involving minimal sample preparation; samples need not to be crushed, sliced or polished to be visualised.
- It involves very short times for image scanning and reconstruction; about an hour scan time, since most of the applications are automated. The method has been proven to save time in sample preparation when compared to the preparation of dozens of polished and thin sections required by conventional 2D microscopy (Elliot and Heck, 2007).

- It provides 3D information of the total volume of sample and the entire volume can be visualised at once.

In spite of the challenges encountered in this exploratory study, 3D computed tomography shows potential for further development, and can be used to complement, and add value to the currently employed conventional 2D mineralogical techniques.

# CHAPTER SEVEN

# DISCUSSION AND CONCLUSIONS

## 7.1. Discussion

This research has attempted to investigate the characterisation of uranium-bearing minerals from the Vaal Reef in the Klerksdorp Goldfield of the Witwatersrand Basin. The study of uranium-bearing minerals has not received as much attention regarding genesis and deposition in the Witwatersrand reefs compared with gold mineralisation.

The Vaal Reef is the principal uranium-gold-bearing reef at AngloGold Ashanti's Kopanang, Great Noligwa and Moab Khotsong Mines. At these mines, the Vaal Reef is split into the C, B and A Facies. The facies were confirmed by detailed core logging of the underground drilled boreholes in Chapter 3. The C Facies is thinner at around 10 - 15 cm than the A Facies at about 1 m. The primary gold-uranium horizon at Kopanang Mine is the C Facies, whereas the A Facies is the primary gold-uranium horizon at Moab Khotsong Mine. These facies occasionally occur together e.g. in the Great Noligwa Mine. The Vaal Reef rests on different lithologies laterally; from the east at Moab Khotsong Mine, the Vaal Reef A Facies generally rests on the Mizpah Reef and Mizpah Quartzite (370 geozone) and directly on the MB5 quartzite (500 and 470 geozones) where the Mizpah Reef and Mizpah Quartzite are absent. The C Facies in the far western part of Kopanang Mine, however, rests on the Witkop and Grootdraai Facies conglomerates (forming the 430 and 460 geozones); where Witkop and Groodraai Facies are absent, the footwall is the MB5 quartzite, overlain by the Vaal Reef C Facies (forming the 440 and 470 geozones).

The C Facies matrix is characterised by predominantly detrital minerals (pyrite, zircon, chromite, rutile) and sheet silicates minerals as compared with the A Facies samples. Uraninite is the main uranium-bearing mineral in the C Facies and occurs in a detrital form. Brannerite and uraniferous leucoxene are secondary uranium-bearing minerals. Based on these differences in mineralogical characteristics between the C Facies and the A Facies, the geozones representing the facies are also different. The Kopanang Mine C Facies is represented by the 430, 440 and 460 geozones and the uranium-bearing minerals, uraninite in particular, are detrital in form and occur with other allogenic minerals in the matrix. The A Fcaies of the Moab Khotsong is mainly represented by samples from the 370 geozone and the

uraninite grains in the samples are entirely enclosed within the carbonaceous matter and secondary sulphide minerals such as galena and sphalerite. Authigenic sulphide overprint in both the Kopanang and Moab Khotsong Mines is common with more sulphide minerals such as pyrite and pyrrhotite, but more pronounced at Moab Khotsong Mine as shown. Therefore, the C Facies and A Facies geozones are different.

Bulk chemical analyses showed that the C Facies is sulphur-rich owing to the high presence of pyrite and authigenic pyrrhotite (which was also supported by high pyrite content detected in XRD, petrography and 3D µXCT) titanium-rich owing to the presence of rutile, and carbon-rich as a result of the presence of the carbonaceous matter. Furthermore, XRD also revealed that phyllosilicate minerals are present in both the C and A Facies samples.

The A Facies is mainly quartz-rich as compared to the C Facies samples; this is due to the low presence of sulphide minerals (mainly pyrite) and sheet silicate minerals (chlorite, chloritoid, pyrophyllite and muscovite). However, the A Facies is highly enriched in gold as compared with the C Facies; the gold is mainly associated with sulphides and the carbonaceous matter and this has been shown geochemically and petrographically. Detrital zircon and pyrite are present in the A Facies in low abundances. A unique feature of the A Facies is the presence of veins of galena-sphalerite, pyrrhotite and massive carbonaceous matter. The sulphide minerals in the A Facies generally display veining and infilling of cracked detrital mineral and is suggested to be recrystallised by comparison with the C Facies e.g. galena and sphalerite veins cross-cutting pyrite and the carbonaceous matter.

Based on the samples analysed by microscopy and 3D µXCT, the occurrence of uranium-bearing minerals in the Vaal Reef geozones is different. Uraninite in particular is distributed throughout the matrix occurring with other detrital minerals in the 440 (sample 1K4) and 460 (sample 3K2) geozones of the Kopanang Mine. On the contrary, the 370 geozone sample (MK367) of Moab Khotsong Mine shows that uranium minerals are mainly enclosed within the carbonaceous matter. A greater abundance of authigenic sulphide minerals has also been observed in the 370 geozone samples.

Three-dimensional microfocus X-ray computed tomography (3D µXCT) was investigated as an exploratory technique, newly applied on the Witwatersrand ores, to understand the 3D distribution of uranium-bearing minerals (predominantly uraninite in this case). The technique was applied to complement the mineralogical results obtained from optical

microscopy and SEM techniques as they only give 2D information on minerals. Therefore, 3D μXCT was used to study the grain sizes, shapes and textural distribution of uraninites in the Vaal Reef. However, uranium-bearing minerals and gold were grouped as one mineral component mainly due to the lack of spartial resolution and partial volume effects of the small-sized gold grains.

Tomography results have shown that uranium group of minerals are uniformly distributed in the quartz-pyrite matrices and also enclosed within the carbonaceous matter. Of major importance, the uraninite grains (from the C Facies of Kopanang Mine samples 1K4 and 3K2) occurring in the matrices generally display detrital features i.e. large oval-shaped grains; the presence of uraninite was confirmed by the use of 2D petrography (optical microscopy and SEM) on the same sample section position. In a 3D volume, these minerals are sub-round to round with similar size distributions throughout the matrices. Digital image processing software (2D Image-J and 3D VGStudioMax) has provided significant evidence of the roundness and sphericity of these uraninite grains. However, the uraninite grains enclosed within the carbonaceous matter (from the A Facies of Moab Khotsong Mine sample MK367) indicate signs of fragmentation and irregular sub-angular shapes and replacement as shown by microscopy and SEM studies. Uraninite grains of the A Facies are therefore, finely distributed throughout the carbonaceous matter. The SEM and optical microscopy examinations have revealed that the sizes of these grains are much smaller than the sizes of the detrital uraninite grains occurring in the quartz-pyrite matrices of the C Facies. Similarly, the shapes are also different to those of the detrital uraninite grains. The main reason for these two generations is that the Vaal Reef carbonaceous matter has extensively fragmented the detrital uraninite grains. The carbonaceous matter has been observed permeating cracks in uraninite grains, as can be seen in the photomicrographs of the C Facies in Chapter 4. On a more advanced level in the A Facies Moab Khotsong Mine, the uraninite grains are entirely fragmented and broken down by the carbonaceous matter.

The 3D μXCT technique has complemented information obtained from the 2D conventional mineralogical techniques of optical microscopy and SEM, described in Chapter 4. However, distinguishing individual minerals is currently not possible; rather minerals were grouped together into minerals with similar attenuation coefficients, owing to grey value overlaps because of the similarities in chemical composition and density of these minerals. The groupings are quartz + phyllosilicates, sulphides and uranium-bearing minerals (comprising

uranium-beraing minerals + gold). Currently the issue of overlapping of mineral grey values makes it difficult to separate these minerals from one another (e.g. uranium-bearing minerals and gold; quartz and phyllosilicates). Another disadvantage is that the technique only gives information related to imaging, such as internal structure and morphology of minerals with no chemical analysis information such as with the energy dispersive X-ray spectrometer (EDS) analysis that the SEM technique offers, to support a confident distinction of separating the mineral phases. Therefore, it is recommended 3D μXCT be used to support the conventional mineralogical techniques such as optical microscopy, SEM, XRD and electron microprobe, and not be applied separately as an independent technique for characterisation of mineralogical properties of rocks.

A paragenetic sequence, as shown in Chapter 4, following the combination of information from the various mineralogical techniques and the 3D μXCT, was developed. The Vaal Reef samples from the C and A Facies in this study are suggested to be represented by four stages of development in the reef:

- The first is the deposition of detrital minerals (quartz, pyrite, zircon, chromite, uraninite, rutile, arsenopyrite and gold).
- The second stage is characterised by the development of secondary minerals mainly sulphide minerals (pyrite, chalcopyrite, gersdorffite, and secondary uranium bearing minerals (brannerite and uraniferous leucoxene).
- Stage three is characterised by the introduction of carbonaceous matter, enclosing detrital uraninite grains, and to a more advanced stage fragmenting and replacing these uraninite grains.
- The fourth stage is marked by the introduction of vein occurrences and anhedral overgrowths of authigenic sulphide minerals (pyrrhotite, galena and sphalerite) and quartz. These late processes are observed in the samples as veins cross-cutting the younger carbonaceous matter. The sulphide minerals in this stage are infillings to the cracked detrital minerals. The most important part of this stage is also the introduction of phyllosilicate minerals which are burial pressure and metamorphic indicator minerals (Phillips, 1987).

This study supports the detrital origin of pyrite, rutile, zircon, chromite, arsenopyrite, uraninite and gold, which are classified as primary allogenic minerals based mainly on their

morphology and mineralogy as shown previously (Ramdohr, 1958b; Pretorious, 1981; England *et al*., 2002; Frimmel and Minter, 2002; Kirk *et al.,* 2003). The shapes of these minerals are mostly oval and sub-round to round. These detrital minerals occur in clusters. The nature of occurrence of these detrital minerals was initially described by Feather and Koen (1975) and many others (Liebenberg, 1955 and Ramdohr, 1958b). These minerals occur in hydraulic equilibrium, meaning that they were transported together into the basin. As shown in Chapter 4, the majority of the C Facies samples from Kopanang Mine have minerals with consistent sub-round to round shapes. The grain size distributions of these minerals range between 70 and 150 μm. Pyrite has, in a number of occurrences, been recorded with larger grain sizes exceeding 500 μm and reaching up to 1.5 mm in diameter. On the other hand, secondary or authigenic minerals occur mainly as anhedral to irregular shaped grains when compared with detrital minerals. More importantly the ages of pyrite, uraninite and gold grains in the Witwatersrand reefs have been shown to exceed just over 3.0 Ga (Kirk *et al.*, 2001; Kirk *et al.*, 2003).

Secondary pyrite-pyrrhotite-galena-sphalerite assemblages in the Vaal Reef (A Facies) have been observed previously by Gartz and Frimmel (1999) and are suggested by Robb *et al.* (1994) to have formed from burial pressure as a result of the deposition of the lower Transvaal Supergroup sediments around 2500 to 2300 Ma. During the deposition of the Transvaal Supergroup, Phillips (1987) indicated that the burial pressure and heat resulted in the development of greenschist metamorphic minerals such as pyrophyllite, chlorite, muscovite and chloritoid assemblages at temperatures around 250-350$^{o}$C. Another important stage in the paragenetic sequence of the Vaal Reef is the maturation of the carbonaceous matter. The carbonaceous matter has long been identified in the Witwatersrand reefs (Liebenberg, 1955; Ramdohr, 1958a; Schidlowski, 1970; Schidlowski, 1981) originally as an organic algal mat that trapped the majority of the heavy detrital minerals and Pretorius (1975 and 1976) called kerogen. It was later suggested that the carbonaceous matter had developed late in the paragenetic sequence of the Witwatersrand reefs and is now referred to as pyrobitumen (Robb and Meyer, 1991; Robb *et al*., 1994). Gray *et al*. (1998) worked on the carbonaceous matter from the Vaal Reef and showed that the bodies have matured from pyrobitumen to form "meso-phase" carbonaceous matter. This study supports the finding that carbonaceous matter was once mobile, since petrography has shown that the detrital uraninites in particular were fragmented and replaced by the carbonaceous matter. The

paragenetic sequence of the Vaal Reef in this study is in agreement with the four stage paragenetic sequence developed by Robb *et al*., (1994 and 1997).

The source area of the gold and uranium in the Witwatersrand Basin has also remained unsolved, until recently where Robb and Meyer (1995) showed that the sedimentary structures on the Witwatersrand reefs indicated that they were deposited by river drainage patterns from the north and west of the basin. Furthermore, this work suggests that the Barberton greenstone belt granitoids were not viable uranium sources due to the lack of primary uraninite and low U/Th (Robb and Meyer, 1995).

The EMPA analyses in this study on uraninite grains from both the C and A Facies of the Vaal Reef show an average Th content of 3.1 and 3.4 % as well high variable ratios of $UO_2/ThO_2$ (13.4 to 85.6) and high Pb contents supporting a statement by Hallbauer (1986) that these grains have been derived from an older granitic or pegmatitic source area and could not have formed from low-temperature hydrothermal fluids. Direct dating (U-Pb) of these uraninite grains in the Witwatersrand reefs has shown that the grains are 3050±50 Ma (Rundle and Snelling, 1977; Saager, 1981). Direct Re-Os dating has also been done on rounded pyrite grains (Kirk *et al.,* 2001) and show an age of 2990±11 Ma. Gold grains in the Vaal Reef (Kirk *et al.,* 2003) have shown ages around 3016±110 Ma by the Re-Os method. All these dates are older than the time of sediment deposition in the Witwatersrand Basin indicating that these minerals are detrital in origin (Frimmel, 2005). Kirk *et al.,* (2003) showed that the possible gold sources for the Witwatersrand reefs might have been the Murchison and Kraaipan greenstone komatiites or metamorphosed basalts occurring north and west of the basin, respectively. These greenstone rocks have significantly high mantle-derived Re-Os isotopes that are similar to most of the gold grains in the Witwatersrand reefs and coincide very well with the basin since they are older than the formation of the basin and they occur north and west of the basin (Frimmel, 2005; Robb and Meyer, 1995; Kirk *et al.*, 2003).

Previous studies have shown that in the Klerksdorp Goldfield, the closest granite dome in the area is the Hartebeesfontein Archaean basement in the northwestern part of the region, where uraninite is abundant as an accessory phase (Robb and Meyer, 1985; Robb *et al*., 1990); this clearly suggests that uranium-bearing minerals in the Vaal Reef of the Klerksdorp Goldfield might have been derived from the Hartebeesfontein Dome and not from younger

hydrothermal fluids as suggested by Barnicoat *et al*., (1997) and Phillips and Law (1994, 2000).

## 7.2. Conclusions

- Three types of uranium-bearing minerals were recorded in the Vaal Reef samples in this study and these are uraninite, brannerite and uraniferous leucoxene. Uraninite is the dominant uranium-bearing mineral and is mainly associated with detrital minerals and is suggested to be detrital in origin. The morphologies of the uranium-bearing minerals are different with detrital uraninite displaying oval to round and the secondary uranium-bearing minerals (brannerite and uraniferous leucoxene) as irregular. Brannerite and uraniferous leucoxene appear to have formed as alteration products of uraninite, through interaction with titanium-rich mineral phases such as rutile and leucoxene.
- Detrital uraninite is associated with gangue minerals such as phyllosilicates, sulphides (pyrite in particular) and the carbonaceous matter; this carbonaceous material fragments and replaces the uraninite grains. This study, through the development of the paragenetic sequence in the Vaal Reef, suggests that the carbonaceous matter post-dates the detrital uraninite grains.
- Uraninite in the Vaal Reef C Facies mainly occurs throughout the matrix and also hosted in the carbonaceous matter at the base of the reef. In the A Facies, the uraninite is mainly enclosed by the carbonaceous matter. Microscopy and 3D µXCT have shown that samples from the 440 and 460 geozones of the C Facies mainly contain uraninite in the matrix and the 370 geozone contains uraninite within the carbonaceous matter.
- Geochemical analyses have shown that the uranium-bearing minerals in the Vaal Reef have a strong relationship with $Al_2O_3$, representing the majority of phyllosilicate minerals in the quartz-pyrite matrices; therefore, the study shows that uranium minerals are associated with phyllosilicate minerals. The presence of these minerals is a further positive indication that the Vaal Reef, similar to many reefs in the Witwatersrand Goldfield, has been exposed to metamorphic conditions of up to around 2 – 3 Kbars and temperatures exceeding 250 -350 $^{o}$C.
- The metamorphism is further responsible for the introduction of post depositional minerals such as authigenic sulphides and the meso-phase carbonaceous matter, known as pyro-bitumen.
- The 3D µXCT as a new method of application and a development study in this thesis has contributed in the characterisation of uranium-bearing minerals; this was achieved by the state of the art technology of 3D visualisation and scanning turnaround time of the

system. The technique, however, cannot distinguish individual minerals with similar chemical composition and density from one another. Overlapping of mineral grey values is also another obstacle to confidently assign mineral peaks on the histogram. Size and shape determination of minerals at a very small size (~ 5 microns and less) is also a big limitation as a result of spatial resolution issues.

- The use of 3D µXCT technique in this study could not distinguish uranium-bearing minerals and gold from each other.
- The 3D µXCT technique currently can only be applied to support the existing conventional mineralogical techniques.
- The 2D and 3D techniques combination in this study has contributed towards the understanding the genesis of the uranium-bearing minerals in the Vaal Reef samples.
- This study concludes that the Vaal Reef uranium-bearing mineralisation is best explained by a modified placer model.

## 8. REFERENCES

AEC (ATOMIC ENERGY CORPORATION), 1984. Uranium in South Africa. 1983 Assessment of Resources and Resources and Production: Report, ISBN 0 86960 763 4, 23pp.

AngloGold Ashanti., 2001. Vaal Reef Architecture. Unpublished. Pp 1-30

Anhaeusser, C.R., 1973. The geology and geochemistry of the Archaean granites and gneisses of the Johannesburg-Pretoria dome. Spec. Publ. geol. Soc. S. Afr. 3, 361-385.

Anhaeusser, C.R. and Robb., L.J., 1981. Magmatic cycles and evolution of the Archaean granitic crust in the eastern Transvaal and Swaziland. Spec. Publ. geol. Soc. Aust. 7, 457-467.

Antrobus, E.S.A., Brink, W.C.J., Brink, M.C., Caulkin, J. and Hutchinson R.I., Thomas D.E., Van Graan and J.A., Viljoen, J.J., 1986. The Klerksdorp Goldfield. Mineral Deposits of Southern Africa, 549-598.

Armstrong, R.A., Compston, W., Retief, E.A., William, L.S and Welke, H.J., 1991. Zircon on microprobe studies bearing on the age and evolution of the Witwatersrand triad. Precambrian Research, 53, 243–266.

Barnicoat, A.C., Henderson, I.H.C., Knipe, R.J., Yardley, B.W.D., Napier, R.W., Fox, N.P.C., Kenyon, A.K., Muntingh, D.J., Strydom, D., Winklert, K.S., Lawrencer, S.R. and Cornford, C., 1997. Hydrothermal gold mineralization in the Witwatersrand Basin. Nature, 386, 820–824.

Catueanu, O. and Biddulph, M.N., 2001. Sequence stratigraphy of the Vaal Reef facies association in the Witwatersrand foredeep, South Africa. Sedimentary Geology, 141-142, 113-130.

Chapman, K.M., Tucker, R.F., and Kidger, R.J., 1986. The Klerksdorp Goldfield. In: Antrobus, E.S.A. (Ed), Witwatersrand Gold – 100 Years. Geological Society of South Africa, 173-198.

Cole, D.I., 1998. Uranium. The Mineral Resources of South Africa, 642-658.

Conroy, G.C. and Vannier, M.W., 1984. Non-invasive three-dimensional computer imaging of matrix-filled fossil skulls by high-resolution computed tomography. Science, 226, 456–458.

Coward, M.P., Spencer, R.M., Spencer, C.E., 1995. Development of the Witwatersrand Basin, South Africa. In: Coward, M.P., Ries, A.C. (Eds.), Early Precambrian Processes. Geological Society Special Publications. The Geological Society, London, pp. 243–269.

Dankert, B.T. and Hein, K.A.A., 2010. Evaluating the structural character and tectonic history of the Witwatersrand Basin. Precambrian Research, 177, 1–22.

de Beer, F.C., Middleton, M.F., and Hilson, J., 2004. Neutron radiography of porous rocks and iron ore. Applied Radiation and Isoptopes, 61, 487-495.

Elliot, T.R. and Heck, R.J., 2007. A comparison of optical and X-ray CT techniques for void analysis in soil thin section. Geoderma, 141, 60–70.

England, G.L., Rasmussen, B., Krapez, B. and Groves, D.I., 2001. The origin of uraninite, bitumen nodules and carbon seams in Witwatersrand gold-uranium-pyrite ore deposits, based on a Permo-Triassic analogue. Economic Geology, 96, 1907–1920.

England, G.L., Rasmussen, B., Krapez, B. and Groves, D.I., 2002. Palaeoenvironmental significance of rounded pyrite in siliciclastic sequences of the Late Archaean Witwatersrand

Basin: oxygen-deficient atmosphere or hydrothermal evolution. Sedimentology 49, 1122–1156.

Eriksson, P.G., Mazumder, R., Catuneanu, O., Bumby, A.J. and Ilondo, B.O., 2006. Precambrian continental freeboard and geological evolution: a time perspective. Earth-Science Reviews, 79, 165–204.

Eriksson, P.G. and Reczko, B.F.F., 1995. The sedimentary and tectonic setting of the Transvaal Supergroup floor rocks to the Bushveld Complex. Journal of African Earth Sciences 21, 487–504.

Feather, C.E. and Koen, G.M., 1975. The mineralogy of the Witwatersrand reefs. Minerals sci. Engng., 7, 189-224.

Feather, C.E. and Glathaar, C.W., 1987. A review of uranium-bearing minerals in the Dominion and Witwatersrand placers. In: Pretorius, D.A. (Ed.), Uranium Deposits in Proterozoic Quartz–pebble Conglomerates. International Atomic Energy Agency, Vienna, pp. 355– 386.

Fleet, M.E., 1998. Detrital pyrite in Witwatersrand gold reefs: X-ray diffraction evidence and implications for atmospheric evolution. Terra Nova, 10, 302– 306.

Fransham, P.B. and Jelen, J., 1987. Displacement of heavy oil visualized by CAT scan. Journal of Canadian Petroleum Technology, 26 (3), 42–47.

Frimmel, H.E., 1994. Metamorphism of Witwatersrand gold. Exploration and Mining Geology, 3, 357–370.

Frimmel, H.E., 2005. Archaean atmospheric evolution: evidence from the Witwatersrand gold fields, South Africa. Earth-Science Reviews, 70, 1–46.

Frimmel, H.E. and Gartz, V.H., 1997. Witwatersrand gold particle chemistry matches model of metamorphosed, hydrothermally altered placer deposits. Mineralium Deposita, 32, 523–530.

Frimmel, H.E. and Minter, W.E.L., 2002. Recent developments concerning the geological history and genesis of the Witwatersrand gold deposits, South Africa. In: Goldfarb, R.J., Nielsen, R.L. (Eds.), Integrated Methods for Discovery: Global Exploration in the Twenty-First Century. Special Publication vol. 9. Society of Economic Geologists, Littleton, pp. 17–45.

Frimmel, H.E., le Roex, A.P., Knight, J. and Minter, W.E.L., 1993. A case study of the postdepositional alteration of the Witwatersrand Basal Reef gold placer. Economic Geology, 88: 249-265.

Gartz, V.H. and Frimmel, H.E., 1999. Complex metasomatism of an Archean placer in the Witwatersrand Basin, South Africa: the Ventersdorp Contact Reef - A Hydrothermal Aquifer? Economic Geology, 94, 689–706.

Gay, A.L. and Grandstaff, D.E., 1980. Chemistry and mineralogy of Precambrian palaeosols at Elliot Lake, Ontario, Canada. Precambrian Research, 12, 349-373.

Godel, B., Barnes, S. and Maier, W., 2006. 3-D Distribution of Sulphide Minerals in the Merensky Reef (Bushveld Complex, South Africa) and the J-M Reef (Stillwater Complex, USA) and their Relationship to Microstructures Using X-Ray Computed Tomography. Journal of Petrology, 47 (9), 1853-1872.

Godel, B., Barnes, S.J., Barnes, S. and Maier, W., 2010. Platinum ore in three dimensions: insights from high-resolution X-ray computed tomography. Geology, 38 (12) 1127–1130.

Goldsheet, 2012. http://www.goldsheetlinks.com/production.htm.

Grandstaff, D.E., 1980. Microprobe analyses of uranium and thorium in uraninite from the Witwatersrand, South Africa, and Blind River, Ontario, Canada. In: Armstrong, F.C. (Ed.), Genesis of Uranium- and Gold-Bearing Precambrian Quartz–Pebble Conglomerates. United States Geological Survey Professional Paper, pp. J1– J5.

Gray, G.J., Lawrence, S.R., Kenyon, K. and Cornford, C., 1998. Nature and origin of "carbon" in the Archean Witwatersrand basin. South African Journal of Geology, 155, 39–59.

Gualda, G.A.R. and Rivers, M., 2006. Qualitative 3D petrography using X-ray tomography: Application to Bishop Tuff pumice clasts. Journal of Volcanology and Geothermal Research, 154 (1-2), 48-62.

Hallbauer, D.K., 1986. The mineralogy and geochemistry of Witwatersrand pyrite, gold, uranium, and carbonaceous matter. In: Anhaeusser, C.R., Maske, S. (Eds.), Mineral Deposits of Southern Africa. Geological Society of South Africa, Johannesburg, pp. 731– 752.

Hallbauer, D.K., van Warmelo, K.T., 1974. Fossilized plants in thucholite from Precambrian rocks for the Witwatersrand, South Africa. Precambrian Research 1, 199–212.

Hallbauer, D.K. and Utter, T., 1977. Geochemical and morphological characteristics of gold particles from recent river deposits and the fossil placers of the Witwatersrand. Mineralium Deposita, 12, 293-306.

Hounsfield, G.N., 1973. Computerized transverse axial scanning (tomography): Part 1, Description of system. The British Journal of Radiology, 46 (552), 1016–1022.

Jolley, S.J., Stuart, G.W., Freeman, S.R., Knipe, R.J., Kershaw, D., McAllister, E., Barnicoat, A.C., Tucker, R.F., 2007. Progressive Deformation of a Late Orogenic Thrust System, From Duplex Development to Extensional Reactivation and Disruption: Witwatersrand Basin, South Africa. Geological Society, Special Publications 272, London, pp. 543–569.

Jolley, S.J., Freeman, S.R., Barnicoat A.C., Phillips G.M., Knipe, R.J., Pather, A., Fox, N.P.C., Strydom, D., Birch, M.T.G., Henderson, I.H.C. and Rowland, T.W., 2004. Structural controls on Witwatersrand gold mineralisation. Journal of Structural Geology, 26, 1067–1086.

Kak, A.C., and Slaney, M., 1999: Principles of computerised tomographic imaging. The institute of Electrical and Electronics Engineers, Inc., New York, 329 pp.

Kalukin, A.R., Van Geet, M. and Swennen, R., 2000. Principal component analysis of multi-energy X-ray computed tomography of mineral samples. IEEE transactions on nuclear science, 47 (5), 1729–1736.

Kamo, S.L., Reimold, W.U., Krogh, T.E. and Colliston, W.P., 1996. A 2.023 Ga age for the Vredefort impact event and a first report of shock metamorphosed zircons in pseudotachylitic breccias and Granophyre. Earth and Planetary Science Letters, 144, 369–387.

Kasteel, R., Vogel, H.T. and Roth, E., 2000. From local hydraulic properties to effective transport in soil. European Journal of soil sciences, 51, 81-91.

Ketcham R.A. and Carlson, W.D., 2001. Acquisition, optimization and interpretation of X-ray computed tomographic imagery: Applications to the geosciences. Computers and Geosciences, 27 (4), 381-400.

Kirk, J., Ruiz, J., Chesley, J., Titley, S. and Walshe, J., 2001. A detrital model for the origin of gold and sulfides in the Witwatersrand basin based on Re–Os isotopes. Geochimica et Cosmochimica Acta, 65, 2149– 2159.

Kirk, J., Ruiz, J., Chesley, J. and Titley, S., 2003. The origin of gold in South Africa: Ancient rivers filled with gold, a spectacular upwelling of magma and a colossal meteor impact

combined to make the Witwatersrand basin a very special place. American Scientist, 91, 534-541.

Kositcin, N., 2003. Textural and geochemical discrimination between xenotime of different origin in the Archaean Witwatersrand Basin, South Africa. Geochimica et Cosmochimica Acta 67, 709– 731.

Kositcin, N. and Krapez, B., 2004. Relationship between detrital zircon age-spectra and the tectonic evolution of the Late Archaean Witwatersrand Basin, South Africa. Precambrian Research, 129, 141–168.

Kretz, R., 1966. Grain size distribution for certain metamorphic minerals in relation to nucleation and growth. Journal of Geology 74, 147–173.

Kretz, R., 1969. On the spatial distribution of crystals in rocks. Lithos, 2, 39–66.

Kretz, R., 1993. A garnet population in Yellowknife schist, Canada. Journal of Metamorphic Geology, 11, 101–120.

Krupp, R., Oberthtur, T. and Hirdes, W., 1994. The early Precambrian atmosphere and hydrosphere: Thermodynamic constraints from mineral deposits. Economic Geology, 89, 1581-1598.

Liebenberg, W.R., 1955. The occurrence and origin of gold and radioactive minerals in the Witwatersrand System, the Dominion Reef, the Ventersdorp Contact Reef and the Black Reef. Transaction of South African Journal of Geology, 58, 101-227.

Long, H., Swennen, R., Foubert, A., Dierick, M. and Jacobs, P., 2009. 3D quantification of mineral components and porosity distribution in Westphalian C sandstone by microfocus X-ray tomography. Sedimentary Geology, 220, 116-125.

Lottering, M.J., Lorenzen, L., Phala, N.S., Smit, J.T. and Schalkwyk, G.A.C., 2008. Mineralogy and uranium leaching response of low grade South African ores. Minerals Engineering, 21, 16–22.

Martin, D.McB., Clendenin, C.W., Krapeˇz, B., and McNaughton, N.J., 1998. Tectonic and geochronological constraints on late Archaean and Palaeoproterozoic stratigraphic correlation within and between the Kaapvaal and Pilbara Cratons. Journal of the Geological Society, 155, 311–322.

McCarthy, T.S., 2006. The Witwatersrand Supergroup. In: Johnson, M.R., Anhaeusser, C.R. and Thomas, R.J., (Eds.), The Geology of South Africa. Geological Society of South Africa, Johannesburg/Council for Geoscience, Pretoria, pp. 155-186.

McCarthy, T.S., Stanistreet, I.G., Cadle, A.B. and Durrheim, R., 1990. The geology of the Ventersdorp Supergroup (Bezuidenhout Valley) outlier to the east of Johannesburg and its relevance to the tectonics of a Witwatersrand Basin margin. South African Journal of Geology, 93, 289–309.

McLean, P.J. and Fleet, M.E., 1989. Detrital pyrite in the Witwatersrand gold fields of South Africa: evidence from truncated growth banding. Economic Geology, 84, 2008– 2011.

Mees, F., Swennen, R., Van Geet, M. and Jacobs, P., 2003. Applications of X-ray computed tomography in the geosciences. Geological Society, London, Special Publications, 215, 1-6.

Meier, D.L., Heinrich, C.A. and Watts, M.A., 2009. Mafic dikes displacing Witwatersrand gold reefs: Evidence against metamorphic-hydrothermal ore formation. Geology, 2009; 37, 607 - 610.

Mellor, E.T., 1916. The conglomerates of the Witwatersrand. Transactions of the Institute of Mining and Metallurgy, 25, 226–348.

Meyer, M., Robb, L.J. and Anhaeusser, C.R., 1985. Uranium and thorium contents of Archaean granitoids from the Barberton Mountain Land, South Africa. Information Circular Economic Geology Research Unit, University of the Witwatersrand, 177, 15pp.

Meyer, F.M., Oberthur, T., Robb, L.J., Saager, R. and Stupp, H.D., 1990a. Cobalt, nickel and gold in pyrite from primary gold deposits and Witwatersrand reefs. South African Journal of Geology, 93, 70-82.

Meyer, F.M., Wallmach, T., Henkel, J. and Schweitzer, J.K., 1990b. Chlorite compositions and fluid conditions in some Witwatersrand reefs. Ext. Abstr. Geocongress '90, UCT, Cape Town.

Meyer, F.M., Robb, L.J., Reimold, W.U. and DeBruiyn, H., 1994a. Contrasting low- and high-Ca granites in the Barberton Mountain Land, southern Africa. Lithos, 32, 63-76.

Meyer, F.M., Möller, P and DeBruiyn, D., Przybylowicz, W.J. and Prozesky, V.M., 1994b. The gold-pyrite association in Witwatersrand reefs: evidence for electrochemical precipitation of gold. Explor. Min. Geol., 3, 207-218.

Mintek., 2012. An overview of the mineralogical and analytical techniques at Mintek. Unpublished. Pp 5 – 29.

Minter, W.E.L., 1976. Detrital gold, uranium, and pyrite concentrations related to sedimentology in the Precambrian Vaal Reef placer, Witwatersrand, South Africa. Economic Geology, 71, 157–176.

Minter, W.E.L., 1978. A sedimentological synthesis of placer gold, uranium and pyrite concentrations in Proterozoic Witwatersrand sediments. In: Miall, A.D. (Ed.), Fluvial Sedimentology. Canadian Society of Petroleum Geologists, pp. 801–829.

Minter, W.E.L., 1999. Irrefutable detrital origin of Witwatersrand gold and evidence of eolian signatures. Economic Geology, 94, 665 – 670.

Minter, W.E.L., Goedhart, M., Knight, J. and H.E. Frimmel, 1993. Morphology of Witwatersrand gold grains from the Basal Reef: evidence for their detrital origin. Economic Geology, 88, 237-248.

Mossman, D.J., Minter, W.E.L., Dutkiewicz, A., Hallbauer, D.K., George, S.C., Hennigh, Q., Reimer, T.O. and Horscroft, F.D, 2008. The indigenous origin of Witwatersrand "carbon". Precambrian Research, 164, 173–186.

Myers, R.E., McCarthy, T.S., Stanistreet, I.G., 1990. A tectono-sedimentary reconstruction of the development and evolution of the Witwatersrand Basin, with particular emphasis on the Central Rand Group. South African Journal of Geology, 93, 180–201.

Nagy, B., 1993. Kerogens and bitumens in Precambrian uraniferous ore deposits: Witwatersrand, South Africa, Elliot Lake, Canada and the natural fission track reactors, Oklo, Gabon. In: Parnell, J. (Ed.), Bitumens in Ore Deposits. Special Publication Society for Geology Applied to Mineral Deposits. Springer, Berlin, pp. 287– 333.

Nshimirimana, R., de Beer, F. and Radebe, M., 2011. The role of SANRAD facility in quantitative and morphological investigation. Nuclear Instruments and Methods in Physics Research A, 651, 305-311.

Parnell, J., 2001. Paragenesis of mineralization within fractured pebbles in Witwatersrand conglomerates. Mineralium Deposita, 36, 689–699.

Perret, J., Prasher, S.O., Kantzas, A. and Langford, C., 2000. A two-domain approach using CAT scanning to model solute transport in soil. Journal of Environmental Quality, 29, 995-101.

Phillips, G.N., 1987. Metamorphism of the Witwatersrand gold fields: conditions during peak metamorphism. Journal of Metamorphic Geology, 5, 307-322.

Phillips, G.N., 1988. Widespread fluid infiltration during metamorphism of the Witwatersrand goldfields: Generation of chloritoid and pyrophyllite. Journal of Metamorphic Geology, 6, 311-322.

Phillips, G.N., Myers, R.E. and Palmer, J.A., 1987. Problems with the placer model for Witwatersrand gold. Geology, 15, 1027-1031.

Phillips, G.N. and Law, J.D.M., 1994. Metamorphism of the Witwatersrand gold fields: A review. Ore Geology Reviews, 9, 1-31.

Phillips, G.N., and Law, J.D.M., 2000. Witwatersrand gold fields: Geology, genesis and exploration. SEG Reviews, 13, 439–500.

Poujol, M., Robb, L.J., and Respaut, J.P., 1999. U–Pb and Pb–Pb isotopic studies relating to the origin of gold mineralization in the Evander Goldfield, Witwatersrand Basin, South Africa. Precambrian Research, 95, 167–185.

Poujol, M., Robb, L.J., Anhaeusser, C.R., and Gericke, B., 2003. A review of the geochronological constraints on the evolution of the Kaapvaal Craton, South Africa. Precambrian Research, 127, 181–213.

Pretorius, D.A., 1964. The geology of the south Rand goldfield. In: S.H. Haughton (Editor), The Geology of Some Ore deposits in Southern Africa, Vol. 1. The Geological Society of South Africa, Hortors, Johannesburg, pp. 219-282.

Pretorius, D.A., 1975. The depositional environment of the Witwatersrand goldfields: chronological review of speculations and observations. Minerals Science and Engineering, 7, 18– 47.

Pretorius, D.A., 1976. The nature of the Witwatersrand gold-uranium deposits. In: Handbook of stratabound and stratiformore deposits. Ed. K.H. Wolf, VII. Elsevier, Amsterdam, 29-55.

Pretorius, D.A., 1981. Gold and uranium in quartz–pebble conglomerates. Economic Geology, 75th Anniversary Volume, 117–138.

Pullan, B.R., Ritchings, R.T. and Isherwood, I., 1981. Accuracy and meaning of computed tomography attenuation values. In: Newton, T.H., Potts, D.G. (Eds.), Technical Aspects of Computed Tomography. Mosby, St. Louis, pp. 3904–3914.

Ramdohr, P., 1955. Neue Beobachtungen an Erzen des Witwatersrandes in Südafrika and ihre geoetische Bedeatung. Abh. Dtsch. Akad. Wiss. Berlin, Kl. Chem. Biol., 5.

Ramdohr, P., 1957. Die "Pronto-Reaktion". N. Jb. Min., Monatsh, 217-222.

Ramdohr, P., 1958a. Die Uran- und goldlagerstätten Witwatersrand – Blind River District – Dominion Reef – Serra de Jacobina: Erzmikroskopische Untersuchungen und ein geologischer Vergleich. Abh. Dtsch. Akad. Wiss. Berlin, Kl. F. Chem., Biol., Nr. 3, 35pp.

Ramdohr, P., 1958b. New observations on the ores of the Witwatersrand in South Africa and their genetic significance. Transactions of the Geological Society of South Africa, 61, 1 –50. (Annexure).

Rantzsch, U., Gauert, C.D. K., Van der Westhuizen, W.A., Duhamel, I., Cuney, M. and Beukes, G.J., 2011. Mineral chemical study of U-bearing minerals from the Dominion Reefs, South Africa. Miner Deposita, 48, 187-196.

Rasband,W., 2005. ImageJ, Image Manipulation Software. National Institute of Health, Bethesda MD, USA. (http://rsb.info.nih.gov/ij/) (Accessed March 2011).

Rasmussen, S.E. and Fesq, H.W., 1973. Neutron activation analysis of samples from the Kimberley reef conglomerate. Report No. 1563, National Institute for Metallurgy, Johannesburg, 241 pp.

Reimold, W.U. and Gibson, R.L., 2006. The melt rocks of the Vredefort impact structure—Vredefort Granophyre and pseudotachylitic breccias: implications for impact cratering and the evolution of the Witwatersrand Basin. Chemie der Erde – Geochemistry, 66, 1–35.

Remeysen, K. and Swennen, R., 2007. Application of microfocus computed tomography in carbonate reservoir sedimentology: possibilities and limitations. Marine and Petroleum Geology, 25 (6), 486–499.

Robb, L.J. and Meyer, F.M., 1985. Uranium distribution and concentration mechanisms in the hinterland of the Witwatersrand Basin. Extended abstract, conference on Concentration mechanisms of uranium in geological Environments, Nancy, France, 105-110.

Robb, L.J., Cathelineau, M., Landals, P., Dubessy, J. and Ballly, L., 1989. The nature of late-stage fluids affecting the Witwatersrand conglomerates: fluid inclusion and mineralogical data. Abstract Gold '89 Europe, Toulouse, France, 31 pp.

Robb, L.J. and Meyer, F.M., 1990. The nature of the Witwatersrand hinterland: conjectures on the source area problem. Economic Geology, 85, 511-536.

Robb, L.J. and Meyer, F.M., 1991. A contribution to the recent debate concerning epigenetic versus syngenetic mineralization processes in the Witwatersrand basin. Economic Geology, 86, 396-401.

Robb, L.J. and Meyer, F.M., 1995. The Witwatersrand Basin, South Africa: Geological framework. Ore Geology Reviews, 10, 67-94.

Robb, L.J., Davis, D., Kamo, S.L. and Meyer, F.M., 1992. Ages of altered granites adjoining the Witwatersrand Basin with implications for the origin of gold and uranium. Nature, 357, 677–680.

Robb, L.J., Landais, P., Meyer, F.M. and Davis, D.W., 1994. Nodular hydrocarbons in granites: implications for the origin of kerogen in the Witwatersrand Basin, South Africa. Explor. Min. Geol., 3, 219-230.

Robb, L.J., Landais, P., Drennan, G.R. and Dubessy, J., 1997. Petrographic, chemical and spectroscopic studies of the carbonaceous matter in the Witwatersrand Basin, South Africa. Economic Geology Research Unit, University of the Witwatersrand, 312, 1-34.

Rundle, C.C. and Snelling, N.J., 1977. The geochronology of uraniferous minerals in the Witwatersrand Triad: an interpretation of new and existing U–Pb data on rocks and minerals from the Dominion Reef, Witwatersrand and Ventersdorp Supergroups. Philosophical Transactions of the Royal Society of South Africa, 286, 567– 583.

Saager, R. 1981. Geochemical studies on the origin of the detrital pyrites in the conglomerates of the Witwatersrand goldfields, South Africa. United States Geological Survey Professional Paper, 1161-L, 1–17.

Saager, R. and Stupp, H.D., 1983. U-Ti Phases from Precambrian Quartz-Pebble Conglomerates of the Elliot Lake Area, Canada, and the Pongola Basin, South Africa, TMPM Tschermaks Min. Petr. Mitt., 32, 83-102.

Saager, R. and Oberthür, T., 1984. Nickel–cobalt sulfides in Precambrian gold and uranium-bearing quartz–pebble conglomerates of South Africa. In: Wauschkuhn, A., Kluth, C., Zimmermann, R.A. (Eds.), Syngenesis and Epigenesis in the Formation of Mineral Deposits. Springer, Berlin, pp. 37–246.

SACS, South African Committee for Stratigraphy, 1980. Part 1: Lithostratigraphy of the Republic of South Africa, South West Africa/Namibia, the Republics of Bophuthatswana, Transkei and Venda. Pretoria, Department of Mineral and Energy Affairs, Geological Survey, 690 pp.

Sanders, J.W., Rowland, T.W. and Mellody, M., 1994. Formation related gold production from the Central Rand Group and the Ventersdorp Supergroup, South Africa. 15th CMMI Congress. Institute of Mining and Metallurgy, Johannesburg, pp. 47–53.

Schidlowski, M., 1970. Untersuchungen zar Metallogenese im südlichen Witwatersrand-Becken (Oranje-Freistaat-Goldfeld, Südafrika). Beih. Geol. Jb., 85, 80 pp.

Schidlowski, M., 1981. Uraniferous constituents of the Witwatersrand conglomerates: Ore-microscopic observations and implications for the Witwatersrand metallogeny. United States Geological Survey, Professional Paper, 1161-N, 23.

Schreyer, W. and Bisschoff, A.A., 1982. Kyanite as a metamorphic mineral in Witwatersrand sediments at Johannesburg and Krugersdorp, South Africa, Transaction of Geology Society of South Africa, 85, 211-214.

Smieja-Krol, B., Duber, S. and Rouzaud, J., 2009. Multiscale organisation of organic matter associated with gold and uranium minerals in the Witwatersrand basin, South Africa. International Journal of Coal Geology, 78, 77–88.

Smits, G., 1984. Some aspects of the uranium minerals in Witwatersrand sediments of the early Proterozoic. Precambrian Research, 25, 37-59.

Spangenberg, J., and Frimmel, H. E., 2001, Basin-internal derivation of hydrocarbons in the Witwatersrand Basin, South Africa: evidence from bulk and molecular δ13C data: Chemical Geology, v. 173, p. 339-355.

Stanistreet, I.G., McCarthy, T.S., 1991. Changing tectonosedimentary. Scenarios relevant to the development of the Late Archaean Witwatersrand Basin. Journal of African Earth Sciences, 13, 65–81.

Stanistreet, I.G., McCarthy, T.S., Charlesworth, E.G., Myers, R.E. and Armstrong, R.A., 1986. Pre-Transvaal wrench tectonics along the northern margin of the Witwatersrand Basin. Tectonophysics, 131, 53–74.

Stephen, J., 2006. Stephen Johnson on Digital Photography. O'Reilly Media inc, California, 17 pp.

Thompson, K.E., Wilson, C.S. and Zhang,W., 2006. Quantitative computer reconstruction of particulate materials from microtomography images. Powder Technology 163, (3), 169–182.

Van Geet, M., Swennen, R. and Wevers, M., 2000. Quantitative analysis of reservoir rocks by microfocus X-ray computerized tomography. Sedimentary Geology, 132 (1–2), 25–36.

Van Geet, M. and Swennen, R., 2001. Quantitative 3D-fracture analysis by means of microfocus X-ray computer tomography (μCT): an example from coal. Geophysical research letters, 28 (17), 3333–3336.

Van Geet, M., Swennen, R. and Wevers, M., 2001. Towards 3-D petrography: application of microfocus computer tomography in geological science. Computers & Geosciences, 27 (9), 1091–1099.

Viljoen, R.P., Saager, R. and Viljoen, M.J., 1970. Some thoughts on the origin and processes responsible for the concentration of gold in the early Precambrian of Southern Africa. Mineralium Deposita, 5, 164-180.

Volume Graphics GmbH. 2012. *VGStudioMax 1.2.1*. Germany [Online]. Available. http://www.volumegraphics.com/en/products.html (Accessed January 2012).

Walraven, F., and Martini, J., 1995. Zircon Pb-evaporation age determinations for the Oak Tree Formation, Chuniespoort Group. Transvaal Sequence; implications for Transvaal-Griqualand West basin correlations. South African Journal of Geology, 98, 58–67.

Watts, M., 2004. The structural evolution of Kopanang Gold Mine: A working model. Submitted in fulfilment of the requirements for the degree of BSc. (Hons.) Geology, Rhodes University, 102 pp.

Young, G.M., von Brunn, V., Gold, D.J.C. and Minter, W.E.L., 1998. Earth's oldest reported glaciation: physical and chemical evidence from the Archaean Mozaan Group (2.9 Ga) of South Africa. The Journal of Geology, 106, 523–538.

Young, R.B., 1917, The Banket of the South African gold-fields: London, Gurney and Jackson, 125

## 9. APPENDIX

APPENDIX 1: Log Sheet GBH 633 from Great Noligwa Mine intersecting the Vaal Reef A Facies at 2764.25 m. The Mizpah Reef conglomerate underlies the A Facies and contains carbon fly-specks.

| **BH no.** | **From** | **To** | **No. Of broken pieces** | **Colour** | **Texture** | **G/size** | **G/shape** | **Mineral composition** | **Remarks** |
|---|---|---|---|---|---|---|---|---|---|
| GBH 633 (GN) | 2763.5 | 2764.25 | 3 | Light grey | Medium | > 2mm | Sub angular | Quartz, chert | MB4 quartz Hanging wall |
| | 2764.25 | 2766.76 | 10 | grey | coarse | 10-15mm | Sub rounded | Quartz, high uranium + pyrite 0.60 sv/h @ | Vaal A Reef Bottom sub facies |
| | 2766.76 | 2766.87 | 2 | Dark grey | med | ± 2mm | Sub ang to sub rounded | Quartz, pyrite veins | Mizpah quartzite |
| | 2766.87 | 2785 | 3 | Greyish-brown | coarse | 10-15mm | Sub rounded | Quartz, pyrite highly radioactive carbon specks 3.00 usv/h | Mizpah Reef congl. |
| | 2785 | | 1 | grey | Med - coarse | > 2mm | Sub angl sub rounded | Quartz, chert 5% | MB5 quartzite Footwall |

APPENDIX 2: Log Sheet GBH 637 from Great Noligwa Mine intersecting the Vaal Reef A Facies at 2779.9 m.

| **BH no.** | **From** | **To** | **No. Of broken pieces** | **Colour** | **Texture** | **G/size** | **G/shape** | **Mineral composition** | **Remarks** |
|---|---|---|---|---|---|---|---|---|---|
| GBH 637 (GN) | 2772 | 2772.76 | 3 | grey | coarse | ± 10 mm | Sub rounded | Quartz, pyrite veins, calcite | Mizpah Reef |
| | 2772.6 | 2774.9 | 11 | grey | medium | ± 2 mm | Sub angl to sub rounded | Quartz, chert, fine mica minerals | Mizpah quartzite |
| | 2779.9 | 2784 | 11 | grey | coarse | ± 10 mm | Sub rounded to rounded | Quartz, pyrite high radioactivity high uranium 0.50 sv/h | Vaal A Reef |
| | 2784 | 2804 | 1 | Light grey | medium | ± 2 mm | Sub angl to sub rounded | Quartz, chert | MB4 quartzite hangingwall |

APPENDIX 3: Log Sheet GBH 645 from Great Noligwa Mine intersecting the Vaal Reef C Facies with flyspeck carbons at 2636 m. the C Facies is underlain by the MB5 and overlain by the A Facies.

| **BH no.** | **From** | **To** | **No. Of broken pieces** | **Colour** | **Texture** | **G/size** | **G/shape** | **Mineral composition** | **Remarks** |
|---|---|---|---|---|---|---|---|---|---|
| GBH 645 (GN) | 2633.5 | 2634.25 | 5 | Mod grey | Coarse | 10-25 mm | Well rounded | Quartz, disseminated pyrite | Vaal A Reef top sub facies |
| | 2634.25 | 2636 | 11 | grey | Coarse | >10 mm | Angular to rounded | Quartz, angular chert, ~10mm euhedral pyrite | Vaal A Reef middle sub facies |
| | 2636 | 2636.40 | 8 | grey | Coarse | > 10 mm | Rounded | Quartz, chert, euhedral pyrite carbon flyspecks with U 1.60 usv/h | Vaal C Reef |
| | 2636.40 | 2640 | 8 | grey | Med - coarse | > 2 mm | Sub angl sub rounded | Quartz, chert 5% | MB5 quartzite Footwall |

APPENDIX 4: Log Sheet K2776 from Kopanang Mine intersecting the Vaal Reef C Facies at 1767.05 m overlain by the B Facies and underlain by the footwall MB5 quartzite.

| BH no. | From | To | No. Of broken pieces | Colour | Texture | G/size | G/shape | Mineral composition | Remarks |
|---|---|---|---|---|---|---|---|---|---|
| K2776 | 1766.0 | 1767.05 | 1 | Light grey | medium | ± 2 mm | Sub-round to rounded | Quartz, pyrite 3% | Vaal B Reef quartzite |
| | 1767.05 | 1767.2 | 1 | Greyish-brown | coarse | >10 mm | rounded | Quartz, pyrite + sulphides | Vaal C Reef congl. |
| | 1767.2 | 1768.5 | 3 | Greyish-brown | Med-coarse | ± 3 mm | Sub-angl. To sub-rounded | Quartz, pyrite and chert | MB5 quartzite Footwall |

APPENDIX 5: Log Sheet K2814 from Kopanang Mine intersecting the Vaal Reef C Facies at 1786 m, with carbon flyspecks. The reef is overlain by the B Facies and underlain by the MB5 quartzite with a radioactive vein.

| BH no. | From | To | No. Of broken pieces | Colour | Texture | G/size | G/shape | Mineral composition | Remarks |
|---|---|---|---|---|---|---|---|---|---|
| K2814 | 1785 | 1786 | 1 | Light grey | medium | ± 2mm | Sub-ang to sub-rounded | Quartz + chert 3-5% | Vaal B Reef quartzite |
| | 1786 | 1786.10 | 3 | grey | coarse | ± 18mm | rounded | Quartz, pyrite, carbon specks with high uranium 3.00 sv/h | Vaal C Reef cong |
| | 1786.10 | 1790.50 | 3 | Greyish yellow | medium | ± 2mm | Sub ang-rounded | Quartz with yellowish alteration. Grey vein – fine grained with high uranium 0.80 sv/h | MB5 quartzite Footwall + u vein |

APPENDIX 6: Log Sheet K4111 from Kopanag Mine intersecting the Vaal A Reef at 2341 m.

| BH no. | From | To | No. Of pieces | Colour | Texture | G/size | G/shape | Mineral composition | Remarks |
|---|---|---|---|---|---|---|---|---|---|
| K4111 | 2341 | 2341.36 | 8 | Dark grey | coarse | ± 8-10 mm | Sub rounded to rounded | Quartz, 2 % chert, pyrite | Vaal A Reef top sub facies |
| | 2341.36 | 2341.59 | 3 | grey | Coarse | ± 10mm | Angular to sub rounded | Quartz, pyrite, grey matrix | Vaal A Reef Bottom sub facies |

APPENDIX 7: Log Sheet K4245 from Kopanang Mine intersecting the Vaal Reef A Facies at 2320.5 m.

| BH no. | From | To | No. Of broken pieces | Colour | Texture | G/size | G/shape | Mineral composition | Remarks |
|---|---|---|---|---|---|---|---|---|---|
| K4245 | 2320.5 | 2321.40 | 14 | Grey | Coarse | ± 10 mm | Sub rounded | Quartz, chert 5%, pyrite high uranium 0.50 sv/h | Vaal A Reef bottom sub facies |
| | 2321.4 | 2321.5 | 1 | Light grey | med | ± 2mm | Sub-angl to sub-rounded | Quartz, chert | Vaal A Reef Middle sub facies |

APPENDIX 8: Log Sheet K5303 from the Kopanang Mine intersecting the Vaal Reef C Facies at 2257.1 m

| BH no. | From | To | No. Of broken pieces | Colour | Texture | G/size | G/shape | Mineral composition | Remarks |
|---|---|---|---|---|---|---|---|---|---|
| K5303 | 2257.1 | 2257.28 | 4 | Greyish brown | Coarse | ± 10-15mm | Sub-angl to sub rounded | Quartz, high uranium + pyrite 2.60 sv/h | Vaal C Reef |
| | 2257.28 | 2260 | 1 | Greyish brown | Medium | ± 1-2 mm | Sub angl to sub rounded | Quartz, grey matrix | MB5 quartzite Footwall |

APPENDIX 9: Log Sheet MK 179 from Moab Khotsong Mine intersecting the Vaal Reef A Facies at 3383.3 m overlying the Mizpah Reef.

| BH no. | From | To | No. Of broken pieces | Colour | Texture | G/size | G/shape | Mineral composition | Remarks |
|---|---|---|---|---|---|---|---|---|---|
| MK 179 | 3383.3 | 3384.15 | | grey | Coarse | ± 10mm | Sub rounded to rounded | Quartz, well pyritised high u with 0.60 usv/h | Vaal A Reef |
| | 3384.15 | 3386 | 9 | grey | Coarse | ± 10mm | Sub angl to sub rounded | Quartz, chert, well pyritised | Mizpah Reef |
| | 3386 | 3400 | 2 | grey | medium | ± 2mm | Sub angular | Quartz, chert | MB5 quartzite Footwall |

APPENDIX 10: Log Sheet MK 283R from Moab Khotsong Mine intersecting the Vaal Reef A Facies at 3306 m overlying the Mizpah Reef.

| BH no. | From | To | No. Of broken pieces | Colour | Texture | G/size | G/shape | Mineral composition | Remarks |
|---|---|---|---|---|---|---|---|---|---|
| MK 283R | 3306 | 3306.96 | 12 | Grey | coarse | ± 10-20 mm | rounded | Quartz, chert, pyrite and high u 0.70 usv/h | Vaal A Reef |
| | 3306.96 | 3308 | 13 | Grey | coarse | ± 10mm | Sub angl to sub rounded | Quartz, chert, well pyritised | Mizpah Reef |
| | 3308 | 3330 | 1 | Grey | medium | ± 2mm | Sub angular | Quartz, chert | MB5 quartzite Footwall |

APPENDIX 11: Seven samples collected from the A Facies drilled boreholes from Great Noligwa, Kopanang and Moab Khotsong Mines.

| Borehole | Geozone | Number of samples | Name | Sample description |
|---|---|---|---|---|
| GBH633 | 370 | 1 | Vaal Reef A Bottom Sub-facies | Sub-rounded 10 to 15 mm quartz conglomerate with pyrite-rich matrix and radioactivity of 0.60 sv/h. |
| | | | | |
| GBH637 | 370 | 1 | Vaal Reef A Facies | Sub-rounded 10 mm quartz conglomerate with pyrite-rich matrix and radioactivity of 0.50 sv/h. |
| | | | | |
| GBH645 | 500 | 1 | Vaal Reef A Middle Sub-facies | Sub-angular to subround 10 mm quartz, angular chert, ~10mm euhedral pyrite. |
| | | | | |
| K4111 | 500 | 1 | Vaal Reef A Bottom Sub-facies | Quartz pebble (10 mm) conglomerate with grey matrix and pyrite. |
| | | | | |
| K4245 | 500 | 1 | Vaal Reef A Bottom Sub-facies | Quartz pebble (10 mm sized) conglomerate with angular chert 5%, pyrite-rich and radioactivity of 0.50 sv/h. |
| | | | | |
| MK179 | 370 | 1 | Vaal Reef A Facies | 10 mm sized quartz, well pyritised with 0.60 usv/h radioactivity. |
| MK283R | 370 | 1 | Vaal Reef A Facies | 10 mm sized quartz pebble conglomerate with angular chert, pyrite and radioactivity of 0.70 usv/h. |
| **Total** | | | **7 samples** | |

APPENDIX 12: Five samples collected from the C Facies drilled boreholes from Great Noligwa, Kopanang and Moab Khotsong Mines.

| Borehole | Geozone | Number of samples | Name | Sample description |
|---|---|---|---|---|
| GBH645 | 500 | 1 | Vaal Reef C Facies | Well-rounded 10 mm quartz pebble conglomerate with chert, euhedral pyrite carbon flyspecks with 1.60 usv/h. |
| | | | | |
| K2776 | 460 | 1 | Vaal Reef C Facies | Well-rounded 10 mm quartz pebble conglomerate with pyrite-rich matrix. |
| | | | | |
| K2814 | 460 | 1 | Vaal Reef C Facies | ± 18mm rounded quartz-pebble with pyrite, carbon specks with high radioactivity of 3.00 sv/h. |
| | | | | |
| K5303 | 460 | 1 | Vaal Reef C Facies | 10-15mm sub-angular to sub-rounded quartz conglomerate with pyrite and high radioactivity of 2.60 sv/h. |
| | | | | |
| MK1033 | 370 | 1 | | |
| **Total** | | | **5 samples** | |

APPENDIX 13: Four samples collected from the Vaal Reef footwall drilled boreholes from Great Noligwa, Kopanang and Moab Khotsong Mines.

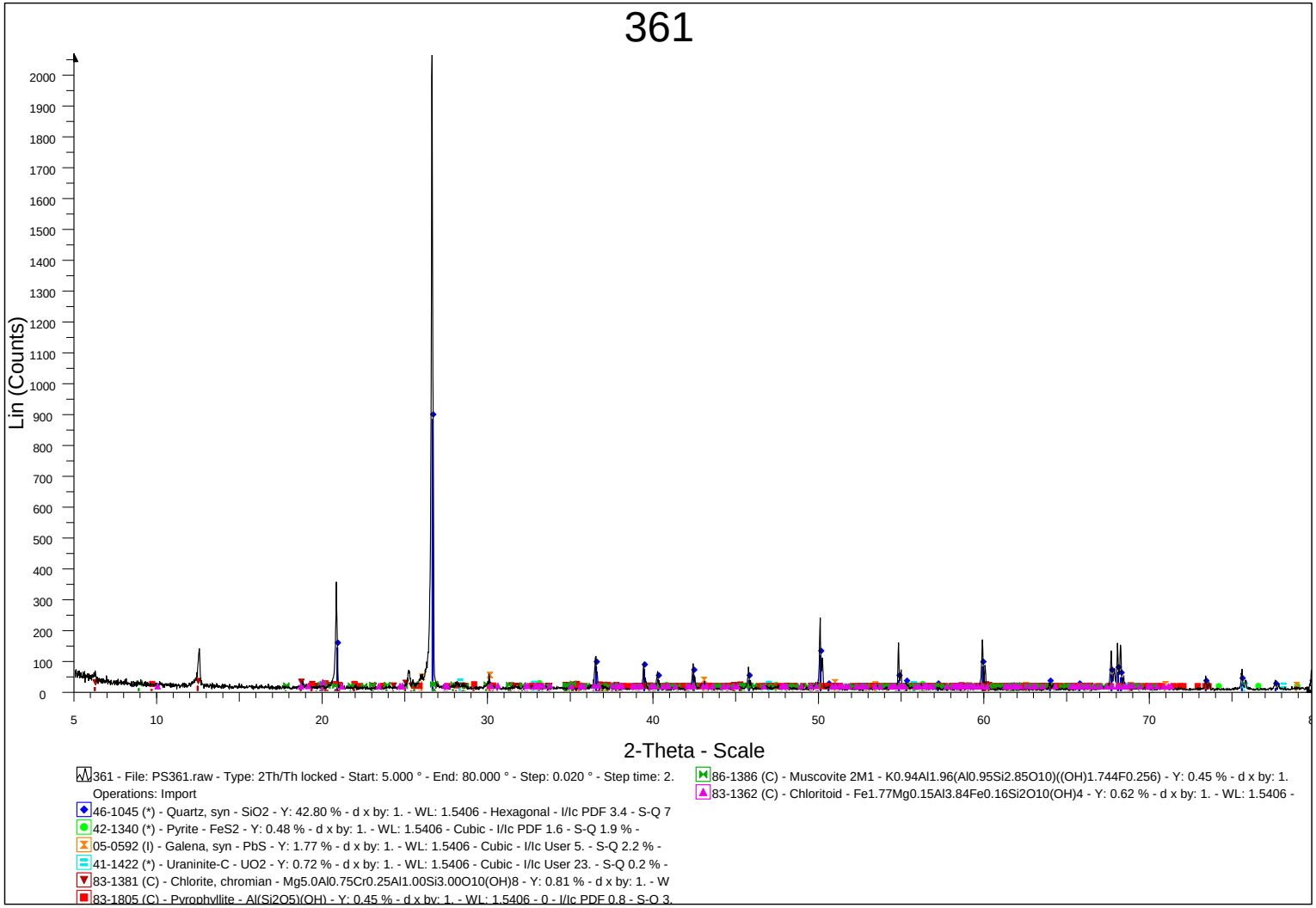
| **Borehole** | **Number of samples** | **Name** | **Sample description** |
|---|---|---|---|
| GBH633 | 1 | Mizpah Reef | Sub-rounded 10 to 15 mm quartz conglomerate with high pyrite content in matrix and highly radioactive carbon specks 3.00 usv/h. |
| | | | |
| GBH637 | 1 | Mizpah Reef | Sub-rounded quartz (10 to 15 mm) conglomerate with pyrite matrix. |
| | | | |
| K2814 | 1 | MB5 quartzite | Very fine-grained grey matrix with radioactive readings of 0.80 usv/h. |
| | | | |
| MK179 | 1 | Mizpah Reef | 10 mm quartz conglomerate with well pyritised matrix. |
| **Total** | | **4 Samples** | |

APPENDIX 14: Seven samples collected from the A Facies underground panels at Moab Khotsong Mine.

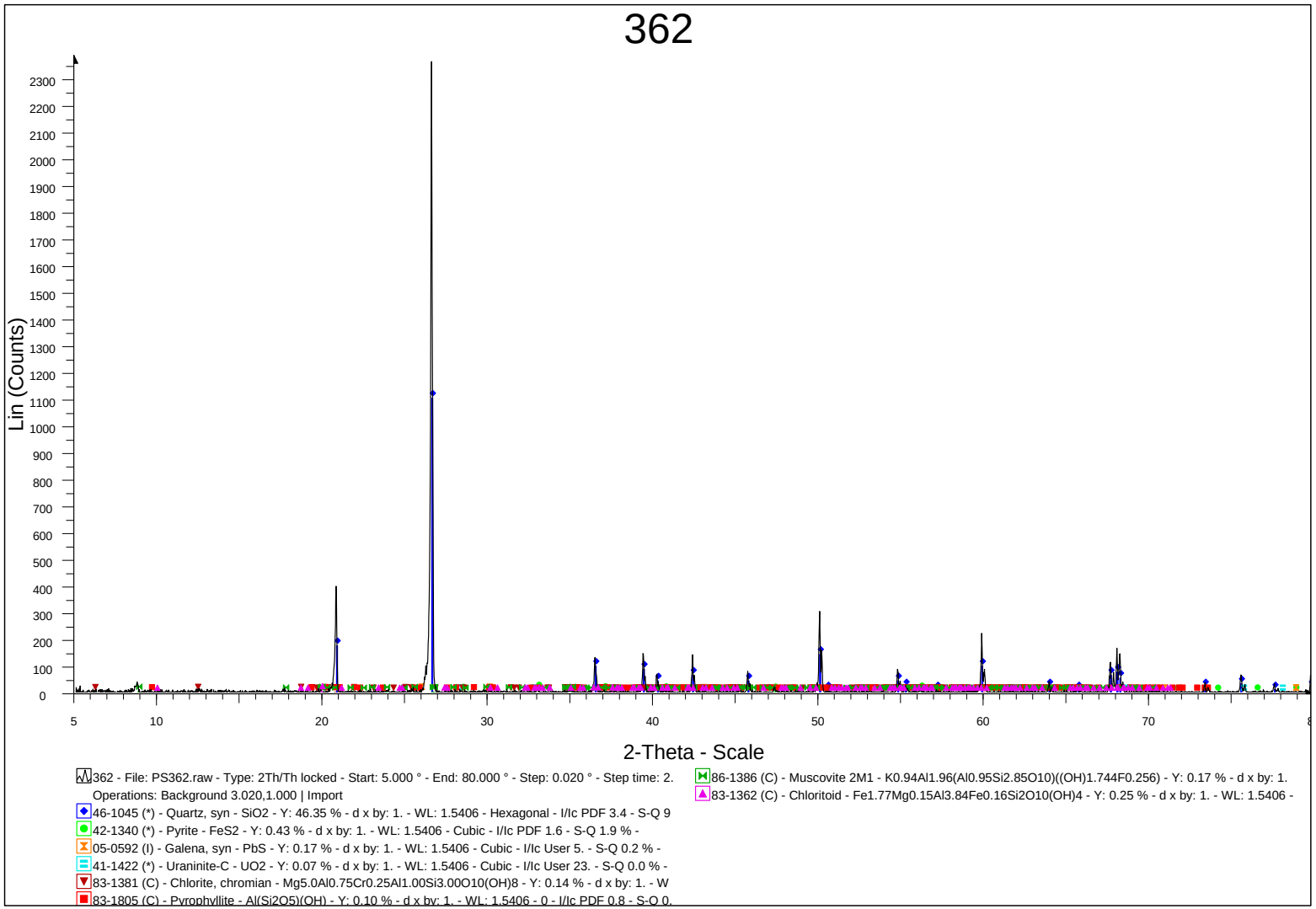
| Sample number | Geozone | Number of samples | Name | Sample description |
|---|---|---|---|---|
| MK361 | 370 | 1 | Vaal Reef A Facies | Oligomictic quartz-pebble conglomerate with pyrite and carbon |
| | | | | |
| MK362 | 370 | 1 | Vaal Reef A Facies | Oligomictic quartz-pebble conglomerate with pyrite and carbon |
| | | | | |
| MK363 | 370 | 1 | Vaal Reef A Facies | Oligomictic quartz-pebble conglomerate with pyrite and carbon |
| | | | | |
| MK364 | 370 | 1 | Vaal Reef A Facies | Oligomictic quartz-pebble conglomerate with pyrite and carbon |
| | | | | |
| MK365 | 370 | 1 | Vaal Reef A Facies | Oligomictic quartz-pebble conglomerate with pyrite and carbon |
| | | | | |
| MK366 | 370 | 1 | Vaal Reef A Facies | Oligomictic quartz-pebble conglomerate with pyrite and carbon |
| | | | | |
| MK367 | 370 | 1 | Vaal Reef A Facies | Oligomictic quartz-pebble conglomerate with pyrite and carbon |
| **Total** | | | **7 Samples** | |

APPENDIX 15: Fifteen samples collected from the C Facies underground panels at Kopanang Mine.

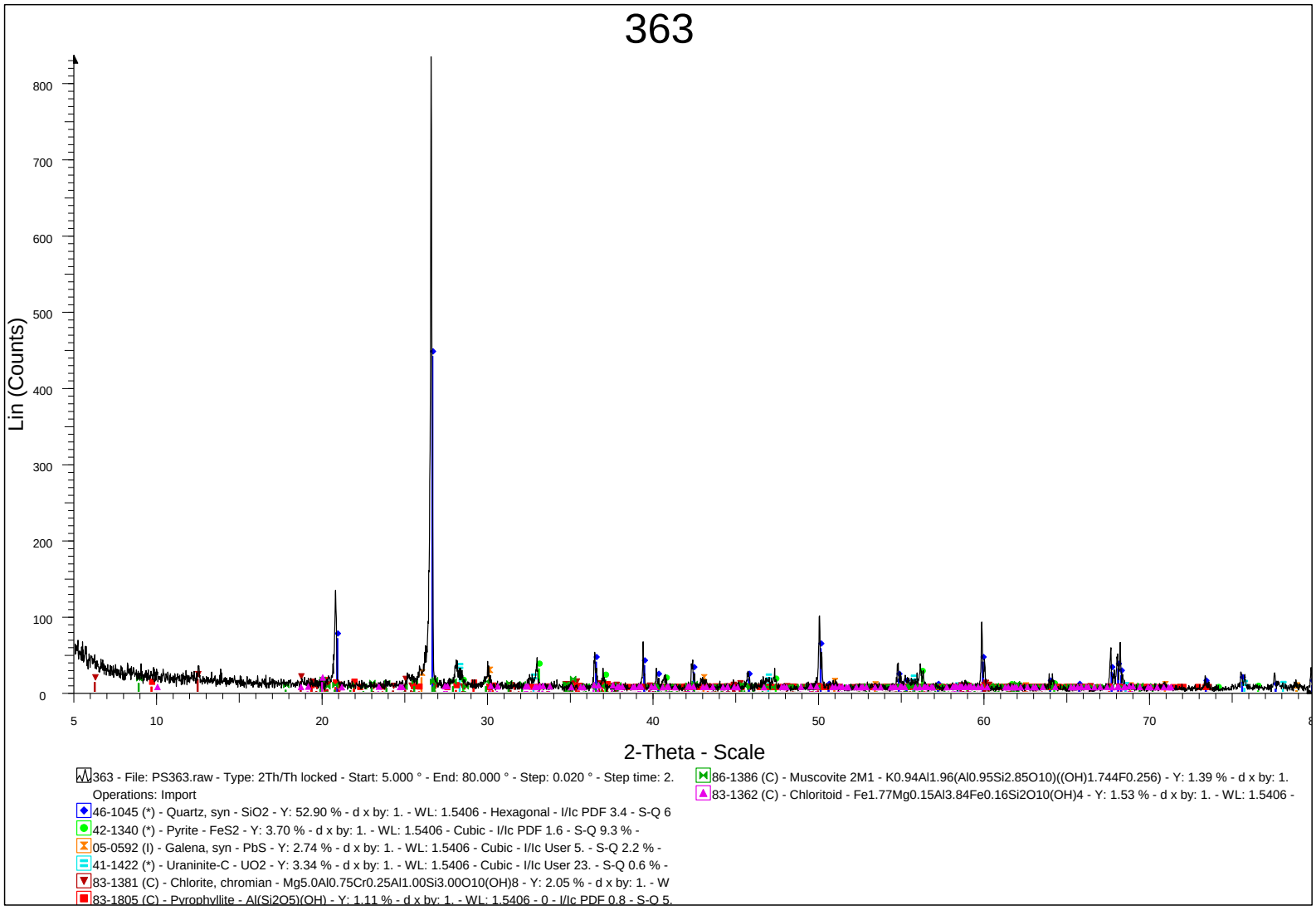
| Sample number | Geozone | Number of samples | Name | Sample description |
|---|---|---|---|---|
| 1k1<br>1k2<br>1k3<br>1k4<br>1k5 | 440 | 5 | Vaal Reef C Facies | Samples were collected from one panel from underground, the quartz-pebble conglomerate has high pyrite content with thin carban seams (~5 mm). |
| | | | | |
| 2k1<br>2k2<br>2k3<br>2k4<br>2k5<br>2k6 | 460 | 6 | Vaal Reef C Facies | Samples display thicker carbons seams (10 mm) |
| | | | | |
| 3k1<br>3k2<br>3k3<br>3k4 | 460 | 4 | Vaal Reef C Facies | Samples have high pyrite contents with thin carbon seams |
| **Total** | | | **15 Samples** | |



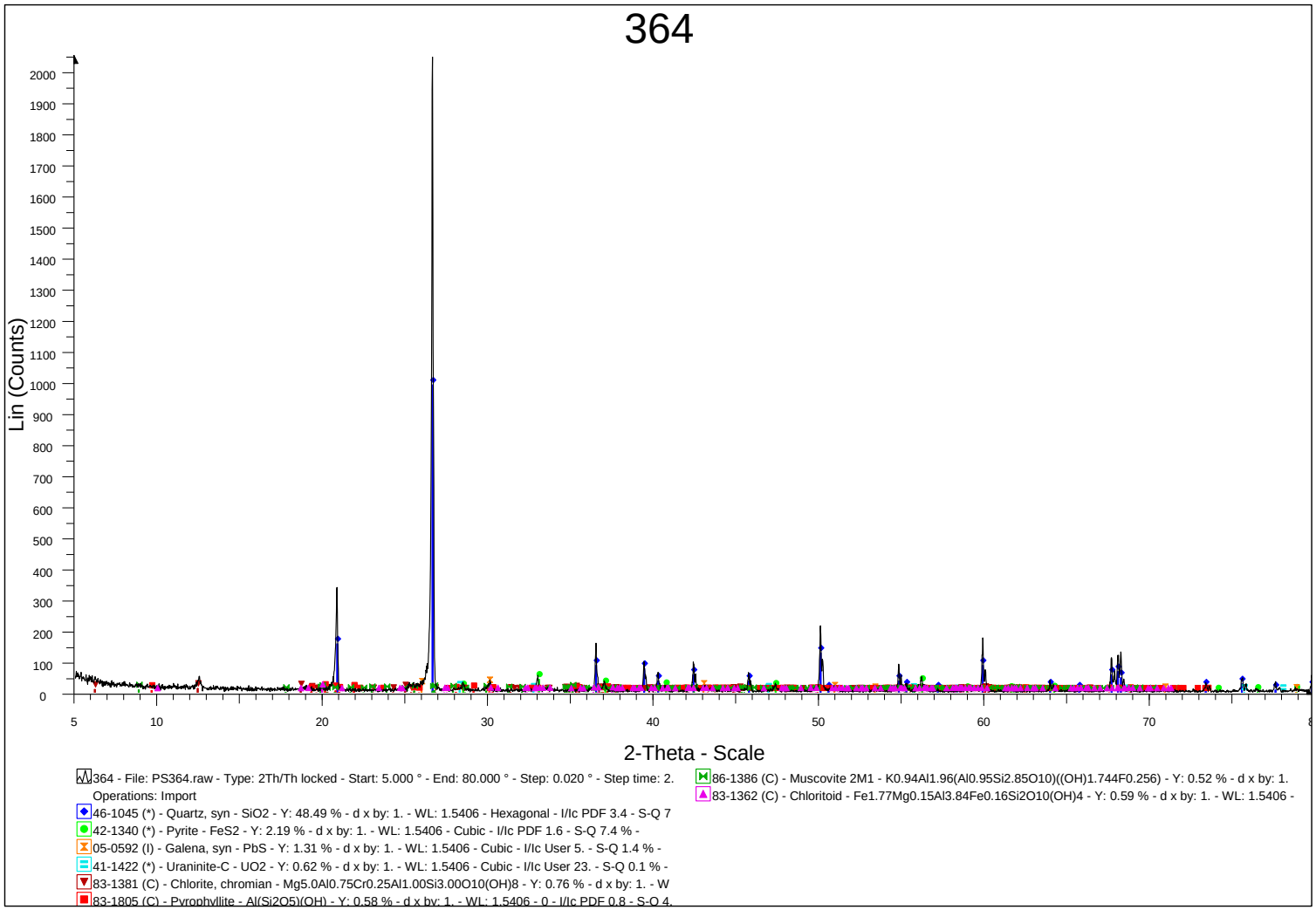

Appendix 16: Diffractogram of sample MK361 from Moab Khotsong Mine representing the 370 geozone.



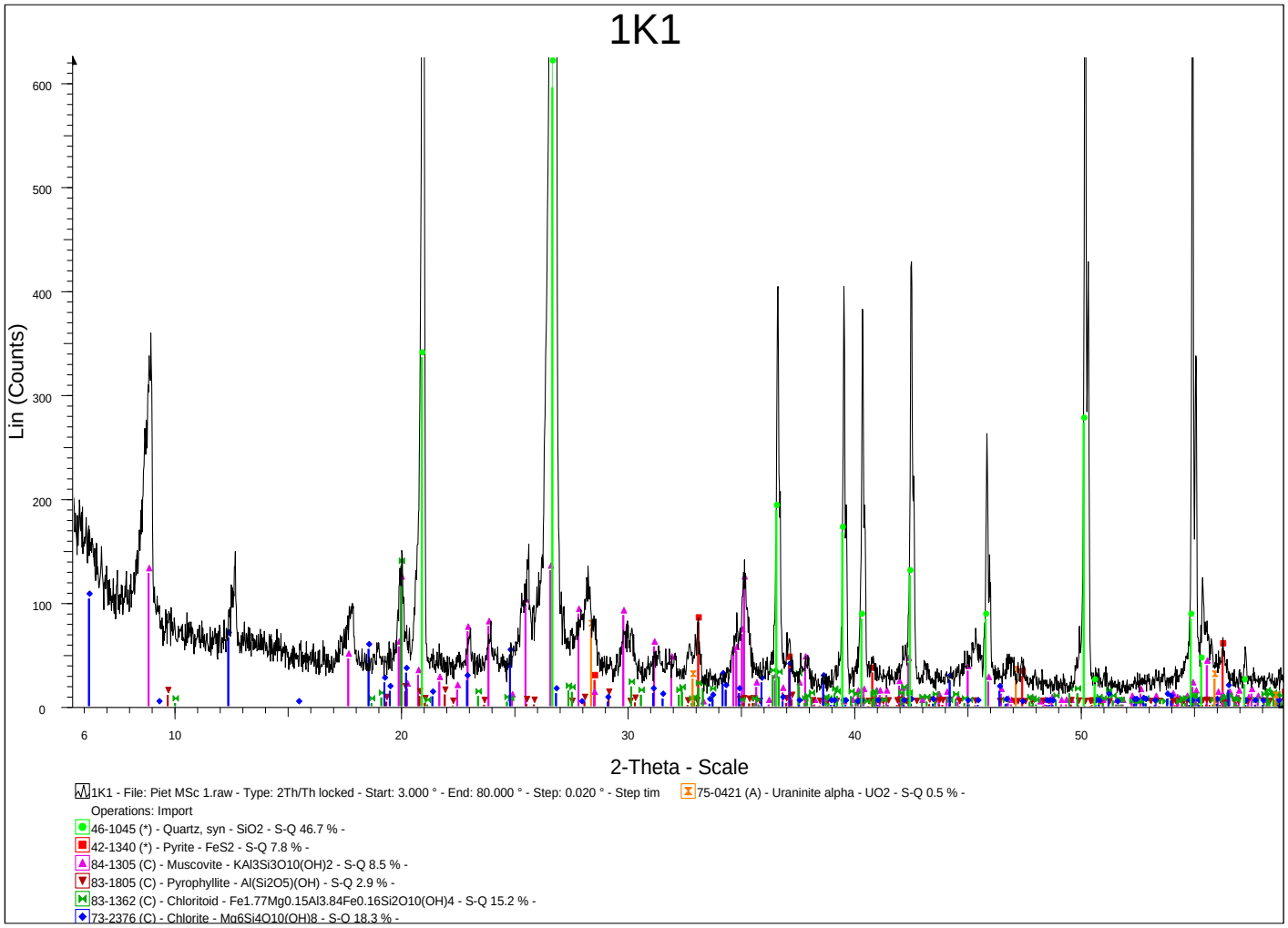

Appendix 17: Diffractogram of sample MK362 from Moab Khotsong Mine representing the 370 geozone.



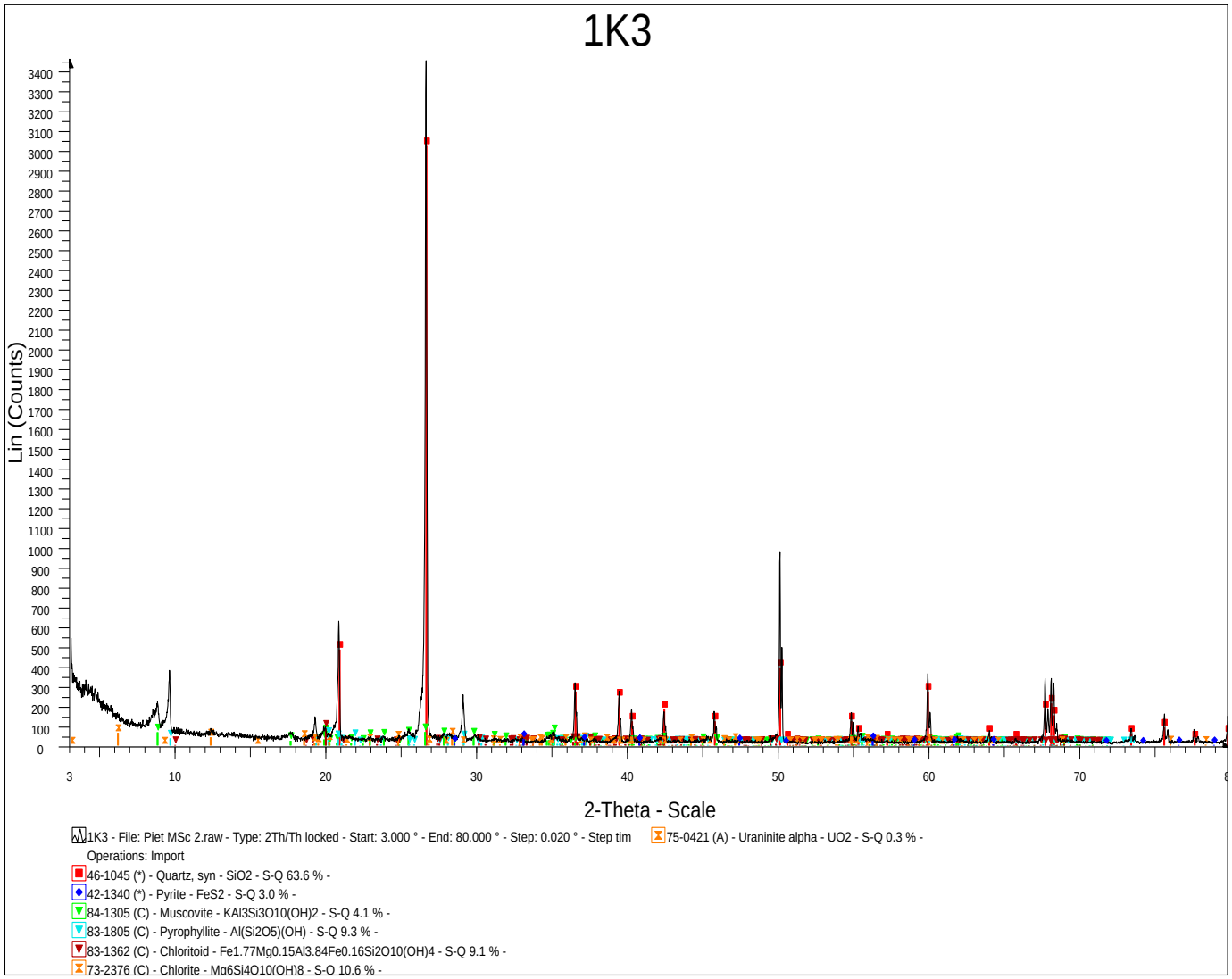

Appendix 18: Diffractogram of sample MK363 from Moab Khotsong Mine representing the 370 geozone.



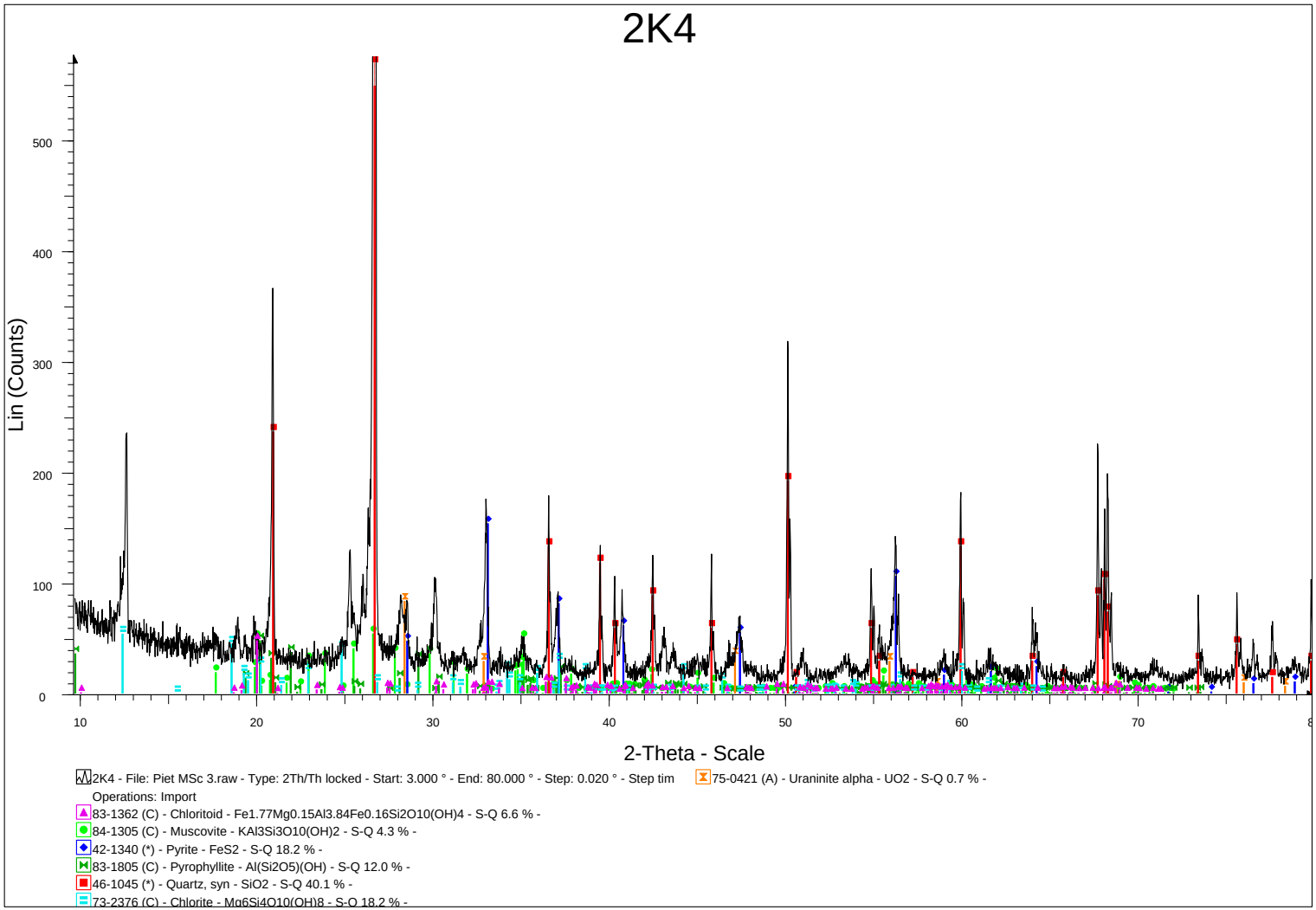

Appendix 19: Diffractogram of sample MK364 from Moab Khotsong Mine representing the 370 geozone.



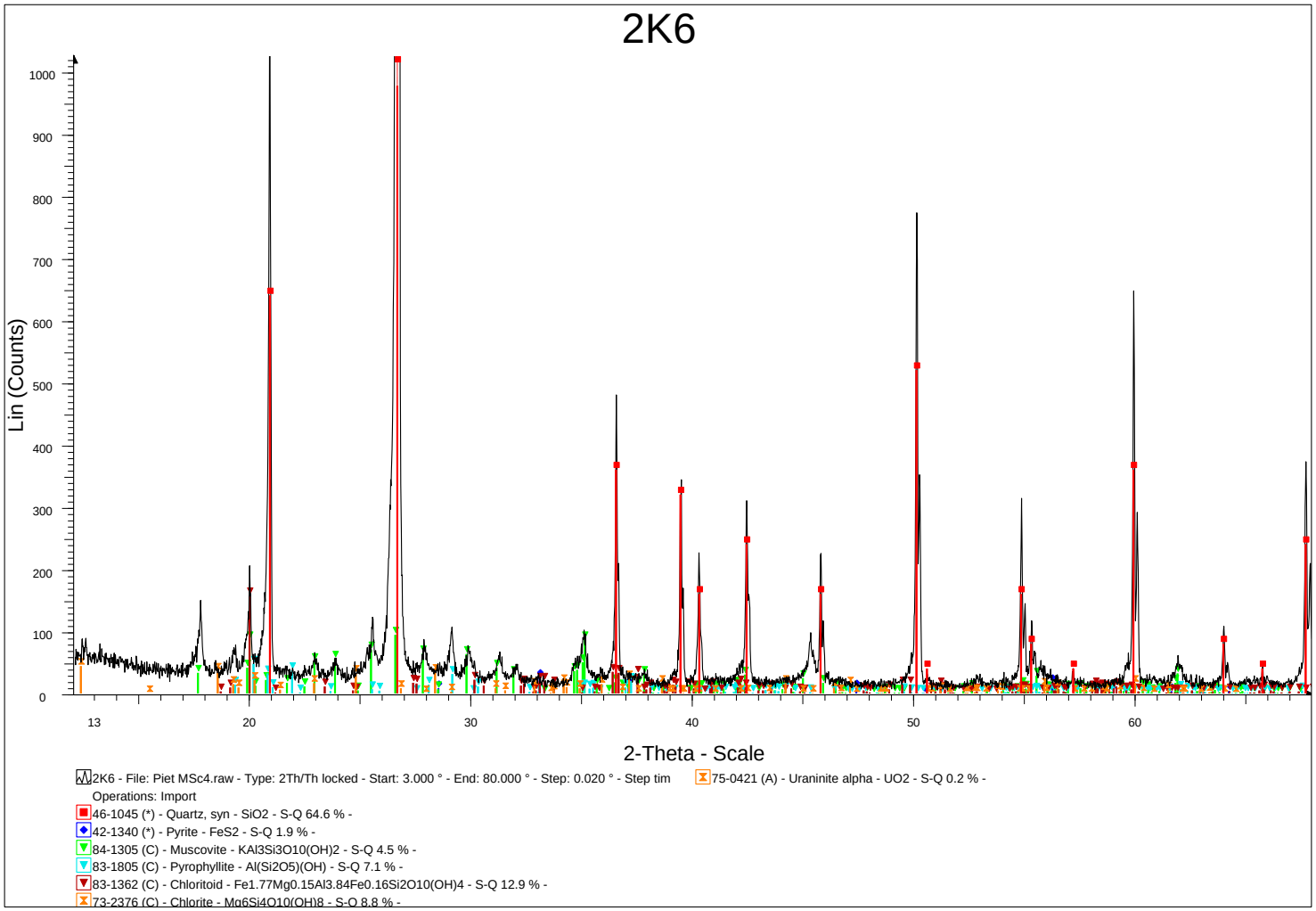

Appendix 20: Diffractogram of sample 1K1 from Kopanang Mine representing the 440 geozone.



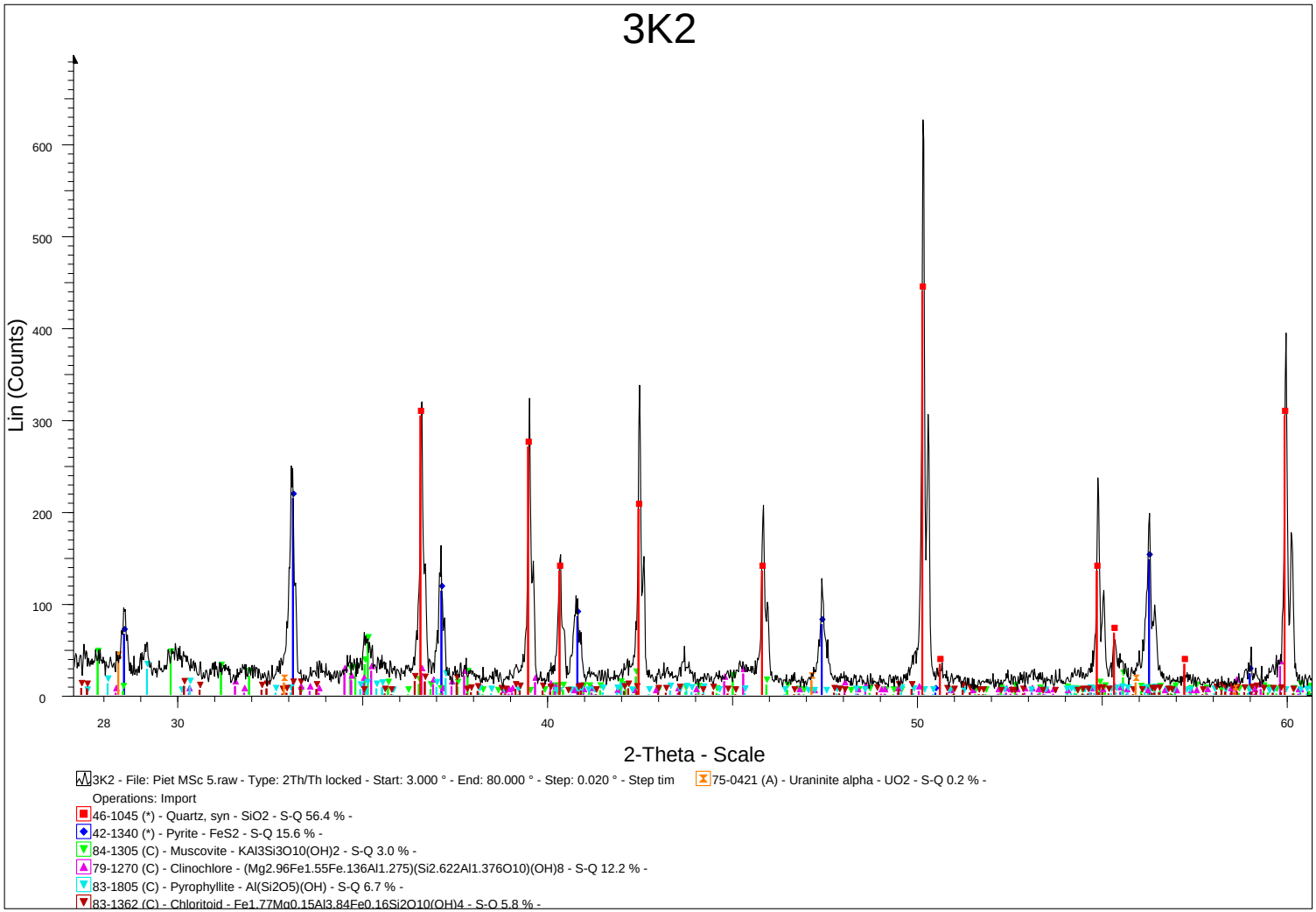

Appendix 21: Diffractogram of sample 1K3 from Kopanang Mine representing the 440 geozone.



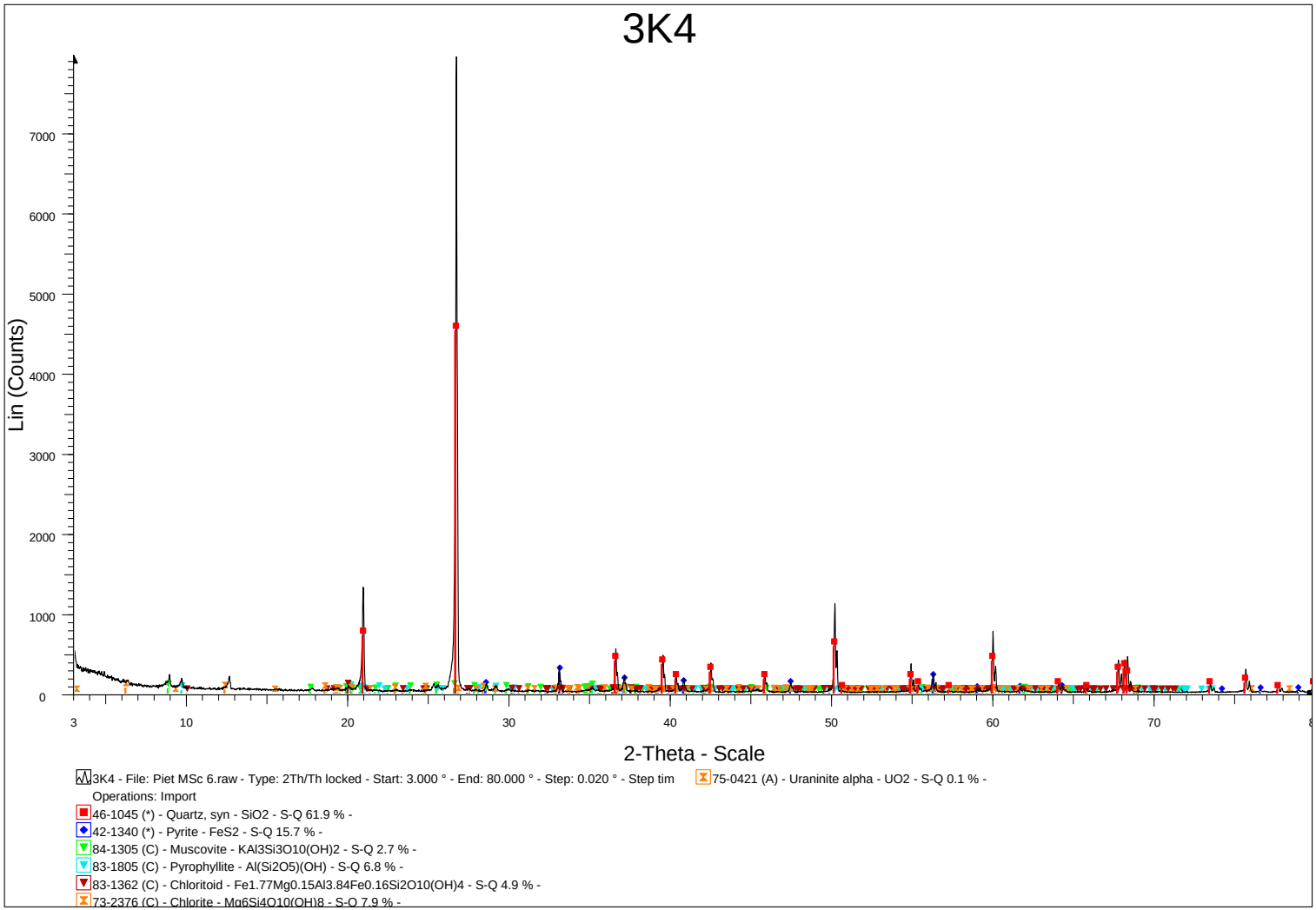

Appendix 22: Diffractogram of sample 2k4 from Kopanang Mine representing the 460 geozone.



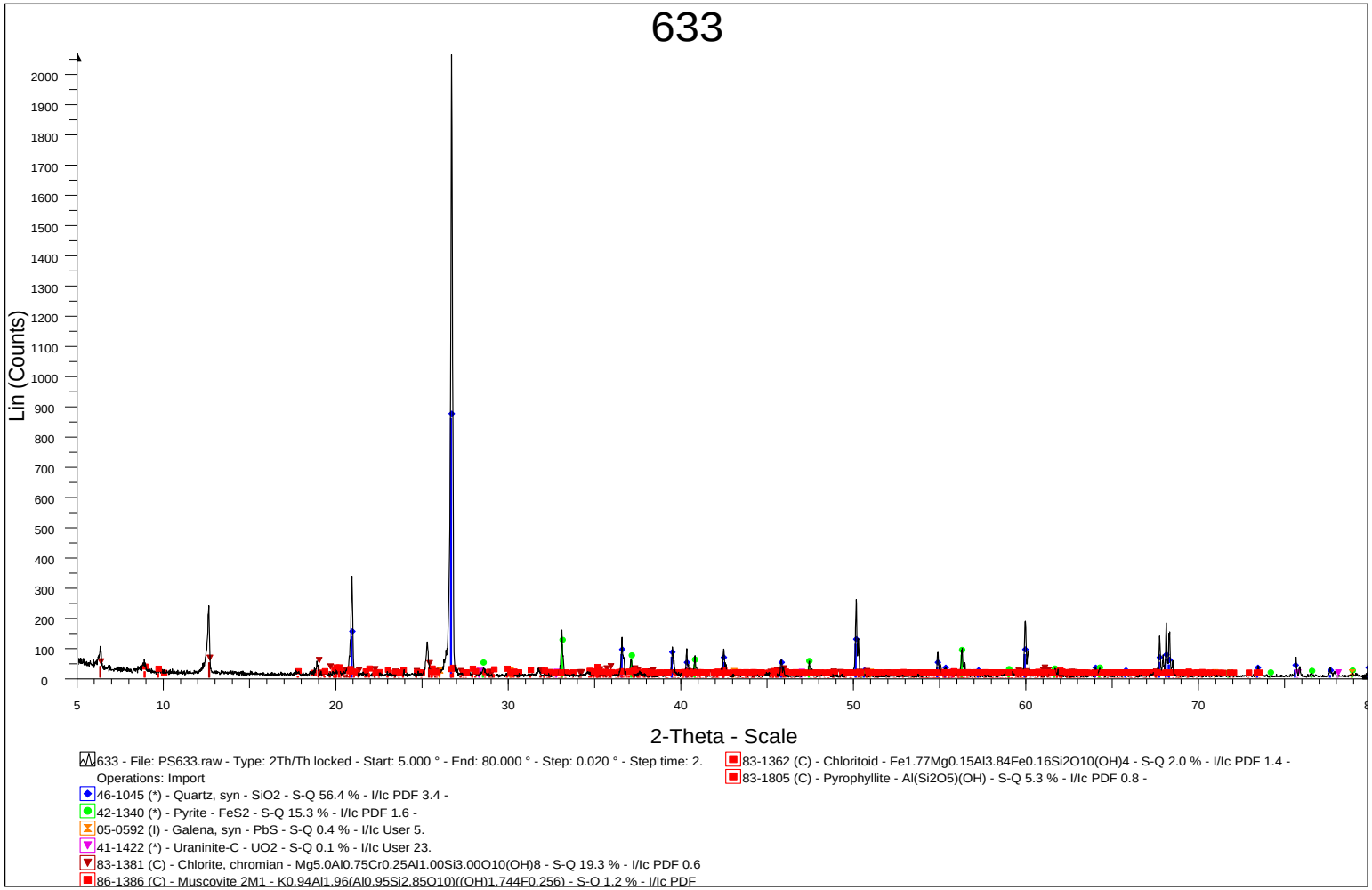

Appendix 23: Diffractogram of sample 2k6 from Kopanang Mine representing the 460 geozone.



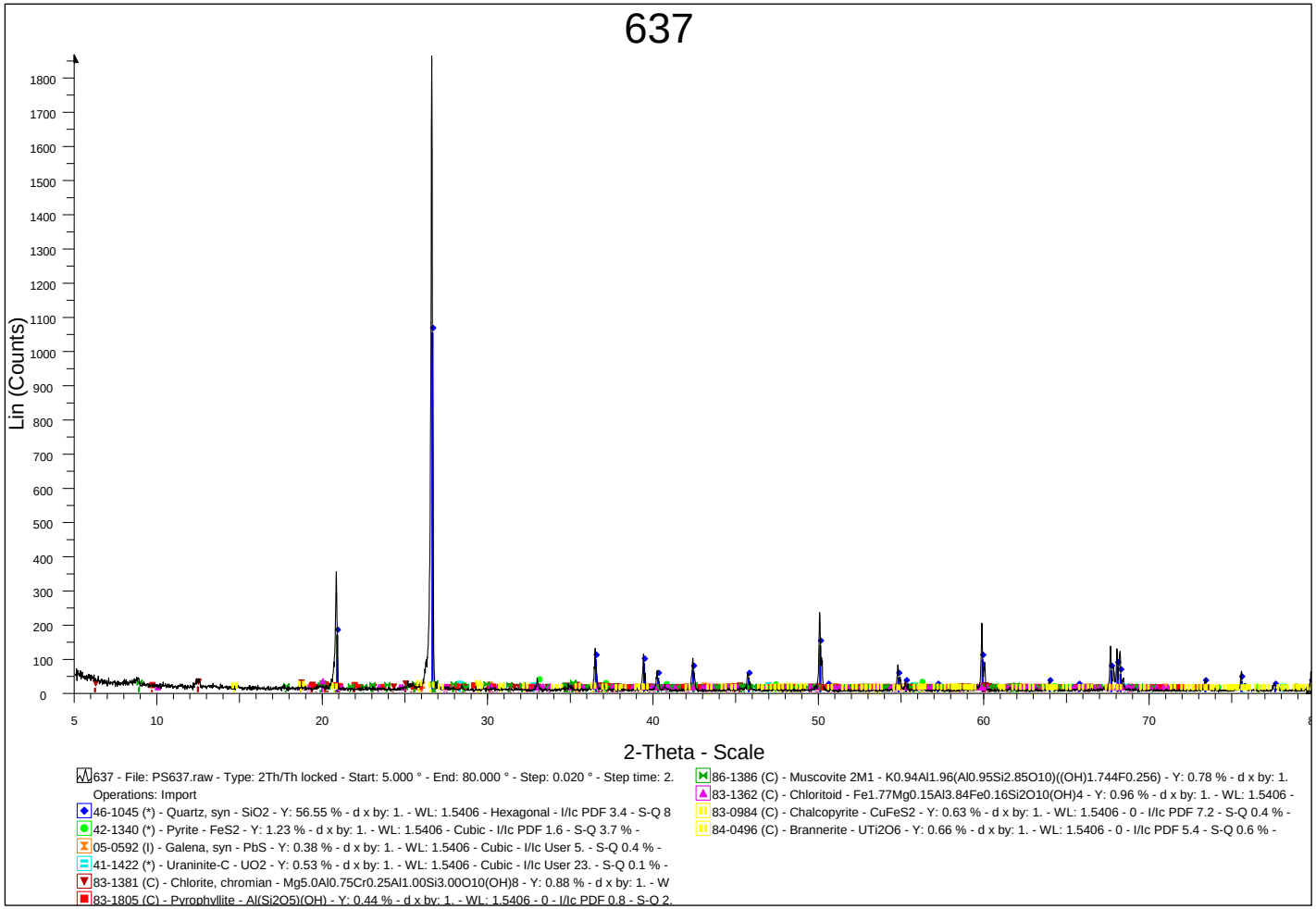

Appendix 24: Diffractogram of sample 3k2 from Kopanang Mine representing the 460 geozone.




Appendix 25: Diffractogram of sample 3k4 from Kopanang Mine representing the 460 geozone.




Appendix 26: Diffractogram of sample GBH 633 from Great Noligwa Mine representing the 370 geozone.




Appendix 27: Diffractogram of sample GBH 637 from Great Noligwa Mine representing the 370 geozone.